Grain Boundary Engineering in Ni-Based Alloys: Processing, Mechanisms and Effect on Mechanical Properties



Yuanbo T. Tang

Supervisor: Prof. A.J. Wilkinson
Prof. R.C. Reed

Department of Materials
University of Oxford

This dissertation is submitted for the degree of
Doctor of Philosophy

St Edmund Hall

Submitted December 2018

Going, going, gone...

Acknowledgements

There are a number of people and organisations I would like to express my sincerest gratitude, with their unfailing support and company, I have embraced an incredible three-year time in Oxford.

I am grateful to my academic supervisors, Professors Roger C. Reed FREng and Angus J. Wilkinson for their patient, encouraging and inspiring training. I have benefited extensively from their combined expertise on nickel superalloys and electron microscopy. Most importantly, I thank them for stimulating my personal and professional development, their charming characters have demonstrated responsibility, judgment and confidence.

I would like to thank the organisations for the provision of project funding, scholarship and grants for me to complete my doctoral studies. Great appreciation deserves St Edmund Hall for financial support through William R Miller Award. Also, I give my special thanks to Mitsubishi Heavy Industries, Ltd (Japan), for sponsoring some part of the work and scholarship. Further, I would like to acknowledge OxMet Technologies Ltd and IHI Corporation for the intriguing side projects and provision of my write-up grants.

I am immensely grateful to my collaborators. To Dr Fauzan Adziman who has been a tremendous mentor to me, I have learnt from him on so many aspects. I also wish to thank my industrial collaborators from Mitsubishi. To Dr Masaki Teneike and Mr Ikuo Okada for providing experimental data and fruitful discussions, as well as Dr Sunao Aoki for sharing his invaluable experience on his world-class project management

skills. A special thank you is owed to Dr Andre Nemeth, Dr Chinnapat Panwisawas and Dr John Clark for taking me on board the additive manufacturing world. I am also very grateful to Dr Phani Karamched, I will always remember our passionate faces while we first discovered some new capacities of SEM. Special thanks should also give to Junliang Liu and Dr Jack Haley, who are my favourite TEM scientists. I am also grateful to Dr Enrique Alabort, who taught me how to operate many mechanical testing facilities. Of course, I also owe Dr Yilun Gong a lot, for patiently solving all my trivial problems. Special mentions deserve Professors Rui Yang and Jian Zhang from Institute of Metal Research and Prof Qiang Feng from University of Science and Technology Beijing. I thank them for the intellectual discussions and suggestions to my research and career.

I would like to thank my wonderful colleagues in both solid mechanics group and micro-mechanics group for providing a dynamic and friendly environment to work, including by not limited to Dr Daniel Barba, Joseph Ghoussoub, Sabin Sulzer, Dr David Crudden, Koji Kageyama, Hirokazu Usuki, Arutyun Arutyunyan, Dr David Collins, Dr Jianglin Huang, Dr Parakevas Kontis, Dr Antonio Pellegrino, Dr Jicheng Gong, Dr Bo-shiuan Li, Dr Haiyang Yu, Dr Junnan Jiang, Dr Anna Kareer, Carles Alabort, Hisham Elamin, Dr Hao Cui, John Waite and Yi Xiong. I am also indebted to Karen Bamford and Rebecca Bradford for excellent organising and support. I must also thank support staffs and technicians in Materials and Engineering department: Gabriella Chapman, Dr Gareth Hughes, Jennifer Holter, Dr Andrew Lui, Jeffery Fullerton, Stuart Carter, Tony Wheeler, Graham Wyatt, Greg Cook and Chris Salter.

I would like to give special thanks to my dear folks. Including but not limited to Dr Shaokai Zheng, Zhengrong Yu, Dr Youmin Rong, Allan Rushforth, Dr Yixing Wu, Qi Meng, Dunhong Jin, Yifan Cai, Xilin Jiang, Zeping Zhu, Dr Fangxin Li, Liwen Tu, Yuzhou Sun, Siping Shan, Yuchen Lu, Muzhe Li, Cong Wang, Lyn Tang, Tongmeng

Li, Dr Yuefeng Cui, Jasphy Zheng. Your diverse interests, inspirations and company never make me bored.

A very special gratitude goes to Yuxin (Corrine) Yin, my lucky charm, my partner, my boat.

Lastly, but most importantly, I would like to give a huge thanks to my parents, Honghou Tang and Xiaohong Liu, and my grandparents, for your moral and emotional support in my life. I owe it all to you!

Preface

Research in this thesis has been prepared for publication as follows:

- **Yuanbo T. Tang**, Phani Karamched, Junliang Liu, Jack Haley, Roger C. Reed, Angus J. Wilkinson *Grain Boundary Serration in Nickel Alloy Inconel 600: Quantification and Mechanisms*, Acta Materialia, under review.

- **Yuanbo T. Tang**, Angus J. Wilkinson, Roger C. Reed *Grain Boundary Serration in Nickel-Based Superalloy Inconel 600: Generation and Effects on Mechanical Behaviour*, Metallurgical and Materials Transaction A, September 2018, Volume 49, Issue 9, pp. 4324-4342, doi: 10.1007/s11661-018-4671-7

- **Yuanbo T. Tang**, Fauzan Adziman, Masaaki Taneike, Ikuo Okada, Roger C. Reed *A Rationalisation of Creep Response of a Nickel-Based Superalloy for Power Generation Applications*, Materials Science and Engineering A, in progress.

- **Yuanbo T. Tang**, Phani Karamched, Roger C. Reed, Angus J. Wilkinson *Characterisation of Dislocation Structures Using On-Axis Transmission Kikuchi Diffraction in Scanning Electron Microscopy*, Scripta Materialia, in progress.

Abstract

The property of polycrstalline nickel alloys are crucially dependent upon grain boundaries, as they are the strength limiting sites at high temperatures. Engineering of grain boundary structure and phases can be effective means of pursuing optimum properties of a component. Grain boundary morphologies are known to have critical impact on time dependent deformation, such as creep and fatigue. However, the reason for such an improvement is only understood qualitatively, the mechanisms of its formation or strengthening are not well understood. Roles of second phase particles on mechanical properties, such as carbides and borides, are still in an open debate. The present research tackled the questions from a fundamental perspective. The results accomplished have gained a deep understanding on the underlying science and satisfied industrial interests. This is achieved by carefully controlled experimentation and advanced characterisation. First, grain boundary morphologies are shown to be sensitive to the heat treatment that is given, and intergranular phases are proven to be responsible for obtaining serrated boundaries. Next, mechanical response between different grain boundary structures are distinctive, which is further elucidated by strain and tomography analysis. Last, minor element additions showed drastic improvement

of creep life by redecoration of grain boundary phases. Overall, the thesis presents the mechanistic study of grain boundary structures, which is thoroughly investigated through the processing parameters on alteration of second phase particles and its influence on mechanical properties.

Table of contents

Preface **ix**

List of figures **xvii**

List of tables **xxiii**

1 Introduction **1**

1.1 Nickel-based alloys 1

1.2 Aim of the research 3

1.3 Structure of the thesis 4

2 Literature Review **9**

2.1 Physical metallurgy of Nickel-based alloys 9

2.1.1 The γ matrix 10

2.1.2 The γ' precipitate 12

2.1.3 Carbides and borides 13

2.1.4 Topological closed packed phases 15

2.2 Physics of Grain boundaries 16

2.2.1 Description of grain boundaries 16

2.2.2 Grain boundary structures 18

2.2.3 Grain boundary segregation 23

2.3 Processing and microstructure control of nickel-based alloys 28

2.3.1 Processing routes for nickel-based alloys 28

2.3.2 Heat treatment types and their aims 33

2.4 Formation of grain boundary serration in Nickel-based alloys 37

2.4.1 Grain boundary serration assisted by intergranular phases . . . 39

2.4.2 Grain boundary serration in relation to chemical compositions . 47

2.4.3 Summary 50

2.5 Effect of grain boundary serration on the mechanical properties in Nickel-based alloys . . . 50
2.5.1 Room temperature mechanical properties . . . 51
2.5.2 High temperature mechanical properties . . . 51
2.5.3 Secondary effect induced by processing . . . 56
2.5.4 Summary . . . 59
2.6 Conclusion remarks . . . 59

3 Experimental and Characterisation Techniques 61
3.1 The material . . . 61
3.1.1 Inconel 600 . . . 61
3.1.2 MGA1400CC . . . 62
3.2 Mechanical testing . . . 64
3.2.1 Creep testing . . . 64
3.2.2 *In-situ* tensile test in SEM . . . 66
3.3 Charaterisation . . . 67
3.3.1 Scanning electron microscopy based characterisation . . . 67
3.3.2 Transmission electron microscopy based characterisation . . . 69
3.3.3 X-ray computed tomography . . . 71

4 Formation Mechanisms and Quantification of Grain Boundary Serration in Inconel 600 73
4.1 Introduction . . . 73
4.2 Methodology and experimental . . . 76
4.2.1 Heat treatment . . . 77
4.2.2 Scanning electron microscope and image processing . . . 80
4.2.3 Transmission based characterisation . . . 82
4.2.4 Quantification of serration using fast Fourier transform . . . 82
4.3 Results . . . 86
4.3.1 Microstructure overview: as-received and heat treated materials 86
4.3.2 Carbide: identification and evolution . . . 90
4.3.3 Serration index & carbide as a function of heat treatment . . . 94
4.4 Discussion . . . 104
4.4.1 Phenomenological study: classification, determination & definition 104
4.4.2 Formation mechanisms on serrated grain boundary . . . 105
4.4.3 Processing map construction . . . 115
4.5 Summary and Conclusions . . . 121

5 Effect of Grain Boundary Serration on Mechanical Behaviour in Nickel Alloy Inconel 600 123
5.1 Introduction . . . 123
5.2 Methodology and Experimental Description . . . 127
5.2.1 Heat treatment . . . 128
5.2.2 Creep testing . . . 128
5.2.3 *In-situ* tensile test in SEM . . . 131
5.2.4 SEM based characterisation . . . 131
5.2.5 X-ray tomography based characterisation . . . 132
5.3 Results . . . 133
5.3.1 Heat treatment and grain boundary serration development . . . 133
5.3.2 Creep tests and fractography . . . 136
5.3.3 *In-situ* tensile testing . . . 140
5.3.4 HR-EBSD on fractured specimens . . . 144
5.3.5 Interrupted creep test . . . 147
5.3.6 X-ray tomography technique . . . 152
5.4 Discussion . . . 159
5.4.1 Carbide distribution and its evolution . . . 159
5.4.2 Dislocation accumulation . . . 163
5.4.3 Assessment of degree of cavitation . . . 166
5.5 Summary and Conclusions . . . 171

6 A Rationalisation of Creep Response of a Nickel Based Superalloy for Power Generation Applications 175
6.1 Introduction and background . . . 175
6.2 Methodology and Experimental Description . . . 177
6.2.1 Material . . . 177
6.2.2 Creep testing . . . 177
6.2.3 X-ray computed tomography . . . 178
6.2.4 Scanning electron microscopy characterisation . . . 178
6.2.5 *In-situ* tensile test in SEM . . . 179
6.2.6 Numerical approach for creep model . . . 179
6.3 Results . . . 182
6.3.1 Creep rupture life: influence of grain size and creep conditions . 182
6.3.2 Microstructure characterisation: virgin and crept materials . . . 183
6.3.3 Specimen shape change due to creep anisotropy . . . 189
6.4 Discussion . . . 193

6.4.1 Creep scattering: influence of dominant slip system and carbide 193
6.4.2 Influence of microstructure in relation to chemical modification . 199
6.4.3 Materials development framework 203
6.5 Summary and Conclusions 204

7 Conclusions and Future Work 207
7.1 Conclusion remarks 207
7.2 Future Work 210
7.2.1 Extension on other alloys 210
7.2.2 Extension on other properties 211
7.2.3 Generalisation of grain boundary engineering with modelling . . 212

References 215

List of figures

1.1 Increase of turbine entry temperature (TET) capability of civil aeroengines since 1940. 2

2.1 Crystallography of disordered γ and ordered $L1_2$ (γ') phases in Nickel alloys. 12
2.2 Three typical morphologies of MC type carbides, blocky, script and nodular. 13
2.3 Five macroscopic degrees of freedom for a grain boundary that include a rotation angle θ (1 DOF) operated along a rotation axis $\boldsymbol{o}$ and grain boundary plane normal $\boldsymbol{n}$ 17
2.4 A schematic illustration of a low angle grain boundary, where the misorientation angle θ is approximately $|\boldsymbol{b}|/d$. 19
2.5 A schematic illustration of structural unit model in a body centred cubic structure. 20
2.6 Energy-misorientation dependency diagram for FCC structure. 21
2.7 2D schematic diagram of a simple cubic bicrystal tilt boundary. 23
2.8 Schematic diagram on heat treatment profile for producing non-equilibrium segregation and three cooling rates on the level of non-equilibrium segregation. 27
2.9 Boron segregation in a nickel superalloy IN617 that improved rupture strength at high temperatures. 29
2.10 An overview of processing route for Ingot & Wrought alloys 30
2.11 An illustration of processing route for investment casting procedures . . 32
2.12 A demonstration of processing route for producing powder metallurgy alloys. 33
2.13 Non-serrated and serration grain boundaries illustrated in 3D. 38
2.14 Non-serrated and serration grain boundaries illustrated in 2D 40
2.15 Dendritic growth of intergranular γ' particles. 41

2.16 Compositional profile of particles in the vicinity of a grain boundary revealed using TEM-EDS analysis 42
2.17 Serration quantification method used in literature. 43
2.18 Grain boundary serration induced by δ and η phases. 44
2.19 Grain boundary morphologies of Nimonic 263 water quenched at different temperatures during slow cooling from solution temperature. 46
2.20 Fracture surfaces of non-serrated and serrated grain boundary material in Nimonic 263. 52
2.21 Creep curves of non-serrated and serrated grain boundary material at different conditions. 53
2.22 Different deformation mechanisms that are revealed at non-serrated and serrated grain boundary materials. 55
2.23 Effect of cooling rate and ageing on the morphology of γ' particles. . . 58

3.1 Mitsubishi Heavy Industries M501J industrial gas turbine engine assembly and schematic illustration. 63
3.2 Demonstration of the locations where the test specimens were taken from (a) and photographs of the blade cross-sesctions at each location. 65
3.3 Demonstration of *in-situ* tensile testing setup in SEM 68
3.4 The setup of Transmission Kikuchi Diffraction (TKD) 71

4.1 Schematic heat treatment profiles applied for triggering grain boundary serration. 78
4.2 Display of typical grain boundaries and intergranular carbide conducted with seven heat treatments. 83
4.3 Operation principle of Fourier transformation that decomposes a wave signal into its constituent sinusoidal waves into power and frequency spectrum. 85
4.4 FFT analysis procedures of serrated grain boundary profiles. 85
4.5 The microstructure overview of the as-received Inconel 600. 88
4.6 Summary of the six types of grain boundaries observed. 89
4.7 Microstructures of material received solution treatment ranging from 1000 - 1140°C. 90
4.8 STEM-EDS line scan across the interface of matrix/carbide. 91
4.9 TEM micrograph and selected area diffraction patterns at carbide and both sides of the matrix in the as received material. 92

4.10 TEM micrograph and selected area diffraction patterns at carbide and both sides of the matrix in the material that contains serrated grain boundaries. 93
4.11 Equilibrium phase diagram of Inconel 600 from 300 - 1500°C showing carbide type and dissolution temperature. 95
4.12 An example of FFT results of 15 analysed grain boundaries. 97
4.13 Serration amplitude and wavelength chart for two microstructures. . . . 99
4.14 Serration index vs amplitude for two microstructures. 99
4.15 Serration amplitude and wavelength chart for four microstructures. . . 101
4.16 Distribution of carbide, serration amplitude and wavelength in two microstructures. 102
4.17 Relationship between processing parameters, carbide distribution and serration index. 103
4.18 Grain boundary movement due to migration pinned by carbides (a) and local features in higher magnifications (b) & (c). 107
4.19 Grain boundary migration as a formation mechanism for serrated grain boundaries. 108
4.20 Grain boundary serration induced by facet carbides. 110
4.21 Strain tensor map for 2 faceted carbides on a grain boundary exhibiting coherency strain induced serration. 113
4.22 Rotation tensor map for 2 faceted carbides on a grain boundary exhibiting coherency strain induced serration. 114
4.23 Processing map of grain boundary serration index as a function of heat treatment parameters. 117
4.24 Microstructure of Inconel 600 that obtains non-serrated grain boundaries. 119
4.25 Heat treatment using step isothermal holding that compares to slow cooling. 120

5.1 Heat treatment profiles for development of non-serrated and serrated grain boundary materials. 130
5.2 Demonstration of X-ray computed tomography setting up 133
5.3 Energy dispersive X-ray spectroscopy (EDS) analysis in a region that contains a serrated grain boundary and planer carbides. 134
5.4 Grain size measurements for non-serrated and serrated materials respectively. 135
5.5 Creep curves for non-serrated and serrated grain boundary architectures at different conditions. 137

5.6 Fractography on representative samples at various conditions with non-serrated and serrated grain boundaries. 139
5.7 Inverse pole figure and pattern quality maps of non-serrated fracture tips at each creep condition. 141
5.8 Inverse pole figure and pattern quality maps of serrated fracture tips at each creep condition. 142
5.9 EBSD IPF images of initial microstructure with non-serrated and serrated grain boundaries underwent *in-situ* tensile tests. 143
5.10 Tensile curves showing engineering stress *vs* engineering strain for both microstructures at two temperatures. 143
5.11 *In-situ* observation of deformation evolution as a function of strain for both grain boundary morphologies at room temperature. 145
5.12 *In-situ* observation of deformation evolution as a function of strain for both grain boundary morphologies at 700°C. 146
5.13 Geometrically necessary dislocation maps obtained for fractured materials from both non-serrated and serrated cases. 148
5.14 Carbide distribution within grain interior and in vicinity of grain boundaries. 149
5.15 Serrated grain boundary sample interrupted by 5% creep strain at two creep conditions. 150
5.16 Geometrically dislocation density maps of interrupted specimens of non-serrated and serrated specimens at 700°C/170MPa 154
5.17 Geometrically dislocation density maps of interrupted specimens of non-serrated and serrated specimens at 815°C/70MPa 155
5.18 Geometrically dislocation density maps of interrupted specimens of non-serrated and serrated specimens at 900°C/40MPa 156
5.19 3D reconstruction of fractured creep specimens from side and top views showing cavitation distribution. 157
5.20 Cavitation number density versus distance from the fracture tip. 158
5.21 Carbide distribution in relation to distance from grain boundary in the serrated case. 161
5.22 Typical cavities observed in non-serrated material during interrupted creep testing at different conditions. 165
5.23 Cavitation counted for non-serrated and serrated case at two engineering strains levels (20 and 40%). 167

5.24 Postmortem analysis on fracture surfaces of *in-situ* specimens and two regions with higher magnifications. 168
5.25 Cavitation volume against frequency for both grain boundary morphology materials. 170

6.1 Larson-Miller Parameter of MGA1400CC and two sample geometries used for creep tests. 183
6.2 Creep life scattering in relation to grain size and creep conditions. . . . 184
6.3 MC carbide distribution and quantification for MGA1400CC in various conditions. 185
6.4 γ' distribution of MGA1400CC in various conditions 185
6.5 Energy dispersive X-ray spectroscopy scan of a grain boundary that revealed Ta/Ti/W/Mo/Cr rich carbides. 187
6.6 Representative fracture surfaces of samples crept at 700°C/706MPa and 870°C/343MPa. 188
6.7 EBSD coupled XCT technique for identification of dominant slip system at 700°C/706MPa. 190
6.8 EBSD coupled XCT technique for identification of dominant slip system at 870°C/343MPa. 191
6.9 XCT reconstruction showing the cross-sectional aspect ratio plot against distance of specimens. 192
6.10 Electron microscopy with evidence on deformation evolution for a specimen crept under $\{1\ 1\ 1\}\ \langle 1\ 1\ 2\rangle$ shear mechanism. 196
6.11 Schematic drawing of the deformation and fracture evolution for a specimen crept under $\{1\ 1\ 1\}\ \langle 1\ 1\ 2\rangle$ shearing mechanism. 197
6.12 *In-situ* tensile test carried out in SEM at different strains. 198
6.13 Fracture analysis of the *in-situ* specimen. 200
6.14 Crystal plasticity creep model showing three grain boundary cases. . . 201
6.15 The framework used for the current alloy development program acquiring new technologies. 204

List of tables

2.1 Compositions in wt-% (Ni-base) of some common polycrystalline superalloys. 11

3.1 Alloy composition for current study in wt-% (Ni-base), measured using ICP-OES, ICP-combustion (Carbon) and Spark OES (Boron) 62
3.2 Nominal alloy composition of MGA1400CC and three other derivative alloys with minor element modifications in wt-% (Ni-base). 64

4.1 Heat treatment matrix performed to generate a database of grain boundary serration in Inconel 600. 79
4.2 Carbide quantification matrix of Inconel 600. 81
4.3 Serration quantification matrix of Inconel 600. 96

5.1 *In-situ* tensile testing results. 140

6.1 Optimised creep model parameters for MGA1400CC 193

Chapter 1

Introduction

1.1 Nickel-based alloys

Nickel-based alloys entered the stage of high temperature materials in 1940s. Before the first superalloy Nimonic 80 was invented, high integrity steels were utilised for applications at elevated temperatures. Driven by the extreme operation conditions required for jet engines and industrial gas turbines, nickel-based alloys were highlighted for exhibiting superior resistance against various loading and environmental attack, such as creep, fatigue, oxidation, corrosion, etc. The historical development of superalloys was always seeking for higher turbine entry temperature (TET) capability, see Figure 1.1. This benefited the theoretical thermal efficiency derived by Cornat [1, 2], *i.e.* increased efficiency can be achieved by raising the TET. A variety of processing methods were subsequently developed to fulfil such needs, including directional solidification, single crystal, thermal barrier coating (TBC), cooling channels and so on.

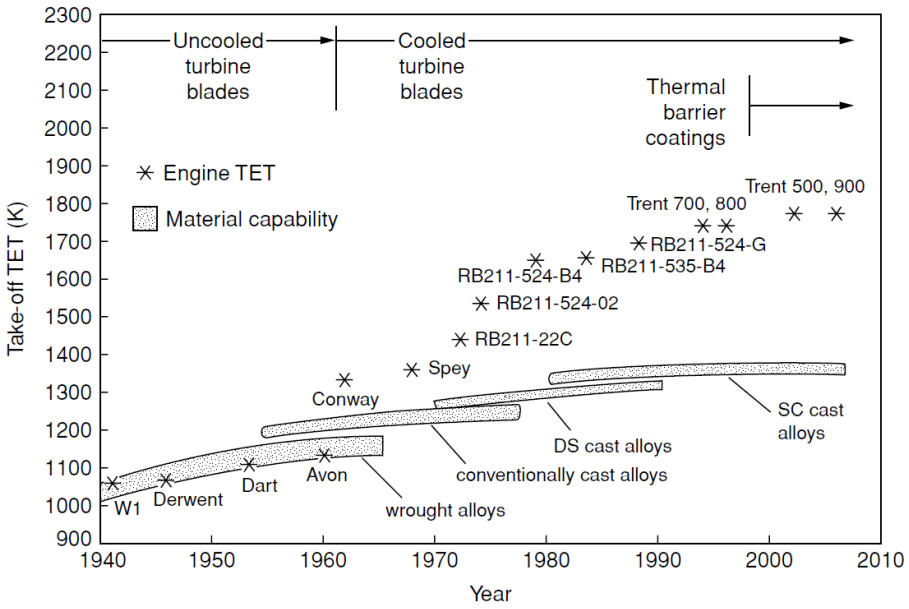


Fig. 1.1 Increase of turbine entry temperature (TET) capability of civil aeroengines since 1940. Adapted from [3]

Depending on the application requirements, different design philosophies contribute to various types of nickel alloys. For example, aero gas turbine applications utilise single crystal for turbine blade and polycrystals for turbine disks. This is because the turbine blades operate at a temperature of 1000°C or beyond, and grain boundaries are weak sites at very high temperatures. However, for lower temperature applications, around 800°C, polycrystalline materials are favoured due to their better processiblity, isotropic mechanical properties and cost. Admittedly, development of polycrystalline superalloy is of great importance for wider applications, particularly in the industrial gas turbine sector.

1.2 Aim of the research

Enormous research effort has been contributed to engineer the interfacial properties between crystals, *i.e.* grain boundaries for achieving the goal of strengthening in order to enhance the overall performance of the component. This includes a variety of approaches that deliberately alter the grain boundary properties, for instance increasing twin boundary fraction, redecoration by grain boundary phases and alteration of grain boundary morphology are common tactics. Minor elements such as carbon and boron are deliberately added to strengthen the grain boundaries by forming carbides and borides that improve interface cohesion. However, excessive amounts of these elements affect the property adversely. Therefore, the amount of minor elements needs to be carefully controlled to achieved the optimum properties. This is particularly difficult as the role of these elements is not thoroughly understood, and the common approach is based on trial and error. Indeed, fundamental understanding on grain boundary engineering mechanisms needs to be further improved.

Grain boundary serration in particular, needs more attention than it has received. As a form of grain boundary engineering, the community has been aware of the phenomenon for over 40 years [4, 5]. Nevertheless, many unknowns still exist in an elemental level that arise complexity for the application of such technology. For example, no objective quantification method of the degree of serration is available in the literature; the formation mechanism of serration is vaguely backed up experimentally; no quantitative approach has been carried out to elucidate the effect of the serrated grain boundaries. Moreover, secondary thoughts are usually ignored — since some

elements are tied-up for grain boundary strength, a change, usually a sacrifice in grain boundary interior strength is expected. Many researchers desire to obtain some degree of serration in the hope of more resistance to grain boundary sliding, though without balancing out possible strength loss from the grain interior due to new processing parameters. The literature rarely address both effects together.

The current research keeps all the above issues in mind and aim to leverage carefully designed experimentation for an unambiguous interpretation of the mechanism and application of grain boundary engineering. Heat treatment was utilised to produce grain boundaries with different characters, and it has proven possible to maintain other microstructural features constant while evaluating the sole effect of grain boundary serration. Secondary thinking on balancing intergranular and transgranular strength have been discussed. Moreover, a specific focus was paid on second phases, *i.e.* carbides and borides on their roles of grain boundary modifiers. As will be discussed later in Chapter 4 - 6, their roles on triggering grain boundary serration and facilitating/resisting grain boundary cavitation is explicitly addressed, supported by advanced charaterisation techniques, such as transmission Kikuchi diffraction, high-resolution electron backscatter diffraction and X-ray computed tomography.

1.3 Structure of the thesis

Chapter 2 provides a background and summary on different aspects of grain boundaries in nickel-based alloys. It starts with the physical metallurgy of nickel alloys, where the

roles of a few crucial phases are discussed. Next, the phenomenon of grain boundaries itself is reviewed in perspectives of crystallographic arrangement/atomic configuration, energy description and segregation. Then, the common processing routes for nickel alloys are reported, the microstructural control tailoring properties via heat treatment is emphasized. Last, the literature on grain boundary serration as a form of engineering approach is carefully reviewed, both on the formation mechanisms and its influence on mechanical properties.

In Chapter 3 the information about processing of the materials used, *i.e.* wrought Inconel 600 and cast MGA1400CC are given. Additionally, the experimental details on various mechanical testing methods and characterisation techniques are specified.

In Chapter 4 the mechanistic studies on grain boundary serration are presented. First, a systematic phenomenological study on grain boundary serration is conducted, where grain boundaries that presented in Inconel 600 are categorised into six types. Based on which, both a definition and a deterministic criterion are provided. Furthermore, a new quantification method, based on fast Fourier transform, is constructed for measuring the degree of grain boundary serration, which has brought the accuracy and objectivity of the quantification of serration to a new level. A new metric, the "serration index" is introduced to interpret the influence of the phenomenon. Moreover, cutting edge electron microscopy using transmission Kikuchi diffraction coupled with cross-correlation based analysis reveals two distinctive formation mechanisms that account for grain boundary serration. Subsequently, a processing map for serration index is constructed as a guideline for future studies in the area.

In Chapter 5 the impact of grain boundary serration is investigated at tensile and creep conditions. Two microstructrual variants — non-serrated and serrated are carried out for comparative studies. First, characterisation confirms the two distinctive grain boundary morphologies achieved, whilst other microstructural features are maintained consistent. Then, repeat creep testing at three conditions indicates a crucial role of serration on creep in high temperature/low stress conditions. High-resolution electron backscattered diffraction further demonstrates the grain boundary structure in relation to strain accumulation, which initiates cavitation. X-ray computed tomography is performed to characterise the cavitation development. It is suggested that the mean cavitaty size is a strong function of grain boundary morphology, but insensitive to creep conditions. *In-situ* tensile testings at high temperature further consolidates the cavitation behaviour in relation to grain boundary serration.

In Chapter 6 the creep properties of an industrial gas turbine nickel alloy are studied, where the role of grain boundary engineering is highlighted. Creep life scattering behaviour is observed for the material, particularly at high stress/low temperature regime. This is rationalised as a change in deformation mode from partial dislocations shearing the γ' particles to octahedral slip. The former mechanism in action requires large crystal rotation and consequently fractures the intergranular carbide. As a result, quasi-brittle failures are facilitated by cativation link-up via fractured carbide. A constitutive model based on the physics of microsturcture is developed for enhanced understanding and predictions. It is validated by further testing using modified chemical compositions, which established a different distribution

of the carbides that is less susceptible to carbide cracking. Significant increase in creep life was achieved. A framework based on the creep model is constructed for a future alloy development scheme.

In Chapter 7 key conclusions from the thesis are summarised. Suggestions for future work are outlined in three aspects, all of these are enhanced through understanding of the effect of grain boundary modifications aided by second phases.

Chapter 2

Literature Review

2.1 Physical metallurgy of Nickel-based alloys

Nickel-based superalloys are notoriously sophisticated, the range of chemical compositions needed for particular applications is vast. To achieve desired properties, usually more than ten elements are required. Composition of some nickel-based superalloys are listed in Table 2.1. It is critical to understand the role of each element in relation to properties, and then control to the right amount to form the desired distribution of phases. For example, chromium is needed for corrosion resistance, cobalt improves the alloy formability, aluminum and titanium are chosen to promote strengthening precipitates and refractory elements provide solid solution strengthening. A nickel-based superalloy typically contains an austenitic γ matrix, intermetallic γ' precipitate, various types of carbide and boride and sometimes detrimental TCP phases. The details of each phases are discussed in the following sections.

2.1.1 The γ matrix

The austenitic γ phase serves as matrix of the material that holds together all other phases. As illustrated in Figure 2.1 (a), it has the crystallography of disordered face centred cubic (FCC) structure. The matrix is formed from the elements that are strongly partitioned to it, such as chromium (Cr), cobalt (Co), iron (Fe), molybdenum (Mo), tungsten (W), rhenium (Re) and ruthenium (Ru) [6, 7]. Their atomic radii are similar to nickel and hence readily form a solid solution. Moreover, each of the elements has been frequently reported to perform different roles in other dimensions. For example, Cr is added to improve corrosion resistance by forming a protective layer of Cr_2O_3 oxide scale [8, 9]. Co improves processability by lowering the γ' solvus temperature that prevents cracking during forging [10, 11]. In addition, it also reduces the stacking-fault energy [12]. As a result, high temperature properties can be improved by making cross-slip difficult [13]. Iron is utilised to some extent to decrease the cost of a component. Refractory elements such as Mo, W, Re and Ru are used to provide solid solution hardening and increase the melting point [14]. As the size of refractory elements are huge, they possess very low diffusivity and strongly partition to the matrix, associated with the improved creep resistance. However, excessive amounts of these elements also causes the formation of detrimental TCP phases [15]. Therefore, a balanced consideration is needed for a particular application.

Table 2.1 Compositions in wt-% (Ni-base) of some common polycrystalline superalloys.

Name	Cr	Co	W	Al	Ti	Ta	Nb	Mo	Fe	C	B	Zr	Re
Waspaloy [16]	19.5	13.5	-	1.3	3.0	-	-	4.3	-	0.040	0.006	0.060	-
René 95 [17]	13.0	8.0	3.5	3.5	2.5	-	3.5	3.5	-	0.065	0.013	0.050	-
RR1000 [18]	15.0	18.0	-	3.0	3.6	2.0	1.1	5.0	-	0.027	0.015	0.060	-
Alloy 10 [18]	11.5	15.0	5.9	3.8	3.9	0.8	1.7	2.3	-	0.030	0.020	0.050	-
Astroloy [7]	15.0	15.0	-	4.4	3.5	-	-	5.3	-	0.060	0.030	0.060	-
GH4169 [19]	18.6	-	-	0.44	1.04	-	5.3	3.0	18.2	0.026	0.002	-	-
TMS-138 [20]	2.9	5.9	5.9	5.9	-	5.6	-	2.9	-	-	-	-	-
René 104 [21]	12.8	20.7	2.0	3.4	3.7	2.3	0.9	3.8	-	0.050	0.025	0.050	-
CMSX4 [22]	6.4	9.6	6.4	5.6	1.0	6.5	-	0.6	-	-	-	-	2.9
Nimonic 80 [17]	20.0	-	-	1.0	2.5	-	-	-	-	-	-	-	-
Inconel 100 [17]	12.4	18.4	-	4.9	4.3	-	-	3.2	-	0.070	0.020	0.070	-
Inconel 718 [23]	19.0	-	-	0.6	0.8	-	5.3	3.0	19.0	0.080	0.006	-	-
Udimet 720Li [24]	14.6	15.9	1.4	2.4	5.2	-	-	3.0	-	0.023	0.016	0.042	-

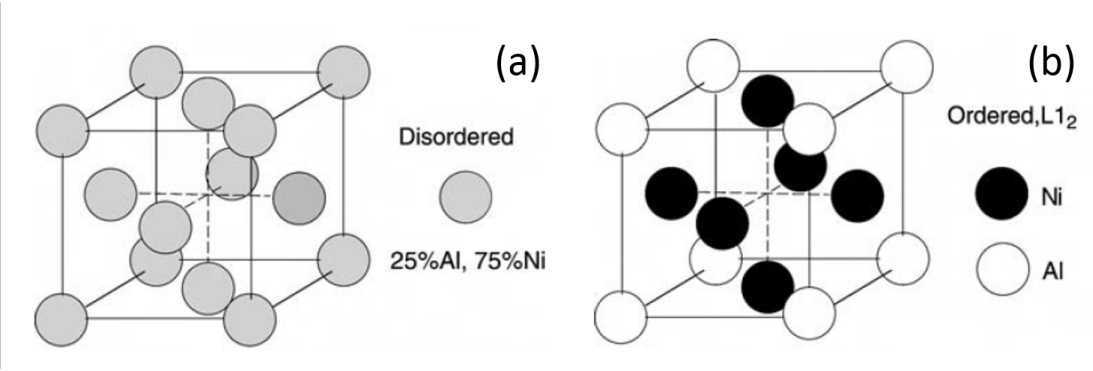


Fig. 2.1 Crystallography of disordered γ and ordered $L1_2$ (γ') phases in Nickel alloys. Adapted from [18].

2.1.2 The γ' precipitate

In contrast to γ matrix, γ' precipitate is an ordered intermetallic phase that displays a cubic, $L1_2$ crystal structure [17, 18]. The basic formula is expressed as Ni_3Al, where the Ni atoms reside on the cubic faces and Al atoms reside in the corners. The phase boundary between the disordered matrix and ordered precipitates exhibit full coherency, which result in a low interfacial energy. Their orientation relationship is widely know as $\{100\}_\gamma//\{100\}_{\gamma'}$ and $\langle 010\rangle_\gamma//\langle 010\rangle_{\gamma'}$. Moreover, Ni and Al are not the only elements that exist in γ'. For instance, Co frequently substitute Ni and occupy the faces, and the corner elements can also be Ti, Ta or Nb [25]. Thus, a generalised formula can be written as (Ni, Co)$_3$(Al, Ti, Ta, Nb).

The subtle alteration in elements causes a change in lattice parameter, which to an extent, results a variation in coherency. Consequently, the lattice misfit between the two phases is then adjusted. The lattice misfit is defined as [18]:

$$\delta = 2 \cdot \frac{a_0^{\gamma'} - a_0^{\gamma}}{a_0^{\gamma'} + a_0^{\gamma}} \quad . \tag{2.1}$$

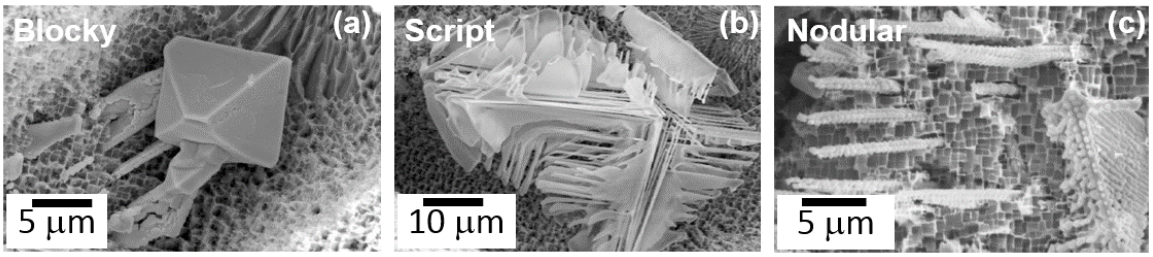


Fig. 2.2 Three typical morphologies of MC type carbides, blocky, script and nodular. Adapted from [17]

where a_0^{γ} and $a_0^{\gamma'}$ represents the lattice parameter for the γ and γ' phases. The lattice parameter can be calculated by Vegard's Law using chemcial composition [26]. The final shape of γ' precipitate is a function of lattice misfit value. If the misfit is small, *i.e.* <0.5%, precipitates first exhibit a spherical morphology, and the coarsening rate is slow. The particles will eventually grow to cuboidal shape with sharp corners during ageing. In the case of large misfit, it exhibits irregular octo-dendritic clover leaf shape precipitates [27].

2.1.3 Carbides and borides

Minor phases, such as carbides and borides are frequently found along grain boundaries. Their roles vary dependent upon the type of each phase. For example, common carbides are MC, M_6C, M_7C_3 and $M_{23}C_6$ types [28, 29]; common borides are M_3B_2 and M_5B_3 [30], where M refers a metal atom, usually Ti, Hf, Ta, W, Mo or Cr.

The MC carbides are usually found to be incoherent with the matrix and display FCC NaCl type crystallography [31]. The typical compositions are refractory elements, such as Ta, Mo, Hf, Ti or W with carbon, whose segregation coefficient is positive

(k less than 1) and they were rejected from γ dendrite cores during solidification. Therefore, they are gradually enriched in liquid, and form MC carbide at the last stage of solidification in the interdendritic regions. The morphologies of MC carbide are displayed in Figure 2.2 which include blocky, script like or nodular [32, 17]. The role of MC carbides is controversial: depending on their size, location and morphology, they can be either detrimental or beneficial. For instance, a network of script like MC carbides affects adversely to intermediate temperature mechanical properties, as it facilitates rapid propagation of cracking due to its brittleness [33, 34]. On the other hand, dispersed blocky MC carbide particles on the grain boundaries are preferred for inhibiting grain boundary sliding [17].

MC type carbide can subsequently decompose into M_6C and $M_{23}C_6$ type through reaction with γ matrix. The reactions are denoted as $MC + \gamma \rightarrow M_{23}C_6 + \gamma'$ or $MC + \gamma \rightarrow M_6C + \gamma'$ [35, 16, 36]. The product depends on the composition available for exchange. For instance, in the case of Ta-rich MC carbide, Cr-rich $M_{23}C_6$ carbide can be promoted in exchange for γ' formation with the excess Ta. On the other hand, if Mo and W are in excess, *i.e.* more than 6 - 8 at% in total, M_6C can be promoted [28]. This controversial debate continues with $M_{23}C_6$ as well. Some researchers have suggested that the positive effect is due to grain boundary sliding resistance and the promotion of serrated grain boundaries [37, 38]. Others argue that the interior brittleness of the carbide is a risk for strength loss. In a recent study, the distribution of $M_{23}C_6$ is also a concern, where agglomeration of the $M_{23}C_6$ is suggested to serve as crack initiation sites, and hence decrease the creep strength [39]. The M_7C_3 is sometimes neglected in

the context of nickel-based superalloy, as their occurrence is relatively rare [29, 28]. It was found that the carbides form during casting or solution treatment, and it would further transform to the more stable $M_{23}C_6$ instead.

Boron level is carefully controlled to achieve optimum performance for advanced nickel-based superalloys [40, 41]. The phases that it promotes are M_3B_2 and M_5B_3, which are thought of as grain boundary strengtheners. Both types of boride show a body centred tetragonal structure where M denotes Mo and Cr [30]. It is proposed that the formation of borides would delay the $M_{23}C_6$ agglomeration [41]. Because boron is smaller and more radical, boride reaches grain boundary first and form borides, and thus consume metal elements in the vicinity of grain boundary that would otherwise form $M_{23}C_6$. However, it has also been reported that excessive boron leads to premature failure due to their intrinsic brittleness [41].

2.1.4 Topological closed packed phases

A series of detrimental phases can form through processing or long term high temperature exposure during service. These infamous phases include σ, μ, η and laves, which are known as topological closed packed (TCP) phases [17]. The number of slip planes are limited and the morphology is needle shape, both features suggest brittle behaviour of the phase. In addition, they are formed at the expense of elements such as Cr, Mo, W or Re [42]. Consequently, the damaging effect of TCP is made into two steps: first, removal of solid solution elements from the matrix decreases the creep strength; second, the brittleness of TCP that are formed on grain boundaries facilitates

crack initiation and propagation [43]. A short stress rupture life and decreased tensile ductility is usually seen in association with the presence of TCP phases.

2.2 Physics of Grain boundaries

A grain boundary is an interface between two crystals that possess the same structure but differ in orientation. It serves as one of the most important microstructural features and governs a wide range of material properties, such as strength, ductility, corrosion, oxidation, electrical conductivity, etc [44, 45]. However, with carefully designed and controlled processing, grain boundary structures can be engineered to achieve desired performances.

In this section, the crystallographic description of grain boundary is introduced, including models and parameters used to characterise such an interface. Next, the atomic arrangement of grain boundary structures is discussed, defined by a number of classical models, such as dislocation model, structural unit (SU) model, coincident site lattice (CSL) model, etc. And last, grain boundary segregation is reviewed, effects related to weakened or strengthened boundaries are discussed in detail.

2.2.1 Description of grain boundaries

A grain boundary is defined by nine parameters, also called degrees of freedom (DOFs), which includes five macroscopic parameters and four microscopic parameters [46, 44, 47]. Amongst the nine parameters, six are used to describe the relationship between

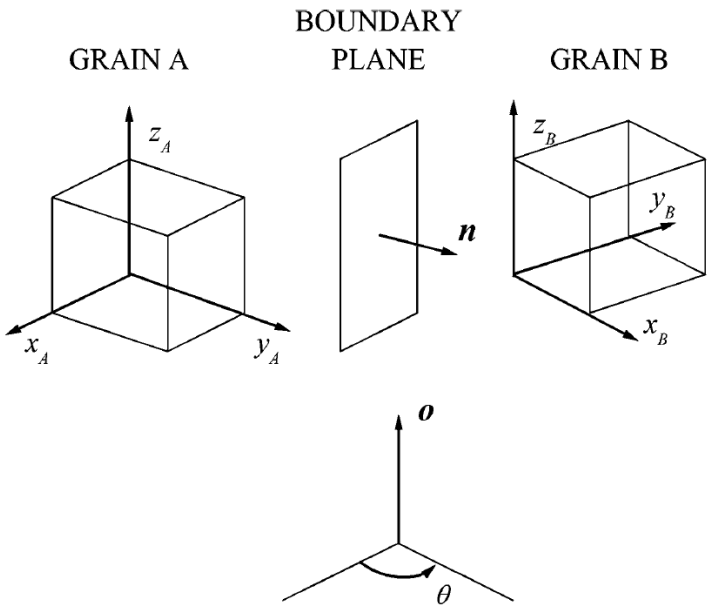


Fig. 2.3 Five macroscopic degrees of freedom for a grain boundary that include a rotation angle θ (1 DOF) operated along a rotation axis $\boldsymbol{o}$ and grain boundary plane normal $\boldsymbol{n}$. Adapted from [44].

the two crystals, and the remaining three are used to describe the interfacial plane. Macroscopically, three degrees of freedom characterise the mutual misorientation between the two grains, with a rotation angle θ (1 DOF) operated along a rotation axis $\boldsymbol{o}$ (2 DOFs), as illustrated in Figure 2.3. The other two degrees of freedom are used to specify the direction of the grain boundary plane normal $\boldsymbol{n}$. These five parameters are independent. Microscopically, three degrees of freedoms are used to describe the translation between crystals and one more parameter determines interface plane. The microscopic parameters are often referred as "energy parameters" [44, 47], determined by equilibrium atomic structures.

In order to illustrate the grain boundary crystallography, five macroscopic degrees of freedom are sufficient. In addition, depending on the geometric relationship between

the rotation axis $\boldsymbol{o}$ and the plane normal $\boldsymbol{n}$, a few categories of grain boundaries are defined. For instance, if the two vectors were parallel to each other, the interface is called a twist grain boundary; in the case when they were perpendicular, it is called a tilt boundary; and if neither relation were satisfied, the boundary is referred as a mixed grain boundary [44]. Moreover, in the case of tilt boundaries, if the grain boundary plane normal could be described using the same Miller indices in both crystals, *i.e.* the grains obtain mirror symmetry along the boundary plane, it is then called symmetrical. Otherwise, it is called asymmetrical.

On the atomic arrangement of a grain boundary, there have been many theories describing the situation. The early models suggested the interface is a glue-like amorphous material [48, 44]. It is believed true in some materials, such as silicon, which is supported by simulation results [49]. More recent studies, however, have established the theory of grain boundaries being crystalline, validated both experimentally and theoretically [50–52, 44, 47]. Models that are introduced in the following sections are based on the theory of crystal-like interfaces.

2.2.2 Grain boundary structures

Misorientation is a convenient way of describing a grain boundary, where two groups of grain boundaries can be differentiated, *i.e.* low angle grain boundaries (LAGB) and high angle grain boundaries (HAGB). The differences between them are not only the mutual misorientations, but also the energy of grain boundaries, which defines a grain boundary property.

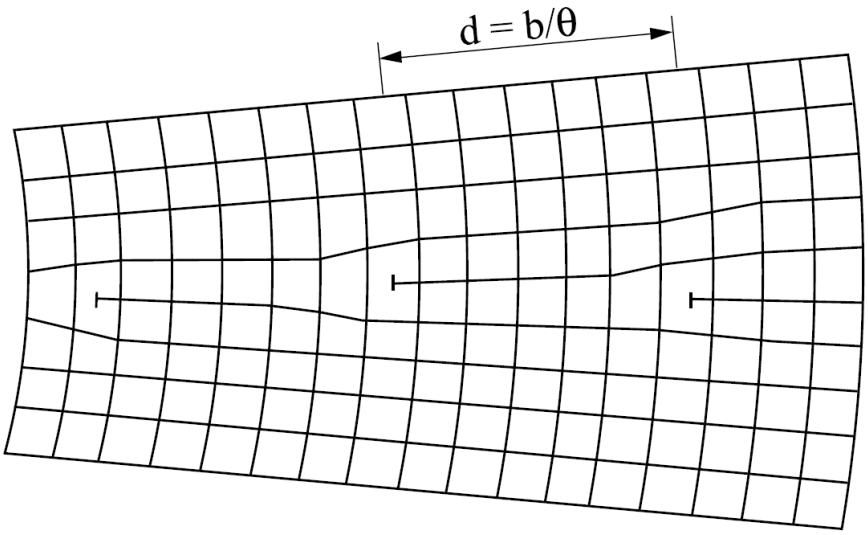


Fig. 2.4 A schematic illustration of a low angle grain boundary, where the misorientation angle θ is approximately $|\boldsymbol{b}|/d$. Adapted from [47].

Low angle grain boundary

If two crystals are separated by misorientation with an angle that is sufficiently low, the interface can be accommodated by an array of dislocations based on the Read and Shockley model [53]. As shown in Figure 2.4, a schematic illustration of a small angle tilt boundary is constructed by a few edge dislocations with a distance d apart from each other. This type of grain boundary are refered as low angle (LAGB), or sub-boundaries. The misorientation angle θ can be approximated as $|\boldsymbol{b}|/d$.

The approach of dislocations on grain boundaries reaches a limitation as angle θ is increased to sufficiently high values. With d in the range $3|\boldsymbol{b}|$ - $6|\boldsymbol{b}|$, equivalent to misorientation angles of 10° - 15°, local relaxation due to overlapping dislocation cores need to be considered and the dislocation model of grain boundary no longer provides a sensible explanation.

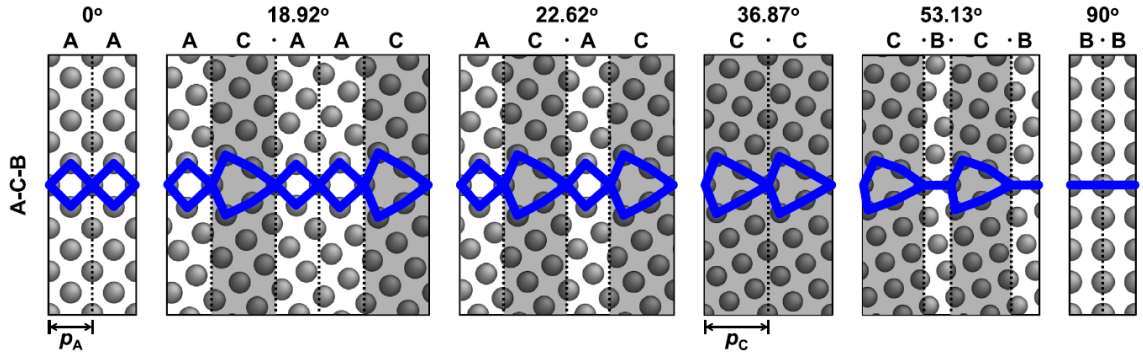


Fig. 2.5 A schematic illustration of structural unit model in a body centred cubic structure. Adapted from [58].

High angle grain boundary

When the misorientation between two crystals exceeds about 15°, the interface is usually referred as high angle grain boundary (HAGB). Since the dislocation model fails to describe the interface arrangement, as dislocations at the grain boundary overlap each other, new models are needed for interpretation.

The structural unit model (SUM) was developed to elucidate the atomic arrangement of the high angle grain boundary [54–58]. The model treats all grain boundaries as a composition of repeated structural units of regular polyhedra. In fact, seven polyhedra were found as "building blocks" for grain boundaries according to Ashby *et al* [59]. Some examples of the structural units representing grain boundaries in a body centred cubic (BCC) structure are displayed in Figure 2.5. Here, 'A', 'B' and 'C' units correspond to misorientation angles of 0°, 36.87° and 90° respectively on the (001) plane of BCC.

Although the SUM demonstrated a rich explanation on the grain boundary structure and enabled predictions of properties of grain boundary [60–62, 57], particularly with tilt

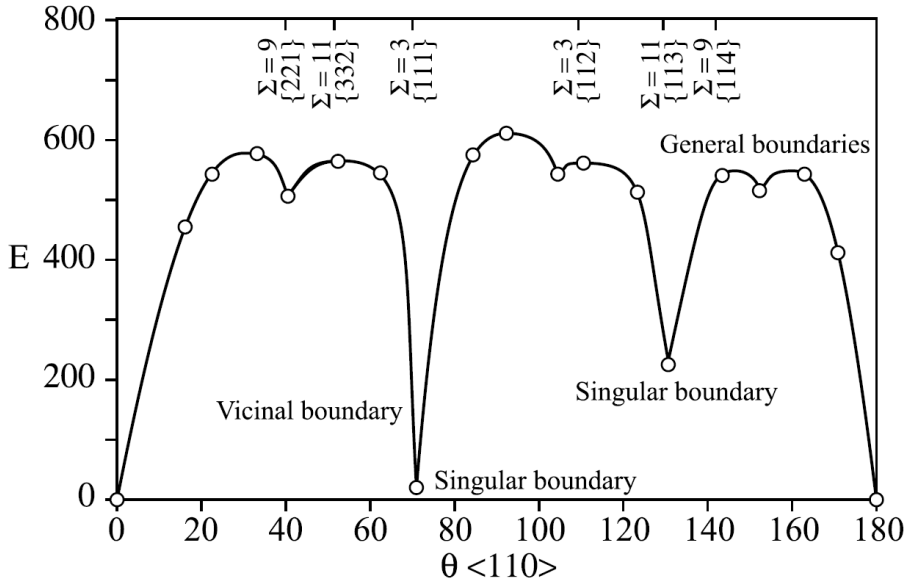


Fig. 2.6 Energy-misorientation dependency diagram for FCC structure. The energy unit was originally quoted as erg cm^{-2}. Adapted from [63].

boundary. The model becomes insufficient for manipulating twist or mixed boundaries and is limited when applied to high index boundary planes [57, 47].

The energy of grain boundary structures are considered next. Since the atomic arrangements are different between grain interior and boundary, the energy required to maintain an equilibrium configuration is higher for a grain boundary than bulk crystal. Thermodynamically, the lower the energy of a grain boundary the more stable the arrangement is. Figure 2.6 demonstrates the energy distribution in relation to misorientation angle along $\langle 1\ 1\ 0 \rangle$ axis for FCC symmetrical tilt grain boundaries [63]. For grain boundaries exhibiting a low minima in the energy-orientation relation, such as $\Sigma 3$ and $\Sigma 11$ in the case, they are called singular boundaries. More often the cases with high energies are addressed as general boundaries, and energy between the two are called vicinal boundaries.

Generally, any grain boundary with an orientation that denotes a significant difference in property from the average, is referred to as a special boundary. The coincident site lattice (CSL) model was developed to specify the special boundaries, it is based on the assumption that lower energy is obtained if more lattice sites of the adjoining grains are in coincident position, the idea being that less bonds are required to break the boundary in such cases[64, 65]. A 2D representation of a simple cubic bicrystal with 36.87° tilt is demonstrated in Figure 2.7, the empty circles represent the coincident sites. The coincidence index Σ is utilised to describe how common the coincident sites are between the two crystals. The Σ value is the reciprocal of the ratio between number of coincidence site in a unit cell and the total number of all lattice sites in a unit cell [44, 47]. Therefore, the lower the number, the higher the coincidence. The evaluation of Σ value in cubic systems can be evaluated by Miller indices $\Sigma = \delta\ (h^2 + k^2 + l^2)$ where $\delta = 1$ if $h^2 + k^2 + l^2$ is odd and $\delta = 1/2$ if $h^2 + k^2 + l^2$ is even. Moreover, special behaviour is frequently reported in FCC systems with the grain boundaries associated with low value of Σ, usually a value lower than 21 [66], and this is the reason why special boundaries are usually referred to low valued CSL boundaries [44].

The CSL model can be further extended to included the displacement shift complete (DSC) lattice or origin lattice (O-lattice), which is usually used for grain boundary dislocation analysis [67–69]. The DSC lattice is constructed by a set of displacement vectors that are preserved while translating the CSL. For instance, the coincidence of two adjoining grains can be re-obtained if one grain is translated to the other with

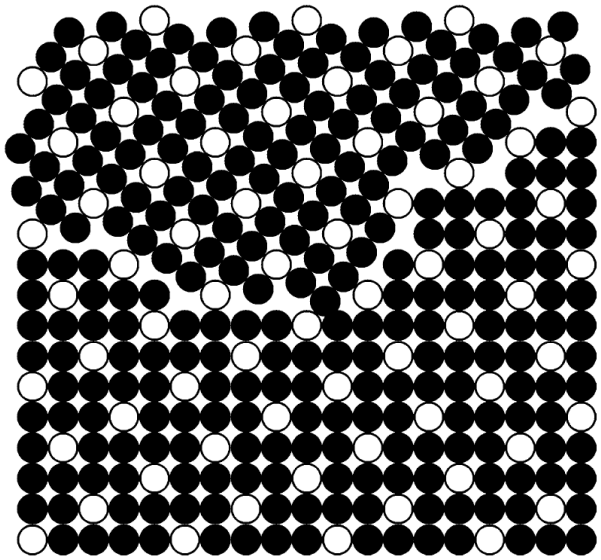


Fig. 2.7 2D schematic diagram of a simple cubic bicrystal tilt boundary. The empty circles represents coincident sites. Adapted from [44].

a particular orientation and displacement, which trace of shifting is described as a vector. In fact, a variety of possible displacement vectors that preserve the original coincidence site lattice, and a new lattice that is defined by the set vectors is called the DSC lattice. Therefore, all displacement vectors that construct the DSC lattice can be possible Burgers vectors for grain boundary dislocations. For energetic reasons, only the ones with the lowest values of the vectors will occur.

2.2.3 Grain boundary segregation

During the processing of material, differences in chemical concentration are frequently observed, and this is usually due to segregation. Depending on the length-scale of the phenomenon, we can distinguish them as macro-segregation, micro-segregation and nano-segregation. The length scale for macrosegregation can be in meters, usually

seen for a cast component; micro-segregation, occurs in micrometre scale, such as the composition difference between dendrite core and inter-dendritic regions. Nano-segregation, for example the grain boundary segregation studied here, only occurs on the nanometer scale. However, the level of chemical difference can be magnitudes higher than those of macro- or micro-segregation [47].

Segregation at crystal interfaces is an important phenomenon, because it might change materials properties drastically. For instance, a number of liberty ships fractured into half during the World War II, as a consequence of sulfur segregation into steels [70]. On the other hand, utilising the segregation appropriately can generate substantial property benefits [71]. Indeed, the decoration of grain boundaries with solute atoms changes a range of properties: fracture resistance, hydrogen embrittlement, grain boundary energy and mobility, etc [45].

Equilibrium segregation

In general, segregation can be sub-divided into two categories — equilibrium and non-equilibrium type — balanced by thermodynamic and kinetic factors. For equilibrium segregation, driven by Gibbs energy, solute atoms find their "comfort zones" at grain boundaries, defect sites or free surfaces due to presence of unsaturated bonds. Thus it gives rise to the inhomogeneity of local chemistry, though very slow kinetics as it is governed by volume diffusion [47, 72].

Two approaches were developed in the studies of grain boundary segregation, namely classic thermodynamics and statistical thermodynamics. The classic thermodynamic

models described the phenomenon in a global manner, such as models suggested by Gibbs, McLean, Seah, Hondros, etc [48, 73, 74, 47]. The approaches were relatively simple and neglected interactions between segregating atoms. This was modified by Guttmann [75, 76] by introducing the bond energy parameter ω, which value determines the weakening or strengthening of segregation. The second approach of using statistical thermodynamcis, based on efforts from classic thermodynamics, was developed more recently through meaningful computational simulation [47, 46]. For a system to achieve energy minimisation, the interaction energy between each type of bonding is considered. Calculations based on static or molecular dynamics (MD) enabled such minimised energy of system to be obtained at a given pressure and temperature, as well as the distribution of solute concentration [77].

Here we summarise the findings of equilibrium segregation that is supported by various models and experimental evidence. First, the level of segregation is very small and usually within the length scale of a few atomic layers in metallic systems. Second, the equilibrium segregation level varies with temperature — at higher temperature segregation finds insufficient energy benefit, whereas at lower temperature solutes are limited by diffusion. Therefore the highest level of segregation occurs at an optimum temperature. Third, the phenomenon takes place within the solubility domain for the segregating element in the solid state.

Non-equilibrium segregation

On the other hand, non-equilibrium segregation can occur from solute-vacancy interactions. As the level of thermal vacancy differs as a function of temperature, a non-equilibrium level of vacancy concentration is established while fast cooling a material. The solute atoms, particularly ones with high values of misfit are attracted to these vacancies and form so-called vacancy-solute complexes. Driven by thermodynamics, the system seeks to lower its energy by redistributing the vacancy-solute complexes, and in principle, equilibrium distribution can only be achieved at infinite time, however, not practically achievable due to low kinetics. Therefore, an intermediate temperature treatment, such as annealing, allows the energy of the system to be lowered by driving vacancies from grain interior to the boundaries. Moreover, due to presence of vacancy-solute complexes, the vacancies can drag away the solute with them, and hence the solute accumulates in the intergranular regions [78, 72, 47]. Figure 2.8 (a) demonstrates schematically the heat treatment needed to produce non-equilibrium segregation, and (b) shows the cooling rate effect on the level of non-equilibrium segregation. A critical cooling rate is often found for a maximum level of non-equilibrium segregation.

Segregation-induced weakening/strengthening effect

Grain boundary segregation can impact on a range of material properties. By decorating boundaries with solute atoms, alteration can be observed in tensile strength, fracture toughness, resistance to corrosion, creep, fatigue, grain boundary energy and diffusion

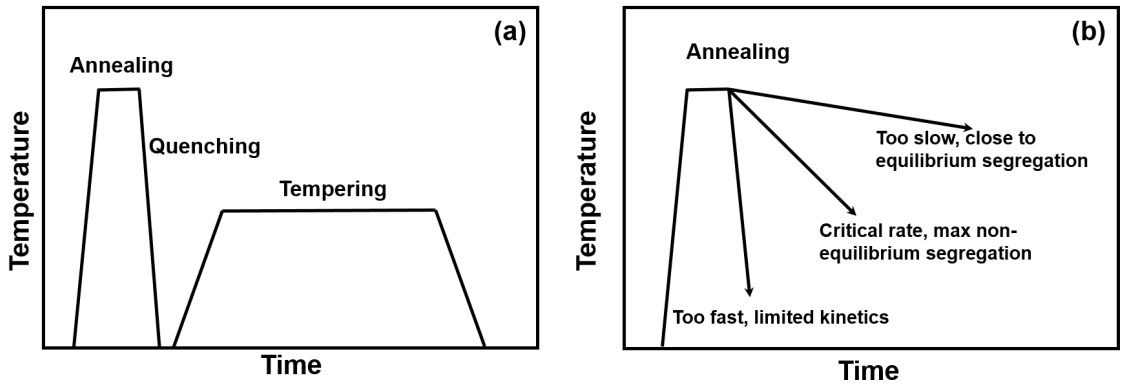


Fig. 2.8 (a): Schematic diagram on heat treatment profile for producing non-equilibrium segregation and (b): three cooling rates on the level of non-equilibrium segregation. Adapted from [72, 44].

[44, 45]. Both beneficial and detrimental examples due to segregation are introduced and their mechanisms are discussed in the following in this section.

Hydrogen embrittlement is one of the foremost concerns in segregation studies, particularly for high strength steels, as it can cause otherwise ductile materials to fail in a catastrophic manner [79]. This famous effect has been known since 1875 [80], and has received decades of attention. Many researchers have contributed to the interpretation of the behaviour, and the generally accepted mechanism is due to decohesion of grain boundaries. Since hydrogen atoms are extremely small, they diffuse very fast and tend to segregate at the microcracks along grain boundaries, which increases the stress ahead the crack tip. Moreover, they have chance to form gas molecules that further stress the microcracks. Under a high level of tensile stress, the microcracks are prone to link up and produces cavities that cause premature failure [44].

Creep rupture behaviour is also known to be affected due to segregation events. For example, bismuth and antimony are shown to be detrimental on the rupture strain

and life for creep of copper [81]. Detailed experimentation indicated that HAGB are very susceptible to creep cavitation, where bismuth and antimony further promote this behaviour. Moreover, brittle failure can be observed due to bismuth, as a result of grain boundary decohesion. On the other hand, creep strength can also be enhanced via grain boundary segregation. Boron is known as a beneficial element that if controlled to the right amount, segregates at grain boundaries and improves grain boundary strength [82, 45, 41]. Figure 2.9 shows grain boundary boron segregation in a nickel alloy characterised by atom probe tomography and transmission electron microscopy that linked to improved creep rupture strength (to a creep life of 10^5 hrs) with boron. Compared with carbon, boron atoms are smaller and hence more readily segregated at grain boundaries. The boron atoms formed borides with transition metals at the expense of continuous carbides, which is prone to cavitation, and thus strengthened the interface [45, 41].

2.3 Processing and microstructure control of nickel-based alloys

2.3.1 Processing routes for nickel-based alloys

Nickel-based alloys are typically manufactured via a few processing routes. They can be categorised into the following classes in respect of the time they were first invented: wrought, cast, powder metallurgy and additive manufacture [83–85, 18, 86, 87].

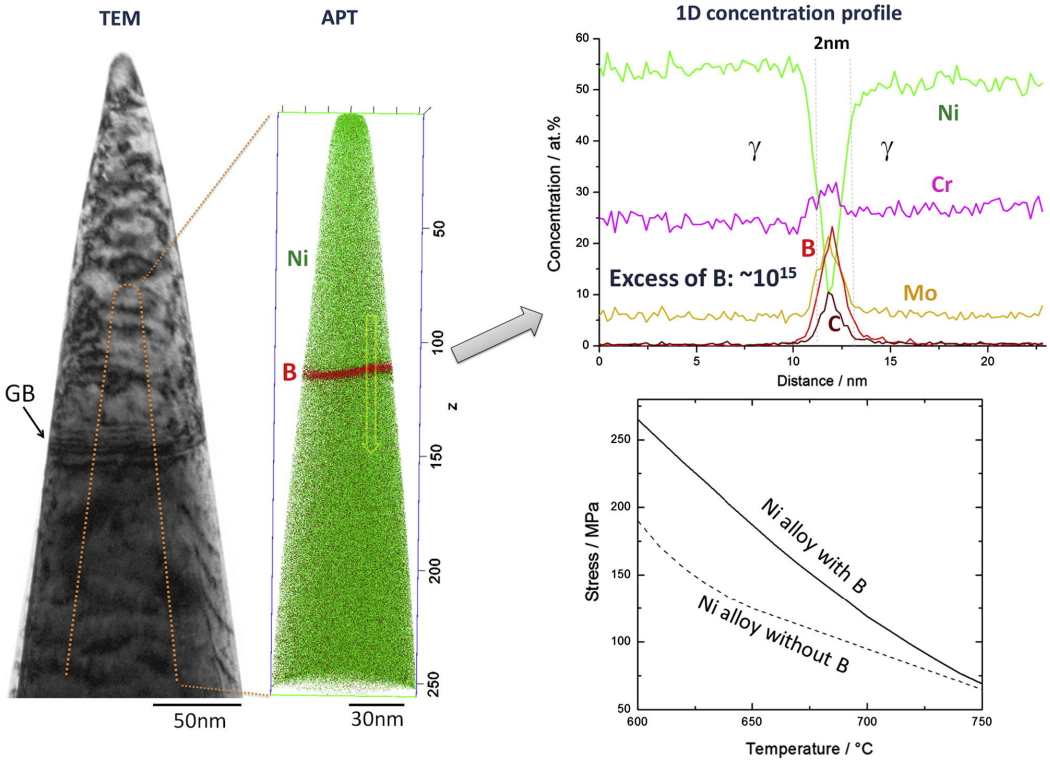


Fig. 2.9 Boron segregation in a nickel superalloy IN617 that improved rupture strength at high temperatures. The segregation is characterised by atom probe tomography and transmission electron microscope. Adapted from [45].

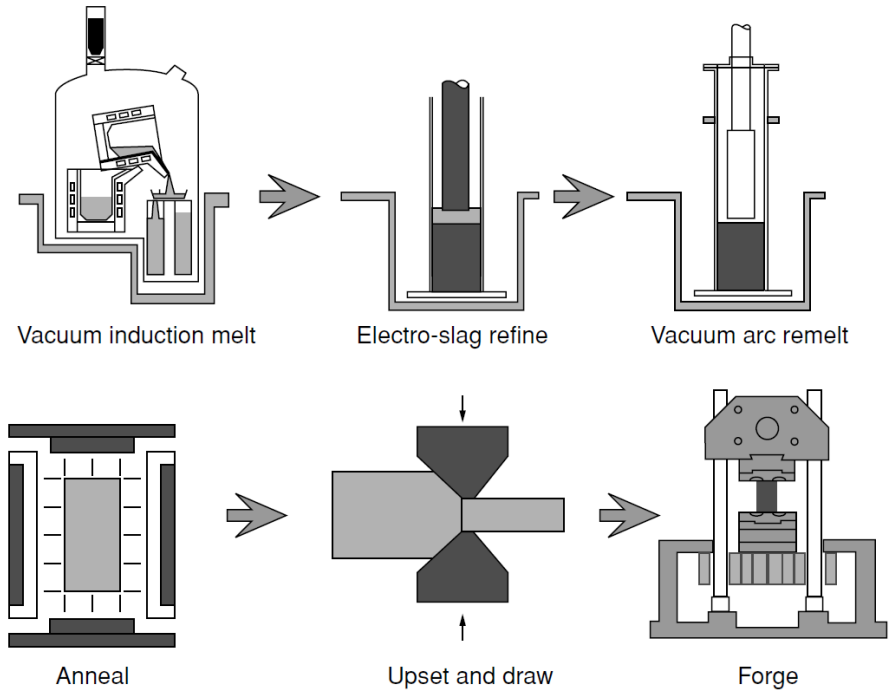


Fig. 2.10 An overview of processing route for Ingot & Wrought alloys. Adapted from [90]

Ingot/Wrought

Processing of wrought alloys start with vacuum induction melting (VIM), and then follows electro slag refining (ESR) and vacuum arc remelting (VAR) [18], see Figure 2.10. These steps produce an ingot and its composition cannot be further modified. To produce the alloy in a near final component shape, annealing, drawing and forging follow. The material could then be further heat treated to obtain the desired mechanical properties. Wrought nickel superalloys contain fine grains (normally 10 - 50 μm) produced by controlled recrystallisation and grain boundary phases, and less γ' fraction (usually less than 40%) [88, 89], which favours use as turbine disks and low temperature turbine blades.

Casting

Casting methods were designed to compensate higher temperature capabilities of a wrought material, as well as to broaden geometrical freedom for complicated parts. For investment casting, most commonly used in the nickel-superalloy industry, includes several delicate steps as shown in Figure 2.11 [91]. The defect density in the final microstructure is significantly influenced by the control of each step. First, a wax model is produced in precision using metallic die injection. Then the model will be invested by ceramic slurries that contains zircon, alumina, silica *et al* [90]. It is then furthered by stuccoing with large particles of the same ceramic. The slurry wetting and stuccoing is normally performed three to six times to achieve the desired mould thickness. Next, the mould is dewaxed using steam and the ceramic mould is heat treated to obtain good mechanical strength. The molten metal prepared by VIM will be poured into the mould and solidifies inside. Finally, the ceramic shell can be removed and component produced can therefore receive a full heat treatment for optimised microstructure.

Powder metallurgy

Powder metallurgy was ustilised for producing fine grained advanced nickel superalloys, particularly for turbine disk components. Figure 2.12 demonstrates an overview of powder metallurgy process [90]. The method begins with VIM and atomisation that a controlled size of metallic powder can be produced, which is usually below 300 μm [92]. The powder is then sieved and canned for different grades (sizes). The screened powder is collected in steel cans which are degassed and sealed. The canned powder is

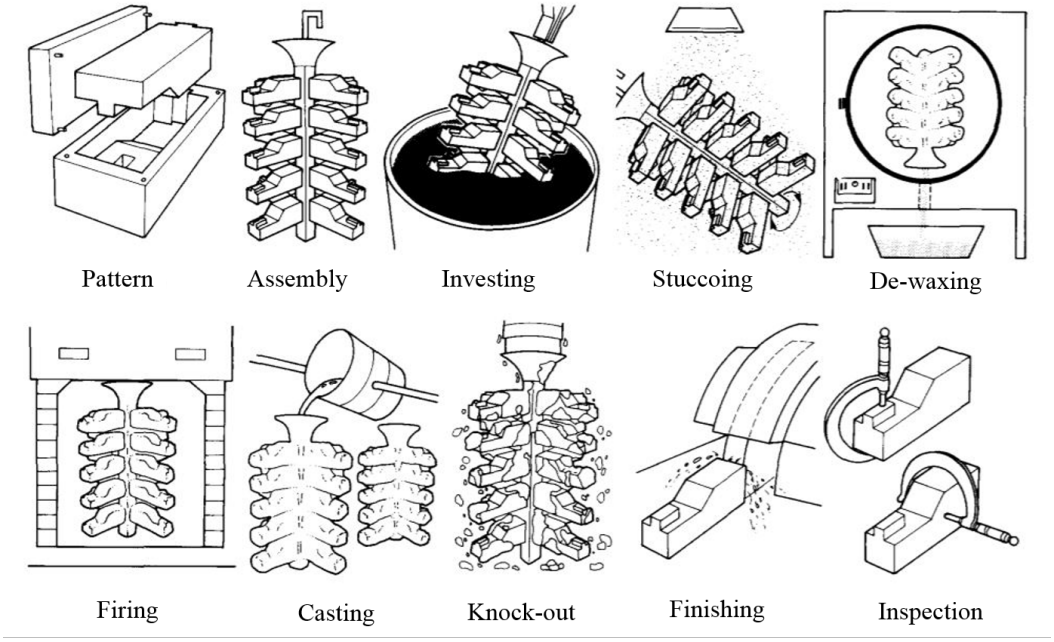


Fig. 2.11 An illustration of processing route using investment casting procedures. Adapted from [91]

further subjected to hot isostatic pressing (HIP) or extrusion that encourages internal pore closure. The materials is then forged, and subsequent heat treatment is applied to achieve optimum properties.

Additive manufacture

Recently, metal additive manufacture (AM) or 3D printing has offered alternative advantages — cost effective and design freedom [87]. In common to powder metallurgy, the method also requires alloy powder to start with. A layer of metallic powder is distributed evenly on a substrate, usually a piece of stainless steel, and then uses either a laser or electron beam to selectively melt the powder bed. Next, another layer of alloy powder will be coated on top of the previous one, and the powder will be melted

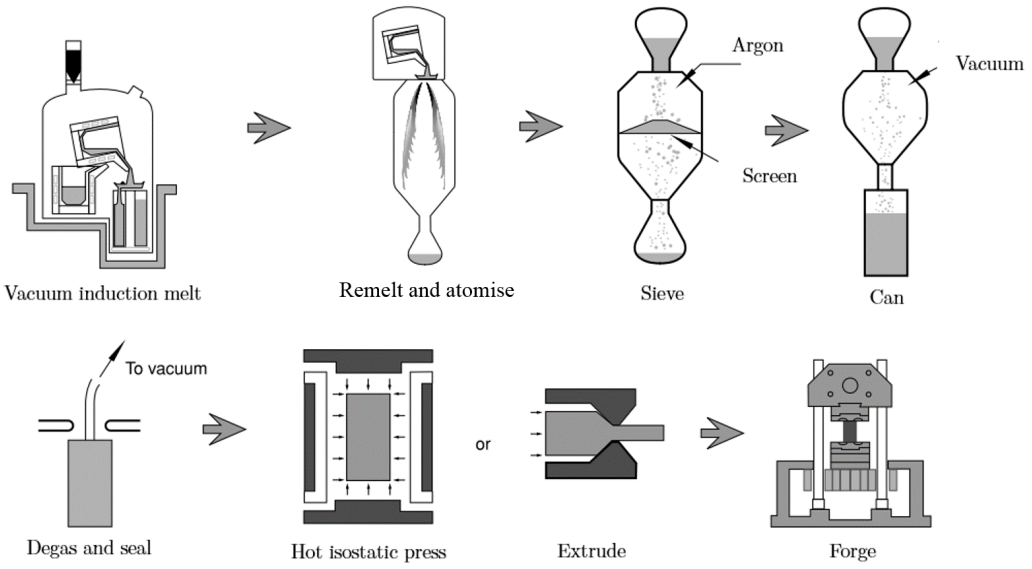


Fig. 2.12 A demonstration of processing route for producing powder metallurgy alloys. Adapted from [90]

selectively again. The layer by layer melting process will be repeated until a component is built. The residual powder will then be removed. Other AM builds such as laser metal deposition operates in a very similar manner. Finally the component will be heat treated to attain the desired properties.

2.3.2 Heat treatment types and their aims

Aforementioned processing routes for nickel-based superalloys all require at least a final heat treatment process. As the last step of all processing methods, heat treatment plays a pivotal role in the final microstructure, and hence properties, for example tensile strength, fatigue life and creep resistance [18]. Its main functionality is to remove processing defects and problematic phases, as well as to yield the optimum distribution of the phases.

Homogenisation & solution treatment

The first step of the thermal process acquires a very high temperature exposure, typically between 2 - 4 hours for cast/wrought alloys. For single crystal superalloys such as CMSX-4, a very high temperature exposure can last for a day or longer [93]. Such heat treatment is referred as homogenisation or solution treatment. The two terms are often used interchangeably in the community, however, their original meanings are slightly different. Homogenisation treatment is only needed for cast alloys, it is meant to remove the chemical segregation on the micro-scale that is produced during casting [94]. Solution treatment, on the contrary, is designed for all processes. It is to dissolve most phases into γ matrix that formed during solidification, *e.g.* γ', γ/γ' eutectic, γ'', $M_{23}C_6$, M_6C, etc. [28, 95, 96, 94]. Furthermore, solution treatment can be classified into two other subsets, *i.e.* supersolvus and subsolvus solution treatment. The difference between the two applies the temperature selected, which is either higher than γ' solvus temperature or lower respectively. Supersolvus heat treatment generally chooses a temperature that is 30°C higher than solvus temperature which dissolves all γ' particles and promote grain growth. Whereas subsolvus heat treatment chooses a temperature that is lower than the solvus temperature. As a result, most secondary and tertiary γ' particles will be dissolved, but primary γ' will remain at grain boundaries to inhibit grain growth, and leave a fine grained material [97]. For casting alloys, homogenisation and solution treatment are normally used together as they achieve their goals in either treatment. In addition, to perform only one high temperature soaking saves time, energy, and prevent excessive grain growth. This is believed to

be the reason why two terms are used interchangeably in context nowadays. The thermally exposed materials are usually cooled in water or in air, achieving fine γ' precipitates. In some cases, a furnace cooling is used to prevent crack formation during fast cooling or modify grain boundary character [98].

Stablisation & **Ageing**

Following solution treatment, further stabilisation and ageing processes will be conducted at lower temperatures. The goal is to grow intragranular precipitates to a size that is most resistant to shearing. The stablisation treatment, sometimes referred as primary ageing, is not an essential step for all alloys. This step is designed for stress relief of the component, which was built up from the previous step, particularly in a case where quenching was adopted. As a result, an increase in the elongation is usually observed [99]. The stablisation is conducted at an intermediate temperature (lower than solution treatment), and hence, secondary γ' particles will also be promoted and coarsened. Their size and distribution can be described as a function of particle nucleation and growth, which is dependent on a few factors: solution temperature, cooling rate and stablisation temperature. For example, higher temperature or faster cooling rate yields finer and more densely distributed particles [100, 98, 101]. Fully coarsened secondary γ' are achieved (typically less than 1 μm) by the ageing process, or sometimes referred to as secondary ageing. It is carried out also to yield nanometer sized spherical γ' particles in the channels between secondary γ'. Moreover, the

ageing treatment also promotes the decomposition of MC carbides into $M_{23}C_6$ through reactions involving γ and γ' phases.

Hot isostatic pressing

Hot isostatic pressing (HIP) is a technique that is designed to minimise defects, such as micro-pores, hot tears or shrinkage cavities through heat and pressure. The process is particularly crucial for casting, powder metallurgy and additive manufacture for defect removal [102–107]. This method can also be implemented for rejuvenation of serviced components [108, 109]. The HIP process involves isostatic pressure at very high temperatures, and thus consolidates the material in order to achieve full densification. The temperature is achieved by a furnace inside a pressure vessel, and the pressure is attained by pumping in inert gases, such as argon or nitrogen. The HIP condition needs to be optimised for each specific material, which is influenced by its interior strength (minimum temperature) and emergence of incipient melting (maximum temperature) [110].

In the cases when HIPping is used collaboratively with conventional heat treatment, for example casting, AM or rejunenation, HIPping is performed prior to the heat treatment. Due to the very high temperature that it uses, most precipitates, apart from MC carbides, can be dissoluted. Thus, a solution treatment may be skipped [41].

Annealing

Wrought alloys some times experience enormous an amount of deformation, for instance through rolling, forming or extrusion, where the extensive work hardening makes the material too strong to be further deformed. In which case, annealing must be conducted for partial or full recovery of the microstructure, which involves considerable stress relief and softening induced by recrystallisation [88, 89]. Therefore, the material can be further deformed without fracture. Annealing process is carried out for thermal exposure at relatively high temperatures. Due to heavy deformation received in previous steps, high dislocation density regions act as nucleation sites for recrystallisation, where strain free crystals grow at the expense of the deformed ones. The degree of recrystallisation can be readily obtained by hardness values or using GAM threshold from an EBSD map [111–113]. The kinetics for such a solid state phase transformation is very complicated, which can be described using the empirical JMAK model [114–116]. In processing terms, it describes the recrystallisation rate in a function of strain, strain rate and temperature exposed. By utilising the appropriate parameters, the final microstructural features and grain size can be designed.

2.4 Formation of grain boundary serration in Nickel-based alloys

Grain boundary, the solid state interface between two crystals, is one of the most significant microstructural features for a material. On the microscale, the architecture

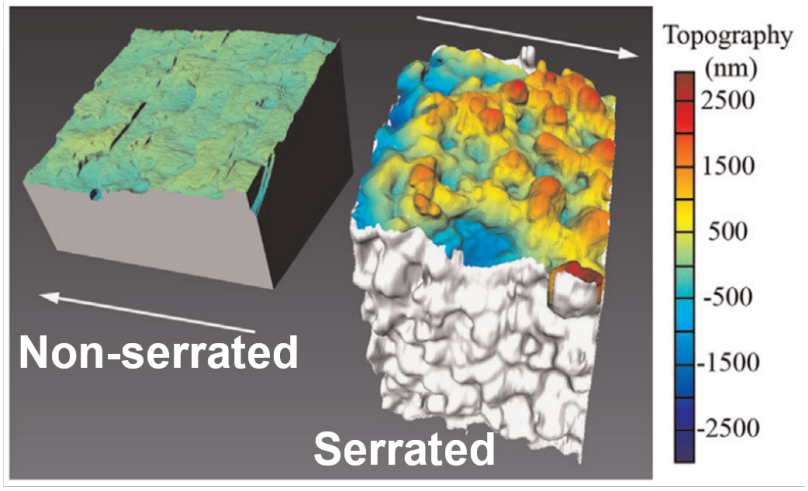


Fig. 2.13 Non-serrated and serration grain boundaries illustrated in 3D, prepared using focused ion beam (FIB). Adapted from [120]

normally exhibits as a smooth plane in most metals and alloys, see Figure 2.13, and hence a straight line if presented in 2D in Figure 2.14. Nonetheless, it could also adopt a serrated or wavy morphology in steel or nickel alloys with a modified heat treatment [117, 118, 5, 119]. As a result, some mechanical properties are improved accordingly. Thus, serrated grain boundaries are often pursued as a type of grain boundary engineering. In this section, the formation of grain boundary serration in various Nickel-alloys is reviewed, and the missing puzzle pieces are suggested.

Grain boundary serration was first observed in stainless steels for improvements of stress-rupture properties during late 1960s [117, 118]. Inspired by steel, controlled furnace cooling were then applied to nickel alloys seeking creep life enhancement by empirical approaches in 1976. Interestingly, the first two research papers on nickel alloys were published side by side in 1976, and their submission dates (late 1975) were very close. In addition, the two research labs that the authors came from were

located in Japan [4] and the America [5], whose co-authors were all associated with institutions either in Japan or the America. No evidence showed they had any academic relationships, hence it is believed both groups observed the phenomenon independently. The next milestone in the research towards serrated grain boundaries was in 1983 [119]. Koul and Gessinger conducted a systematic study on a range of alloys, backed up both by experiments and modelling, to address the driving force for serration formation. In 1993, Henry *et al* made use of higher resolution microscopy and subsequently modified the model, which is more widely accepted. The idea is then further extended to low γ' fraction alloys in 2009 [37], where similar morphology can be obtained with the assistance of carbide phases.

Apart from the aforementioned serrated grain boundary, which were usually produced with an annealing process. Other types of grain boundary discontinuities can also be observed and simulated with aid of computation [121], such as steps and kinks [122, 123]. The formation of those interfaces are not limited to f.c.c. structures [121], and are commonly associated with deformation, short periodicity or faceting on the nanometer-scale.

2.4.1 Grain boundary serration assisted by intergranular phases

Grain boundary serration, sometimes referred as wavy grain boundary or zig-zag grain boundary, is readily reported in various nickel alloys [125, 126, 119, 127–131, 37, 124, 100, 132, 38, 98, 133]. Three similarities in processing and microstructure can be found

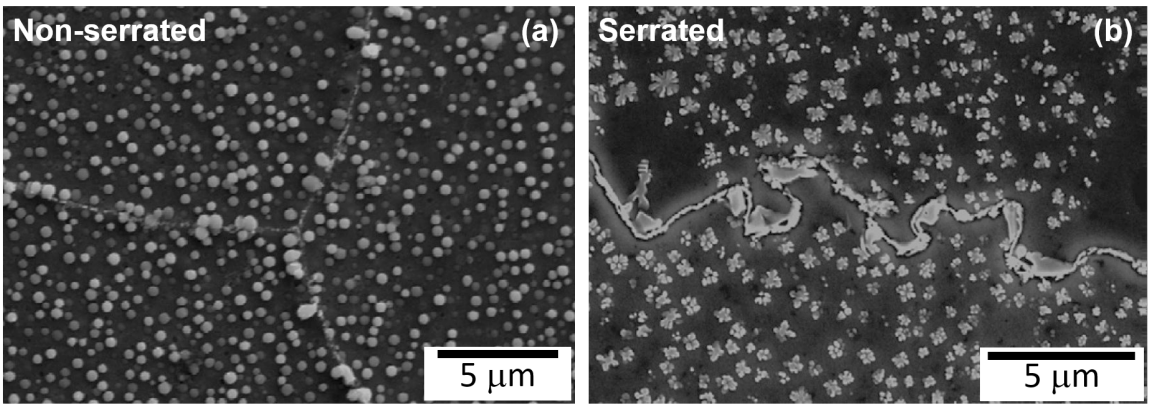


Fig. 2.14 Non-serrated and serration grain boundaries illustrated in 3D. Adapted from [124]

amongst all the studies. First, serrated grain boundaries were generated using heat treatment, particularly a slow cooling process from solution treatment is a prerequisite. Second, serration was always found in association with some intergranular phases. Third, the phases that presented on the grain boundary also demonstrated coherency with one side of the matrix. Details about the role of different phases and chemistry will be discussed in the following sections.

Serration induced by γ' phase

Early work on grain boundary serration was focused on improving the creep properties of a material, particularly creep ductility [5, 134, 119]. The alloys studied often possess relatively high fraction of γ' phases, such as IN792, René 95, Astroloy, etc. It was observed that in some circumstance, γ' has the preferred formation site along the grain bounday. Due to the coherency relation with the matrix, growth of γ' is directional to one side which eventually twists the grain boundary. Pioneer research was conducted on IN738, Nimonic 115 & Nimonic 105 [119, 135, 136]. A supersolvus solution treatment

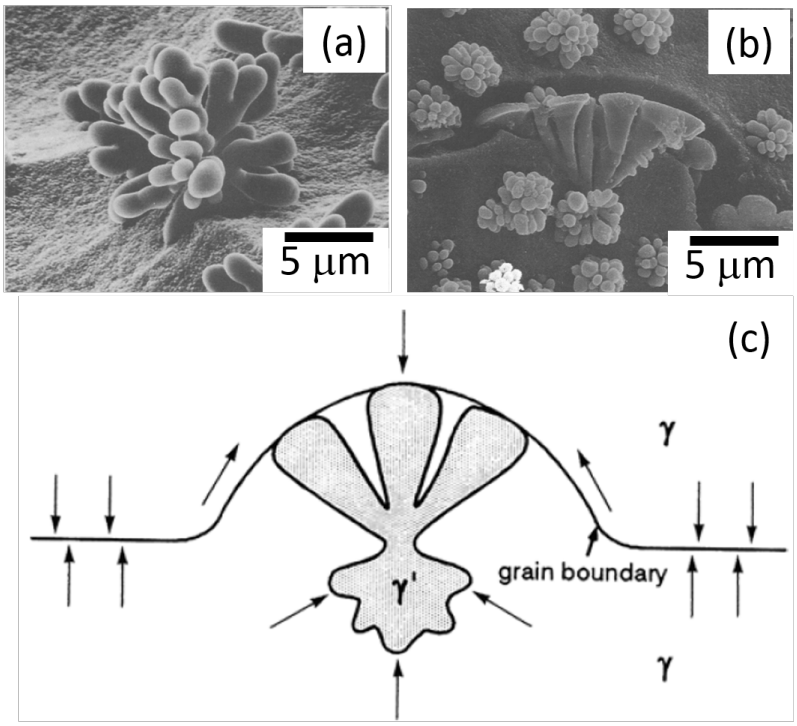
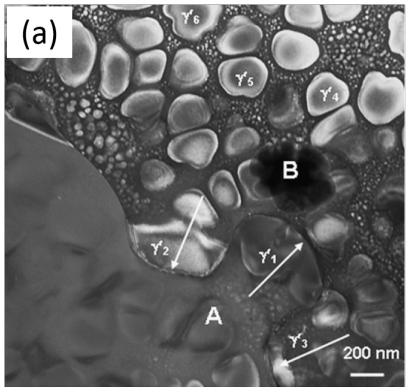


Fig. 2.15 Dendritic growth of intergranular γ' particles. Adapted from [129]

was utilised followed by a controlled furnace cooling process, serrations were observed using electron microscopy, where closed association of serration and γ' were revealed. A model is then constructed that considers the driving force coming from the net strain energy differenctial between coherent and incoherent side of the boundary that causes γ' particle migration, whose assumptions were then challenged and proved invalid [129].

Later efforts by Henry *et al* on a model alloy agreed on the association with γ' precipitates, however, they proposed a different mechanism [129]. With the aid of electrolytic etching, 3D morphologies of γ' near serrated grain boundary were first revealed, see Figure 2.15. It demonstrates the γ' particles grow predominantly in dendritic form under super saturation solid solution treatment followed by slow cooling. The γ' particles grow preferentially towards the incoherent boundary and



(b)

	Grain boundary γ′			Grain interior γ′		
	γ'_1	γ'_2	γ'_3	γ'_4	γ'_5	γ'_6
Al	4.94	5.40	5.39	4.08	4.06	5.56
Ti	8.29	8.43	8.57	4.65	6.20	8.33
Cr	2.97	2.90	3.05	13.28	9.33	2.78
Co	10.52	10.12	10.22	16.41	14.07	9.57
Ni	66.81	66.43	66.28	54.25	60.15	66.85
Mo	1.38	1.34	1.19	4.62	2.99	1.81
Ta	3.63	4.19	4.40	2.38	2.66	4.22
Zr	0.20	0.14	0.15	0.05	0.08	0.08
Hf	1.26	1.06	0.76	0.29	0.45	0.80

Fig. 2.16 Compositional profile of particles in the vicinity of a grain boundary revealed using TEM-EDS analysis. Adapted from [137]

ultimately produce serration. The proposed mechanism account solute transport at grain boundaries where solute atoms from lattice diffusion move rapidly to incoherent boundary. In addition, the study also reported that a sub-solvus treatment, followed by slow cooling, can produce serrated grain boundary as well. The investigation has clearly elucidated the evolution of γ' in relation to serration subsequent to a solution treatment.

More recent studies by Mitchell *et al* has further validated the explanation by Henry *et al* using high resolution chemical analysis as shown in Figure 2.16 [137]. Transmission electron microscope (TEM) equipped with an energy dispersive X-ray spectroscopy (EDS) was implemented for RR1000. A chemical composition distribution was revealed across the grain boundary and grain interior, which suggests a difference in solute transportation kinetics within bulk and grain boundary. High resolution imaging again confirms protuberance along grain boundary assisted by the growth of γ'. This study is in good agreement with Henry, Danflou, Lu and Yao [129, 130, 138, 139]. Moreover,

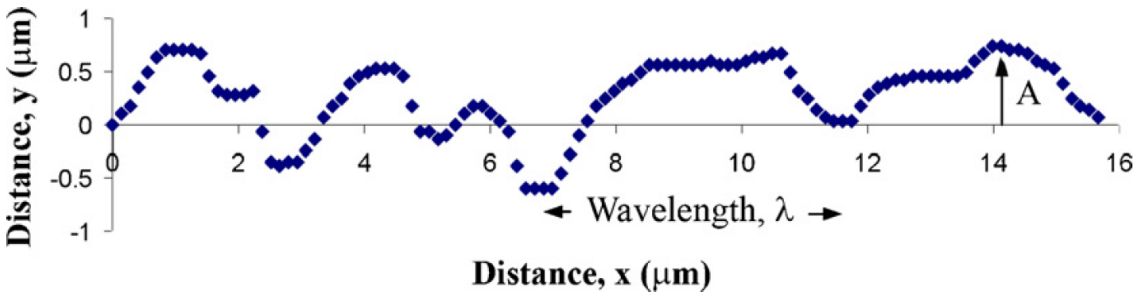


Fig. 2.17 Serration quantification method used in literature. Adapted from [137]

Mitchell *et al* has suggested a way of measuring the size of serration, yet in a subjective sense [137], see Figure 2.17.

Serration induced by δ and η phase

For alloy systems with relatively high Nb and low Al/Ti in composition, such as IN718 or IN718Plus, γ' is not the only strenghening phase. In addition, body centred tetragonal γ'' (Ni_3Nb), orthorhombic δ (Ni_3Nb) phases are frequently observed as demonstrated in Figure 2.18 [140–142]. In some cases, a hexagonal η (Ni_6AlNb) could also be observed in the vicinity of grain boundaries [142]. The δ phase forms on the grain boundary, and is usually used for inhibiting grain boundary migration, and hence to control the grain size [143]. However, the role of δ is often debated for strength loss due to depletion of γ''.

Recent studies have reported the necessity of δ or η phases in assisting the generation of grain boundary serration [141, 142]. Yeh *et al* illustrated improved creep resistance and ductlity coming from the presence of grain boundary serration [141]. By adopting a similar heat treatment accompanied by the slow cooling process, the formation of

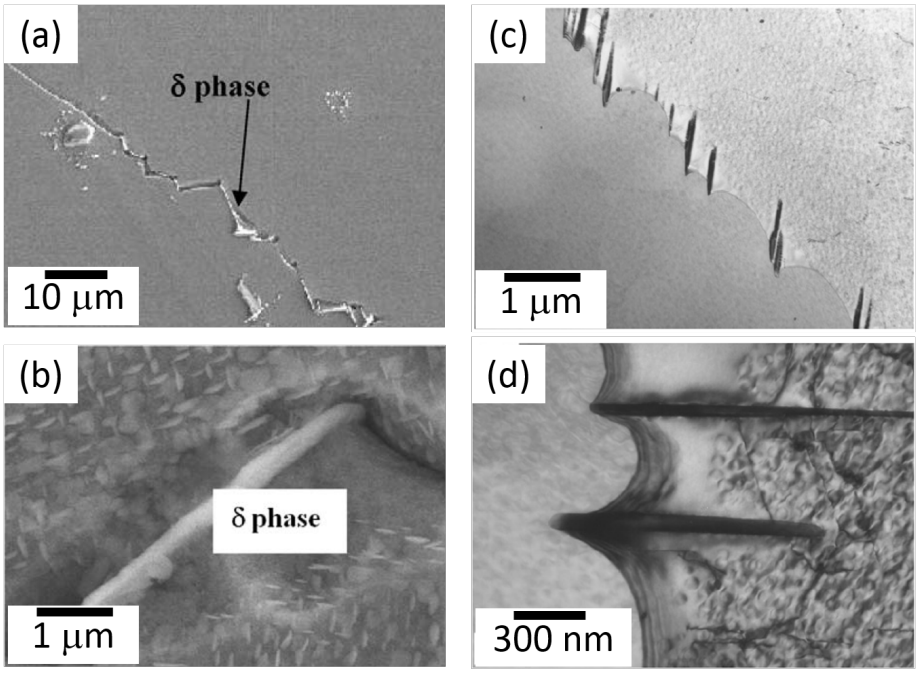


Fig. 2.18 Grain boundary serration induced by δ and δ' phases. Adapted from [141, 142]

grain boundary serration is achieved. A plate-shape phase is in close association with serration, which is jointly suggested as δ phase using TEM and EDS. Once again, coherent crystallographic relation were observed between the δ orientation and close packed plane of the matrix.

Serration induced by carbides

For alloys containing small or no fraction of γ' (less than 25%), serrations were reported in association with grain boundary carbides. The pioneering study was conducted by Hong *et al* on Nimonic 263 [37], which was futher extended to other systems such as Haynes 230, Inconel 690, Inconel 617 and some model alloys [132, 144, 38, 145–148, 133]. Close examination using electron microscopy with aid of chemical analysis has indicated that planar Cr-rich carbides are associated with grain boundary serration

in all aforementioned alloy systems. It is also frequently found that the degree of serration (indicated by wave amplitude) has a positive relationship with increasing solution temperature and decreasing cooling rate [37].

On the understanding of the carbide type, TEM diffraction pattern was utilised. It is elucidated that the $M_{23}C_6$ carbide is observed in Haynes 230 [132]. A model is then constructed that considers energies in both coherent and incoherent interfaces and tension balance relation. It is then further deduced that different diffusivity of carbon and chromium in the coherent and incoherent interfaces that initiated the oriented growth of $M_{23}C_6$ carbide. This research was furthered by Tang *et al* on the same alloy [144]. The emphasis was on the susceptibility of serration as a function of crystal misorientation angle, as determined using EBSD technique. Random high angle grain boundaries with misorientation angle between 20 - 40° demonstrated formation preference [144]. By contrast, no evidence has been shown of a relationship between CSL boundaries and serration formation.

Nevertheless, another formation hypothesis was proposed by Hong *et al* on reducing interfacial energy per unit area [37, 146–148]. Although the grain boundary serration is associated with carbides at all times, they claimed the formation of serrations is preceded the carbides. This was experimentally demonstrated by sequential quenching at different stages of slow cooling, see Figure 2.19. However, with closer attention, grain boundary morphologies had changed from Figure 2.19 (b) to (c), *i.e.* from faceted to sinusoidal. It is not entirely clear with only one high magnification SEM

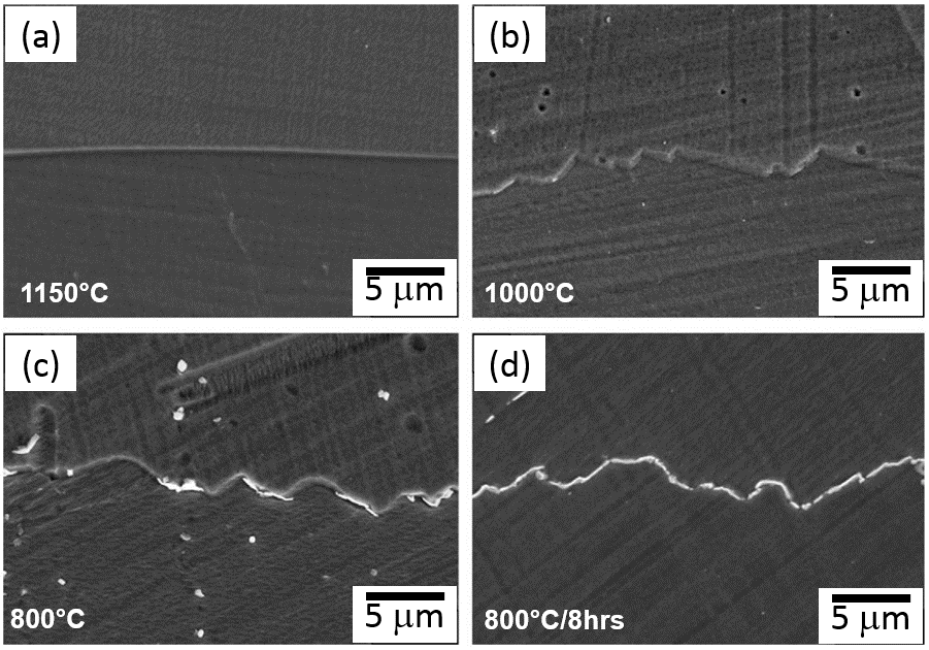


Fig. 2.19 Grain boundary morphologies of Nimonic 263 water quenched at different temperatures during slow cooling from solution temperature. Adapted from [37]

image to support the argument, as similar morphology can be obtained from a growing incoherent twin boundary segment [149].

The formation sequence of serration and carbide can be further discussed. TEM results have shown that carbide resides predominantly on low index planes with {100}, {110} or {111} to one of the matrix grains. These are the grain boundaries with low interfacial energies, which it suggested to be the driving force for formation by decreasing the interfacial energy of grain boundary per unit area. The hypothesis was further elucidated using electron energy-loss spectroscopy (EELS), where it was suggested that discontinuous segregation are the cause of serration [150]. During the segregation of both carbon and chromium atoms, the lattice might have accumulated distortional strain due to atomic radii difference, which consequently become responsible

for the onset of grain boundary serration. In spite of the characterisation work, one may not be totally convinced by the hypothesis — lacking modelling or direct experimental evidence for quantitative proof.

2.4.2 Grain boundary serration in relation to chemical compositions

Intergranular phases have demonstrated sensitivity in generating grain boundary serrations, in this section, we will review how the chemical composition influences the formation of the phases, and hence how it changes the effectiveness of the generation of grain boundary serration.

Role of Carbon, Chromium, Molybdenum & Zirconium

The sensitivity of carbon, chromium, molybdenum and zirconium content in relation to the degree of serration was studied [38, 145, 133] in Inconel 690 and several model alloys. In the case study of Inconel 690, the carbon content was varied from 0.02 to 0.03 wt%, to yield more $M_{23}C_6$ carbide. As a result, an increase in serration wave amplitude was achieved with carbon content, though using a semi-quantitative approach. On the other hand, modifications were made to Cr and Zr content, from 10 to 30 wt% and 0 to 0.5 wt% respectively. By conducting the same heat treatment for the model alloys, a positive correlation was illustrated between Cr content and serration amplitude, which changed from 1.5 to 3.5 μm while Cr content was increased from 10 to 30 wt%. Addition of Mo in the alloy, however, showed no effect on promoting the

serration formation. In the case of Zr containing alloys, the situation becomes more complicated, as serrations are observed to generate with Zr-rich precipitates with fairly low amplitude. Notwithstanding, due to the qualitative nature of the observations and a lack of deterministic criterion, the role of Zr on initiating the serration is not clear.

Though not mentioned explicitly in the above literature, the strength and cohesion of $M_{23}C_6$ carbide varies with its morphologies, and hence its role during deformation. Blocky, film and lamellar $M_{23}C_6$ can readily form in nickel-based alloys because of its stable nature [28, 151, 152, 41]. Fine carbides along the grain boundaries, particularly in the blocky shape have been reported as a grain boundary strengthener, which it resist grain boundary migration at high temperatures. On the other hand, due to its high hardness, the $M_{23}C_6$ carbide can also serve as fracture initiation site during low cycle fatigue by decohesion at the interface [28]. The lamellar type, however, should always be avoided. This type of carbide grows from the grain boundary into the matrix, which is associated with a decrease in alloy strength due to carbide fracture [28, 151].

Role of Boron

The addition of boron has been suggested to promote the formation of grain boundary serration [41, 153]. It is found that with a certain level of boron (more than 0.03 at%), grain boundary morphology changes from straight to serrated, whereas further boron does not seem to be useful for achieving larger degree of serration. The difference in microstructure is suggeseted by the grain bounday character that is modified by boron, where it breaks down the agglomerated $M_{23}C_6$ carbide, and promotes the formation of

M_5B_3 boride instead. Therefore, the coarsening of γ' can be facilitated by the absence of coarse $M_{23}C_6$ and MC on the grain boundaries, and consequently they possess some degree of serration. Furthermore, it also suggests that once sufficient coarse carbides have transformed to borides, the potency of serration generation is unchanged with further boron content.

Synergy between γ' and $M_{23}C_6$

The above arguement can be furthered by investigating the synergy between γ' and $M_{23}C_6$ phases. In the systematic study carried out by Koul *et al*, various alloys were carefully examined, where only Nimonic 105 was observed to be free of serration [119]. This is then furthered by thermodynamic interpretation using phase diagrams. It is indicated the unique difference between Nimonic 105 and other alloys studied is the dissolution temperature of the $M_{23}C_6$, which is higher than that of γ'. This suggests prior formation of the carbide than γ' during heat treatment, where growth of the grain boundary γ' may be retarded by the pinning force from $M_{23}C_6$ carbide. On the contrary, this opinion was challenged by more recent investigations [132, 144, 38], where $M_{23}C_6$ carbide have the potential to form serrations on their own. Nonetheless, the complication of the alloy systems are not entirely comparable, as the interaction between γ' and $M_{23}C_6$ are not yet clear. Therefore, high resolution elemental mapping techniques using EELS or EDS and strain analysis using HR-EBSD are encouraged for further study on in the vicinity of grain boundaries, which is believed to provide further evidence on the generation of grain boundary serrations.

2.4.3 Summary

Grain boundary serration in nickel-based superalloys is indeed intriguing — with a slight modification of heat treatment parameters, one can expect different morphologies, and hence properties. Literature has shown success in the search for processing parameters, chemistry and phases which can produce such grain boundaries in an empirical manner, however, a few crucial questions remain in open debate or are seldom addressed. For example, what is the definition of grain boundary serration? What is the criterion to determine whether a boundary is serrated or not? How best to quantify the degree of serration in an objective manner? Can the proposed mechanism be validated by direct experimental observations? How possible is it to produce a processing map for serration? Admittedly, a long journey lies ahead in answering them explicitly. Driven by engineering needs, previous studies focused primarily on particular applications in complex alloy systems that are processed differently, and hence it is difficult to gain fundamental understanding of the phenomenon. Therefore, it is suggested to utilise simple alloy systems, as well as advanced characterisation techniques to tackle the questions from a fundamental perspective.

2.5 Effect of grain boundary serration on the mechanical properties in Nickel-based alloys

Grain boundary serration introduced by heat treatment modifications inevitably changes the mechancial properties to some extent — this can be beneficial or detrimental. The

critical question is to understand how much it has changed in relation to the presence of grain boundary serration. Moreover, the underlying mechanism that cooperates with serration is needed for designing the optimum grain boundary morphology. In this section, both room temperature and high temperature mechanical properties will be reviewed for serrated and non-serrated nickel alloys. Furthermore, secondary effects, for example change in γ' size induced by modified heat treatment will also be discussed.

2.5.1 Room temperature mechanical properties

The effect of grain boundary serration on room temperature properties in Nimonic 263 has been systematically studied [37]. Samples with and without grain boundary serration showed no difference in ultimate tensile strength, yet a slight decrease (less than 5%) in yield stress. These results are in good agreement with other researchers [127, 131]. Interestingly, the ductility of the material has shown signiciant improvement (more than 50%) with the presence of serrated grain boundary [37]. This is believed due to a change in failure mode. As illustrated by fractography in Figure 2.20, non-serrated samples showed a faceted intergranular fracture surface, whereas a mixture of intergranular and transgranular fracture surfaces is observed in the serrated case, which is believed to toughen grain boundaries in resisting failure.

2.5.2 High temperature mechanical properties

Enhanced creep behaviour in association with grain boundary serration was first reported in 1976 for a low γ' fraction alloy [4]. In the condition of 700°C and 294MPa,

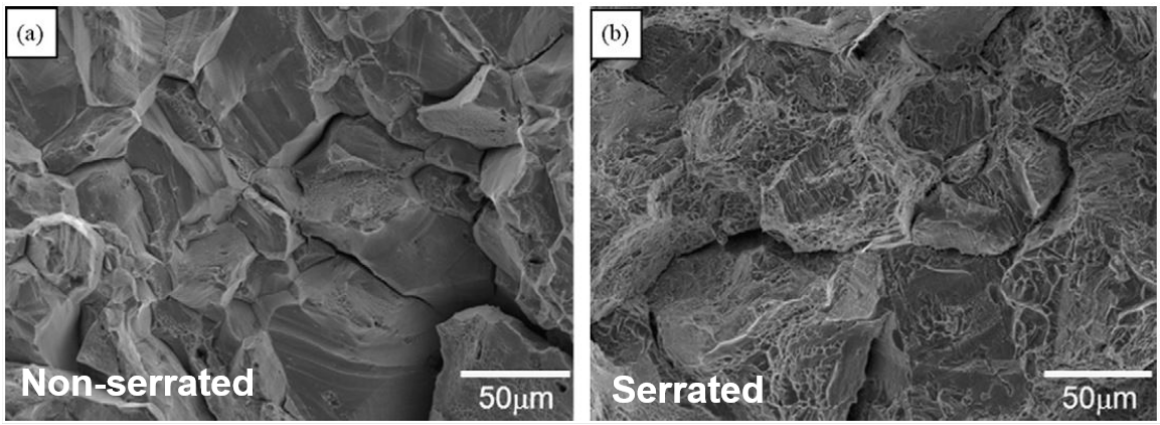


Fig. 2.20 Fracture surfaces of non-serrated and serrated grain boundary material in Nimonic 263. Adapted from [37]

the serrated grain boundary material showed lower minimum creep rate and higher creep ductility. This implies an increase in resistance against grain boundary sliding. Microscopy has suggested the prevention of wedge-like cracking by the presence of serration. The results and conclusions were somewhat empirical and qualitative, understandably due to the limited characterisation technique. More recent researchers have further consolidated the hypotheses with detailed examinations in similar creep conditions [37, 141, 146–148], which also emphasised the importance of intragranular strength in relation to heat treatment. Typical creep curves in comparison are presented in Figure 2.21. Another early study on higher γ' fraction Inconel 792 also demonstrated improved creep properties [5, 154], *i.e.* prolonged stress-rupture life and slower crack growth rate in the 650 - 760°C range. Due to the nature of the serrated shape, an increase in grain boundary area can be expected, which provides a longer diffusion path as well as a physical locking mechanism.

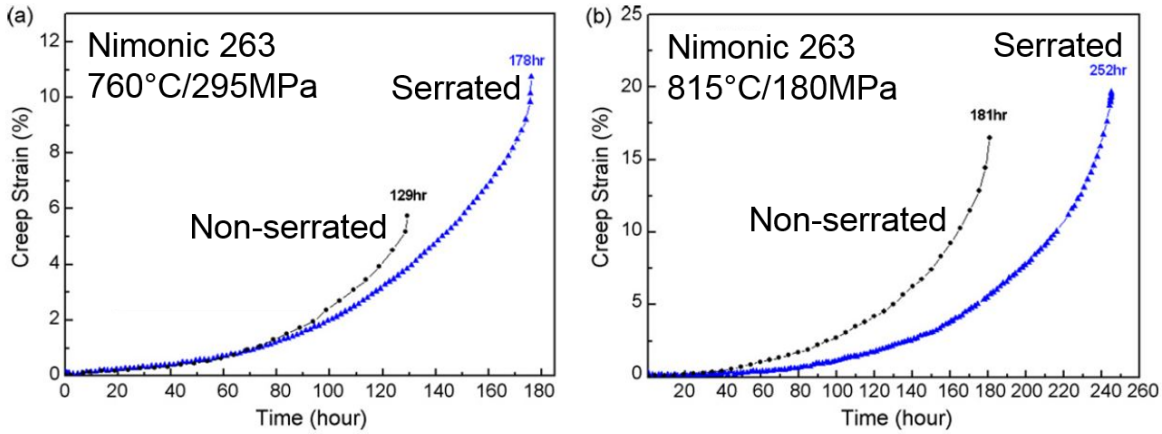


Fig. 2.21 Creep curves of non-serrated and serrated grain boundary material at different conditions. Adapted from [37]

Similar successes were also repeated in Inconel 738 [155, 126], where they demonstrated the beneficial effect that can be achieved over non-serrated boundaries regardless of the heat treatment parameters. In addition, different degrees of serration were generated using various cooling rates — the largest serration corresponded to the slowest cooling rate. Unexpectedly, the best creep life was not achieved with the largest serration, but an intermediate one. Indeed, slow cooling has altered the γ' phase both within the grain boundary and interior, which leads to γ' coarsening and a loss of matrix strength. Therefore, considerations must be taken to balance both.

More complex experimentation was performed at creep fatigue condition (dwell fatigue) on Astroloy [128]. The pre-notched specimen was exposed to 650°C at a frequency of 20Hz for 10 seconds, followed by a 300 seconds dwell at maximum stress, for a loading ratio = 0.05R. The serrated grain boundary material exhibited 3-5 times slower propagation rates. A similar trend was explained in terms of misorientation angle and coincidence site lattice theory on a PM alloy using EBSD technique[131].

The preference for serration sites often coincides with high angle random boundaries, which are relatively weak boundaries at high temperature. Thus strengthening these boundaries homogenised the strength and eventually improved crack propagation resistance.

To understand the strain evolution during high temperature deformation in relation to grain boundary serration, combined techniques using EBSD, digital image correlation (DIC) and focused ion beam (FIB) have fulfilled these requirements. Carter *et al* compared the non-serrated and serrated grain boundaries under interrupted creep test at 700°C/1100MPa [156, 157, 120]. The deformation mechanism between the two grain boundary morphologies showed a clear difference, see Figure 2.22: grain boundary sliding occurred in the non-serrated case whereas strain accumulation in the serrated case. The findings on grain boundary sliding has provided direct experimentation evidence to previous studies [4, 128]. Moreover, the DIC method also captured the role of $\Sigma 3$ twin boundaries on the susceptibility of strain accumulation, where non-serrated grain boundaries illustrated notable strain accumulation near twin boundaries, though more evenly distributed in the serrated case.

Dislocation movements were also considered different with the presence of serrated grain boundaries by Zhang *et al* on Udiment 710 alloy at 850°C/343MPa [158]. They have gained insight into dislocation substructures in grain interior and associated evolution of grain boundaries. It is evidenced that for the non-serrated case, dislocation only climbs over γ' within the matrix, whereas dislocations both climb and cut through γ' in the serrated case. This is explained by different morphologies of γ', spherical and

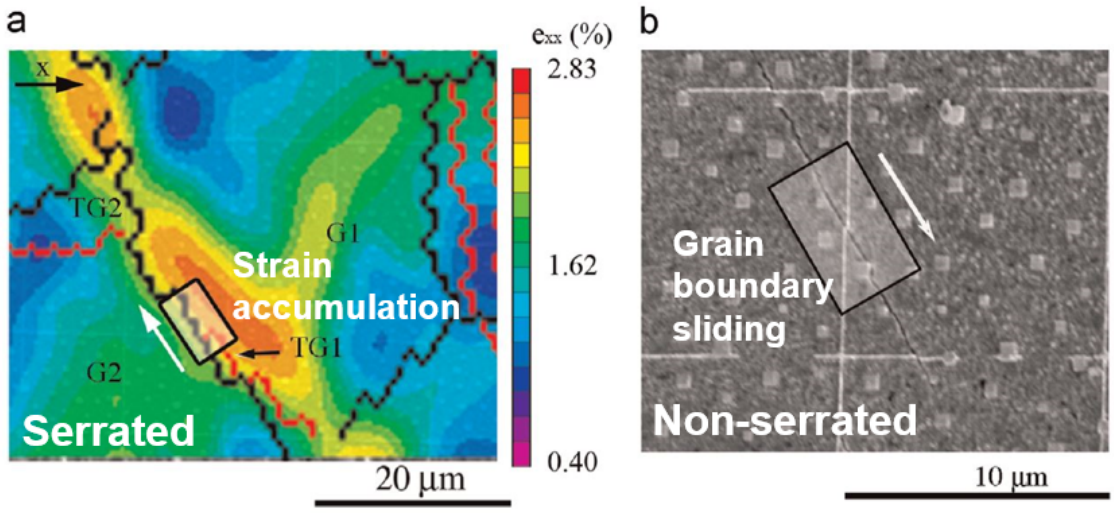


Fig. 2.22 Different deformation mechanisms that are revealed at non-serrated and serrated grain boundary materials. Adapted from [120]

cubic, that is differed as a result of slow cooling. Furthermore, it was also shown that the serrated grain boundary experience a "straightening" effect, as it decreases the amplitude of serration and eventually initated cavitation. However, the non-serrated case skipped the "straightening" event and the cavitation started at an earlier stage, which produced a shorter creep life as a result.

Other mechanisms have been discussed as well based on a substantial research on modified Waspaloy [124]. To gain more insight into different creep regime, *i.e.* dislocation or diffusion controlled, three creep conditions were selected. The results demonstrated the serrated grain boundary material obtains a higher minimum creep rate within the dislocation controlled regime, however, a lower minimum creep rate in the diffusion controlled regime. Understandably due to coarser γ' that is less resistant to dislocations but possesses longer effective diffusion path. Interestingly, it was hypothesized that the inhibition of dynamic recrystallisation due to serration is

the cause of creep life improvement. The non-serrated grain boundary material, for example, exhibited recrystallised grains at failure, which is considered as a sign of strength loss. Though no further explanation was made explicitly on the phenomenon.

Most recent effort conducted by Alabort *et al* has rationalised the role of grain boundaries using cohesive zone modelling in a crystal plasticity framework [159]. The grain boundary strength is modelled with a threshold value, for which if the load exceeded, the interface fails. Simulation coupled experiment jointly suggested the strengthening and toughening effect due to the presence of serrated grain boundary. The serrated morphologies altered the distribution of strain to be inhomogeneous, as evidenced by model and experiment, which it retarded grain boundary damage initiation. As a result, serrated grain boundary induced more transgranular damage where the highest ductility is achieved, as the failure transited from intergranular to transgranular mode.

2.5.3 Secondary effect induced by processing

The property of a material is strongly dependent upon its microstructure, and the microstructure of the same composition can be completely different dependent on the processing routes. In the aforementioned sections, heat treatment modification is proven to be essential to possess grain boundary serrations. However, other microstructural features may also vary due to the adopted slow cooling, such as γ' distribution and morphologies, carbide phases, grain size, twin boundary fractions, etc. Because the thermodynamic driving force for precipitation and time for diffusion are altered. The

corresponding change of microstructure may also have an influence on the final property, particularly the γ' precipitation. In this section, the effect of cooling rate on second phase nucleation density, precipitation size, final morphology of γ' and its implications for mechanical properties is discussed in the following case studies. It aims to gain insight into the secondary effect from grain boundary serration that also influences the behaviour of a material.

To obtain high tensile strength at room temperature, a high quenching rate is usually adopted to achieve fine secondary phase particles [160, 161], as the nucleation density is increased due to significant undercooling. However, the strength may be insensitive at higher temperatures [127]. A systematic study on heat treatment was reported, where René 95 was subjected to two solution temperature (1105 & 1135°) and three cooling rate (48 - 660°C/min) [127]. It was illustrated that γ' volume fraction and size increases with slower cooling rate, where the fraction varied by a factor of 1.8 times, and the size varied from 30 - 250 nm. The coarse γ' precipitates obtained from slow cooling affects adversely creep at high stress level, despite is large volume fraction. The dominant mechanism changed from particle shearing (small) to Orowan looping (coarse). The creep mechanism may change in the case of a higher temperature/lower stress condition in a diffusion controlled creep regime.

Recent research conducted by Chen *et al* in RR1000 has furthered the investigation on γ' distribution in relation to compositional variations [162]. As suggested by SEM and TEM, the precipitate fraction and size are in good agreement with Bhowal *et al* [127]. Additionally, slower cooling rates result in multi-modal distribution of particles.

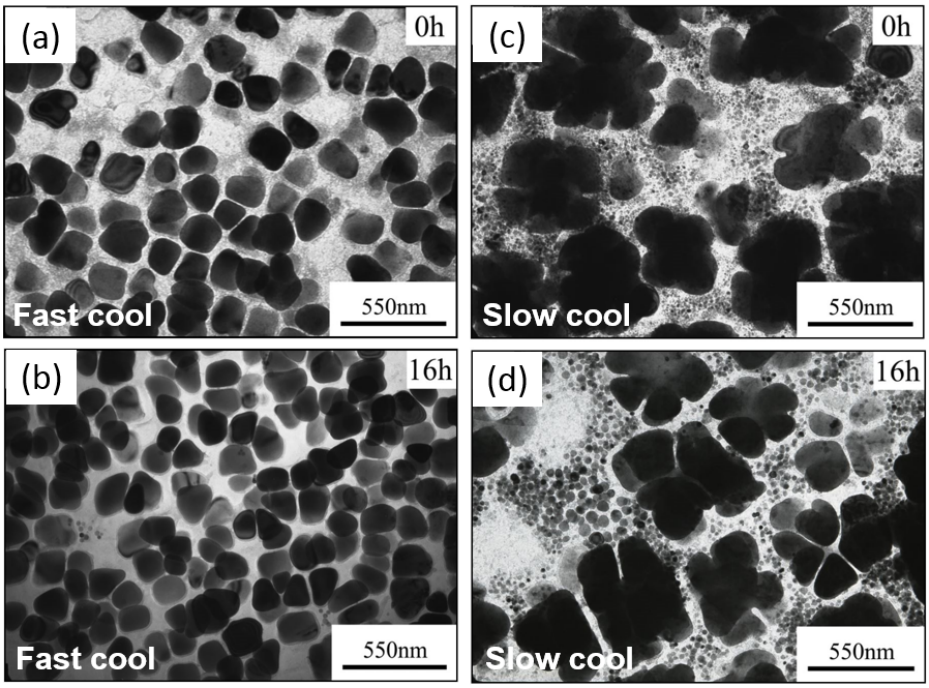


Fig. 2.23 Effect of cooling rate and ageing on the morphology of γ' particles. Adapted from [101]

Moreover, compositional variation is observed between γ' of different sizes, which is particularly pronounced in the slow cooled samples. The research findings are consistent with Singh *et al* [100], Li *et al* [98] and Mitchell *et al* [101].

The study is furthered by assessing the effect of ageing in relation to the final microsturcture [101]. As illustrated in Figure 2.23, it appears that an increase in γ' size with a slow cool ultimately changed the composition of γ' particles, and hence their morphologies. A transition from cuboidal to octo-dendritic with emerging tertiary precipitates during the splitting of secondary γ' was correlated to a decrease in cooling rate. The behaviour of splitting is related to the lattice misfitting that the inverse coarsening reaction is more pronounced for materials with a higher coherency strain, consistent with findings elsewhere [163]. The coherency discrepancy introduced is

thought to influence dislocation motion [164–166], and consequently a change in creep deformation. Therefore, an optimum heat treatment should be considered carefully balancing all subsequent alterations.

2.5.4 Summary

Effect of grain boundary serrations in nickel-based alloys was reviewed at various testing conditions that include: room temperature tensile test, high temperature creep tests and dwell fatigue tests. Frequent successes were reported by adopting serrated grain boundaries, particularly with prolonged creep life, extended creep ductility and lowered crack growth rate, although usually not all these benefits are achieved with a particular alloy. Furthermore, a few strengthening mechanisms were proposed, such as inhibiting grain boundary sliding, cavitation or dynamic recrystallisation, yet in a qualitative manner. Nonetheless, the corresponding change in microstructure on the influence of properties were seldom addressed or not kept consistent, for example, γ' size, morphology and distribution, twin boundary fractions, grain sizes. These factors are well known to have a profound influence on the properties tested. Therefore, the mere impact of grain boundary serration is not entirely unequivocal.

2.6 Conclusion remarks

The 40+ years study of grain boundary serration in nickel alloys was carefully reviewed from the earliest available publication to the most recent ones. Two major aspects

were covered on the phenomenon in a broad spectrum of nickel-based alloys: formation and effect on mechanical properties. Clearly, as an effective method of grain boundary engineering, it is widely pursued for engineering applications. However, many aspects of the phenomenon is still unclear on an elemental level, for example, how to define a serration and what metric should be used? How possible to quantitatively link the processing parameters with resultant serration amplitude? What mechanisms are operating at different test conditions and if they can be quantified?

The proposed research has tackled the questions in a fundamental and systematic manner — starting with a simple alloy composition, we have performed a series of carefully designed tests and investigated using advanced characterisation techniques. The quantified results in the study clarified many aforementioned unknowns and served as pillars and guidelines for future engineering designs.

Chapter 3

Experimental and Characterisation Techniques

3.1 The material

3.1.1 Inconel 600

Inconel 600 was selected as the candidate material for studies on serrated grain boundaries. The material was provided by Deutsche Nickel GmbH in cylinder forms. The bars are 16 mm in diameter and 200 mm in length. The material in the as-received state was cold drawn and annealed that gave a fine grain size, estimated to be around 15 μm by the manufacturer. The composition is shown in Table 3.1, which was measured by Element Materials Technology Ltd (UK) under UK accreditation service testing standard (UKAS). Inductively coupled plasma optical emission spectrometry

(ICP-OES) were utilised to measure metal elements, carbon content was measured using OES combustion method and boron was measured using Spark OES.

Table 3.1 Alloy composition for current study in wt-% (Ni-base), measured using ICP-OES, ICP-combustion (Carbon) and Spark OES (Boron)

Name	Ni	Cr	Fe	C	Co	B	Ti
Inconel 600	Bal	15.75	9.12	0.071	0.04	0.004	0.22

3.1.2 MGA1400CC

An equiaxed polycrystalline nickel-based superalloy MGA1400CC was provided by Mitsubishi Heavy Industries, Ltd. (MHI) in Japan. The nominal composition is displayed in Table 3.2. The material provided was manufactured using conventional casting (CC) method. The component is used as rotating blades on the fourth row (last stage) for industrial gas turbine in G, F & J-type engines such as M501J, as illustrated in Figure 3.1, whose normal operating temperature is 700°C. The material used for the current studies came from three locations of a turbine blade, which is displayed in Figure 3.2 (a). The material in the as-cast form was hot isostatically pressed (HIPped) and then fully heat treated. The HIP condition used was 1200°C and 147 MPa for 4 hours. Subsequent heat treatment was conducted at 1120°C for 2 hours and 850°C for 8 hours. The grain size was found to vary across different locations of the cast blade — larger grains are located at the blade root and smaller grains at the airfoil. Three grain size variants were selected to evaluate the creep scattering behaviour, which are fine (1.77 mm), medium (3.52 mm) and coarse (6.82 mm), as shown in Figure 3.2 (b).

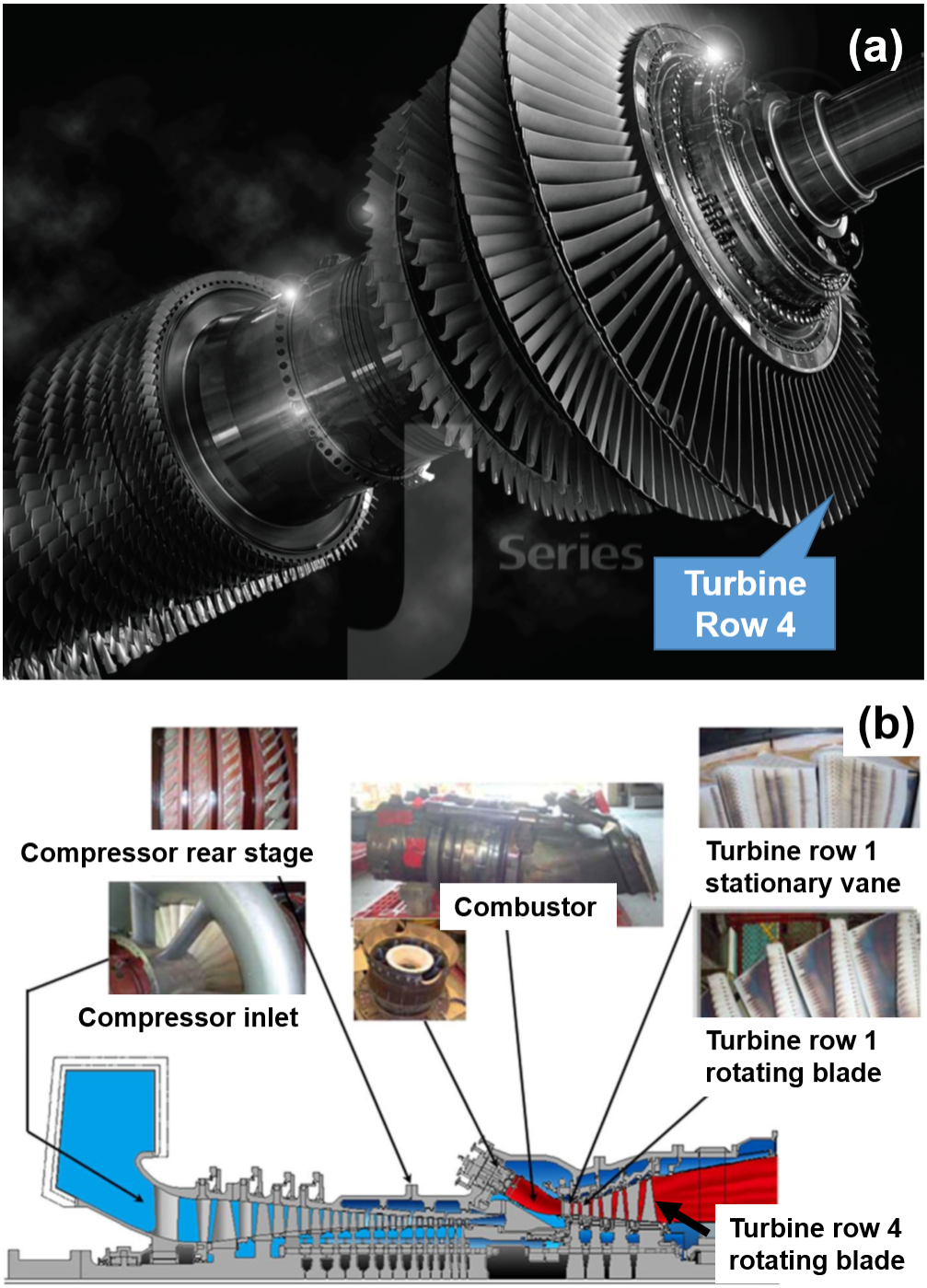


Fig. 3.1 Mitsubishi Heavy Industries M501J industrial gas turbine engine assembly displayed in brochure (a) and in schematic illustration (b). The MGA1400CC material used for the study comes from the fourth stage rotational turbine blade. Adapted from [167, 168]

Table 3.2 Nominal alloy composition of MGA1400CC and three other derivative alloys with minor element modifications in wt-% (Ni-base).

	Ni	Co	Cr	Mo	W	Al	Ti	Ta	C	B	Zr
MGA1400CC	bal	10.0	13.2	1.7	4.6	4.0	2.4	4.8	0.08	0.015	0.025
B alloy	bal	10.0	13.2	1.7	4.6	4.0	2.4	4.8	0.11	0.03	0.025
B+C alloy	bal	10.0	13.2	1.7	4.6	4.0	2.4	4.8	0.08	0.03	0.025
B+Zr	bal	10.0	13.2	1.7	4.6	4.0	2.4	4.8	0.08	0.03	0.06

3.2 Mechanical testing

3.2.1 Creep testing

Tensile creep rupture tests for Inconel 600 were performed using an Instron 8862 servo-electric machine, where the strain was measured using an electromechanical actuator equipped in the lower end of the crosshead operated at a frequency of 1Hz with the precision of 1 μm/hour. Creep test specimens were machined from heat-treated cylindrical bars, whose diameters were reduced from 16.4 mm to 4 mm after heat treatment to avoid any effect of oxidation damage on specimen gauge section. The creep specimens possessed the gauge section of 4 mm diameter and 20 mm length. Temperature was monitored using K-type thermocouples placed in contact with the crosshead next to the specimen. Each specimen was held at the testing temperature for 1 hour prior to loading, for consistency of oxidation damage to each sample.

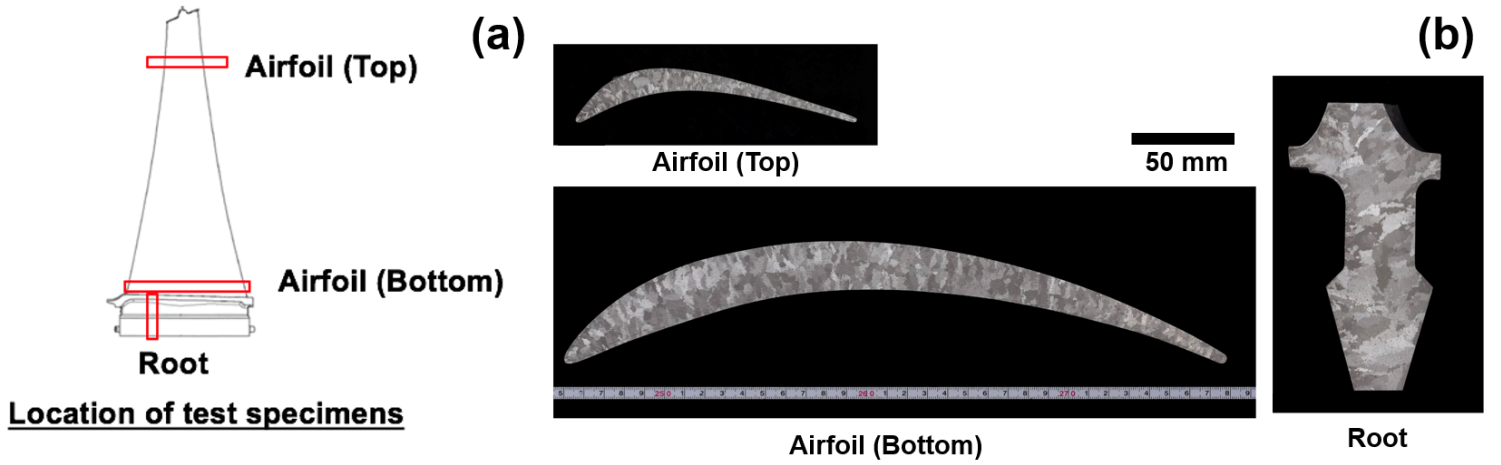


Fig. 3.2 (a): Demonstration of the locations where the test specimens were taken from, and (b): photographs of the blade cross-sesctions at each location.

Tensile creep tests for MGA1400CC was carried out by industrial collaborator in Japan. Two sample geometries were adopted, that include plate and bar shapes. The plate specimen obtained a gauge section of 3.2 mm width × 1.5 mm thickness × 12 mm length. The bar specimens had a specimen gauge of 4 mm diameter and 20 mm length. Creep tests were carried out by creep machines using conventional furnace heating. For plate specimens, only the final creep life and elongation were measured. For bar specimens, extensometer were equipped and creep curves were obtained.

3.2.2 *In-situ* tensile test in SEM

In-situ tensile tests were performed at room temperature (22°C) and 700°C under displacement control with a speed of 2 μm s^{-1}, which provides a strain rate, $\dot{\varepsilon}$ of approximately 10^{-3} s^{-1}. A Kammrath-Weiss *In-situ* module was utilised in a Zeiss Evo SEM with a LaB_6 filament. Dog bone specimens were machined using EDM. The gauge volume of 2 mm length × 1.5 mm width × 1 mm thickness was used. The surfaces were polished using standard metallographic methods with 40 nm colloidal silica finish for about 2 mins. EBSD scans were conducted prior testing, for acquiring crystal orientation information.

For the tests carried out at 700°C, a resistance heating stage was place underneath the sample by contact, and gold leaves were mounted between the heater and sample for improved heat conduction. A pair of thermocouples were spot-welded on the surface next to the gauge section, for monitoring temperatures during the tests. Secondary electron micrographs were taken at 5% increment of engineering strain until failure for

capturing deformation evolution. An illustration of the experimental set up is shown in Figure 3.3.

3.3 Charaterisation

3.3.1 Scanning electron microscopy based characterisation

Metallographic specimens were prepared using standard procedures, removal of materials were achieved by grinding and polishing. Grinding were performed with three pads of different size of resin bonded diamond, which are 220, 500 and 1200 respectively. The surface finish is comparable to SiC paper with the same number of grits. Polishing is achieved by cloth pads with water-soluble diamond suspension of 9, 3 and 1 μm respectively. All samples were finished with 40 nm size coloidal silica suspension for 2-5 minutes.

A Zeiss Merlin field emission gun scanning electron microscope (FEG-SEM) was utilised for most SEM charactersations. The machine is equipped with a Genimi 2 electron column with an acceleration voltage between 1 - 30 kV. Secondary electron (SE), in-lens and back-scattered electron (BSE) detectors were available for topological and compositional contrasts. In addition, a high-resolution Bruker electron backscatter electron (EBSD) system is also equipped with the SEM, which is capable of acquiring EBSD partterns with a maximum resolution of 1600 $\times$ 1200 in 16 bits. Compositional contrast of the BSE image is used for determining phases from the matrix, for example Cr-rich carbide appears darker and Ta-rich MC carbide appears brighter than the

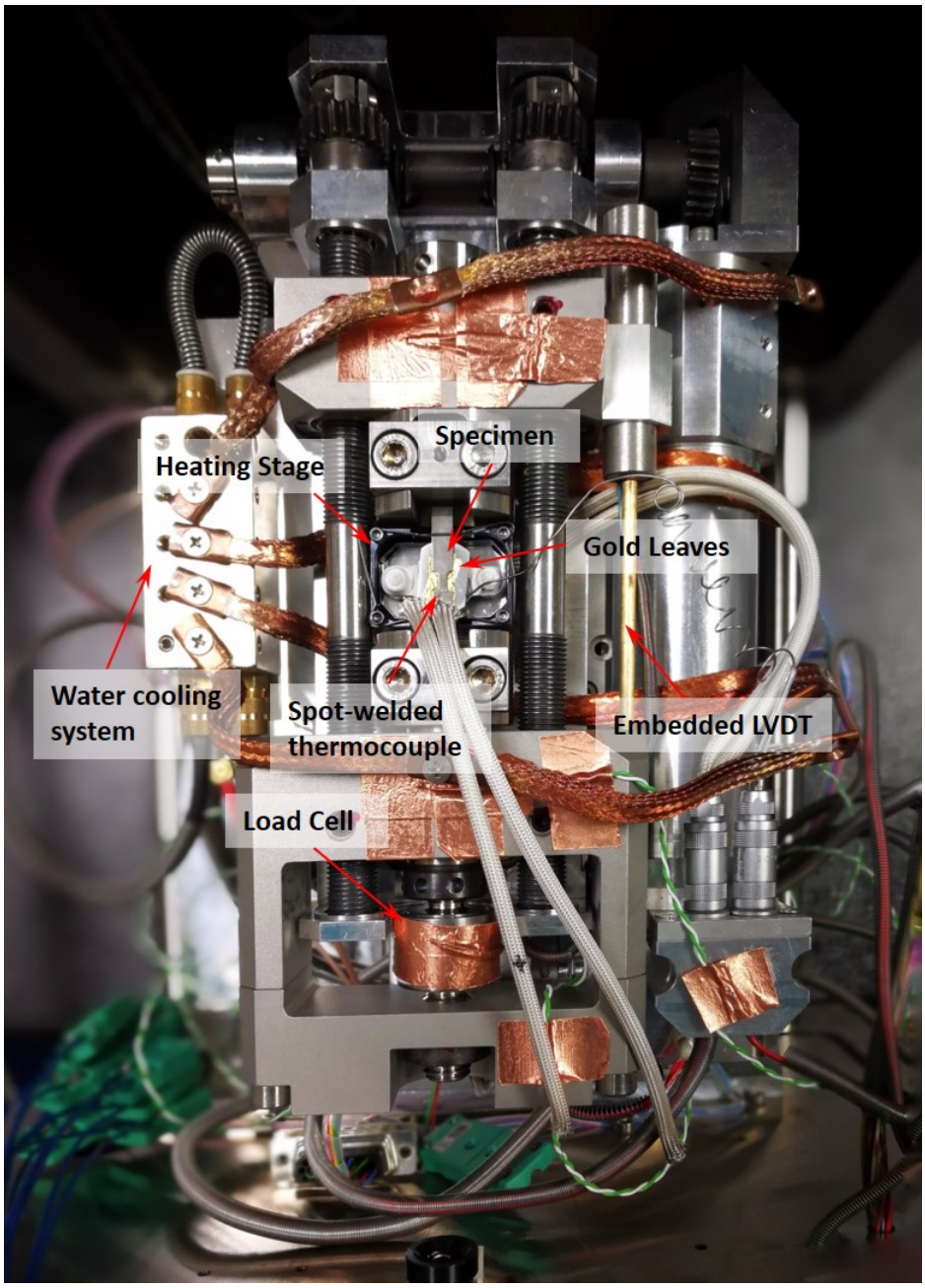


Fig. 3.3 Demonstration of *in-situ* tensile tesing setup in SEM.

matrix. ImageJ and Paint.net softwares were utilised for segmentation of the shape based on image intensity. Energy dispersive X-ray spectroscopy (EDS) were utilised for chemical analysis, which is performed by a Zeiss Crossbeam FEG-SEM system, using the Oxford Instruments X-MAX detector. Lower resolution EBSD were conducted using Zeiss Evo W-filament SEM for measuring the grain sizes. The grain size measurements were processed using Brucker's ESPRIT 2.0 software.

3.3.2 Transmission electron microscopy based characterisation

Preparation of electron transparent foils

For characterisation using transmission based microscopy, foil samples of 3 mm diameter were prepared. The samples were first mechanically grinded down to around 100 μm thick and then polished with diamond and colloidal silica suspension until a scratch-free surface is obtained. The samples were then thinned to electron transparency (less than 100 nm) using a Struers Tenupol-5 twin-jet electropolishing unit. Electropolishing was conducted using an electrolyte of 5% perchloric acid ($HClO_4$) in methanol at -40°C. The polishing was conducted at 20 V, which produced a current through the sample of 100 mA. The electropolishing produces a mirror finish free of any mechanical defamation. Preparing foils in this manner produced hundreds of nm^2 of transparent material that is ideal for further transmission techniques.

Transmission Kikuchi Diffraction (TKD)

An overview of the SEM-TKD setup is displayed in Figure 3.4. A Zeiss Merlin FEG-SEM system was operated using 30 kV voltage with a probe current of 2 nA or lower for the prepared foil samples. The working distance used was 5 mm and the step size ranging from 1 - 10 nm. An OPTIMUS^{TM} TKD detector was placed beneath the sample. The integrated detecting system includes an ARGUS^{TM} forescattered electron (FSE) detector and a horizontal phosphor screen. The ARGUS^{TM} detector was consisted of three Si diodes, thus it enabled bright field imaging (central diode) and dark field imaging (side diodes) that provided strong diffraction and phase contrast. The phosphor screen was used to record Kikuchi diffraction bands, whose pattern center is projected in the middle of the screen that minimised any pattern distortion. The pattern resolution acquired was 800 $\times$ 600 in 16 bits, which facilitated further strain and dislocation density analysis using a cross-correlation based technique [169–171]. In addition, the detector can move in the horizontal direction, as illustrated in Figure 3.4, to align the beam and detector in use.

Transmission Electron Microscopy (TEM)

Micrographs were captured using a JEOL JEM-3000F FEG-TEM microscope operating at 300 kV. To determine the crystal structure of the carbides, selected-area diffraction (SAD) patterns were recorded from a carbide on three different zone-axes. The patterns were indexed by measuring the spacing, d1 and d2, of two different g-reflections, and the angle between them. The appropriate hkl reflections were identified as the allowed

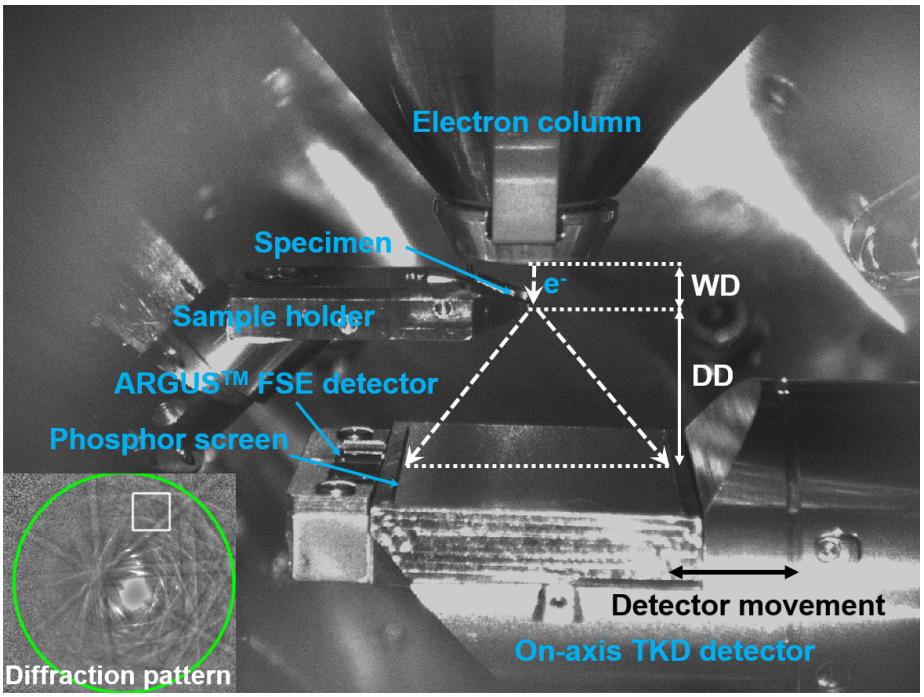


Fig. 3.4 The Transmission Kikuchi Diffraction (TKD) setup for the current study with a typical EBSD diffraction pattern acquired using the technique.

reflections required to produce the correct angle and d1/d2 ratio. Complementary to the diffraction patterns, high-resolution TEM micrographs were also captured down the zone axis to facilitate interpretation of the patterns. Moreover, compositional information across the interface of matrix and carbide was revealed using the energy dispersive X-ray spectroscopy (EDS) under the scanning (STEM) mode with a step size of 1 nm.

3.3.3 X-ray computed tomography

X-ray computed tomography (XCT) was used to quantify cavity size and distribution in fractured samples from creep tests. Tomography analysis carried out using a North Star Imagix system at 150 kV and a current of 27μA, with a voxel size of 4.86μm.

Depending on the area of interest of the sample, a height of roughly 5 - 10 mm was characterized using 1440 - 3600 projections and a helical scan used to reconstruct the 3D volume. ImageJ and Avizo softwares were utilised for quantification of cavity size and distribution using histogram-based methods.

Chapter 4

Formation Mechanisms and Quantification of Grain Boundary Serration in Inconel 600

4.1 Introduction

Manipulation of interfaces, such as grain boundaries, offers cost effective strengthening mechanisms for a range of engineering alloys that pushes their performance further [172, 45, 173–178]. Instead of conventional methods that engineer the twinning/coincidence site lattice (CSL) boundaries, grain boundary serration has shed light on improving high temperature material integrity under various loading or severe conditions [5, 4, 126–128, 131, 124, 37, 141, 98, 146, 147, 153, 159, 179]. The industrial and scholarly attention has increasingly focused on improving understanding, particularly in the search of creep

life and ductility enhancement for component life. Increasing intergranular strength of nickel at extreme conditions, for example turbine disk for jet engines and turbine blade for industrial gas turbines (IGT), provides higher temperature capability that takes advantage of higher thermal efficiency.

Serrated grain boundaries were first highlighted in nickel alloys in the 1970s [5, 4]. Numerous alloys have been observed to exhibit grain boundary serration and pronounced benefits of time-dependent deformation has been demonstrated. The formation mechanism is still an open debate. From a practical perspective, serrations can be triggered by some specific heat treatment parameters within a certain window, though detailed processing maps are missing for microstructural prediction. The promise of uncomplicated modification of heat treatment offering notable enhancement for alloy performance is clearly an attractive proposition.

The conceptual idea for distorting grain boundaries into irregular shapes is closely associated to the reformation of intergranular precipitates, such as γ', $M_{23}C_6$ carbide, δ, etc [119, 129, 37, 150, 132, 141]. Several researchers reported success in generating serrated grain boundaries using similar supersolvus solution treatment followed by slow cooling. Second phases re-precipitating along grain boundaries are strongly associated with serration initiation. In addition, with aid of transmission electron microscope (TEM), coherency relationships between the decorating particle and the matrix have frequently been reported [137, 37, 132, 150, 141].

In search of the underlying mechanism(s) for how and why such grain boundary serrations form, a few hypotheses were proposed. Koul and Gessinger [119] first

concluded the importance of γ' phase and net strain energy differential between boundaries based on observations of a set of alloys. The theory was then modified by Henry *et al* [129] to incorporate solute transport during the process, which assisted preferential growth of coherent γ', for which later work by Mitchell *et al* [137] has provided further validation. On the other hand, particularly for low γ' fraction alloys whose serration is triggered by carbide, diffusivity and segregation of Cr and C are discussed in detail [145, 38, 180]. Based on these observations, other mechanisms on oriented growth and discontinuous precipitation/segregation have also been proposed.

Notwithstanding the efforts from previous studies, a few key pieces of the puzzle are still missing for a complete picture, understandably due to the complicated nature of the problem. The methods for measuring and quantifying the degree of serration being used are often subjective and often, neither criteria nor definition exist for deterministic descriptions, which leads to ambiguous identification of the serration. Processing parameters can thus only vaguely be correlated to final microstructure as the key factors of serration is not well parameterised. Here we seek to unpick the mechanism for serration by examining many heat treatments, and thus need to develop metrics describing the grain boundary serration. Armed with this we aim to answer the following questions to help understand the serration mechanisms. What is the relationship between second phase particles and the occurrence of serration? Is slow cooling necessary for the initiation of a serrated architecture? What is the possilibty of constructing a map that links processing parameters and final microstructure? New

quantification methods and definitions are clearly needed to answer the questions above.

In this study, 19 heat treatments were conducted to generate grain boundary serration. Advanced techniques, such as high resolution transmission based microscopy were carried out to understand the synergy of carbides and grain boundaries. Furthermore, two mechanisms of serration generation for Inconel 600 are proposed. A new quantification method based on Fourier Transform of the grain boundary traces will be presented, which improves the objectivity of serration assessment. Based on which, an index that describes the degree of serration is proposed. A set of heat treatments was designed to understand the relationship between processing, precipitates and serration, which leads to the construction of the processing map. Last, the effect of each heat treatment parameter is discussed in details with the aid of the map.

4.2 Methodology and experimental

Nickel-based alloy Inconel 600 was selected as the candidate material for gaining fundamental understanding on serration formation mechanism, because of its potency in forming serrated grain boundaries [179]. In addition, the uncomplicated microstructual phases that it presents — γ matrix with Cr-rich carbides — makes the microstructural variables feasible to control. Admittedly, the clarity of microstructure improves understanding of the interaction between precipitates and grain boundaries. Detailed information about the material is given in Chapter 3.

4.2.1 Heat treatment

Detailed heat treatments were carried out using Carbolite TZF 15/610 tube furnace, the temperatures and ramping rates were calibrated by N-type thermocouple in advance. In total, four types of heat treatment (labelled A - D) were utilised for the current study, as illustrated in Figure 4.1. In order to evaluate the effect of processing parameters, solution treatment, cooling rate and isothermal holding have been varied to a certain extent to examine their impact on triggering grain boundary serration. The design of heat treatment aims to yield serrated and non-serrated grain boundaries with various carbide distribution. Figure 4.1 (a) is selected to yield non-serrated grain boundary, as a fast cooling rate "freezes" the microstructure in solid solution, where all carbides are dissolved. Heat treatment (b) is utilised to design serrated boundaries, because with slower cooling rate carbide nucleation is more selective, preferentially along the grain boundaries which changes grain boundary morphology. Quenching from an intermediate temperature is optional, which increases productivity. In addition, (c) and (d) are developed to capture the effect of prolonged ageing to size of carbide and degree of serration, which is base upon heat treatment (b).

Table 4.1 illustrated the heat treatment matrix in search of the influence of each parameter. For example, the effect of solution treatment was conducted at 4 temperatures, 1000, 1070, 1100 and 1140°C (B1, B2, B4 & B9); the effect of cooling rate was evaluated ranging from 0.25°C/min to water quenching (B6 - B11, A1 & A2); the effect of subsequent ageing was performed by heat treatment D1; and the effect of intermediate temperature was traced at 900 and 1040°C (B7 & B12).

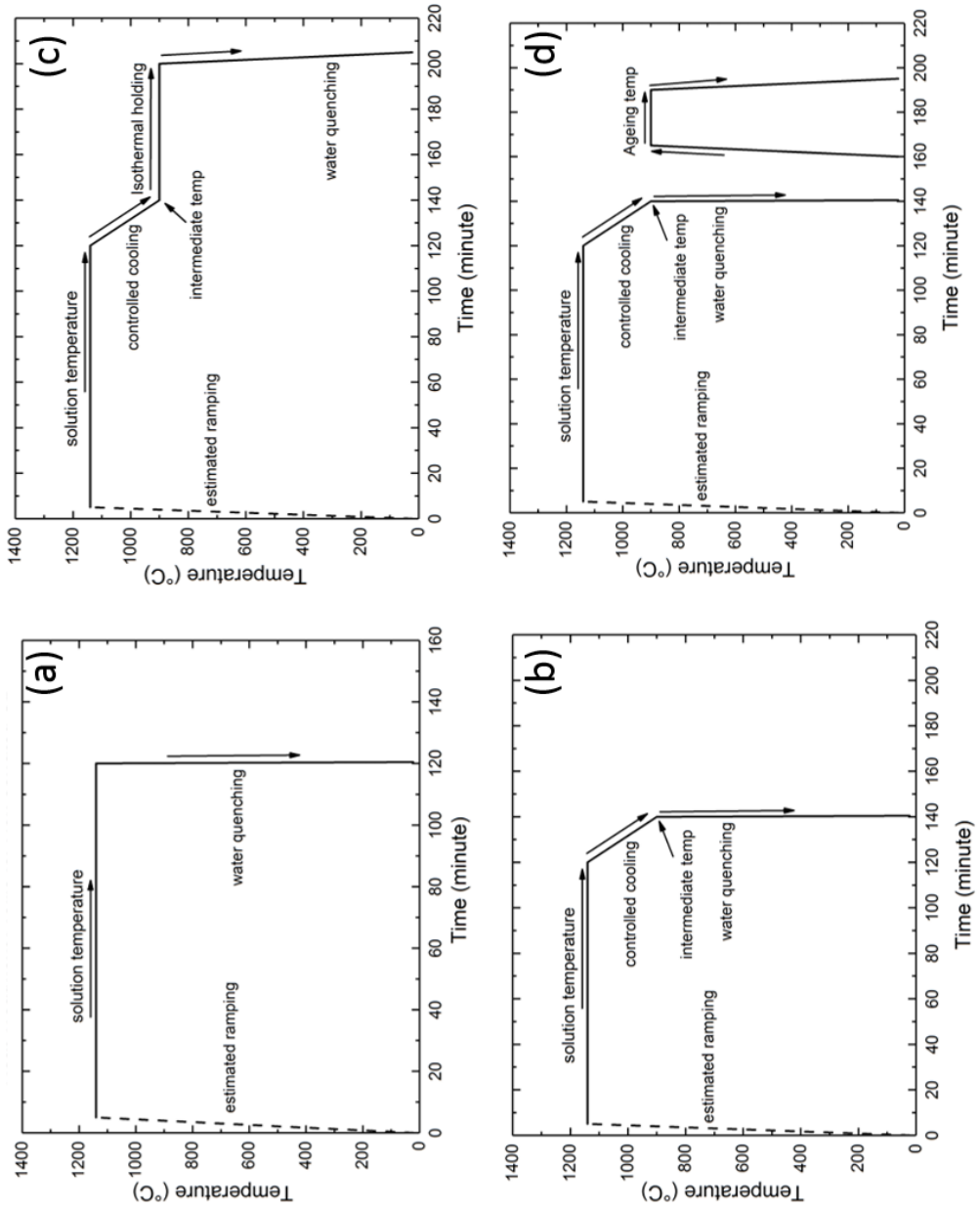


Fig. 4.1 Four types of heat treatment applied to the material. (a) Solution treatment followed by constant cooling rate (air/water quenching), (b) solution treatment followed by slow cooling to an intermediate temperature for quenching, (c) solution treatment followed by slow cooling to intermediate temperature and isothermal holding before quenching and (d) additional ageing added to (c).

Table 4.1 Heat treatment matrix performed to generate a database of grain boundary serration in Inconel 600. First letter in label refers to heat treatment type described in Figure 4.1. The criterion used for serration identification is based on discussion in section 4.4.1. The grain boundary type labeled (a-f) can be found in Figure 4.6.

	Solution treatment	Cooling	Intermediate treatment	Cooling	Ageing	Serration	Boundary type
Unit	°C	°C/min	°C	°C/min	°C & min	N/A	N/A
A1	1140/2hrs	600	22	N/A	N/A	N	a
A2	1140/2hrs	WQ	22	N/A	N/A	N	a
B1	1000/2hrs	12	900	WQ	N/A	N	c
B2	1070/2hrs	12	900	N/A	N/A	N	c
B3	1100/2hrs	0.25	900	WQ	N/A	N	c
B4	1100/2hrs	12	900	WQ	N/A	Y	d - f
B5	1100/2hrs	30	900	WQ	N/A	Y	d - f
B6	1120/2hrs	3	900	WQ	N/A	Y	d - f
B7	1140/2hrs	0.25	900	WQ	N/A	Y	d - f
B8	1140/2hrs	3	900	WQ	N/A	Y	d - f
B9	1140/2hrs	12	900	WQ	N/A	Y	d - f
B10	1140/2hrs	30	900	WQ	N/A	Y	d - f
B11	1140/2hrs	60	900	WQ	N/A	Y	d - f
B12	1140/2hrs	0.25	1040	WQ	N/A	Y	d - f
C1	1140/2hrs	0.25	1040/30min	WQ	N/A	Y	d - f
C2	1140/2hrs	12	900/30min	WQ	N/A	Y	d - f
C3	1140/2hrs	12	1040/30min	WQ	N/A	N	a
C4	1140/2hrs	12	1060/30min	WQ	N/A	N	a
D1	1140/2hrs	12	1040/30min	WQ	900/30min	N	b

4.2.2 Scanning electron microscope and image processing

Metallographic specimens were prepared using standard procedures, finished with 40 nm size coloidal silica suspension for 2 minutes. A Zeiss Merlin field emission gun scanning electron microscope (FEG-SEM) was utilised for charactersation. Back-scattered electron (BSE) images were collected with a step size of 46.5 nm at all conditions. For each microstructure, 15 randomly picked grain boundaries were captured for analysis. The grain boundary length that contributed for analysis was in excess of 1 mm for each specimen.

In the cases where serrations were generated, intergranular carbides were then taken for analysis aided by image processing. Compositional contrast of the BSE image is used for determining carbides from the matrix. ImageJ and Paint.net softwares were utilised for segmentation of the shape based on image intensity. Feret diameters are used as shape descriptors, where Feret max/min represents the maximum/miminum distance between two parallel planes touching both sides of the particle profile. Hence the Feret max and Feret min are quoted as carbide length and thickness respectively. Circularity is defined as $4\pi \times \text{area}/\text{perimeter}^2$, which is used to describe the aspect ratio of a carbide that indicates the stage of growth. Carbide analysis results of a range of the serrated cases are displayed in Table 4.2.

Table 4.2 Carbide quantification matrix of Inconel 600.

	Heat Treatment		Carbide					
	Solution	Cooling rate	Size	Length	Thickness	Circularity	Nucleation density	Carbide coverage
	°C	°C/min	μm^2	μm	μm	N/A	mm^{-1}	
B4	1100/2hr	12	0.35	2.05	0.37	0.33	276.3	0.57
B5	1100/2hr	30	0.25	1.19	0.34	0.49	326.3	0.39
B6	1120/2hr	3	0.56	2.40	0.55	0.41	288.0	0.69
B7	1140/2hr	0.25	6.36	6.99	1.72	0.36	109.2	0.76
B8	1140/2hr	3	0.67	2.06	0.49	0.38	371.0	0.76
B9	1140/2hr	12	0.34	1.71	0.37	0.43	417.3	0.71
B11	1140/2hr	60	0.09	0.59	0.22	0.70	694.6	0.41
C1	1140/2hr	0.25	2.45	5.78	1.00	0.27	116.2	0.67
C2	1140/2hr	12	0.44	1.86	0.44	0.45	432.1	0.80

4.2.3 Transmission based characterisation

Both TEM and TKD techniques were performed to gain insight into the formation mechanisms and crystallography of phases in Inconel 600. The same samples were characterised by both techniques. The preparation of electron transparent foils and both techniques were provided in detail in Chapter 3.

4.2.4 Quantification of serration using fast Fourier transform

The method used for quantification of the degree of serration in literature approximate each serration profile as a sinusoidal wave [137, 37], however, generally the nature of the serration shapes are much more complex and there is some subjectivity in fitting a single sinusoid. Consequently, the same grain boundary can be measured with different amplitudes, depending upon which part of the boundary was quantified. Figure 4.2 shows 28 grain boundaries observed in the present study, none of those can be easily regarded as a wave with a specific wavelength and amplitude, thus estimating the degree of serration is ambitious and challenging. Therefore, new methods were required to improve understanding of heat treatment parameters on the degree of serration.

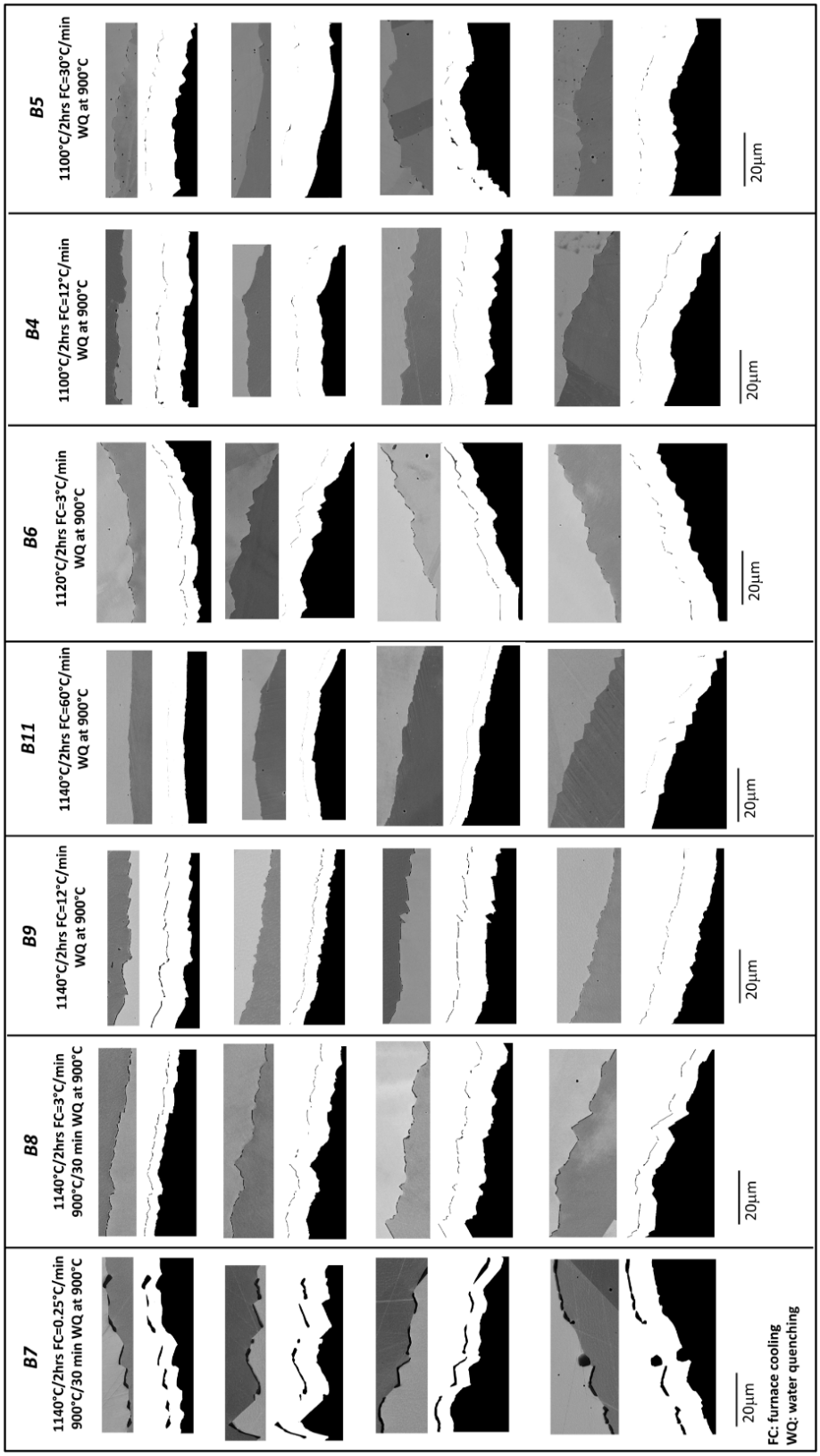


Fig. 4.2 Typical grain boundaries studied in seven heat treatment conditions that obtain serrated morphologies, *i.e.* B4 - B9 & B11. For each boundary that displayed, intergranular carbide and boundary trace were outlined.

With the aforementioned issues in mind, a Fourier based method was utilised. Fast Fourier transform is a numerical tool for sophisticated wave/signal analysis that is widely used to solve science and engineering problems [181–183]. The operation decomposes a signal that contains time/space domain information and transforms it into frequencies and power that is shown schematically in Figure 4.3. The quantification of serration in the current study is based upon the FFT implementation in MATLAB. Figure 4.4 shows the approach step by step: (a) shows a typical grain boundary being captured where grain boundary and its vicinity were decorated by some precipitates. Image processing was performed for increasing contrast and the removal of interior precipitates/artifacts for ease of following automated grain boundary segmentation. The updated image (b) was then binarised using a threshold value in the histogram. Correction of the skewness is performed in (c), where a straight line is drawn connecting the end-to-end distance of the segmented curve. Figure 4.4 (d) exhibits the perpendicular distance between each pixel on the curve from the straight line between the start and the end points. The curve displayed in (d) is then analysed using FFT with MATLAB, where frequencies of sinusoidal waves with its corresponding amplitude are extracted. Physical interpretation of the frequency is the number of complete cycles that it exhibits in the image, shown in Figure 4.4 (e). Last, with known distance of signal length and number of complete cycles, the wavelength of each wave displayed in the figure is obtained in (f).

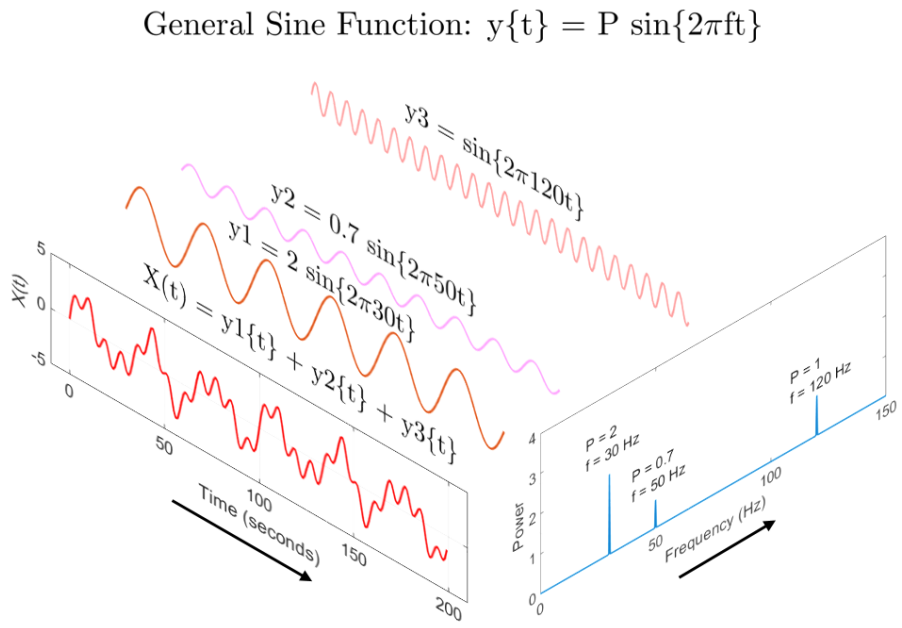


Fig. 4.3 Operation principle of Fourier transformation that decomposes a wave signal into its constituent sinusoidal waves into power and frequency spectrum.

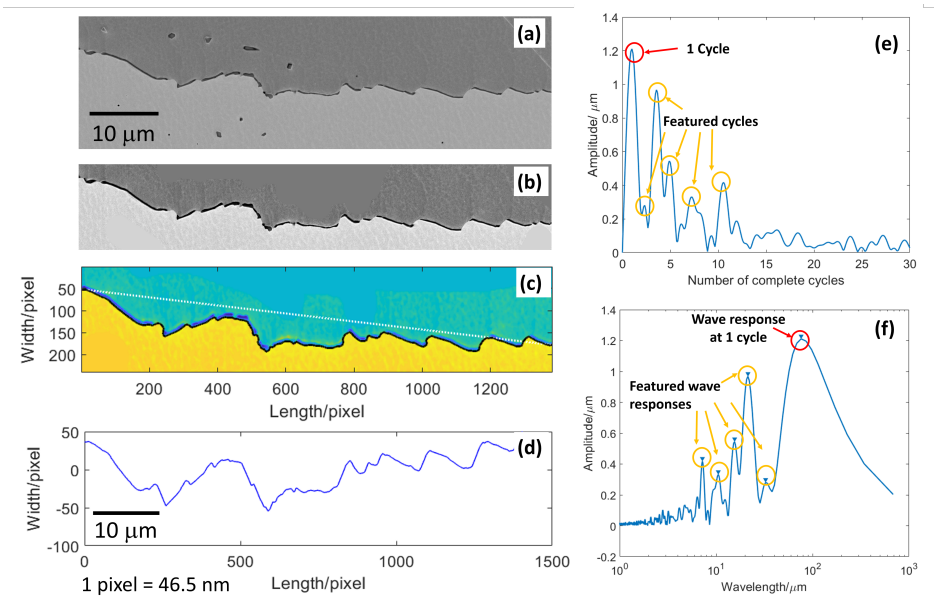


Fig. 4.4 FFT analysis on grain boundary serration. (a) is the original image of a grain boundary and (b) is the digitally processed image using brightness/contrast and removal of artifacts. (c) is the binarised image with its boundary trace outlined and (d) is the baseline-corrected wave function. (e) is the Power/Frequency specturm after transformation and (f) is spectrum in wavelength and amplitude.

4.3 Results

4.3.1 Microstructure overview: as-received and heat treated materials

The characterisation of the material in the as-received state is shown in Figure 4.5. Two magnifications of SEM BSE images are displayed in (a) & (b). Granular carbides decorated both grain boundaries as well as the grain interiors. TKD bright field imaging also revealed carbides along a grain boundary and in the matrix next to it, see Figure 4.5 (c), where a group of dislocations are evident between them. The geometrically necessary dislocation (GND) density map shown in (d) has revealed strong correlation between the high GND density region and the location of dislocation cluster, seen in the bright field image.

19 heat treatment profiles were carried out and eleven of these conditions successfully generated serrations. The heat treatment matrix used is displayed in Table 4.1, where the first letter (A-D) indicates the type of heat treatment that applied to it, see Figure 4.1. Figure 4.2 demonstrated seven benchmarking heat treatments and their typical grain boundaries, along with intergranular carbide and boundary profiles. Not surprisingly, grain boundaries and carbides obtained approximately the same shapes. All the serrated grain boundaries examined corresponded to random high angle grain boundaries, and no serrations were observed on $\Sigma 3$ twin boundaries. For classification purposes, we have identified six categories (labelled a-f) in order to describe all boundary

types found in the material, summarised in Figure 4.6. A criterion used for serration determination is discussed in section 4.4.1 in details.

Solution heat treatment studies have varied temperature from $1000 - 1140°C$ and fixed the duration at 120 minutes. Figure 4.7 demonstrated the effect of solution temperature on grain growth as well as carbide dissolution. The results enabled the identification of the solution window that triggers serration. Limited carbide dissolution and grain growth was observed at 1070°C/120 mins (B2). However, notable grain growth and carbide dissolution were observed at 1100°C/120 mins (B4), accompanying with some degree of grain boundary serration. Another benchmark was determined under investigations on critical cooling rates — air cooling (measured at 600°C/min by N-type thermocouples) or higher is not sufficient to generate serrated grain boundaries (A1). In addition, isothermal holding with subsequent ageing could develop grain boundary carbides, as shown in Figure 4.6 (b), but not sufficient to yield serration with the fine carbides that formed (D1). Whilst comparing C1 & C3, both conditions obtained the same solution treatment and intermediate temperature, a slower cooling rate has shown that it is possible to yield serrated boundaries in association with intergranular carbides.

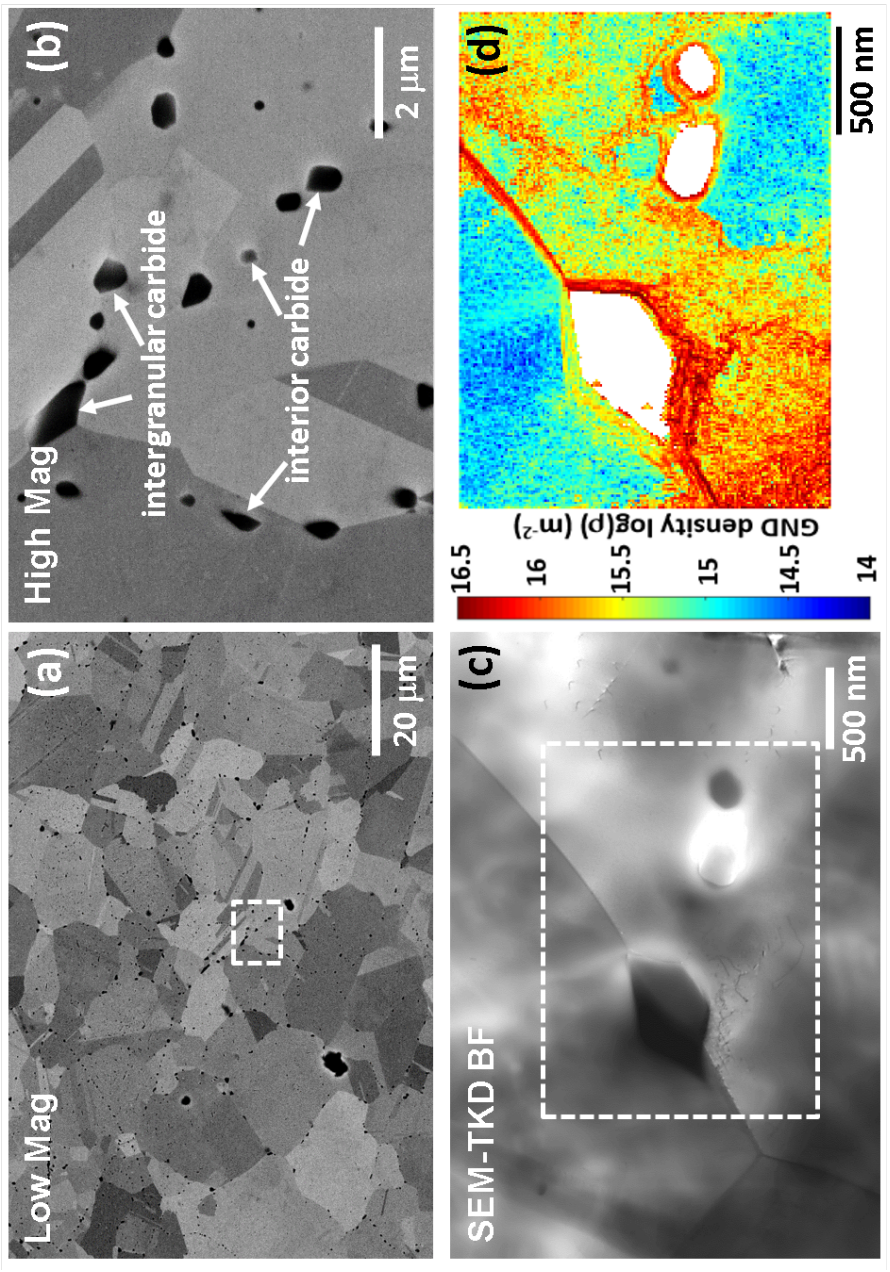


Fig. 4.5 The microstructure overview of the as-received Inconel 600. (a) & (b): SEM BSE images obtained from two magnifications, where granular carbides were observed both on the grain boundaries and inside the grains. (c): TKD bright field image of an intergranular carbide and (d) represents the GND density map of the same region.

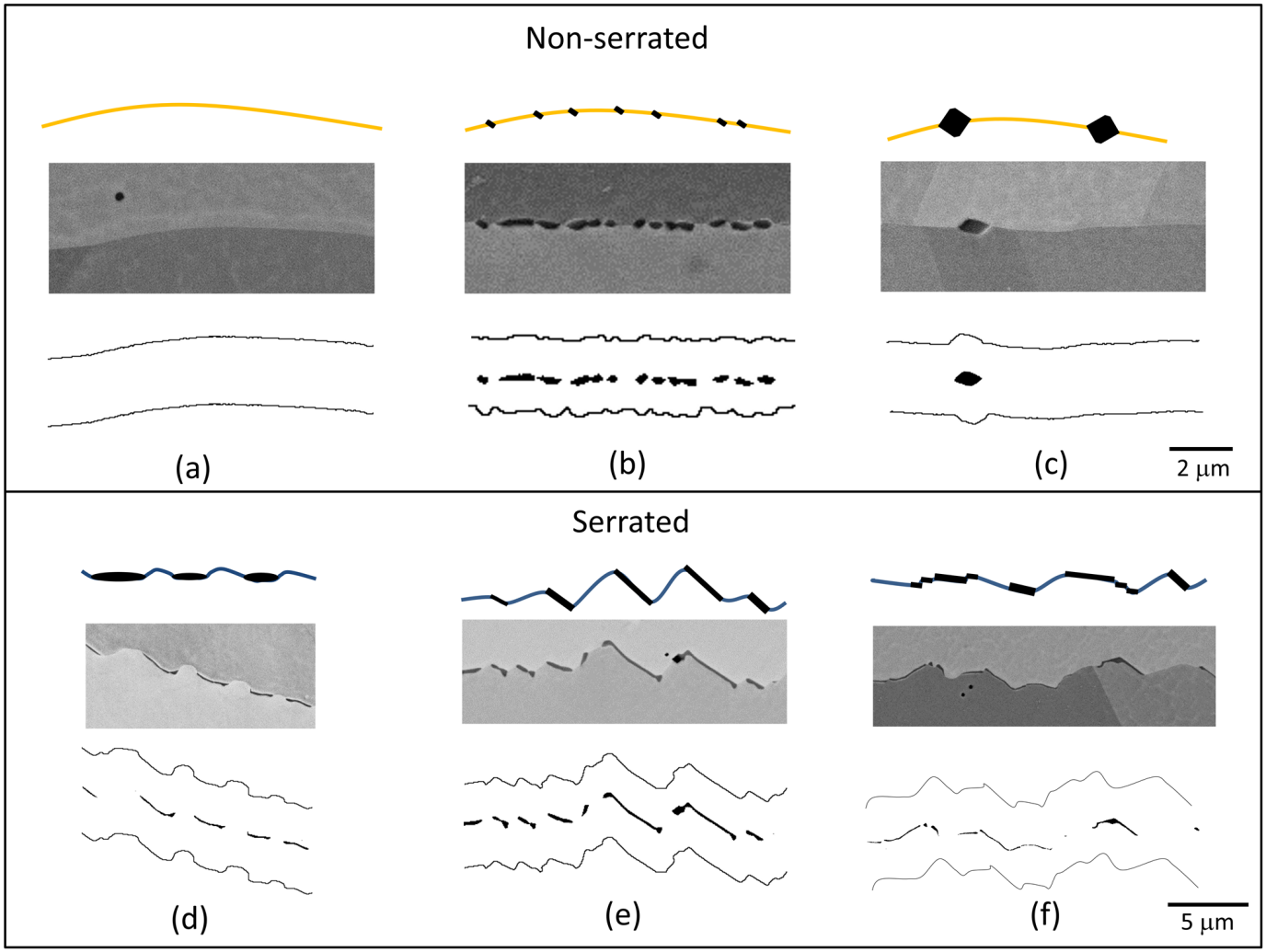


Fig. 4.6 Summary of the six types of grain boundaries observed. (a-c) represent non-serrated grain boundary and (d-f) displayed serrated grain boundary.

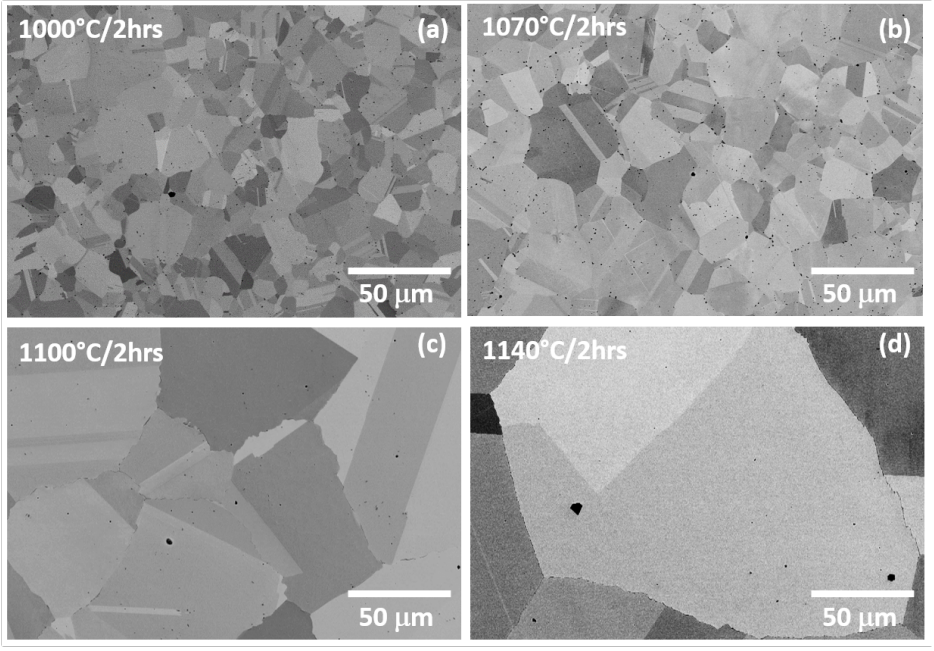


Fig. 4.7 Effect of solution temperature on microstructure ranging from 1000 - 1140°C. (a-d) are microstructure obtained from B1, B2, B4 and B9 respectively.

4.3.2 Carbide: identification and evolution

Chemical composition analysis carried out using STEM-EDS is presented in Figure 4.8, where a line scan was performed over the matrix/carbide interface. In the carbide the ratio between metal and carbon was around 7:3, which suggested the M_7C_3 type carbide. A slight decrease of carbon content over distance was also observed, which was likely to be caused by an overlay of carbide and matrix, as suggested by a more gradual composition profile. Interestingly, a spike of carbon concentration was captured while scanning through the a cluster of dislocations, which is suggestive of pipe diffusion via crystal defects.

Furthermore, TEM diffraction was performed at three different zone axes for determination of the carbide crystal structure in both the as-received and serrated

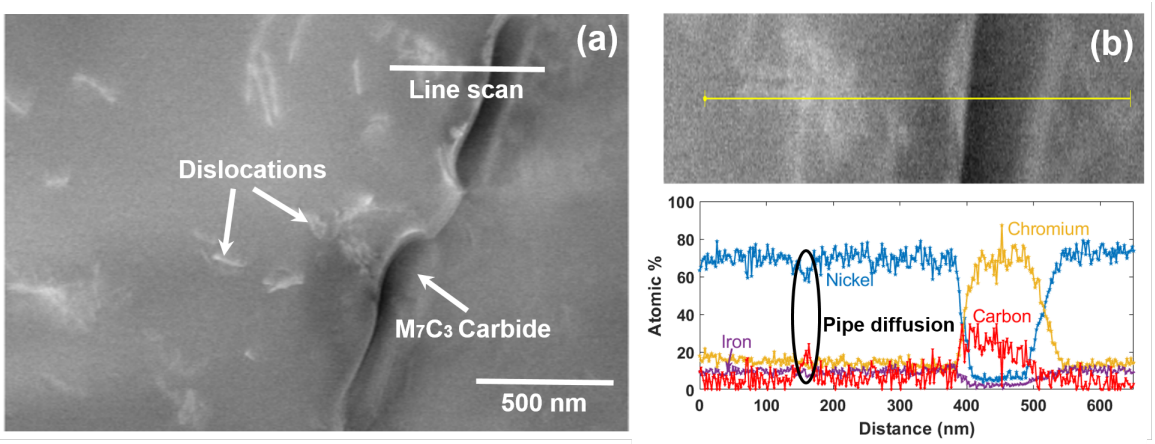


Fig. 4.8 (a): EDS line scan across the interface of matrix/carbide and (b): the compositional profile acquired.

grain boundary specimen (B7). As displayed in Figure 4.9 and Figure 4.10, two intergranular carbides and their surrounding γ matrices were also indexed. The carbide present in both specimens were determined as orthorhombic M_7C_3 type, where d1 and d2 spacing were interpreted according to literature [184]. Additionally, the plate-like carbide in Figure 4.10 demonstrated a coherent interface with the matrix (right) next to it. The orientation relation can be expressed by $\{111\}_\gamma//\{100\}_{M_7C_3}$. Nevertherless, the carbide present in the as received state was incoherent on both sides of γ matrices. HR-TEM performed on both carbides facilitated direct measurements of the d spacing in the $\{100\}_{M_7C_3}$ direction, where lattice constant is measured between 4.39 - 4.60 Å as opposed to 4.51 Å by calculation [184]. The slight discrepancy may be caused by the internal strain.

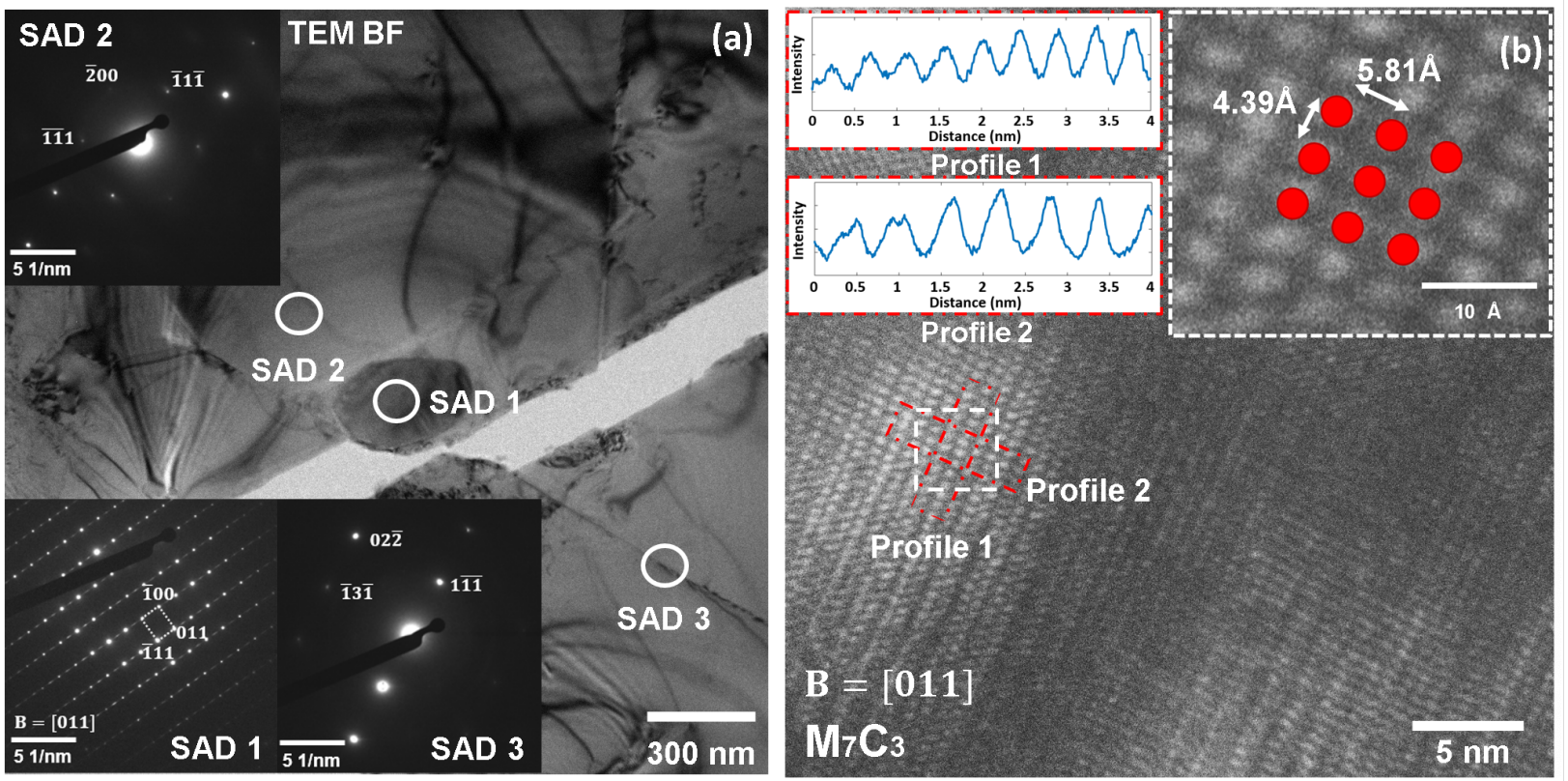


Fig. 4.9 (a): TEM micrograph and selected area diffraction patterns at carbide and both sides of the matrix in the as received material. (b): HR-TEM showing the atomic spacing of the carbide.

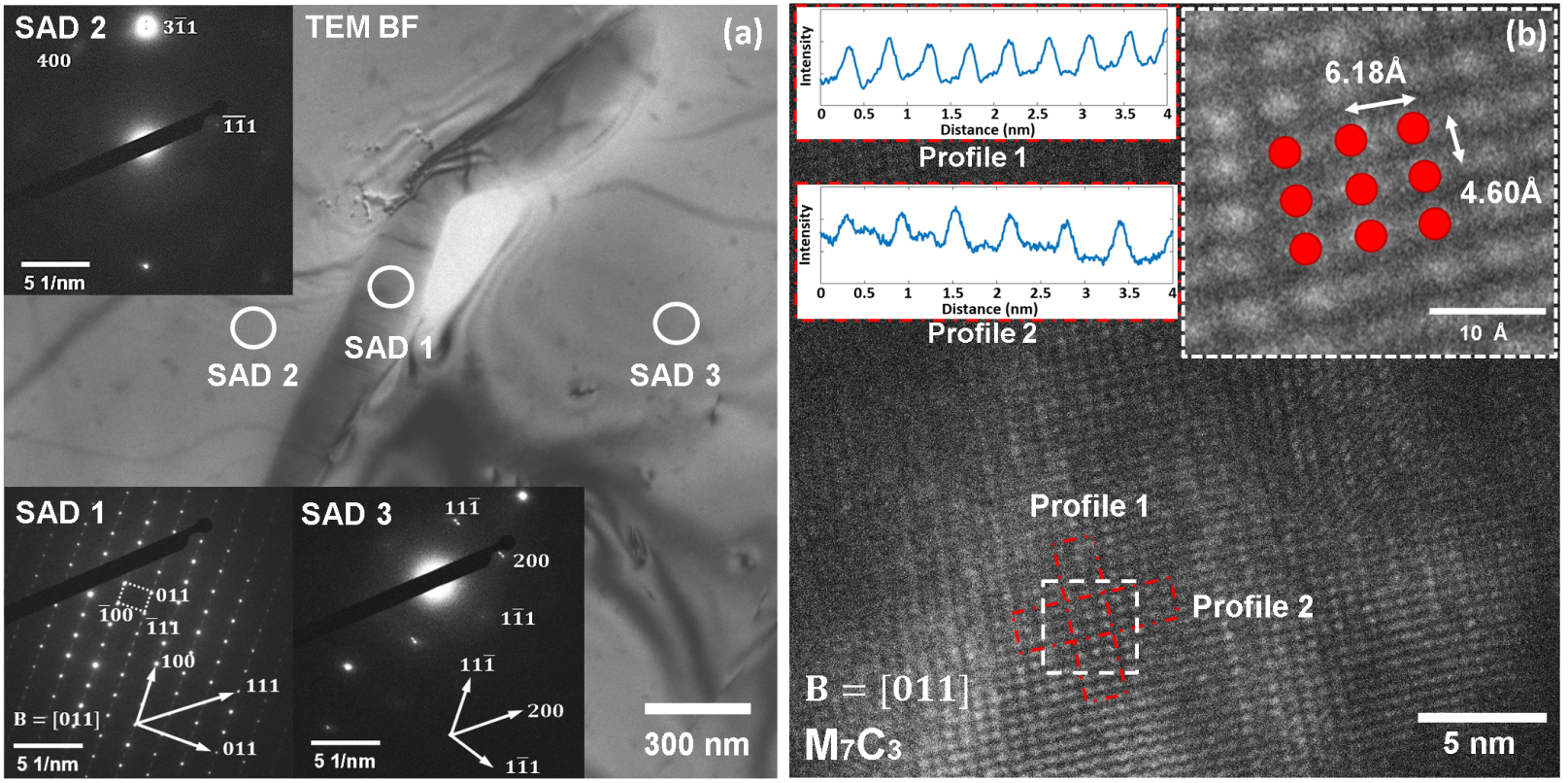


Fig. 4.10 (a): TEM micrograph and selected area diffraction patterns at carbide and both sides of the matrix in the material with serrated grain boundaries. (b): HR-TEM showing the atomic spacing of the carbide.

On the micro-scale level, although the carbide crystallography (orthorhombic M_7C_3) remained consistent in response to heat treatments, the morphology, shape and distribution has altered drastically. Thorough investigation of carbide characters that exhibited grain boundary serration is displayed in Table 4.2. The average carbide size, length, thickness, circularity were measured assisted by ImageJ using a binarised threshold method. In addition, carbide nucleation density was calculated by total number of carbide per unit length of grain boundary profile that was measured. To exemplify the thermodynamic properties of the material studied, a phase diagram was plotted with the ThermoCalc software using the TCNI8 database, as illustrated in Figure 4.11. The M_7C_3 carbide dissolution temperature was found at 1007°C by calculation, which is reasonably close to the experimental value estimated between 1040 - 1070°C, as determined by heat treatments B2 & B12.

4.3.3 Serration index & carbide as a function of heat treatment

Each serrated grain boundary profile was transformed into its constituent sinusoidal waves. For interpretation, waves with an amplitude greater than 0.2 μm were regarded as featured waves and carried further in the analysis. Additionally, the peak at 1 cycle per frame length was neglected for further analysis, as it represented smooth long range undulation of the boundary. On average, each boundary profile was shown to possess seven intrinsic waves, and hence the method has demonstrated an improved representation of the boundary profile compared to approximating them as a single

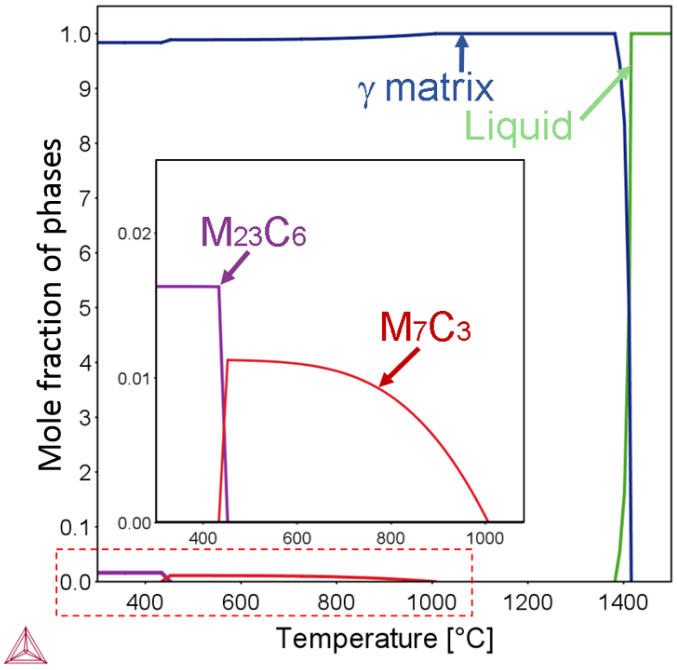


Fig. 4.11 Equilibrium phase diagram of Inconel 600 from 300 - 1500°C showing carbide type and dissolution temperature.

sinusoid [137, 37]. However, a new metric is needed to describe the degree of serration, preferably combining the multiple wavelengths and amplitudes into a single scalar value. Three waves with highest amplitudes were then chosen to represent the overall shape of the serrated grain boundary. Since the degree of serration ultimately influences the grain boundary area, an index using the multiplication of the average value of wavelength and amplitude was utilised to address the effectiveness such boundary might have in resulting grain boundary sliding, in the units of μm^2. The serration indices and its standard deviation across the multiple boundaries analysed for heat treated material are given in Table 4.3. Trends between this serration index and the heat treatment parameters are illustrated in Figure 4.17.

Table 4.3 Serration quantification matrix of Inconel 600.

	Heat Treatment		Serration			
	Solution	Cooling rate	Wavelength	Amplitude	Index	Std Dev
	°C	°C/min	μm	μm	μm^2	μm^2
B4	1100/2hr	12	19.02	0.64	12.07	7.39
B5	1100/2hr	30	13.70	0.62	8.47	3.02
B6	1120/2hr	3	21.60	0.75	16.12	9.30
B7	1140/2hr	0.25	24.54	0.92	22.65	15.10
B8	1140/2hr	3	23.80	0.77	18.22	10.80
B9	1140/2hr	12	23.44	0.58	13.62	8.26
B11	1140/2hr	60	21.83	0.47	10.35	2.91
C1	1140/2hr	0.25	21.03	0.59	12.41	8.35
C2	1140/2hr	12	26.15	0.62	16.15	10.69

An explicit example of FFT analysis is presented in Figure 4.12. The alloy heat treatment that produced the spectrum is B9. There were 15 randomly selected grain boundaries analysed using in-house FFT method, and each single one of them yields a specific power/frequency spectrum, which illustrates the serration amplitude and number of complete cycles of their constituent waves. For all peaks that obtain a value higher than 0.2 μm is labeled automatically using MATLAB, which is referred as featured waves and assigned with individual amplitude and wavelength. Apart from the lowest frequency peak — the one describe the overall undulation of the wave, the three strongest waves were collected for further analysis. Serration index is calculated by the amplitude times the wavelength of each wave response — three indices were obtained for each profile — the overall serration index for a specific boundary is defined as the average value of the three indices. Hence, the serration index of a heat treatment is the mean value of the 15 boundaries analysed.

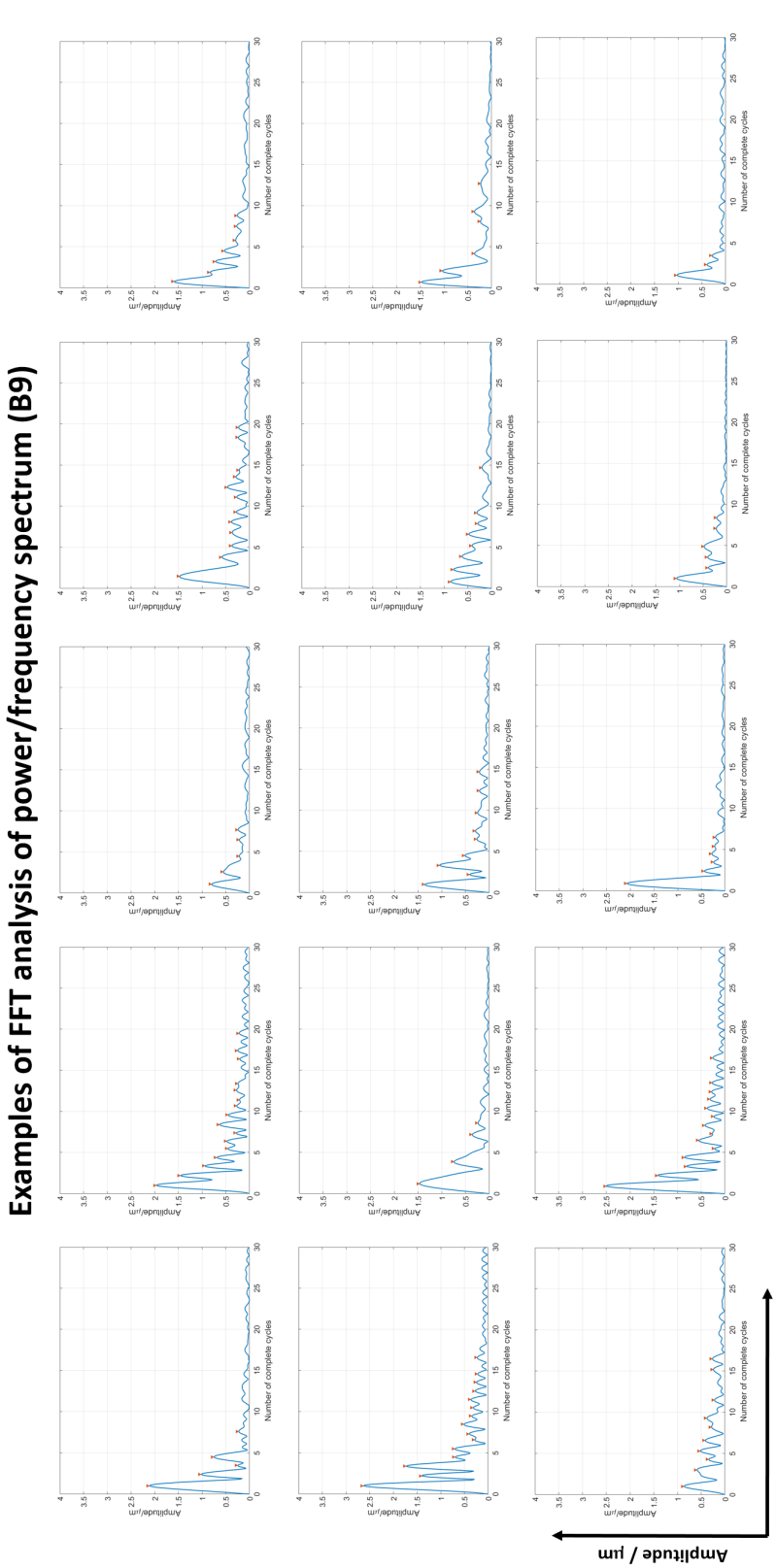


Fig. 4.12 An example of FFT results of 15 analysed grain boundaries. The specific alloy that yield the spectrum is B9.

To further rectify the choice of using three strongest wave is illustrated in Figure 4.13, where two examples of heat treatments that present the plots of amplitude vs wavelength (B7 & B9). The left hand side blue bars, (a) & (c), demonstrate the wavelengths and amplitudes of all collected waves, and the right hand red bars demonstrate the strongest three waves only. The bar charts are made transparent on purpose to visualise the overlapping. It is clear that a great number of small waves with low values of amplitude and wavelengths present in each microstructure, which is overwhelming. Therefore having all those accounted for serration index would result in significant noise. In contrast, if only the top three waves were selected, the distribution looks balanced. The wavelength population also displays a discrete nature, where a few specific wavelengths are more frequently observed than others. For example, wavelengths $\sim$ 11, 15, 22, 28, 40, 47 μm in B7 and $\sim$ 10, 14, 18, 22, 32, 36, 56 in B9. Moreover, the same trend can also be elucidated using the serration index versus amplitude plot. Figure 4.14 shows the individual index of a wave and its corresponding amplitude. The left column is based on the data given in Figure 4.13 (a) and (c), which represents all waves decomposed from FFT. The right column only displays the major three waves. It is clear that noise reduction is successful with the strongest three waves, and the serration index is fairly evenly distributed across all amplitudes. A mean value calculated based on data points showing in the graph — the serration index — is therefore considered to be representative of the overall degree of serration in a microstructure.

For the same solution treatment condition (1140°C/2hrs) and different cooling rates, for example (B7, B8, B9 & B11) (0.25 - 60°C/min). Figure 4.15 demonstrates

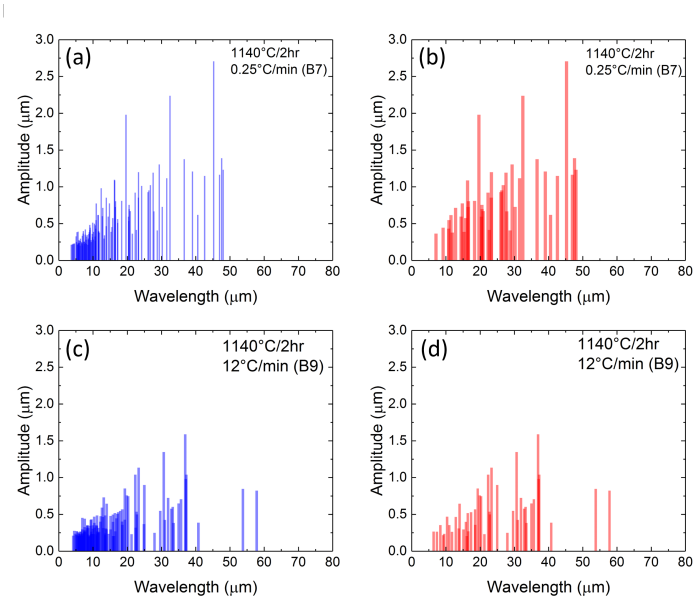


Fig. 4.13 Serration amplitude and wavelength chart for B7 and B9. (a) and (c) represents the amplitudes against the wavelengths for all waves decomposed from 15 grain boundaries; (b) and (d) represents only for data from the three strongest featured waves.

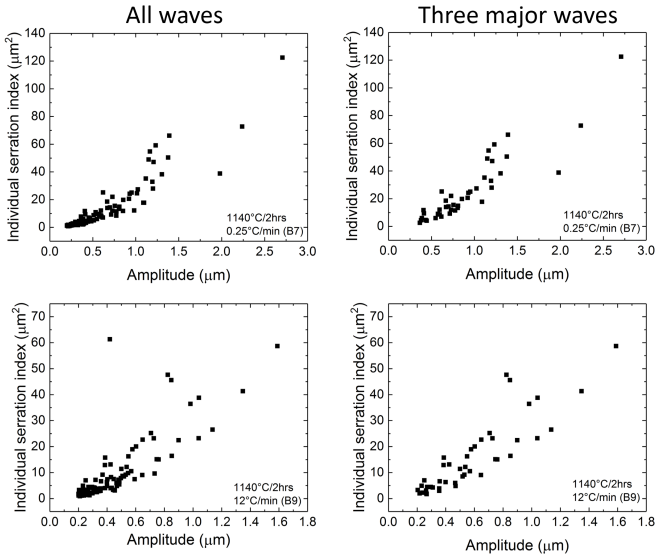


Fig. 4.14 Serration index for each individual vs amplitude for B7 & B9. (a) and (c) represents the indices against the amplitudes for all waves decomposed from 15 grain boundaries; (b) and (d) represents only for data from the three strongest featured waves.

the amplitude/wavelength spectrum for all the three featured waves of different cooling rates. This set of raw data illustrates the evolution of serration regarding to cooling rate. For instance, the size of serration amplitude has decreased with increasing temperature, which results in a lower degree of serration indices from 22.65 to 10.35 μm^2. On the other hand, the wavelength of each microstructure obtains a similar distribution, *i.e.* no wavelength exceeds 60 μm. The alteration of the degree of serration amplitude is thought to be related to carbide distribution — the carbide size also decreased drastically from 6.36 to 0.09 μm^2 while increasing cooling rate, with carbide length and width following similar trends. On the other hand, the carbide nucleation density was affected strongly and increased from 109.2 to 696.6 mm^{-1}. Carbide coverage — a fraction showing how much in proportion that a grain boundary was covered by carbide is calculated by the multiplication of carbide length and linear nucleation density. The coverage decreased from 0.74 to 0.41 with increased cooling rate (B7 & B9). However, this is a collective measure of carbide size and nucleation density, which it cannot describe the explicit nature of the two metrics individually. Moreover, circularity of carbide shows positive correlation with cooling rate, and since slower cooling rates obtains larger carbides. The growth of carbide is suggested to have preferred orientations as it loses circularity while it grows larger in size. Furthermore, the above observations on the serration indices and carbide share the same trend at a lower solution temperature of 1100°C (B3-B5). Consequently, a correlation between serration and carbide is established. Figure 4.16 demonstrates two examples (B7 & B9) of distribution of carbide length, serration amplitude and wavelength. The

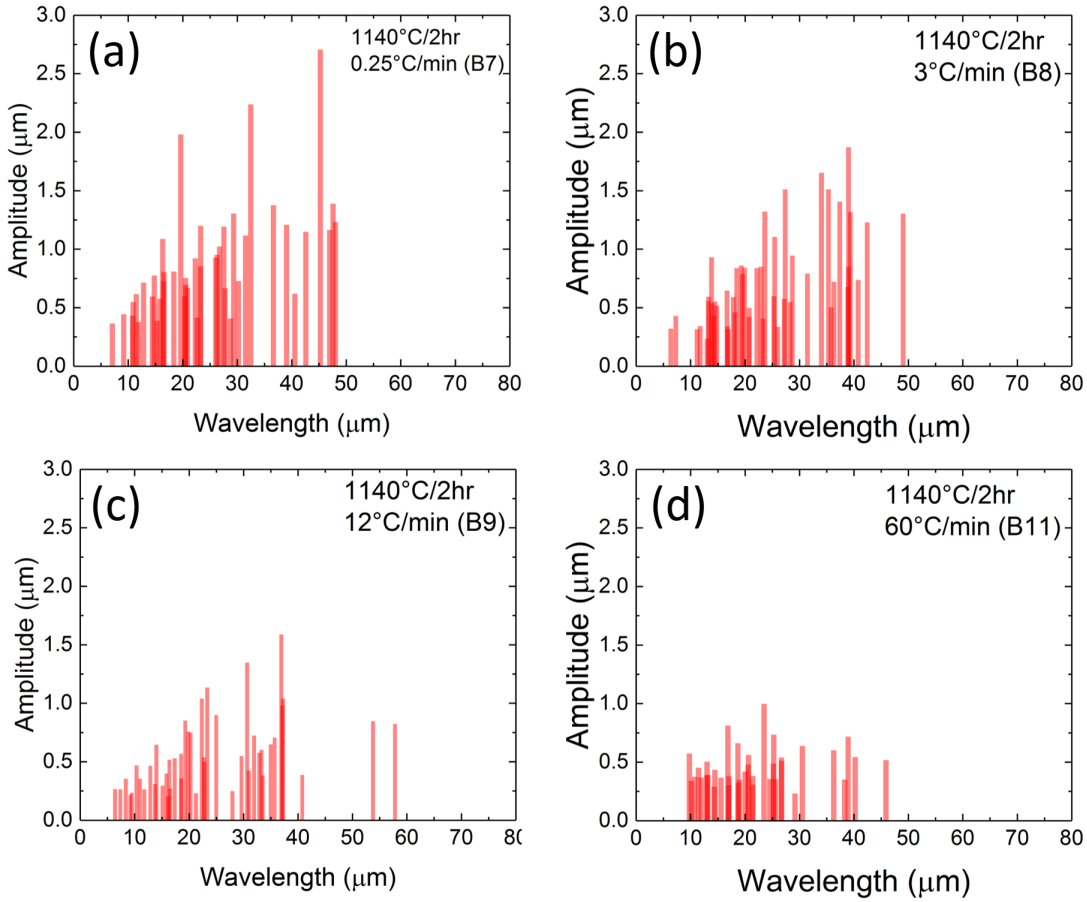


Fig. 4.15 Serration amplitude and wavelength chart for B7, B8, B9 & B11.

carbide length and serration amplitude follows a similar trend for both B7 and B9 — a near Gaussian distribution with a tail on the larger value side is observed for B7 and the distribution shows a positive skew in B9. On the other hand, wavelength shows insensitive to carbide length. It is indicative that carbide size and serration amplitude is coupled, which will be discussed further in the following section.

While maintaining the same cooling rate, the serration index and carbide size demonstrated positive correlation with solution temperature (B6 & B8 and B4 & B9). In addition, an isothermal hold has shown some enhancement in generating

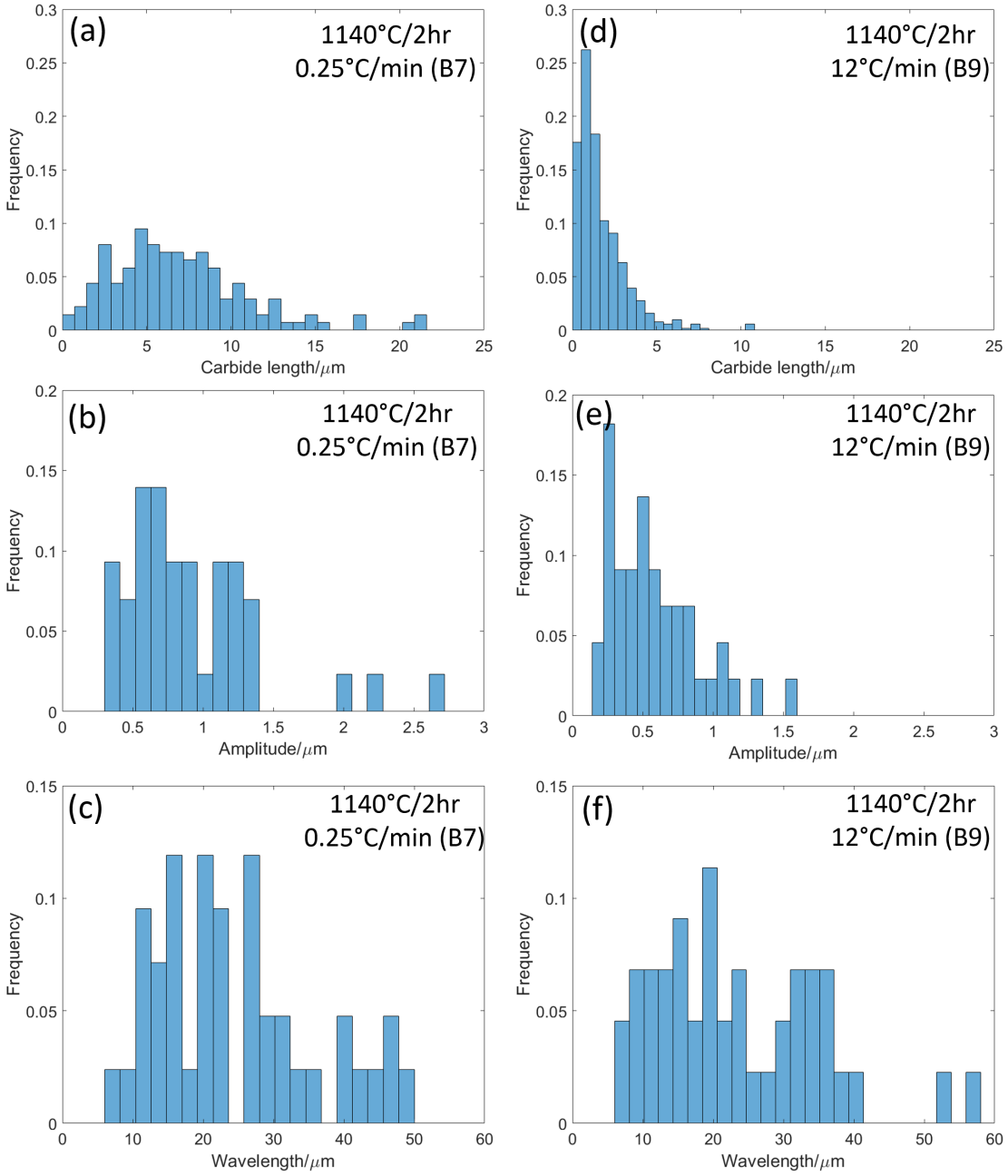


Fig. 4.16 Distribution of carbide, serration amplitude and wavelength in B7 & B9.

both serrations and carbides. For example, an isothermal hold at 900°C for 30 mins increased the serration index from 13.62 to 16.15 μm^2 and the carbide size from 0.34 to 0.44 μm^2 (B9 & C2).

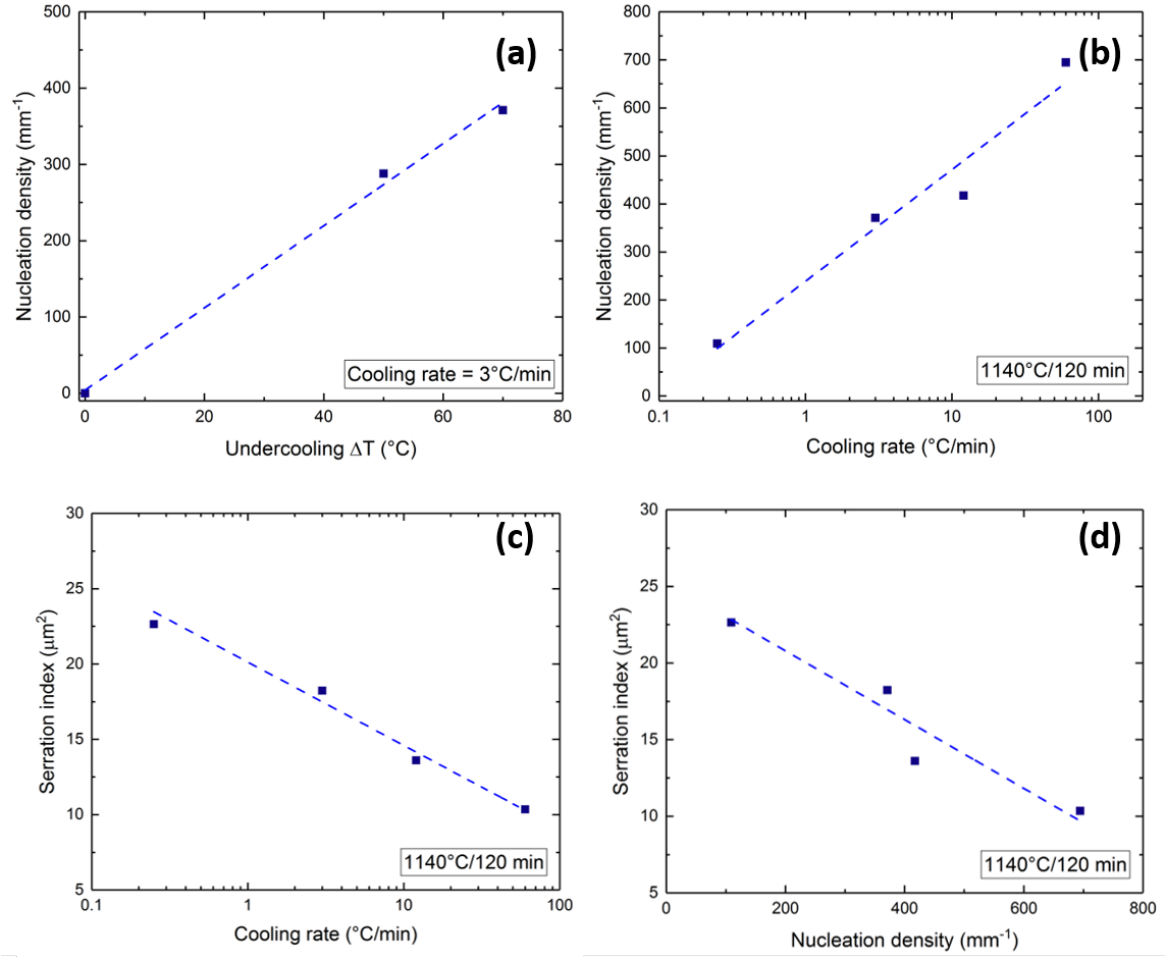


Fig. 4.17 Relationship between processing parameters, carbide distribution and serration index. (a): Nucleation density in relation to the amount of undercooling at 3°C/min. (b): Nucleation density is a logarithmic function of cooling rate. (c): Serration index as a logarithmic function of cooling rate and (d): Serration index in adverse relation to nucleation density of carbides. Scatter points are actual data points and dotted lines are linear best fit lines.

4.4 Discussion

4.4.1 Phenomenological study: classification, determination & definition

A database for grain boundaries of Inconel 600 was constructed using hundreds of micrographs, from advanced charateristaion techniques such as FEG-SEM, HR-TEM, STEM-EDS & HR-TKD. Every serrated grain boundary examined was associated with intergranular carbides without exception. In summary, six types of grain boundaries were classified from all boundaries observed, schematic diagrams and typical SEM images are displayed in Figure 4.6. Among the six types, only (a) exhibited clear grain boundary without decoration of carbide that is able to be described as non-serrated without doubt. However, Figure 4.6 (b) and (c) also shows intergranular carbides that grow on the grain boundary, where a smooth grain boundary seems to be opened up by some irregular shaped particles which locally deflect the grain boundaries to give the some traces of serrated profile. Admittedly, it is difficult to determine whether these boundaries are serrated at this step. In contrast for cases to (d-f) of Figure 4.6, all boundaries are clearly serrated with carbides obtaining coincident profiles with boundaries, where carbide growth in (f) is an incomplete version of (e). Closer attention was then paid to the boundary traces of both sides of the particle, as outlined next to the actual boundary in Figure 4.6. It is not difficult to notice the difference between (b) & (c) vs (e - f), where the boundary traces are mostly mirror images of each other in the former cases, as they are separated by particles. However, the boundaries obtain

almost identical shape to each other in the latter cases. Here we propose a criterion for the determination of intrinsic serrations: profile of boundaries along each side of particles should share the same trend of curvature and approximately match up once overlapped. Hence, the mirror image type profiles in Figure 4.6 (b) & (c) are classified as non-serrated grain boundary.

In the literature, another type of serrated grain boundaries has been reported [185, 186, 162, 187], in which serrations are formed during significant deformation, caused by absorption of dislocations walls or nucleation of nano-sized grains where dynamic recrystallisation had initiated. Grain boundary serration formed in this context, we categorise as deformation grain boundary serration. However, the serrations studied here generated via annealing treatment with minimal internal strain, we refer to as annealing grain boundary serration. Here we define the annealing grain boundary serration as: *irregularly shaped architecture with saw/wave-like appearance of a random high angle grain boundary that is produced via heat treatment involving an annealing process.*

4.4.2 Formation mechanisms on serrated grain boundary

Figure 4.6 (d-f) displayed three types serrated grain boundaries, each of which is thought to be dominated by a specific mechanism. With closer attention, Figure 4.6 (d) possessed a grain boundary profile that appears smoother and more wave-like. While (e) obtained faceted carbides that grow in a specific orientation, and hence the grain boundary profile appears more triangular with a sawtooth shape. The differences

between the shapes of boundaries evoked the underlying mechanisms that formed them. Additionally, (f) possesses characteristics of both aforementioned serration types, thus believed to be a mixture of both mechanisms.

The first mechanism suggested is of grain boundary migration between pinned particles, as demonstrated by the bright field images in Figure 4.18, where the upper grain is attempting to migrate toward the lower one but impeded by carbides. Migrating boundaries are revealed with more detail in Figure 4.18 (b) and (c). Multiple arrays of dislocation lines were emitted at a specific orientation as the grain boundary migrated from the upper grain to the lower one. Clearly, the Zener-type pinning induced grain boundary serration suggests moderate grain growth still emerges while slow cooling, however, the pressure from the intergranular carbide counteracts boundary motion and inhibits it. As a result, the part of a boundary that is in contact with carbide stayed immobile while the other part of the boundary moved marginally. For more detailed elucidation of driving force for such situation, we have performed TKD scanning on one of those boundaries. The grain average misorientation (GAM) map in Figure 4.19 (b) shows the lower grain acquires a higher degree of misorientation as opposed to the upper grain, which favours the grain boundary migration as it reduces crystal misorientation. This mechanism is operative while carbide nucleation density is not very high which leaves some room for the boundaries to migrate between the carbides.

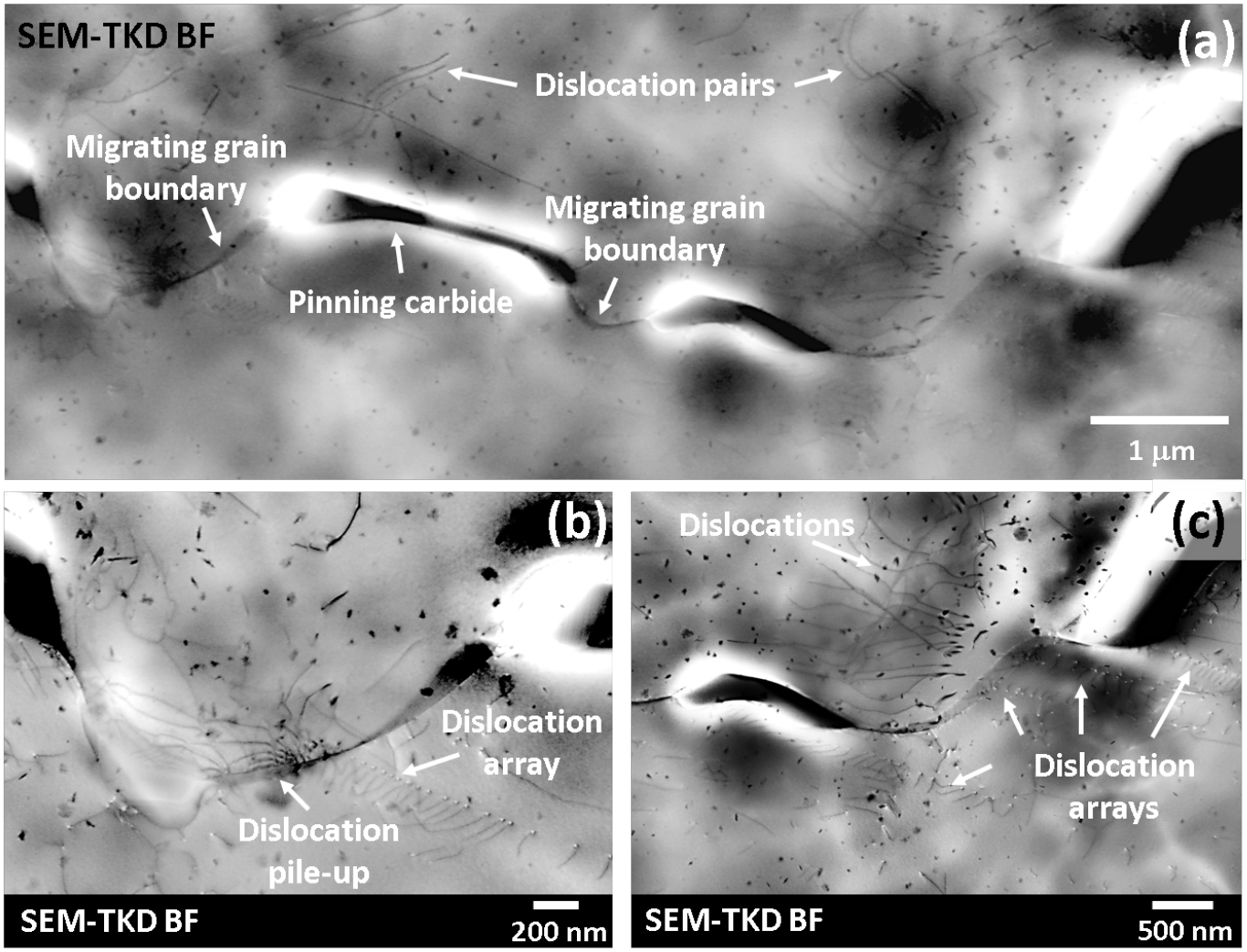


Fig. 4.18 Grain boundary movement due to migration pinned by carbides (a) and local features in higher magnifications (b) & (c). The black dots in the image could be copper from the sample prep process.

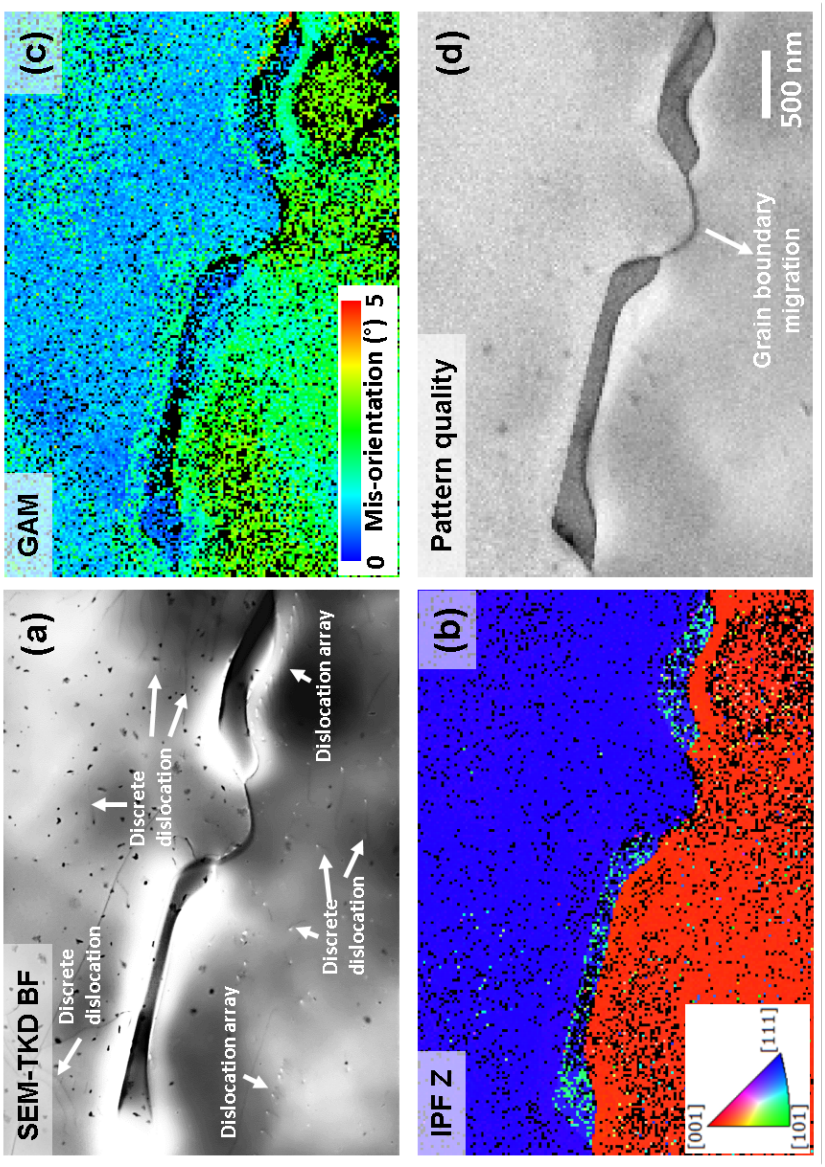


Fig. 4.19 Grain boundary migration impeded by 2 carbides leads to serration. (a): Bright Field (BF) Argus image showing dislocation in arrays and discretely. (b-d) Grain average misorientation (GAM) map, inverse pole figure (IPF) from Z direction and pattern quality map.

Another mechanism exhibited in Figure 4.20 reveals the impact of faceted growth of carbides. As frequently reported in the literature [37, 132], the $M_{23}C_6$ carbide grows along the habit plane of {1 1 1} shared by the carbide and the matrix. Similarly, the coherency relation between the M_7C_3 carbide and one side of the matrix can be expressed as $\{111\}_\gamma//\{100\}_{M_7C_3}$ in the present case. The M_7C_3 carbide first nucleated at the grain boundary, and then followed a preferred growth direction and formed facets. The specific growth orientation is likely to be associated with the coherency stress that exhibited at the interface for energy benefits. As demonstrated in Figure 4.20 (b), the growth direction is $\sim 30^\circ$ anticlockwise to the vertical axis, and the carbide has clearly distorted the grain boundary, where a curvature is created from A to B. In addition, due to the curvature introduced by the carbide, an array of dislocations was emitted where the curvature ends at point B. On the other side of the carbide as illustrated in Figure 4.20 (c), a cluster of dislocation were generated to compensate plasticity induced by the both carbides adjacent to it.

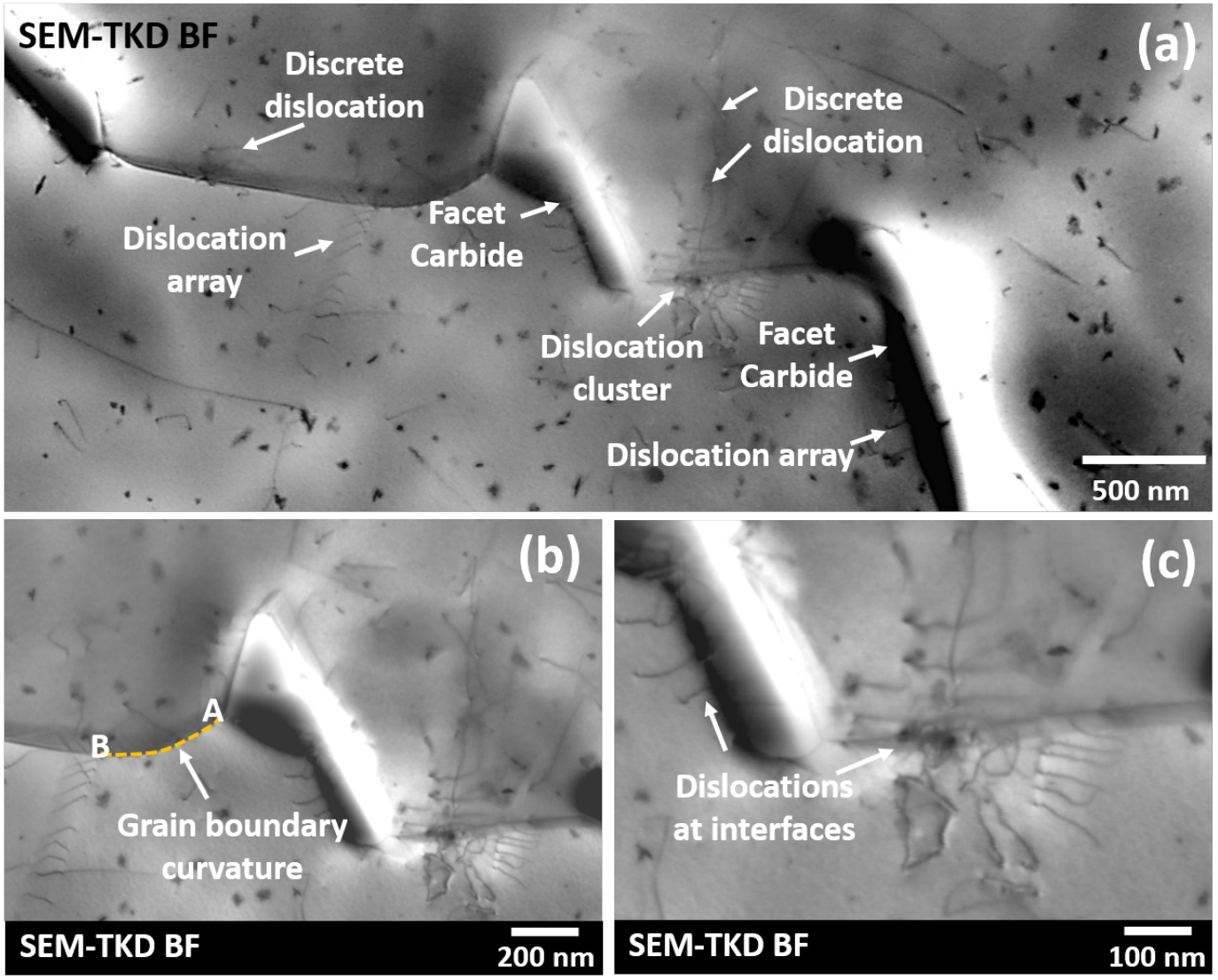


Fig. 4.20 Grain boundary deformed by facet carbides (a) and local features in higher magnifications (b) & (c). The black dots in the image could be copper from the sample prep process.

For further evidence of the carbide growth in relation to grain boundary and surrounding matrix, HR-TKD scanning as well as cross-correlation based calculation were conducted at a more local region of the same carbides. Figure 4.21 demonstrated the elastic strain tensor calculated from the measured on-axis TKD patterns. For better interpretation, the strain matrix rotated the X & Y axes -30° along the Z-axis to align with the carbide growth direction, as shown in the maps. Admittedly, the strain state is complex around the carbide, which is believed to associate with a combination of coherency strain at the interface during carbide growth and thermal contraction during heat treatment. The difference in linear thermal expansion coefficients reported for M_7C_3 and γ matrix is $4.2 \times 10^{-6}K^{-1}$ [188], therefore, the thermal strain estimated is on the order of 10^{-3}, which is in the same magnitude of measured elastic strain. The coherency misfit, however, is more significant by estimation. The spacing of $\{100\}_{M_7C_3}$ plane is larger than $\{111\}_{\gamma}$ spacings by about 10 % [189]. The value is considerably large, which suggests the actual interface may be semi-coherent at some regions. The plasticity involved, as reflected by dislocation activities in the vicinity of grain boundary and carbides, is thought to originate from volume change due to phase transformation from γ matrix to carbide. The metal atom volume of Cr_7C_3 is $\Omega_{Cr_7C_3} = 0.01376$ nm^3 according to [190]. In contrast, the lattice parameter for FCC γ matrix in Inconel 600 is measured at 0.3549 nm [191], which gives the atom volume $\Omega_{\gamma} = ({a_{\gamma}}^3)/4 = 0.01118$ nm^3. The volume discrepancy between the two is estimated at ∼23%, which will generate marked compressive stress and believed to associate with strain by triggering dislocation events. Figure 4.22 illustrates the rotation tensor

and the geometrically necessary dislocation (GND) density map. A notable amount of lattice rotation near the carbides has induced higher GND density near the grain boundary and around the carbides. Moreover, this is validated by the SEM-TKD BF images in Figure 4.20, where a number of dislocation lines were revealed. The locations of dislocation activities *i.e.* discrete, arrays and clusters, are shown to correlate well with the GND density map. It is deduced that the dislocations at the grain boundary are in association to the growth of carbides.

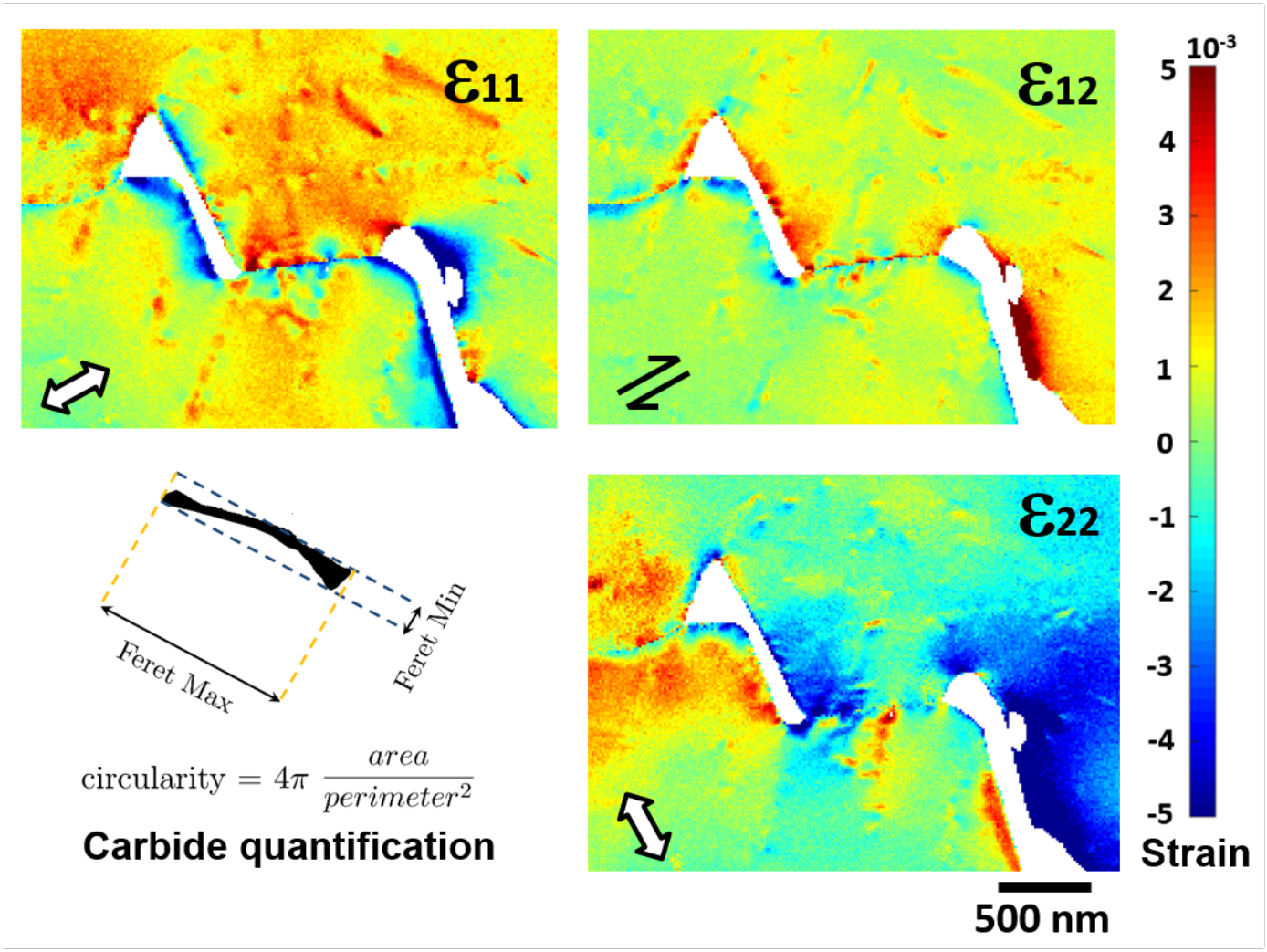


Fig. 4.21 Strain tensor map for 2 faceted carbides on a grain boundary exhibiting coherency strain induced serration.

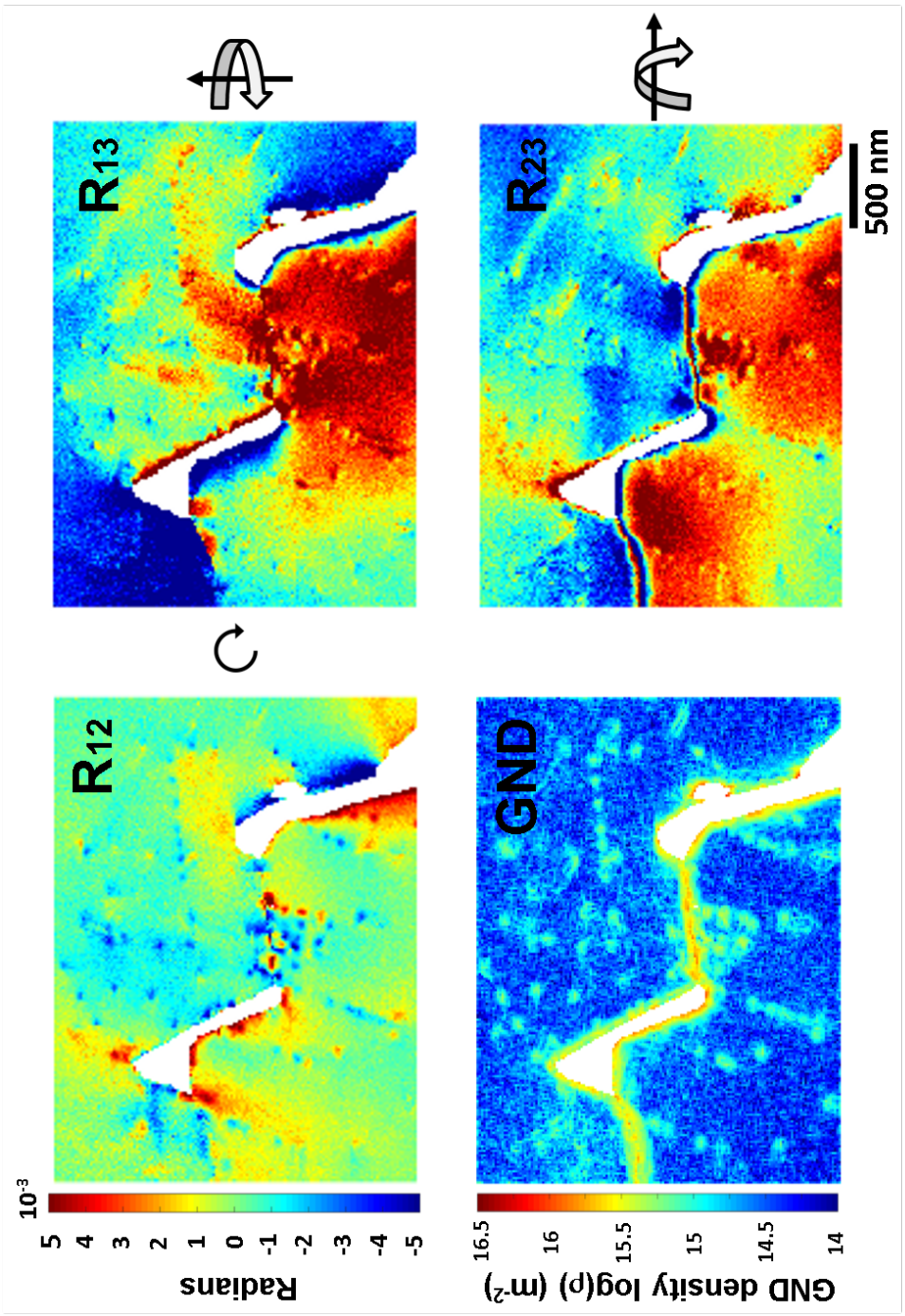


Fig. 4.22 Rotation tensor map for 2 faceted carbides on a grain boundary exhibiting coherency strain induced serration.

Of course these two mechanisms may act together to different extents at different grain boundaries. The determination of the dominant mechanism for a particular grain boundary is unlikely to be thoroughly justified, owing to the unknown third dimension not available in 2D SEM/EBSD images. A general grain boundary has five degrees of freedom [44], with input from EBSD measurements, there are still two degrees of freedom not accounted for. As a result, the appearance of a grain boundary may be very different from a different viewing perspective. Hence, the aforementioned two mechanisms seems to dominate in a particular boundary is de facto owing to the limitation of 2D images.

4.4.3 Processing map construction

A processing map is constructed through analytical methods using a quantified microstructure database and knowledge developed. The prediction of the final microstructure is of particular attraction to academics, but also serves as a guide line for industrial production.

First, a few bounding conditions were identified, *i.e.* cooling rates and solution treatment temperature. For example, a solution temperature at 1070°C/120min (B2) is not sufficient to generate serration, because limited dissolution of carbide and grain growth were observed. Since the driving force of the serration formation requires the synergy of carbide reprecipitation and grain boundary with certain mobility, it is deduced that no serration could be triggered for a solution temperature equal or lower than this. Therefore, the serration index at 1070°C equals 0 at all cooling

rates by definition, as demonstrated in Figure 4.23 (a). Similarly, A1 is then used as another bounding condition, where a cooling rate around 600°C/min or higher will not trigger serration, due to the kinetics for re-precipitation on the grain boundary limiting the size of carbides present. The rest of the conditions tested in the matrix are presented in Figure 4.23 (a), with its calculated serration index next to it. The graph is then transformed into a processing map by interpolating serration index into a contour plot, implementing "contourf" function in MATLAB, see Figure 4.23 (b). The serration index is displayed as a function of solution temperature (fixed at 120 mins) and cooling rates with a fixed intermediate temperature at 900°C. Thereafter, desired microstructure can be designed with altering processing parameters.

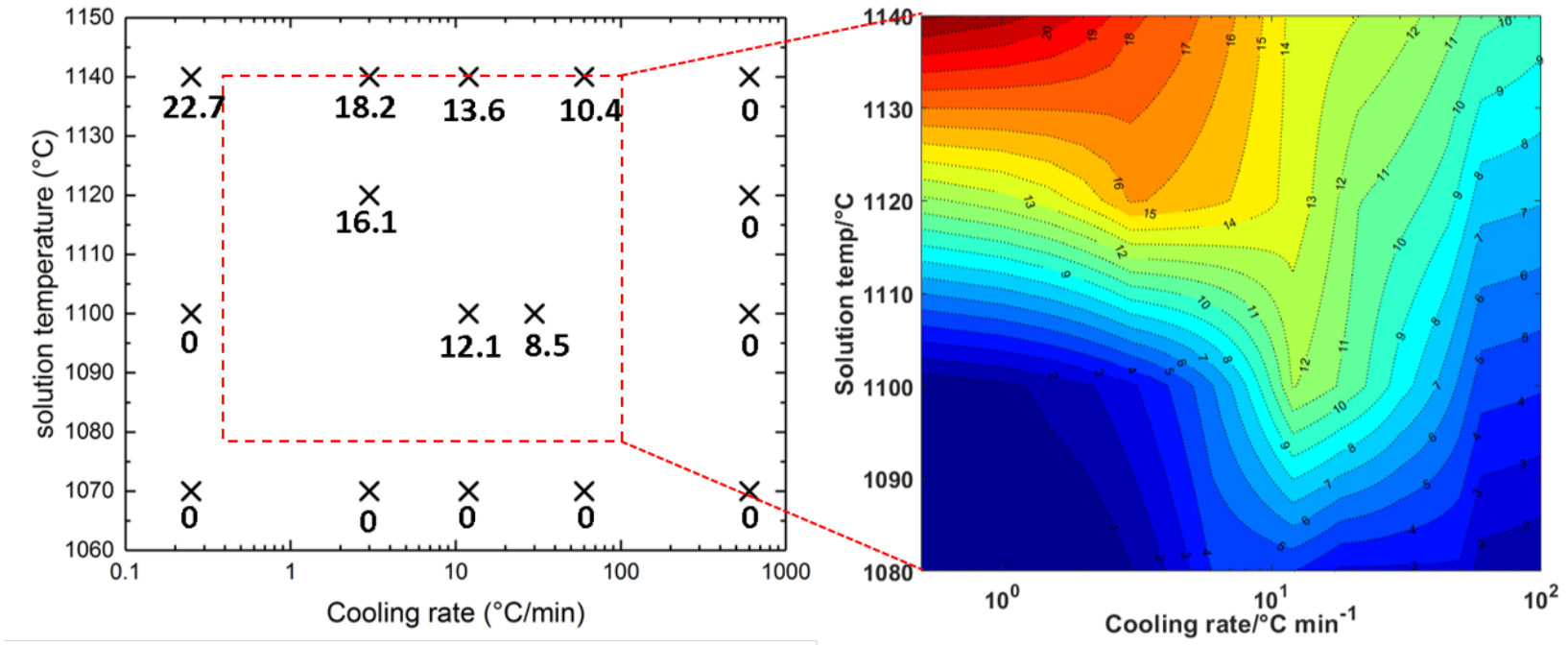


Fig. 4.23 (a) Serration index obtained for a range of solution temperature and cooling rate. Crosses indicate actual data points and the number below them are serration index measurements. (b) Contour plot of serration index as a function of solution temperature and cooling rate. Solution treatment time is 2 hours and intermediate temperature is 900°C in both graphs.

The effect of processing parameters can then be readily interpreted by the processing map, as illustrated in Figure 4.17. For example, for any particular cooling rate, solution temperature has significant influence on the degree of serration, while with decreasing solution temperature the serration is then suppressed. The cooling rate also plays a crucial role in the formation of serration — with a solution temperature at 1140°C, the degree of serration has declined drastically from 0.25 - 60°C/min, in agreement with other reports [37, 137]. The logarithmic relationship between serration index and cooling rate are established, as displayed in Figure 4.17 (c). Section 4.3.2 and Figure 4.17 (b) presents another logarithmic relation between carbide nucleation density and cooling rate. Therefore, the serration index is suggested to be a function of carbide nucleation event. Figure 4.17 (d) shows the adverse linear relation between serration index and nucleation density generated as fewer particles are nucleating on a grain boundary, both formation mechanisms would be favoured due to reduced boundary tension.

Nonetheless, the situation possesses an anomaly with a solution treatment at 1100°C. From the above analysis and deduction, one would expect to see higher degree of serration with very slow cooling rate, yet the microscopic observation confirmed negligible serration was found, see Figure 4.24. Since the 1100°C/120 minutes only dissolves the carbide partially and increase the grain size moderately, which leads to less available carbon atoms having potency for precipitation in a even larger grain boundary area. As a result, carbide precipitation may become more selective with a preference on grain triple junctions. Some carbides show a tendency to facet or impede

grain boundary migration in Figure 4.24, however, the degree of serration is negligible overall. Whereas, a faster cooling rate, for example 12°C/min generates a larger higher undercooling in comparison, and thus, more carbides formed and interacting with the grain boundary and eventually generating serration.

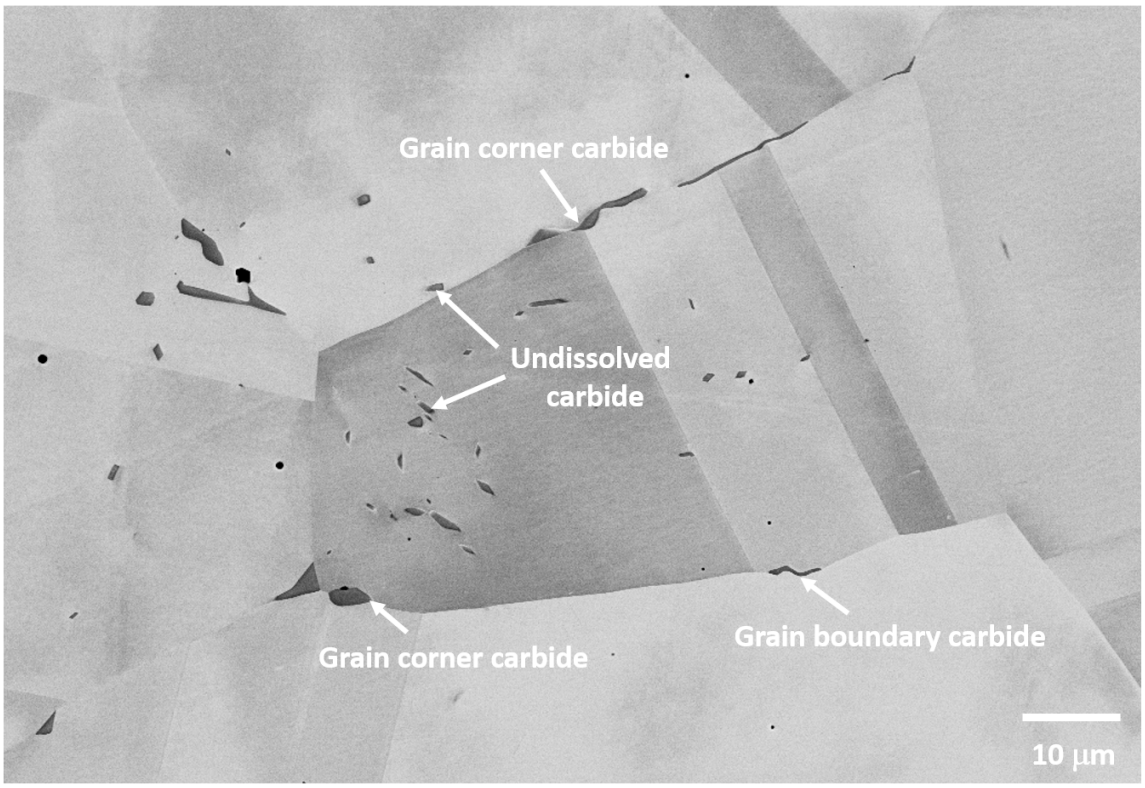


Fig. 4.24 Microstructure of B3 that obtains non-serrated grain boundary. The carbide achieved partial dissolution and remained in grain interior. Reprecipitation of carbides are found primaryly on grain corners and boundaries, which possesses granular and/or blocky morphology.

A step isothermal heat treatment has been implemented to determine the necessity of slow cooling in regard to serration formation. It aimed to use repeated isothermal holding to mimic the slow cooling process, see Figure 4.25. In comparison to B7, both treatments had 1140°C/120 minutes solution treatment and intermediate temperature

of 900°C/120 minutes. Instead of obtaining a continuous cooling process, the new heat treatment acquired 9 isothermal hold followed by quenching, in an increment of 30°C for 120 minutes. In contrast to thick planer intergranular carbides as shown in Figure 4.25 (c), the step aged sample obtains both inter/intragranular carbides. The continuous granular carbides formed on the grain boundaries are due to high nucleation density as a result of quenching, and then coarsened with subsequent isothermal holding. Slow cooling from solution treatment passing through carbide dissolution temperature is believed to be an essential condition.

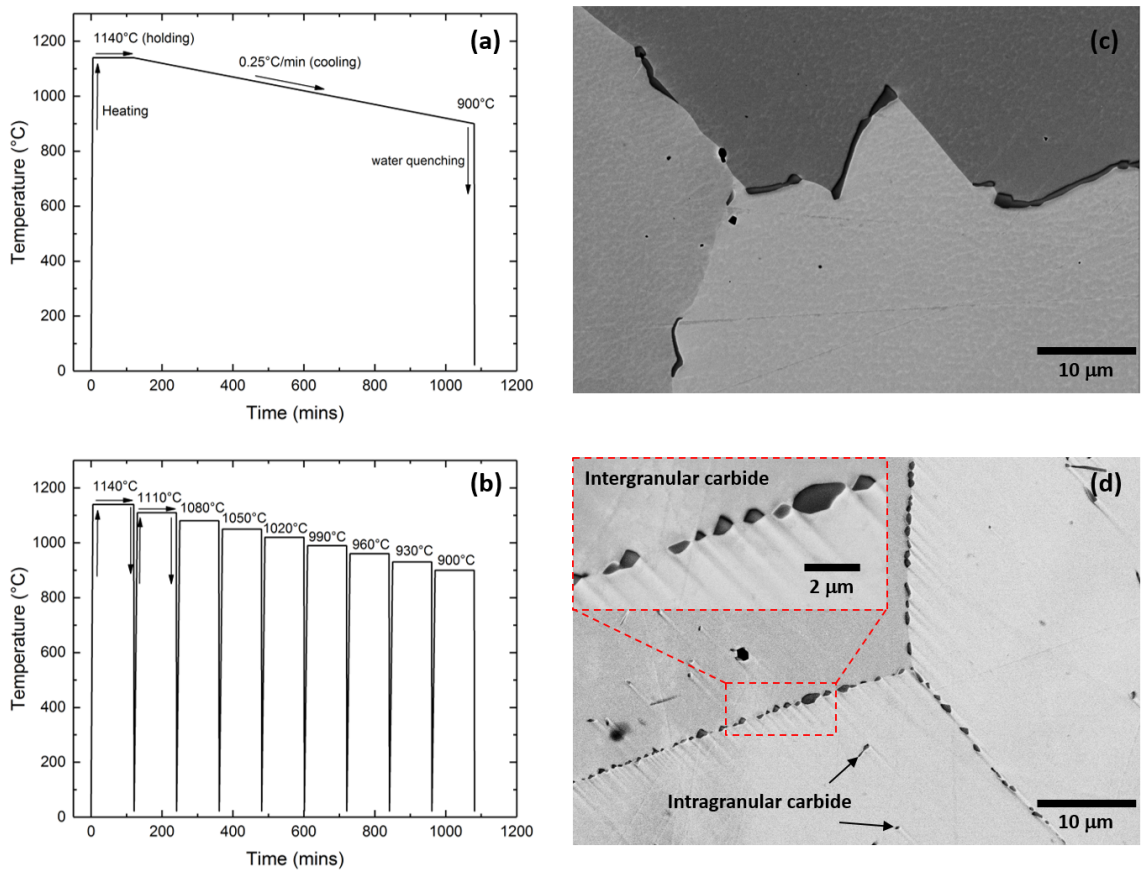


Fig. 4.25 Heat treatment profile for B7 with a step isothermal holding that mimics it, and their corresponding microstructures.

4.5 Summary and Conclusions

1. Serrated grain boundaries have been categorised into two types with respect to their generation: by deformation or annealing. The current study treats the annealing grain boundary serration, and has first provided a definition to it. Classification of grain boundaries were also provided for serration identifcation, assisted with a determinative criterion.

2. Prerequisite conditions that triggered serration during annealing in Inconel 600 were identified. The solution treatment followed by slow cooling was required and could not be replaced by isothermal holding. The synergy of carbide and grain boundaries is the driving force to form serrated grain boundaries, however, carbide itself is not sufficient to initiate serration.

3. Carbides present in the material were identified as orthorhombic M_7C_3 type in both the as-received state and the heat treated state. Carbides showed a coherency relation to one side of the matrix after heat treatment, where the orientation relation can be expressed by $\{111\}_{\gamma}//\{100\}_{M_7C_3}$.

4. A new approach was established for quantification of grain boundary serration based on Fourier analysis of the boundary trace. The method utilised a combination of microscopy, image analysis and mathematical transformations that performed decomposition of the complex serrated morphologies. The results demonstrated a new quantitative approach to serration measurements.

5. Wavelength and amplitude of the three strongest sinusoids were combined into one metric that describes the degree of serration. The physical interpretation of this serration index is proportional to the area that the zig-zag area covers.

6. Two formation mechanisms were verified using advanced characterisation. The first mechanism concerns the migrating grain boundary being held back by intergranular carbides. The second mechanism corresponds to faceted carbide growth, which eventually distorted the boundary. In some cases, both mechanisms are observed. Preferred formation mechanism of serration is dependent upon solution temperature and nucleation density of the carbide.

7. Formation of grain boundary serration was related to heat treatment details, through an extensive microstructure database. The introduction of serration index allowed a processing map for serration to be constructed by interpolating experimental data. It is of particular interest to industrial manufacturers.

Chapter 5

Effect of Grain Boundary Serration on Mechanical Behaviour in Nickel Alloy Inconel 600

5.1 Introduction

Grain boundary serration has long been known as an intriguing phenomenon, particularly for the nickel-based superalloys of the type studied here. The scholarly and industrial attentions were caught for the following reasons. First, there is complexity arising from the inapplicability of the generally accepted picture of smooth or gently curved grain boundaries, as observed on the microscale. Second, there is the fundamental question of why grain boundary serration arises in the first place. Third, effects of serration on the mechanical behavior of these materials are not well understood.

What are the underlying fundamental effects which cause it? At present, no truly unequivocable explanation exists. Carefully designed experimentation that accounts detailed microstructural quantification and advanced charaterisation is required to conduct a systematic study for revealing the mechanism.

Grain boundary serration were first applied in 1960s as a form of grain boundary engineering in steels [117, 118] for acquiring intergranular strength. Serration of grain boundaries in nickel alloys was first reported by Larson *et al* [5] and Miyagawa *et al* [4] in 1976; slow cooling from above the γ' dissolution temperature was employed. Since then, attempts have been made to elucidate the formation mechanism, details of heat treatment and the role of alloy composition [119, 127, 129, 130, 37, 100, 132, 38, 133]. The work of Koul & Gessinger on the Inconel 738, Nimonic 115 and Nimonic 105 alloys [119], involving an impressive combination of experimentation and modelling, identified the role of γ' migration on serration. The role of the γ' phase has since been confirmed by a number of researchers [130, 135, 137–139]. But what happens in the absence of the γ' phase? Alloys containing very few or no γ'-forming elements have also been shown to form serrated grain boundaries, for example Haynes 230, Inconel 690, Inconel 617 and Nimonic 263 [37, 38, 147, 148]. Cr-rich $M_{23}C_6$ carbide are a necessity for the formation of grain boundary serration for these alloys, though the underlying mechanism is still in open debate.

The phenomenon has proven itself of great academic interest, but are there remarkable beneficial effects which confer technological advantage? Indeed, for nickel-based superalloys, the most concerned properties are time dependent deformation, for example

creep lifetime, crack growth rate, fatigue, etc. Early research conducted on Inconel 792 and 20-11P confirmed reduced creep rate and increased creep strength [5, 4], although the postmortem analysis was limited by the characterisation techniques available at that time. Later studies on IN738, Astroloy, PM alloy-10, Waspaloy and RR1000 have proven similar influences [126, 125, 128, 131, 124, 98]. The work up to date on STAL-15 again revealed a similar trend; with both extensive experiments and modelling efforts [41, 153, 159]. In addition, for alloys with low or no γ' phase, creep life and ductility are significantly enhanced [37, 141, 146]. In summary, grain boundary serration has been demonstrated to improve mechanical properties such as creep, low cycle fatigue (LCF) and dwell fatigue remarkably in various superalloys. A few hypotheses have been proposed for taking account of the improved behavior, e.g. prevention of grain boundary sliding, increased grain boundary diffusion path, impedance of crack growth. However, no unambiguous mechanism is yet supported strongly by substantial experimental evidence or modelling. The past efforts have mostly extended the serration effect from different angles in a qualitative manner, such as alloy composition, mechanical properties and cooling rates, but little work has been attempted to control other microstructural variables at the same time. The critical missing piece of the puzzle is lack of quantitative measurements to support each of the above mentioned mechanisms, therefore, even with sensible assumptions and experimental evidence, the hypotheses is still yet to be validated.

Furthermore, the complexity of the experimentation is highlighted if secondary effects are also considered, *i.e.* are the advantageous impact really contributed by

grain boundary serration alone, or are there other changes to microstructure while obtained grain boundary serrations? In fact, few researchers have really addressed this issue and studies on the serration effect have seldom controlled the microstructure very well, understandably due to the nature of the problem. Creep is one of the most complicated continuum damage processes, and many factors are well known to be crucial: grain size, γ' size, morphology and distribution, twin boundary fraction, carbide type/morphology and size, etc. All are likely to be affected by cooling rate to some extent. For example, the γ' size and distribution can be directly influenced by nucleation density within the γ matrix, which is a function of solution treatment condition and cooling rate [127, 100, 98, 162, 101]. The slow cooling causes larger γ' size and sometimes a bimodel distribution. Moreover, slow cooling extends the total time for grain growth, and partial dissolution of MC carbides [192, 193], which makes good control of microstructual variables even harder. Admittedly, very carefully designed experimentation and detailed is required.

The research conducted in this chapter was performed with the above issues in mind and aimed to tackle the questions from a fundamental level. The nickel-based superalloy Inconel 600 is chosen for study; an advantage is then that the alloying elements Al and Ti are absent, so that any involvement of the γ' phase $Ni_3(Al, Ti)$ on the serration effect cannot then arise. Furthermore, any role of Ta- or W-rich MC carbides is avoided, because Ta and W are absent. Instead, the Cr-rich M_7C_c carbide become critical to the development of grain boundary serration, with the cooling rate through the carbide solvus temperature also playing a crucial role. Here, serrated and non-serrated grain

boundaries were first prepared and characterised using scanning electron microscopy, with the grain size distribution and twin boundary fractions proven to be unchanged; the creep response was then tested. Quantitative high angular resolution electron backscatter diffraction (HR-EBSD) and X-ray computed tomography (XCT) are used to gain insights into the creep deformation modes which are operative. Attention is paid not only to postmortem analysis, but also to *in-situ* and interrupted studies. In the final part of the chapter, the implications of the serration effect on the mechanical response of this alloy are considered with an emphasis on carbide evolution, cavitation and dislocation sub-structures which arise.

5.2 Methodology and Experimental Description

Inconel 600 was selected to understand the effect of serration on mechanical properties. As introduced in Chapter 4, thorough investigations on heat treatment was conducted, where various degrees of serration can be achieved by altering heat treatment conditions. In addition, the Inconel 600 is chosen particularly on account of the relative simplicity of its chemical composition. In this alloy, Al or Ti are present at only trace levels so that any influence of the γ' phase on grain boundary serration cannot then arise. Moreover, refractory elements such as Ta, Mo or W are also absent; therefore, grain boundary MC-type carbides enriched with these elements have no contribution to microstructure; neither $M_{23}C_6$ nor M_7C_3 carbides could be formed from MC-carbide

decomposition. Specimens were taken from a cold-drawn and annealed bar of circular cross-section with a diameter of 16 mm, in which the virgin grain size was about 15 μm.

5.2.1 Heat treatment

A moderate level of serration is chosen from the heat treatment matrix, *i.e.* a cooling rate of 12°C/min from solution temperature. For obtaining the non-serrated grain boundary is via water quenching directly from the same solution treatment. A solution heat treatment of 1140°C for 2 hours was used throughout, which is significantly higher than the estimated carbide solvus temperature of $1040 - 1070$°C with heat treatment as shown in Chapter 4. Such solution heat treatment was employed to maintain the same level of grain size, grain distribution and $\Sigma 3$ twin boundary fraction in both microstructures, which are considered to be crucial microstructural variables for creep and other mechanical properties. The selected heat treatment compensated for small variations in total heat treatment time caused by different cooling rates and it proved possible to develop significant grain boundary serration at the microstructural level. Heat treatment profiles and representative microstructures are illustrated in Figure 5.1.

5.2.2 Creep testing

Tensile creep rupture tests were performed from 700°C to 900°C, where the details of the test setup can be found in Chapter 3. To observe deformation and fracture mechanisms at each condition in order to evaluate the influence of serration. The tests were carried out for conditions varying significantly in temperature and stress:

700°C/170MPa, 815°C/70MPa and 900°C/40MPa. In addition, another 6 tests were interrupted at 5 % strain. Temperature was monitored using K-type thermocouples placed in contact with the crosshead next to the specimen. Each specimen was held at the testing temperature for 1 hour prior to loading, for consistency of oxidation damage to each specimen.

Fig. 5.1 (a) and (b): Heat treatment profiles for development of non-serrated and serrated grain boundary materials, and (c) and (d) corresponding microstructures obtained from heat treatments described in (a) and (b). The curves are drawn to illustrate grain boundary morphologies only and are deliberately offset so as to not obscure the grain boundaries in the micrographs.

5.2.3 *In-situ* tensile test in SEM

In-situ tensile tests were performed at room temperature (22°C) and 700°C with a strain rate, $\dot{\varepsilon}$ of approximately 10^{-3}. This is conducted in a Zeiss Evo SEM with a LaB_6 filament. Dog bone specimens were machined from heat treated cylindrical bars using EDM for two materials, both with serrated and non-serrated grain boundaries. The gauge volume of 2 mm length × 1.5 mm width × 1 mm thickness was used. EBSD scans were conducted prior testing, to acquire crystal orientation information. Secondary electron micrographs were taken at 5% increments of engineering strain until failure to capture the deformation evolution. More details on the test setup can be found in Chapter 3.

5.2.4 SEM based characterisation

A Zeiss Merlin FEG-SEM was used to charaterise the grain boundaries by heat treatments, which was also used for the fractography and HR-EBSD scans. For each condition, a representative sample, i.e. the sample with median rupture life among three, was first taken for fractography analysis. The fractured sample was then cut by wire-based electrical discharge machining (EDM) from the middle of fracture tip along the axial direction. The sectioned sample was mounted and then prepared via standard metallography procedures, with 2 minutes colloidal silica to finish. The SEM is equipped with a Bruker EBSD detector, which was used to capture EBSD patterns at a resolution of 600 × 800 for maps collected at a step size of 220 nm. Furthermore, 6 interrupted specimens were also cut by EDM in the same way and scanned by HR-

EBSD using the same conditions. A cross-correlation based analysis was used on the stored EBSD patterns [169–171]. Lower resolution EBSD were conducted using Zeiss Evo W-filament SEM for measuring the grain sizes. Three EBSD maps were scanned for each microstructure, the grain size measurements were processed using Brucker's ESPRIT 2.0 software. EDS mapping was also conducted with Oxford Instruments X-MAX detector to confirm elemental distribution of intergranular regions.

5.2.5 X-ray tomography based characterisation

The crept specimens were observed with significant cracks on the surface, which implies some degree of cavitation may also contribute to deformation and fracture, therefore, X-ray computed tomography was used to quantify cavity size and its distribution. One representative fracture tip was taken for each creep condition and tomography analysis carried out using a North Star Imagix system at 150 kV with a voxel size of 4.86 μm. For each sample, a height of roughly 10 mm was characterised using 3600 projections and a helical scan used to reconstruct the 3D volume. ImageJ and Avizo softwares were utilized for quantification of cavity size and distribution using histogram-based methods [194]. Comparisons of cavity size and distributions were then made for samples with and without grain boundary serration. For this, quantification of a 3D cylindrical volume of about 3 mm diameter and 5 mm height was selected as illustrated in Figure 5.2.

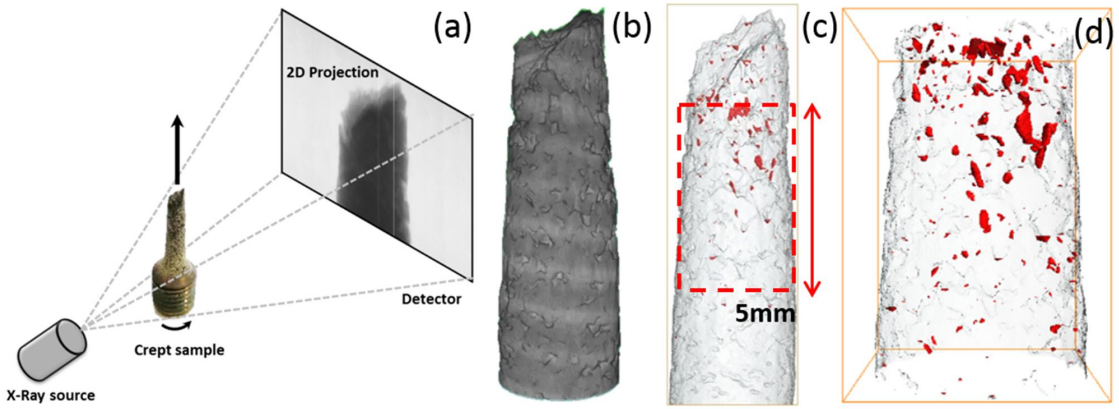


Fig. 5.2 Postmortem X-ray tomography set-up and computed results – quantification of cavitation distribution. (a): X-ray technique set-up. (b): Volume of the specimen reconstructed by X-ray tomography. (c) Surface reconstruction completed by Avizo with internal cavities labeled in red. (d) A cylindrical volume of 5 mm height from lower end of the fracture tip were used for cavity size and distribution analysis.

5.3 Results

5.3.1 Heat treatment and grain boundary serration development

The development of two distinctive types of grain boundary morphologies were investigated first. As illustrated in Figure 5.1, heat treatment profiles for each case were displayed along side with representative grain boundaries. For illustration purposes, curves highlighting the grain boundary morphologies are displaced laterally from the actual boundaries. For the non-serrated grain boundary case, no second phases were observed at the FEG-SEM resolution; however, the serrated grain boundaries were always associated with intergranular carbides at the microscale. Energy dispersive X-ray spectroscopy (EDS) was used to probe the chemical distribution of the carbide

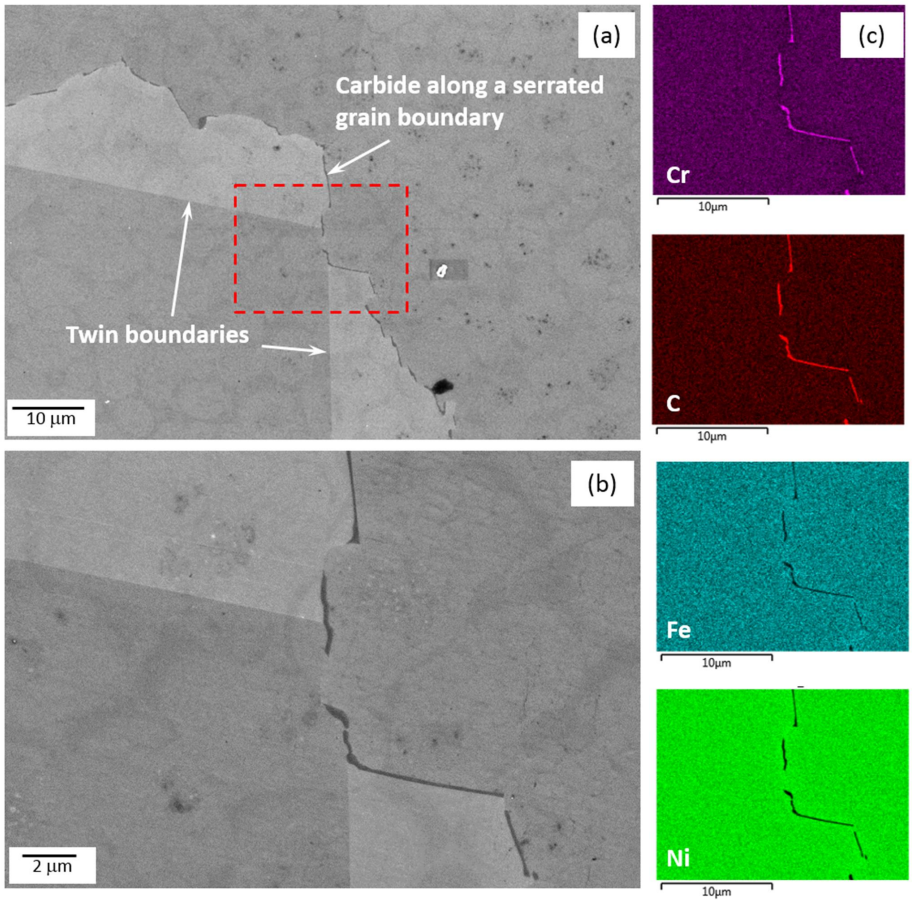


Fig. 5.3 Energy dispersive X-ray spectroscopy (EDS) analysis in a region that contains a serrated grain boundary and planer carbides. (a) and (b) shows the region at two magnifications. (c): Composition maps indicate segregation of Cr and C and depletion of Fe and Ni at the grain boundary.

in the vicinity of a serrated grain boundary and Figure 5.3 shows a typical composition map. The map determined the carbides enriched in chromium but depleted in iron and nickel, which is consistent with findings in Chapter 4. In addition, no elemental segregation was detected along twin boundaries.

To maintain minimum discrepancy between the two microstructure, grain size and twin boundary fractions were measured, as they can have a great influence on creep. The EBSD data were post-processed using the ESPRIT software, with a threshold

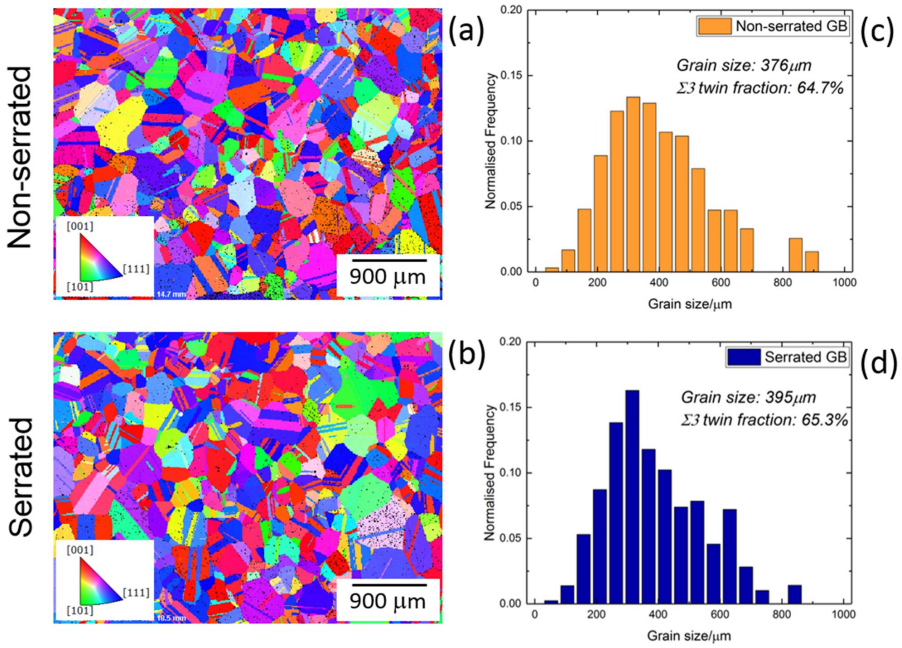


Fig. 5.4 (a) and (b) are examples of inverse pole figure maps used for grain size measurements for non serrated and serrated materials respectively. (c) and (d) displayed grain size distribution for each microstructure. Average grain sizes are 376 μm and 395 μm, twin boundary area fractions are 64.7% and 65.3% respectively for non-serrated and serrated grain boundary materials.

grain boundary mis-orientation angle defined as 10°. Representative EBSD maps are illustrated in Figure 5.4 (a) and (b) for the non-serrated and serrated microstructures respectively. Grain size distribution histograms are shown in Figure 5.4 (c) and (d), where two distributions overlap with each other and both are skew with tails on the high grain size side. Mean values of grain size with boundary length fraction of $\Sigma 3$ (twin) boundaries are given on the distribution plots and show very little variation between the two microstructures. Hence, any effect coming from grain size and twin boundary fractions are assumed negligible to creep.

5.3.2 Creep tests and fractography

Figure 5.5 has presented the creep data for both non-serrated and serrated grain boundary samples at all conditions tested. The creep curve of median creep life at each condition was presented, early stage creep up to 5 hours were displayed next to the curve. The bottom row displays a summary of rupture life and creep ductility with error bars representing ± one standard deviation. For rupture life, the serrated grain boundary microstructure conferred no life enhancement at 700°C. However, an increase in creep rupture life was measured at the higher test temperatures of 815°C and 900°C. From the average creep ductility, it is evident that the serrated grain boundary case surpassed the non-serrated in all conditions by a moderate margin. Particularly, a notable decrease in creep ductility was observed for alloys crept at the higher temperature and lower stress regime. The fracture mechanism is suggested different which is evident by the ductility drop.

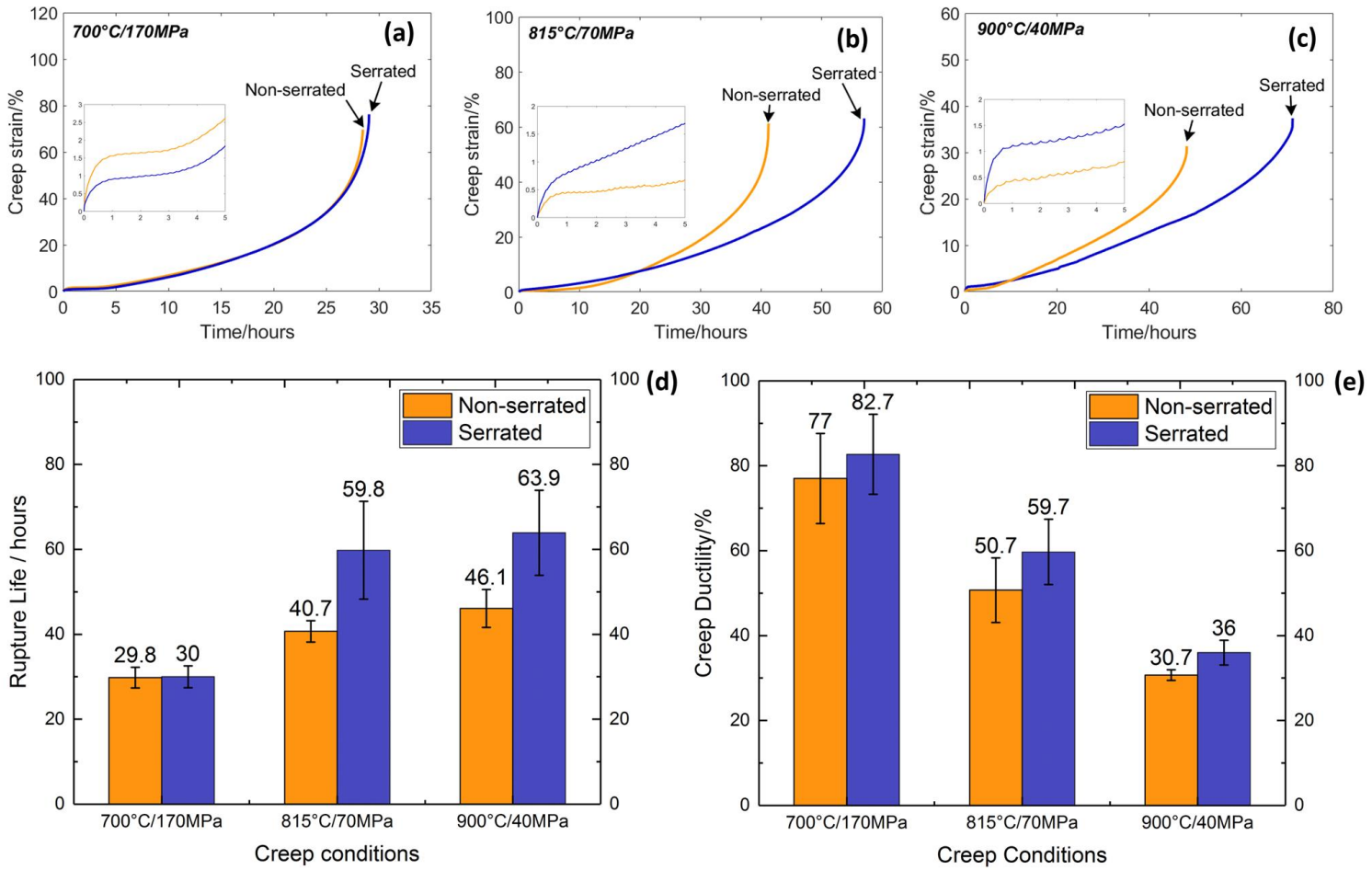


Fig. 5.5 Creep data for non-serrated and serrated architectures, see (a-c) at conditions of 700°C/170MPa, 815°C/70MPa and 900°C/40MPa. Top row: Representative creep curves for median rupture life samples. (d) demonstrated average rupture lives displayed with error bars. (e) demonstrated average ductility displayed with error bars. Serrated grain boundary shows no creep life improvement at 700°C, however, enhancement at 815°C and 900°C. Creep ductility was increased due to serration by a moderate margin in all conditions.

Fracture surfaces of samples in each condition were characterised by FEG-SEM, for which illustrative results are given in Figure 6.6. Specimens with both microstructures showed similar transition behavior from low to high temperature in fracture mode. A clear switch from transgranular dominated features at low temperature to intergranular dominant cracking at higher temperatures was observed. The largest difference was seen at the 815°C/70MPa condition: for which the serrated samples remained mostly transgranular, whereas the non-serrated sample showed much more evidence of intergranular processes. This is believed to account for the marginal increase of ductility observed.

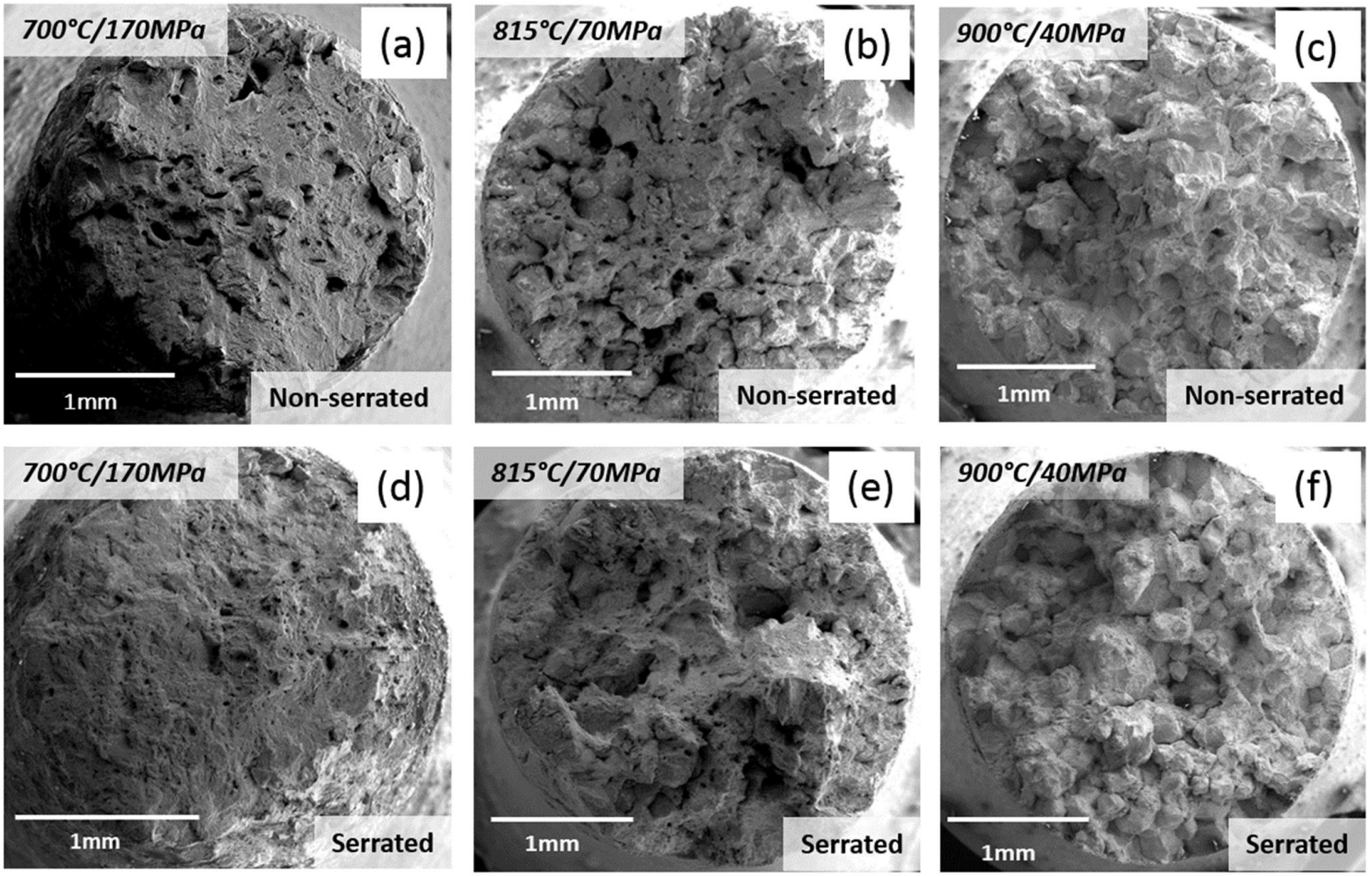


Fig. 5.6 Fractography on representative samples at various conditions with non-serrated grain boundary, see (a-c) and with serrated grain boundary, see (d-f). (a): Transgranular dominant deformation with limited signs of intergranular cracking, i.e. a few microvoids. (b) Intergranular dominant cracking with limited transgranular deformation. (c): Intergranular cracking. (d): Transgranular dominant deformation (e): Mix-mode of trans/intergranular cracking. (f): Intergranular cracking.

Conventional fractography was conducted on ruptured sample at each condition. Low magnification EBSD scans revealed crystal orientations and intergranular cracking failures, see Figure 5.7 and Figure 5.8 for non-serrated and serrated samples respectively. Pattern quality maps were overlaid with grain boundary, twin boundary and sub-grain boundary ($< 5°$) next to EBSD maps. It is clear to see the contrast of cavitation behavior between the two microstructures, particularly at 700°C and 815°C conditions, where notably more cavities were formed in the non-serrated case. In addition, twin boundaries in each case displayed higher integrity, no cracks were found to propagate through them despite the absence of carbides.

5.3.3 *In-situ* tensile testing

Initial microstucutre before *in-situ* testing was captured using EBSD for acquiring crystallographic information on specimens, as illustrated in Figure 5.9. Equiaxed grains were observed in all microsturcture that obtains the same distribution as suggested in Figure 5.4, except from the serrated case at room temperature testing possesses bigger grains. Tensile test curves are displayed in Figure 5.10 and testing results are shown in Table 5.1.

Table 5.1 *In-situ* tensile testing results.

	Non-serrated		Serrated	
Temperature (°C)	22	700	22	700
Yield stress (MPa)	209	105	209	113
Ultimate strength (MPa)	559	304	549	277
Ductility (%)	120	70	120	95

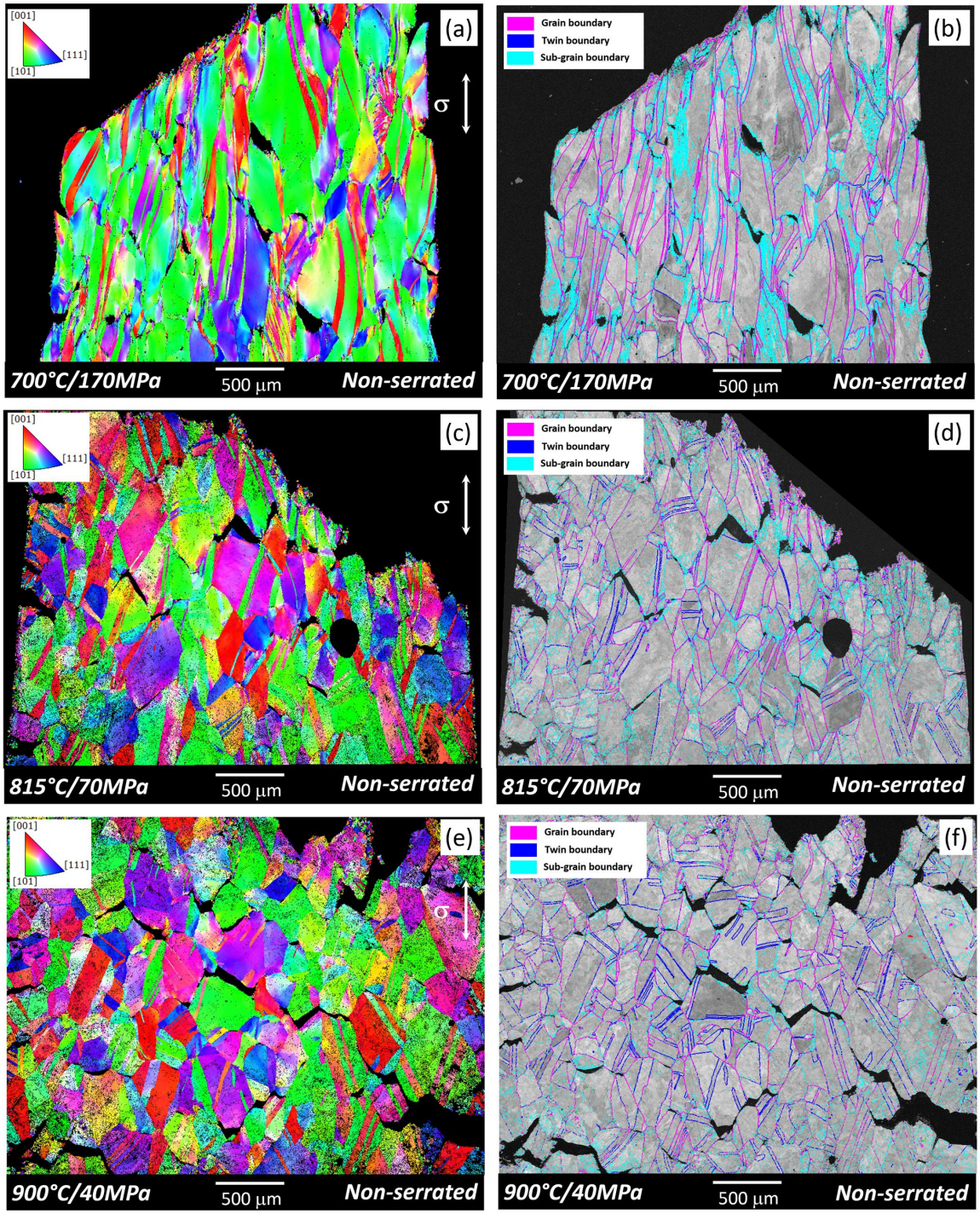


Fig. 5.7 Inverse pole figure (IPF) corresponding to X-axis (a), (c) & (e) and pattern quality (b), (d) & (f) maps of non-serrated fracture tips at each creep condition. The pattern quality map is overlaid with grain boundary, twin boundary and sub-grain boundary. Cavitation exhibited were mostly intergranular cracking in all samples. A circular black spot were displayed in (c) & (d), which is caused by surface contamination rather than cavitation.

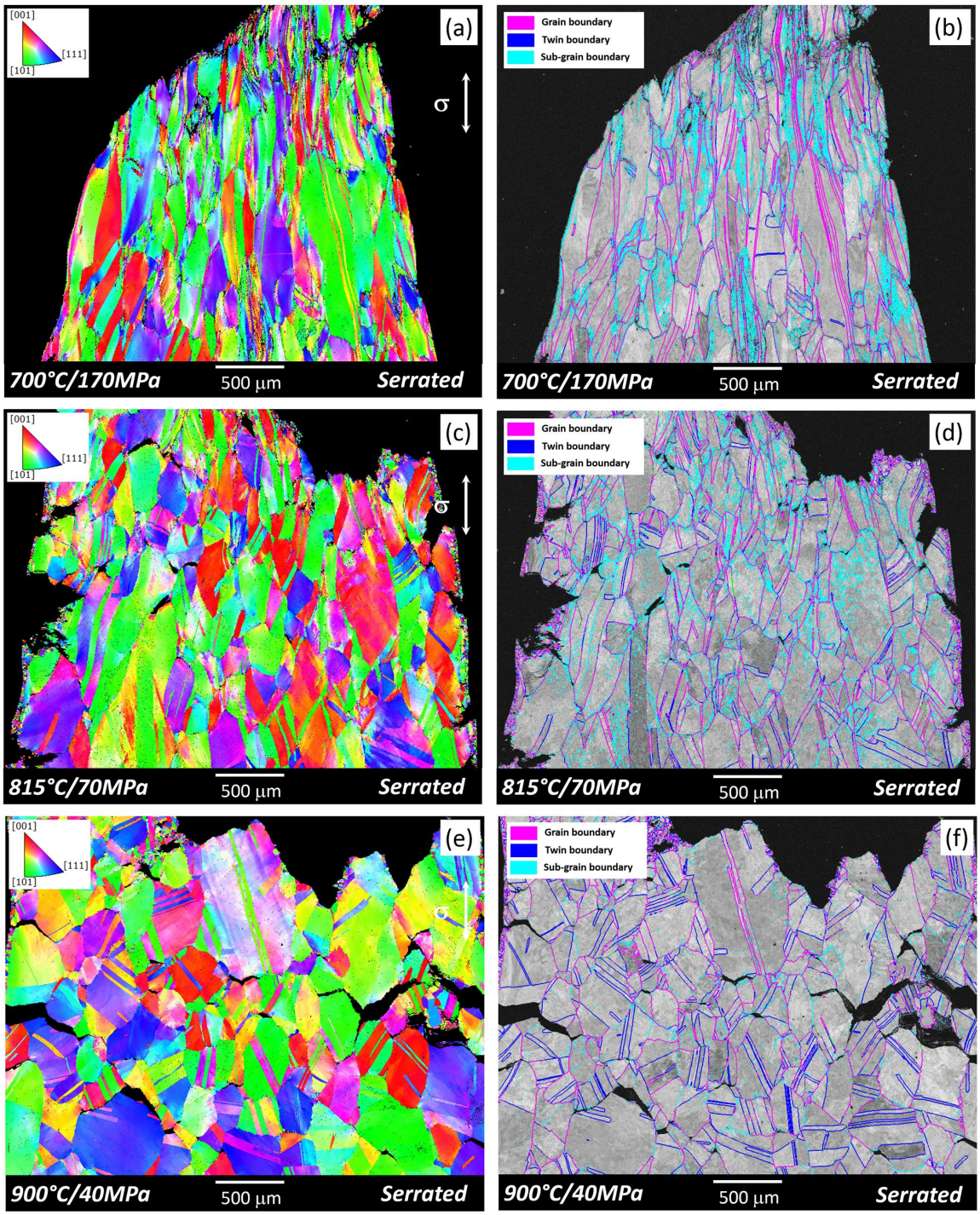


Fig. 5.8 Inverse pole figure (IPF) corresponding to X-axis (a), (c) & (e) and pattern quality (b), (d) & (f) maps of serrated fracture tips at each conditions. The pattern quality map is overlaid with grain boundary, twin boundary and sub-grain boundary. Cavitation exhibited little cavitation at 700° sample and were mostly intergranular cracking in other samples.

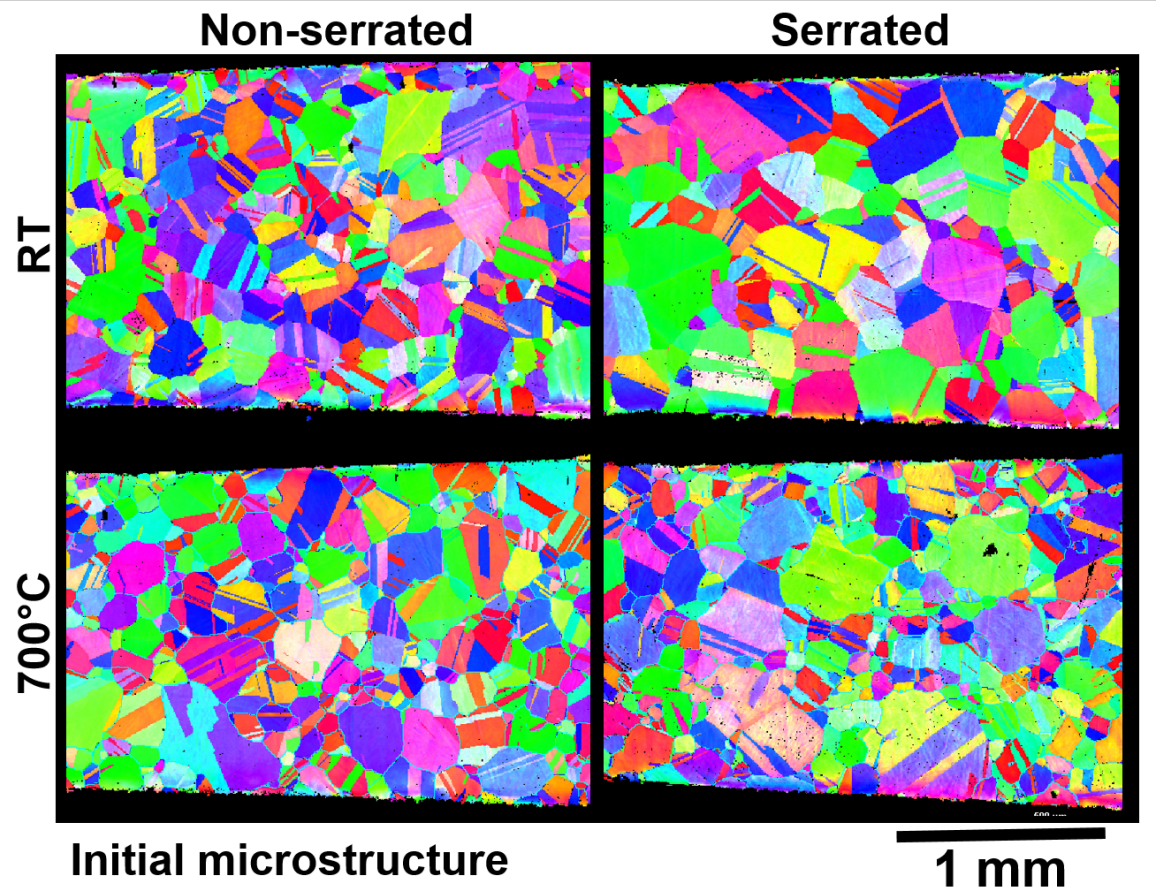


Fig. 5.9 EBSD IPF images of initial microstructure with non-serrated and serrated grain boundaries underwent *in-situ* tensile tests.

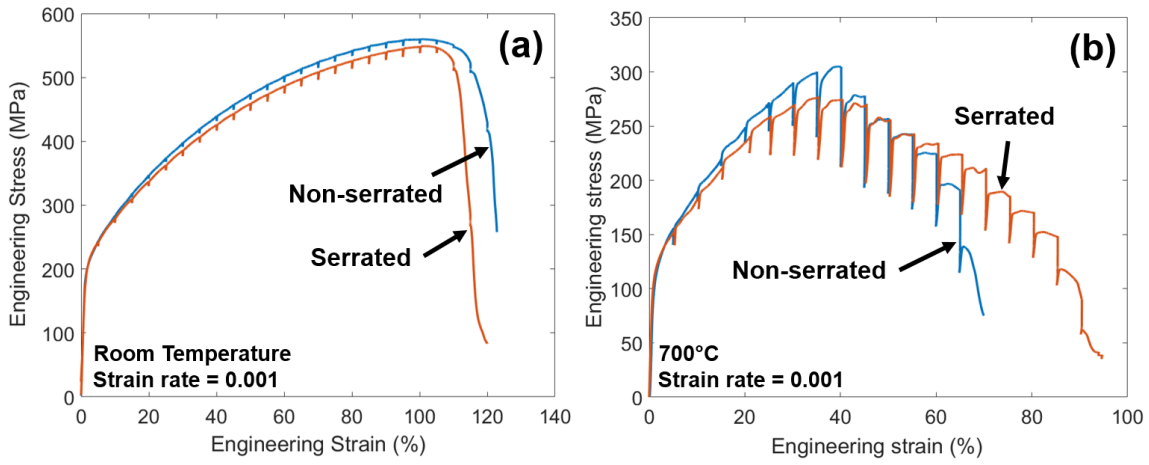


Fig. 5.10 Tensile curves showing engineering stress *vs* engineering strain for both microstructures at two temperatures.

The deformation evolution with strain for both materials underwent tensile deformation are exhibited in Figure 5.11 & Figure 5.12 for room temperature and 700°C respectively. At room temperature, grain boundaries exhibited adequate strength and no failure has initiated from them. Although there was a change in grain size, no real properties were altered due to the sample between serrated or non-serrated grain boundaries. The slip events are accounted for the strain in both cases, as multiple slip systems are observed to operate regardless to grain boundary morphologies. On the contrary, grain boundary cavitation played a compelling role at 700°C. At the same time, there were also a very large amount of crystal plasticity contribution during the deformation, as witnessed by the drastic change of crystal shapes.

5.3.4 HR-EBSD on fractured specimens

Micro-mechanical analysis was performed on sections through fractured samples using cross-correlation based method described in [170, 195]. Geometrically necessary dislocation (GND) density maps were plotted for tests at 815°C/70MPa and 900°C/40MPa conditions. Dislocation cell structures consisting of high GND density walls and low GND density interiors were developed within the grains after the large strain (over 0.3) creep deformation, see Figure 5.13. Cell sizes were measured for each specimen by drawing 10 straight lines across each map (horizontally and vertically) and then counting the number of intersections with cell walls. Cell walls were defined by a minimum threshold GND density of $2 \times 10^{14}\,\mathrm{m}^{-2}$, suggested by previous work on face centred cubic (FCC) copper [180]. For both microstructures, the cell size increased

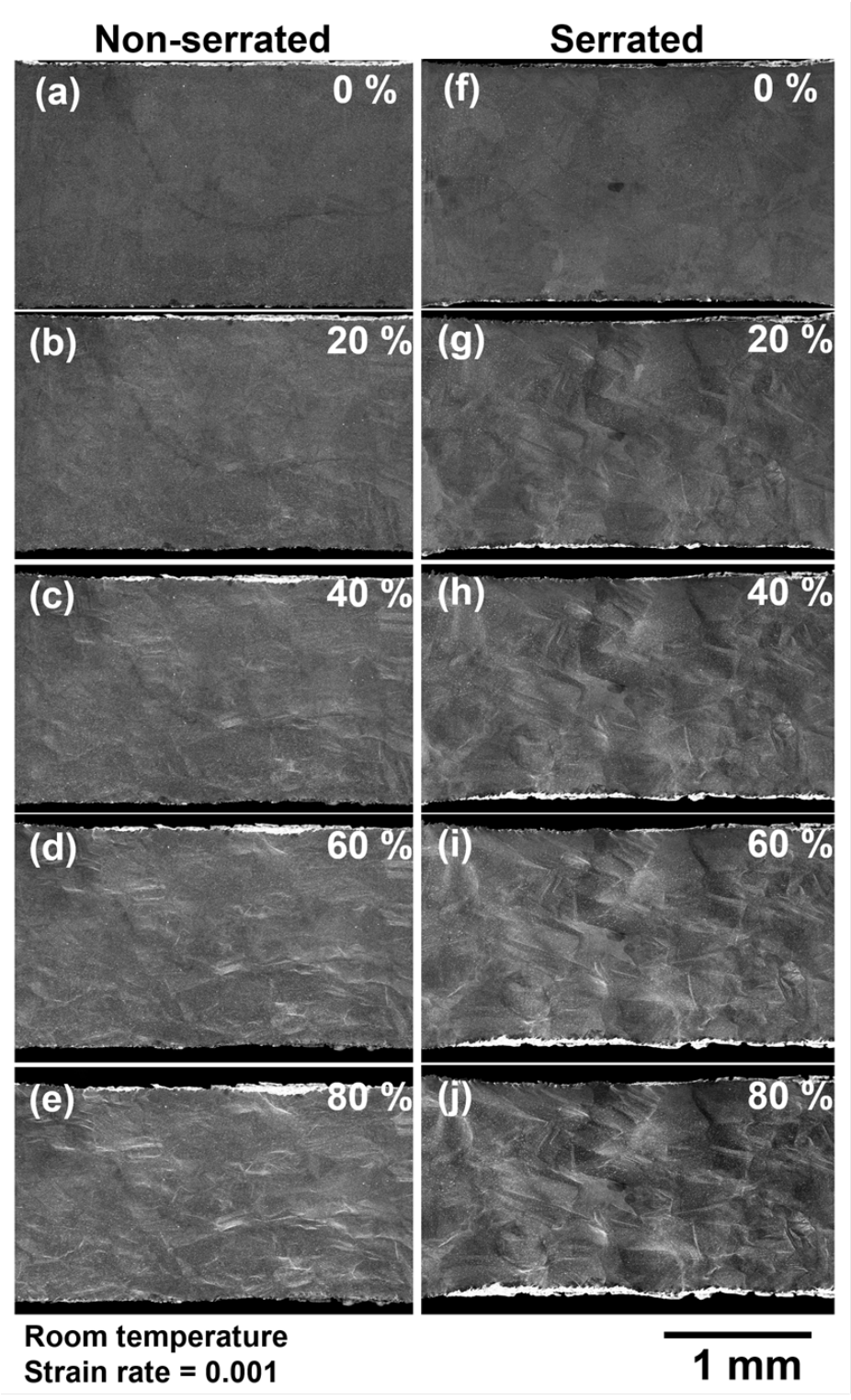


Fig. 5.11 *In-situ* observation of deformation evolution as a function of strain for both grain boundary morphologies at room temperature.

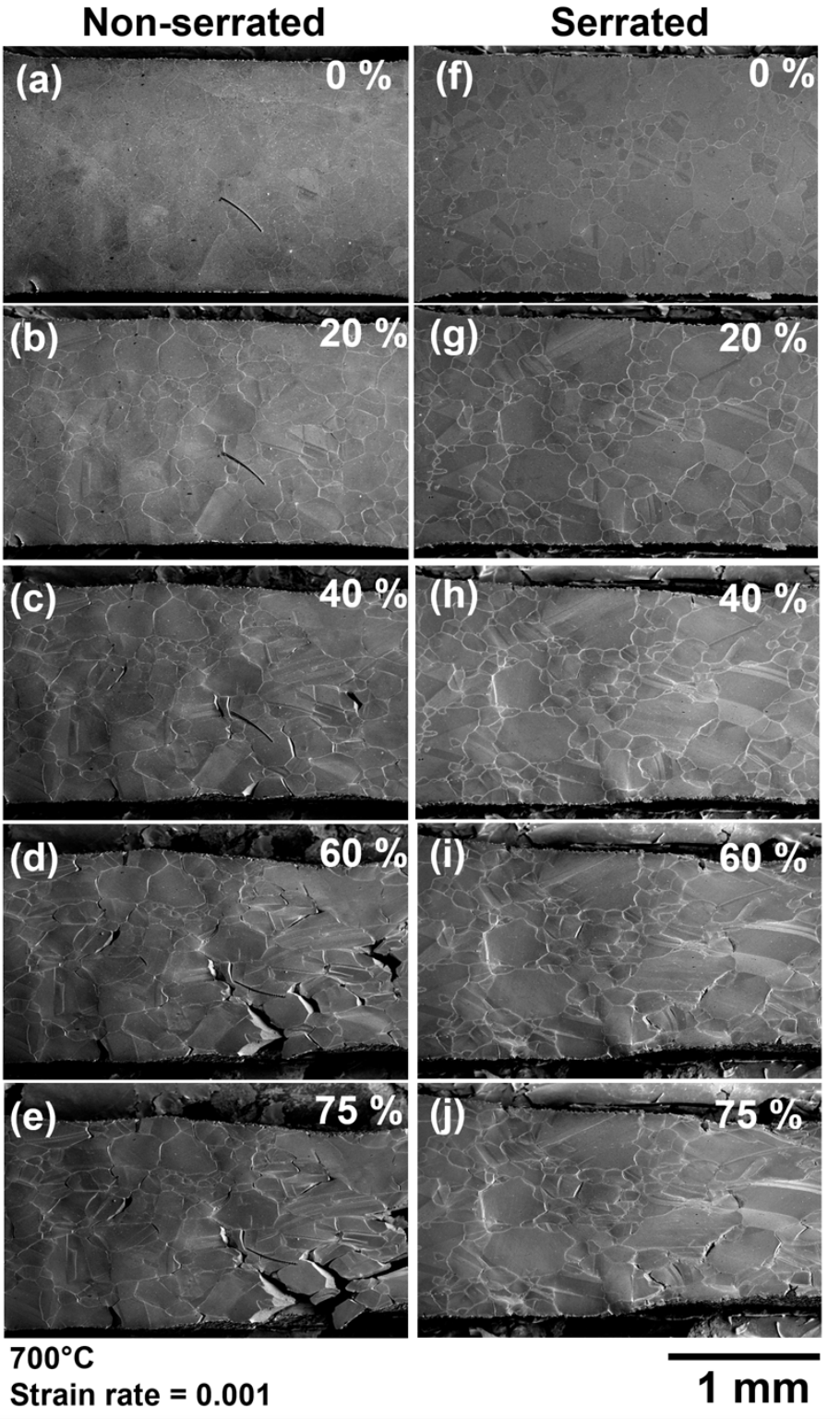


Fig. 5.12 *In-situ* observation of deformation evolution as a function of strain for both grain boundary morphologies at 700°C.

with decreasing stress, from 4.4 μm to 5.2 μm for the non-serrated case and from 4.8 μm to 6.8 μm for the serrated case respectively. The cell size, however, also shows tendency with the grain boundary architecture, as the serrated case always possesses a bigger cell size than the non-serrated case.

5.3.5 Interrupted creep test

The gradual development of carbide was explored using backscattered electron (BSE) imaging of sectioned samples at interrupted conditions. Figure 5.14 shows images of the non-serrated and serrated microstructures after creep to 5% strain at 900°C. Image intensity was used to segment the images and identify the carbides which are shown alongside the BSE images in Figure 5.14. For the non-serrated microstructure a relatively uniform dispersion of fine carbides develop across the grain interiors. In contrast, the carbide dispersion that develops in the serrated microstructure is heterogeneous and shows much greater number density nearer to the grain boundaries than towards the centre of the grains. The average carbide size is larger in the serrated case (1000 nm) compared to the non-serrated case (520 nm). The other striking feature is that for the serrated case the carbides are clearly dispersed along bands in well-defined directions within each grain. Figure 5.15 compares carbide distributions in the serrated microstructure after testing at 900°C and 815°C. With the assistance of the EBSD technique, the carbide growth directions are shown in parallel with the {1 1 1} slip systems of the matrix.

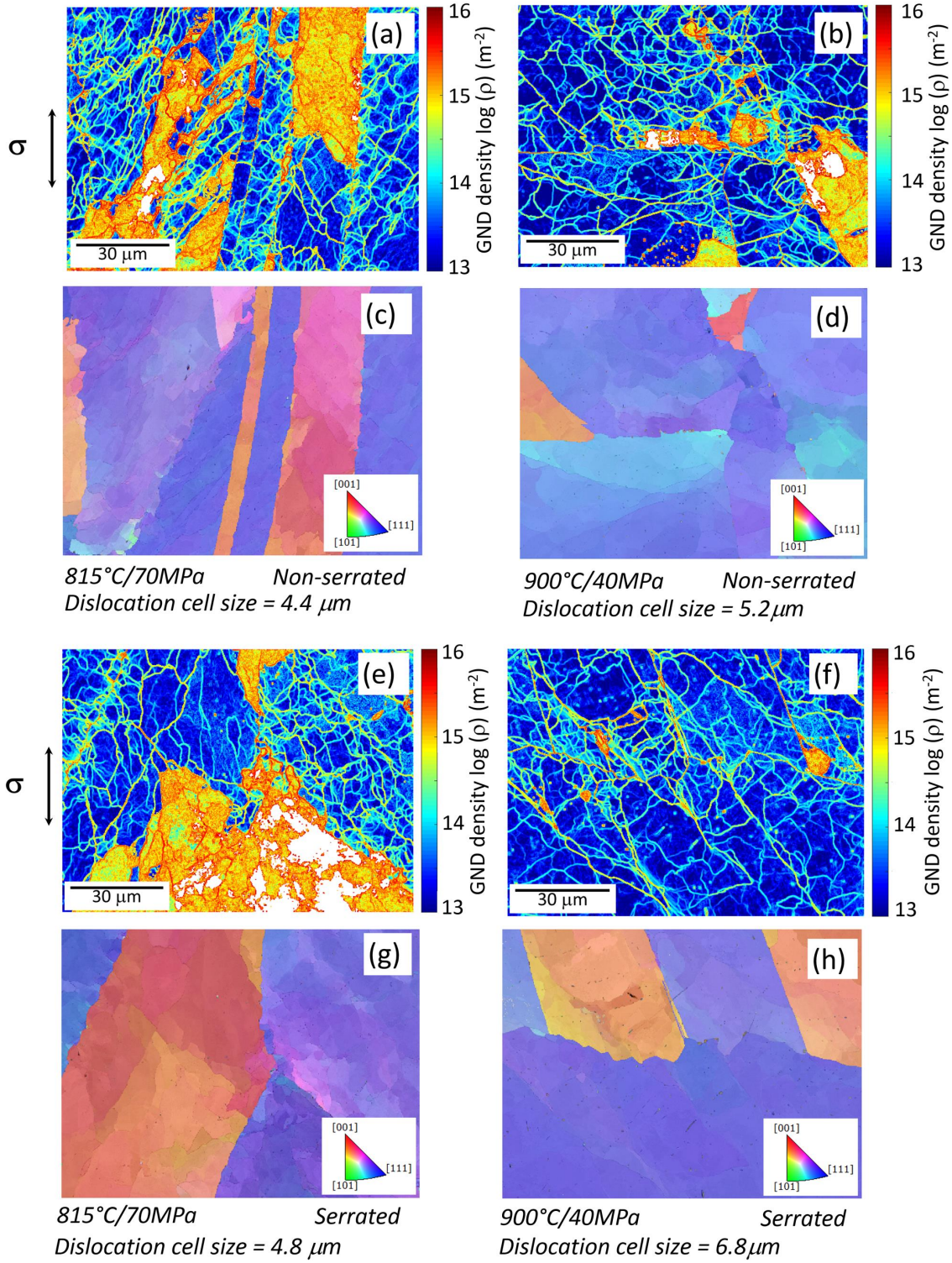


Fig. 5.13 (a), (b), (e) & (f) displayed GND density maps obtained from 815°C/70MPa and 900°C/40MPa for both materials, along with the inverse pole figure map corresponding to Y-axis, see (c), (d), (g) & (h). Dislocation sub-structures are clearly revealed in each map. Cell sizes increase with stress level. In particular, non-serrated specimens display smaller cell size than serrated ones in both condition.

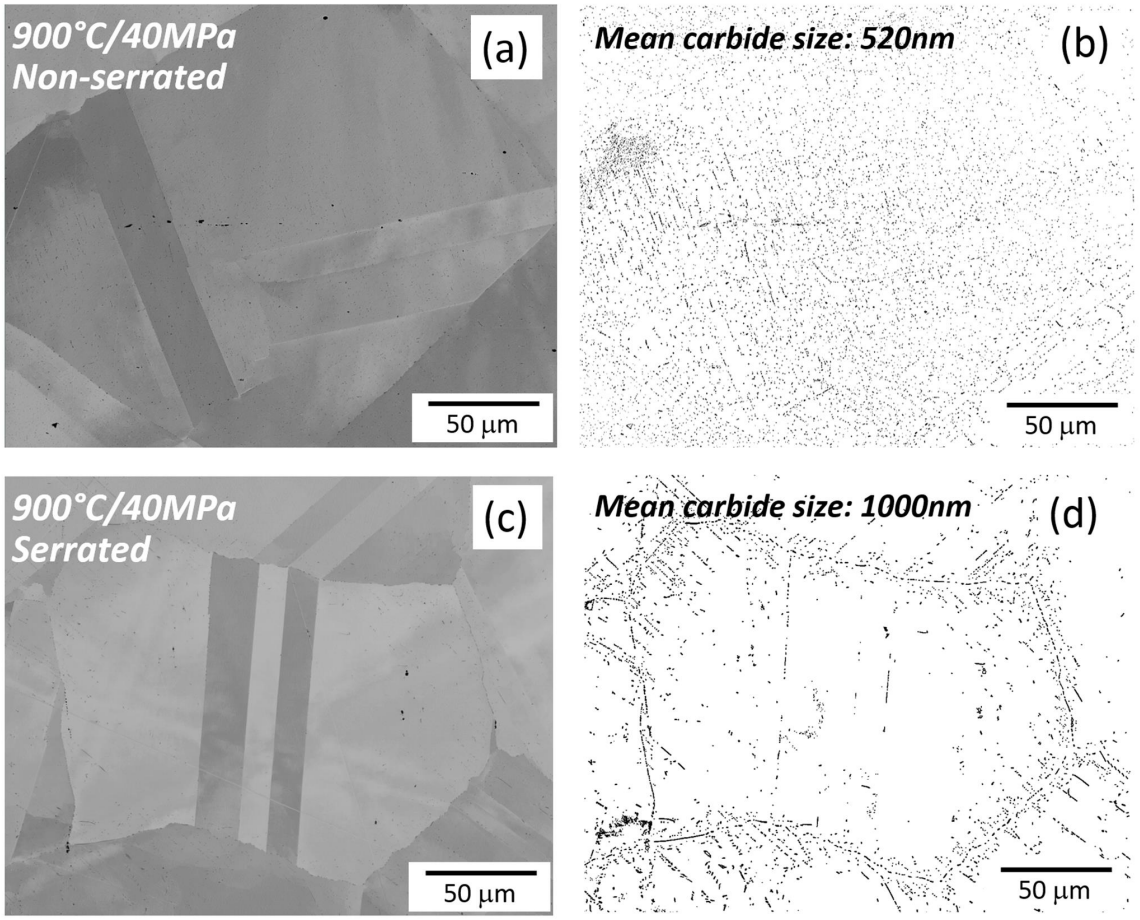


Fig. 5.14 Carbide distribution within grain interior and in vicinity of grain boundaries. ImageJ has been utilized for outlining carbides. (a) and (c) are the back-scattered image of the non-serrated and serrated material from creep tests interrupted at 5% strain. (b) and (d) are the graphs with outlined carbides. Carbides are fine and evenly distributed in non-serrated grain boundary material. By contrast, carbides are coarser and elongated in serrated material, predominantly distributed near grain boundary region with specific orientations.

Fig. 5.15 Serrated grain boundary sample interrupted by 5% creep strain at (a) 815°C/70MPa and (c) 900°C/40MPa. Carbides are outlined in (b) and (d) where it demonstrated preferred growth orientations. Unit cell orientations were extracted from EBSD data and stitched next to each grain. $\{1\ 1\ 0\}$ directions on $\langle 1\ 1\ 1 \rangle$ planes are labeled with yellow arrows. These directions are parallel to the carbides. It suggests carbide growth is facilitated by mass transport on slip systems.

More micro-mechanical strain analysis adopting HR-EBSD was also performed for the interrupted tests. At the lowest test temperature of 700°C there were quite obvious differences between GND density distributions for the two microstructures, as shown in Figure 5.16. For the non-serrated case there are some linear bands of raised GND density that are aligned with the {1 1 1} slip plane traces in each grain but there is little evidence of higher GND density near the grain boundaries suggesting slip transfer was relatively easy. In contrast, for the serrated case there is prominent accumulation of raised GND density near the grain boundaries. Alignment of raised GND density regions into straight linear features is less marked and there is evidence of dislocation cell formation near the grain boundaries. This suggests a more difficult slip transfer process for the serrated grain boundaries.

However, the linear features are suppressed for both microstructures at 815°C as a reflection of mechanistic change in deformation, see Figure 5.17. For the non-serrated case there is raised GND density and dislocation cell formation near the triple junctions, and to a lesser extent where twin boundaries intersect with high angle grain boundaries. For the serrated case, higher GND density are associated in the vicinity of high angle grain boundaries (not twins) and reasonably evenly distributed.

The GND maps between the two grain boundary morphologies appeared more distinctive distributions at the highest test temperatures at 900°C. For example, the accumulation of GND density near grain boundaries is less marked. There is little evidence of GND density accumulation near the triple junction toward the centre of the map for the non-serrated case, though the density is increased near the intersection

of a twin boundary with a general high angle grain boundary. Accumulation of raised GND density around the intragranular carbides is evident, and it is most obvious for the serrated case where the carbides are larger and aligned along slip bands.

5.3.6 X-ray tomography technique

As illustrated by Figure 5.7 and Figure 5.8, marked cavitation damage is observed. For characterising this in greater detail for each condition and microstructure, the X-ray tomography technique was employed. 3D reconstructed surfaces of each fracture tip showing cavitation (labeled red) distributions across the specimen are displayed in Figure 6.9 (a-c) for non-serrated and (d-f) for serrated microstructures. Figure 5.20 has shown the number density of cavitation versus distance from fracture tip. In general, cavities are at higher density and coarser near the fracture tip, and the damage declines slightly over distance from its fracture surface. To describe the damage caused by cavitation quantitatively, two metrics are considered here: cavitation frequency and total volume of cavitation. Cavitation frequency – contributed predominantly by small cavities – increased dramatically from 700 - 900°C, *i.e.* from 714 to 3813 counts for non-serrated and from 46 to 6194 counts for serrated. Another metric using cavitation volume, however, accounts contributions by larger cavities. This is considered to be a better metric of accumulated damage because the large-volume cavitation is governing the failure as they grew by small-crack coalescence. The total cavitation volume implies the degree of porosity in the material, which is linked to the gauge area reduction and ultimately an increase in true stress. For the avoidance of doubt, the technique is

limited by its spatial resolution — the voxel size is just under 5 μm — cavities less than 10 μm cannot be detected. This means early cavity nucleation and development are neglected, which requires the SEM to conduct study on the interrupted tests. Fracture mechanism, however, can be derived according to the XCT method, as the cavitation of enormous sizes are responsible to the failure, and are very well characterised in this way.

Fig. 5.16 GND density maps of interrupted specimens of (a) non-serrated and (b) serrated specimens at 700°C/170MPa, together with inverse pole figure and Schmid factor map, which it shows the locations of grains. GND density were highest at triple junction and twin-grain boundary intersections in the non-serrated specimen, in constrast, GND density were highest near entire grain boundary region where carbides located.

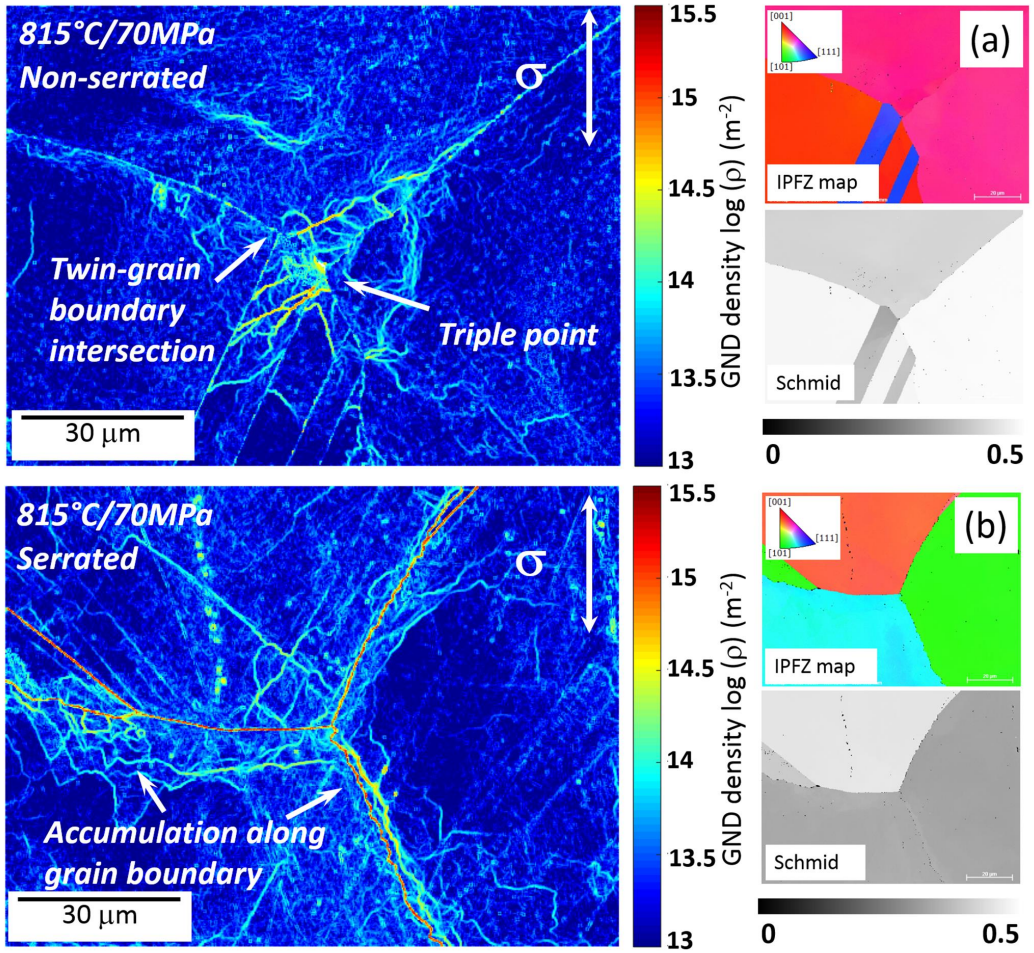


Fig. 5.17 GND density maps of interrupted specimens of (a) non-serrated and (b) serrated specimens at 815°C/70MPa, together with inverse pole figure and Schmid factor map, which it shows the locations of grains. GND density are accumulated near grain boundary in serrated sample, whereas slip transfer seems to be fairly easy for non-serrated specimen.

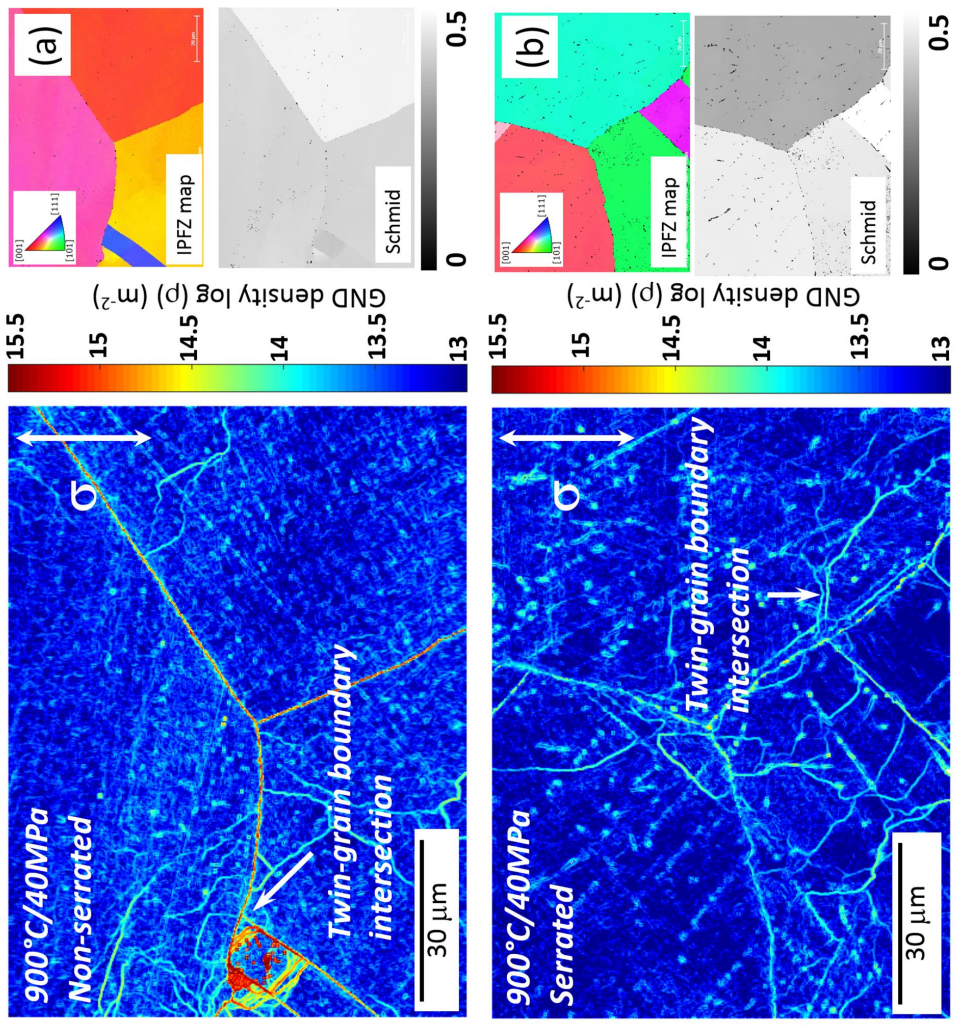


Fig. 5.18 GND density maps of interrupted specimens of (a) non-serrated and (b) serrated specimens at 900°C/40MPa, together with inverse pole figure and schmid factor map. Dislocation cell structures started to grow. GND density were again accumulated at twin-grain boundary intersection for non-serrated specimen. Serrated specimen shows only higher GND density near carbides.

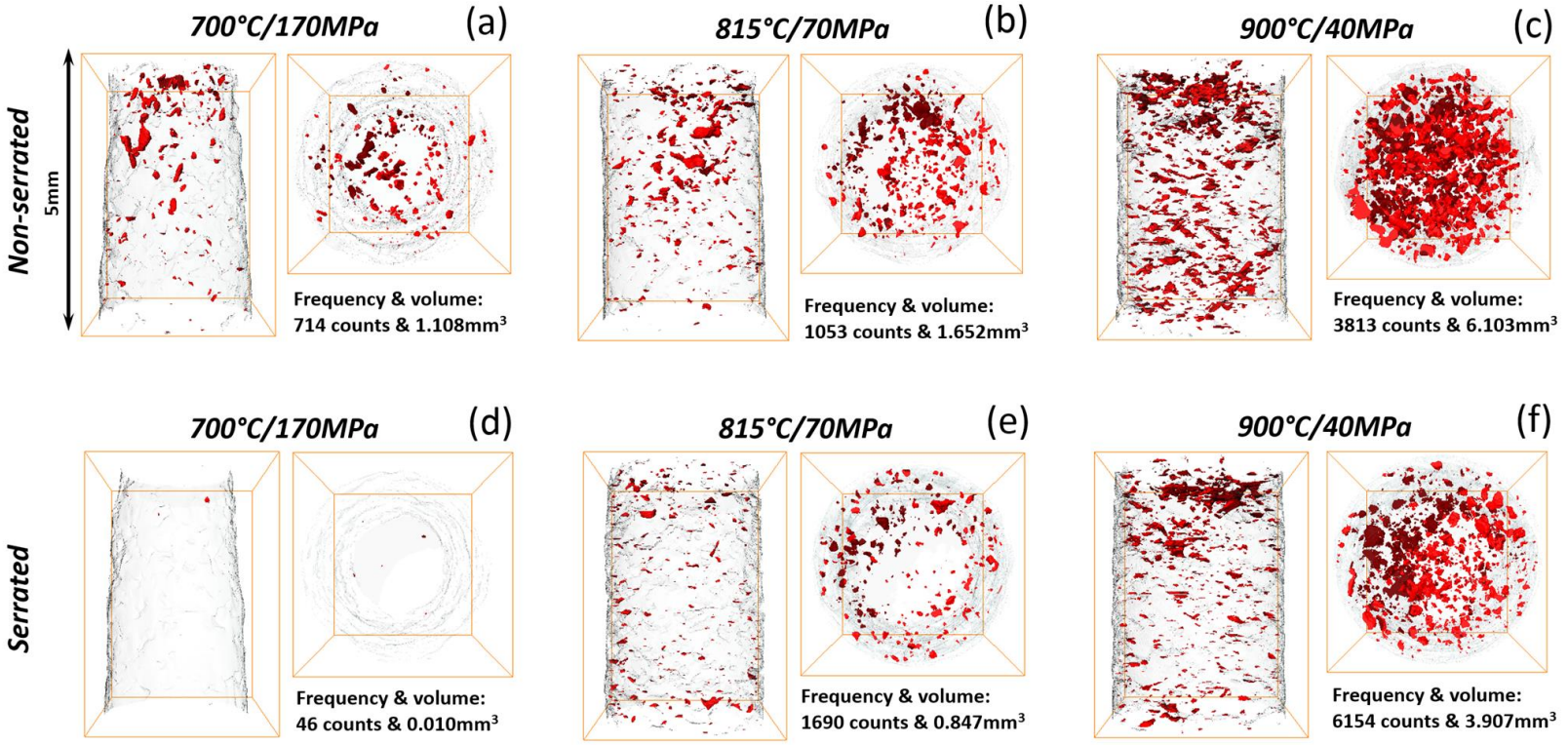


Fig. 5.19 3D reconstruction of fractured creep specimens from side and top views showing cavitation distribution, where red represents cavities. Two metrics were used for damage assessment, cavitation counts (frequency) and volume, which are labeled next to each specimen. (a-c) displayed non-serrated samples and (d-f) for serrated ones. In higher temperature and lower stress regime, cavitation content is increased. Serration has strong resistance in cavitation propagation, as demonstrated with reduced cavitation volume by inhibiting coalescence of small cracks.

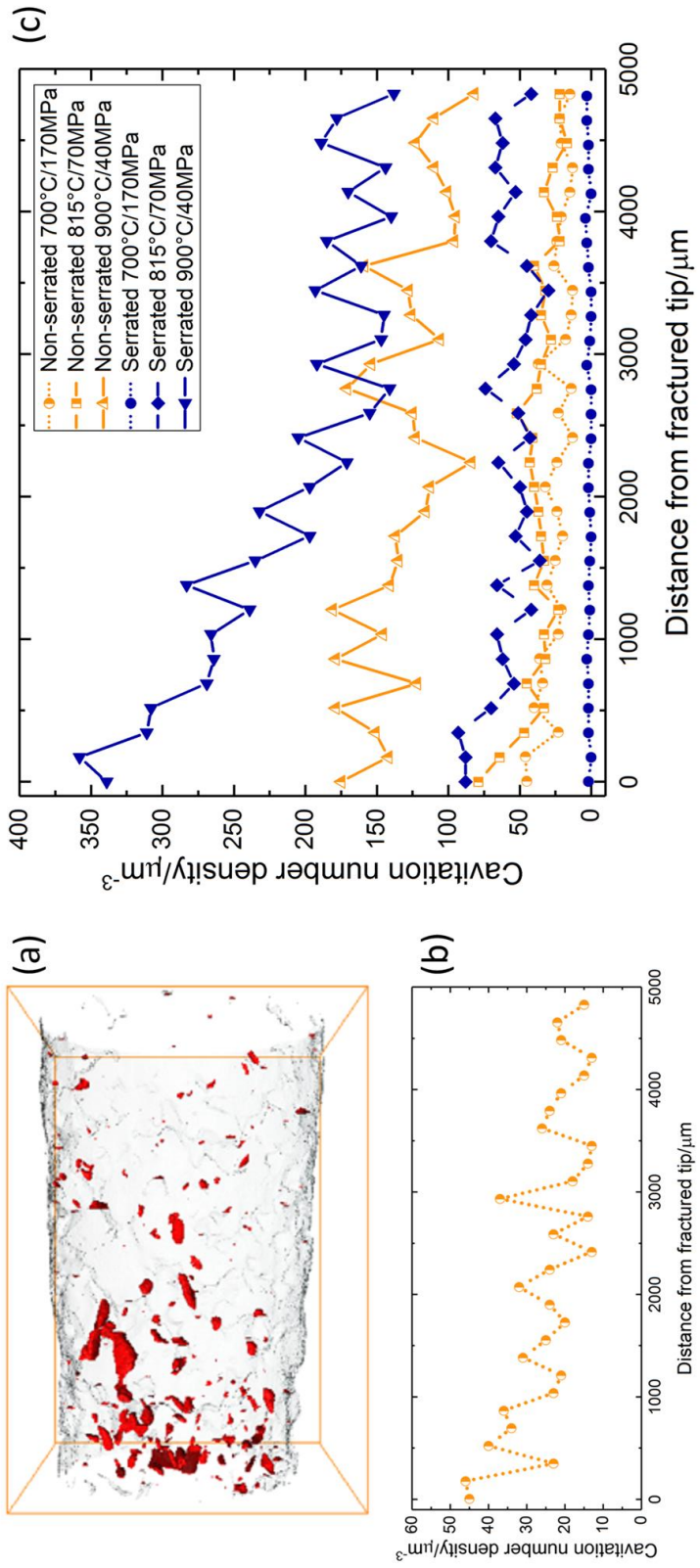


Fig. 5.20 Cavitation number density versus distance from the fracture tip. (a) and (b) represents a specific example of such a fracture tip and its cavitation profile over distance. (c) represents cavitation profile over distance for both microstructures at all creep conditions.

5.4 Discussion

Two distinctive grain boundary morphologies, *i.e.* serrated and non-serrated were developed by different heat treatment parameters, as well as maintaining other features in the microsturcture stayed unchanged. This enabled charaterisation of grain boundary serration impact on mechanical properties isolated from other secondary changes induced by heat treatment. In summary, the results clearly demonstrate 3 key findings. First, for both microstructures, a transition from transgranular to intergranular fracture was observed with increasing temperature and decreasing stress. This transition was offset to higher temperatures by grain boundary serration. Second, grain boundary serration has demonstrated great impact on creep properties in Inconel 600, in particular, it promotes enhancement in creep rupture life at high temperatures. However, at the lowest test temperature, no measurable difference was found. Third, the carbide distribution evolves significantly during creep testing and is distinctively different in the two microstructures. The differences in carbide distributions affect the movement and accumulation of dislocations during creep. Each of these aspects are discussed in detail in the following sessions.

5.4.1 Carbide distribution and its evolution

Two distinct carbide distributions were observed for different microstructure at the interrupted conditions. As illustrated in Figure 5.14, fine carbides are distributed in the non-serrated case homogenously, however, coarse carbides are distributed heteroge-

neously in the serrated case. This is a phenomenon caused by a combination of the heat treatment and subsequent creep deformation. In the conventional quenched non-serrated case, carbon atoms are relatively uniformly dispersed, so a uniform dispersion of carbides during thermal exposure in testing was obtained. The non-conventional slow cooling leads to strong segregation of carbon atoms to grain boundaries and triggered grain boundary serration with intergranular carbides. In addition, the carbides in serrated samples are seen to grow in a preferred crystallographic orientation. This is verified using diffraction patterns obtained by EBSD. Figure 5.15 demonstrated that carbide growth direction is aligned with the {1 1 1} slip planes. Investigation of the carbide distribution in the serrated case was carried out in all test conditions. SEM image intensities were used to segment carbide particles and their centre of mass were recorded relative to the position of the grain boundary. The number density of carbides as a function of distance from the ground boundary was averaged over 3 representative boundaries and are shown in Figure 5.21. No carbides were observed at 700°C, but carbides were frequently observed at higher test temperatures. The width of the carbide region is more spread out at greater temperature, around 35 μm at 815°C and 85 μm at 900°C, which is deduced that the intergranular carbides were decomposed and dispersed in the vicinity of grain boundaries.

Interestingly, the aforementioned carbide distribution has offered an explanation to the creep behaviour: the non-serrated samples possess lower minimum creep rate at the initial stage of creep, despite their lower final creep life, as shown in the magnified images were shown in Figure 5.5. From the investigation on carbide distribution at interrupted

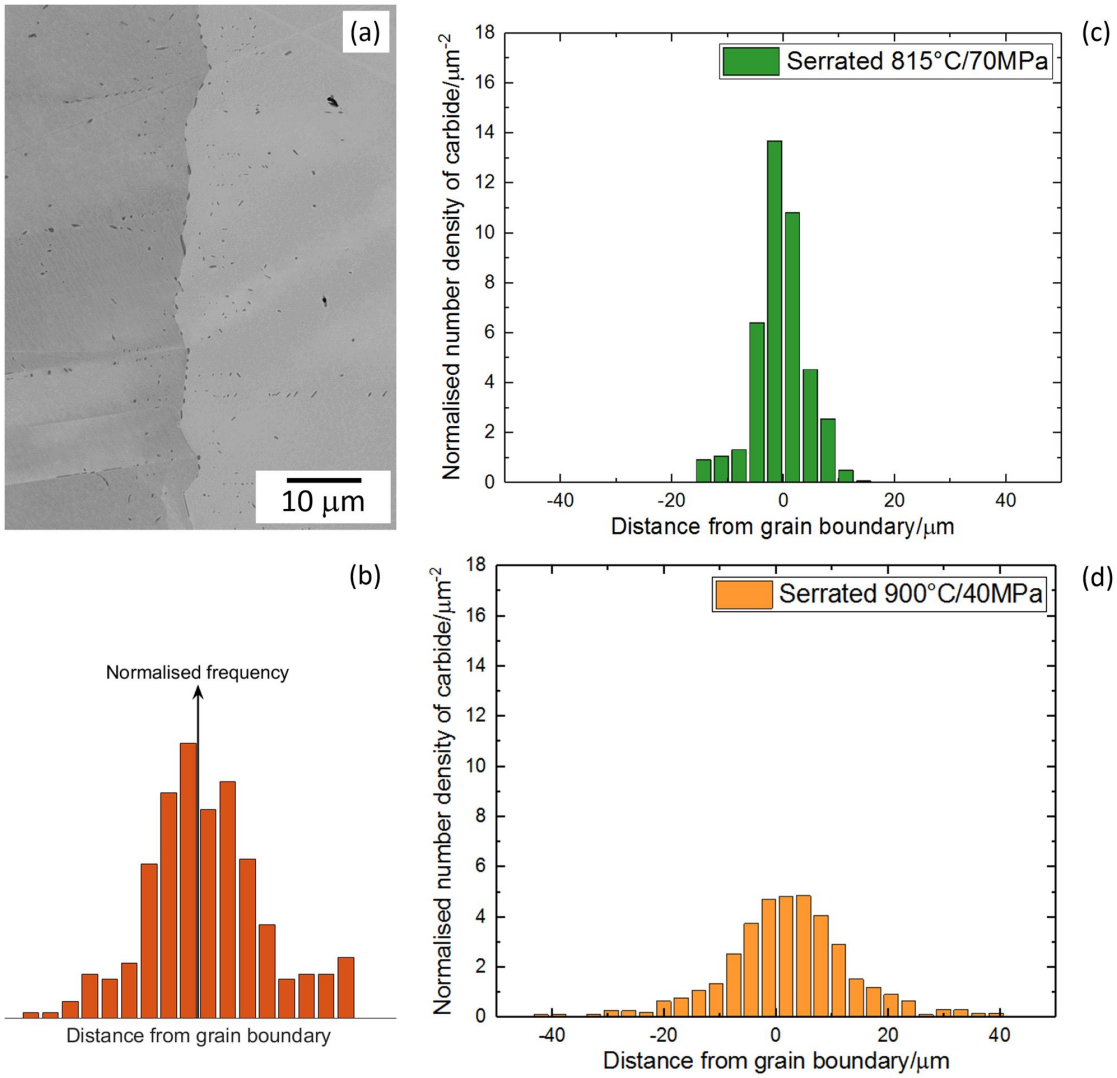


Fig. 5.21 Carbide distribution in relation to distance from grain boundary in the serrated case. (a) and (b) represent a specific example of a grain boundary used for analysis taken from interrupted specimen tested at 900°C/40MPa. Its number density frequency versus distance is represented in (b). Accumulated carbide distribution measured for many grain boundaries for 815°C and 900°C are exhibited in (c) and (d).

conditions, this is believed contributed by *in-situ* precipitation of smaller and higher density of intragranular type carbides that provided precipitation strengthening. On the contrary, much of carbon in serrated samples was consumed via precipitation of grain boundary carbides and less intragranular carbides were able to form. It is also interesting to note the co-existence of grain boundary precipitates and serration is always the case at the present study, which agrees well with findings in literature. The phenomenon of serration is de facto always associated with some type of grain boundary precipitates. As thoroughly studied in Chapter 4, the carbide is essential and responsible for the formation of serrations. Therefore, to explicitly evaluate the effect of grain boundary serration and precipitates that formed in correspondence is not feasible. Admittedly, the co-existence of precipitate/serration may not always be beneficial, as the final properties might be sacrificed by losing some intragranular strength.

Two proposed mechanisms were hypothesized to facilitate the carbide formation near grain boundaries. The first one is due to faster diffusion path (pipe diffusion) where the nucleation sites are provided by dislocations. Another possible mechanism may be mass transport by dislocation climb, analogous to γ' phase rafting [196], when a gliding dislocation being trapped by an intergranular carbide in the first grain, it climbs at matrix/carbide interfaces and eventually escapes. The latter is believed to be dominating during the process, because with decreasing stress, slip bands are less pronounced from 170MPa to 40MPa, as is the number of nucleation sites. In contrast,

slip transfer may be easier at higher temperatures, due to a thermally activated climb mechanism as an alternative way of passing despite the pinning carbides.

5.4.2 Dislocation accumulation

Enormous amount of strain and deformation were stored during creep testing, hence it is not at all surprising to observe induced dislocation cell structures. Average cell sizes were smaller for the higher stress/lower temperature tests, and were consistently slightly smaller for the serrated microstructure. For the tests interrupted at 5% strain the dislocation cell structures had not yet formed fully, but there are signs of this beginning preferentially in regions close to grain boundaries and triple junctions. At 700°C, the GND density is more localised around grain boundary regions with the serrated architecture, which suggests a role of carbides in preventing slip transfer. At 815°C, for non-serrated samples the intersections between three grain boundaries or twin-grain boundaries, were shown to be associated with high GND density. In contrast the serrated samples, showed no particular dislocation accumulation in such grain intersections, instead, it shows entangling GND with coarse carbides near the whole grain boundary region. At 900°C, such intersections were more pronounced where twin boundary and grain boundary intersects. Nonetheless, serrated grain boundary samples are always free from GND accumulations at twin-grain boundary intersections. More GND maps at similar regions (triple junction and twin-grain boundary intersections) further support the phenomenon — GND accumulation at

twin-grain boundary intersections for non-serrated microstructure, but not the serrated case.

Moreover, the Schmid factor maps displayed next to each GND density map further supports the observation. In Figure 5.16 - 5.18 lighter grains are the ones possessing higher magnitude of Schmid factors, and hence are more prone to slip. For non-serrated grain boundaries case at 815°C, the high GND density was localised at regions where with notable Schmid factor difference were found, *i.e.* the triple junction in this case. This is understandble due to the incompatibility of plasticity of different grains. However, despite the difference in the serrated case, GND density localisation seems mostly independent of Schmid factor values. It is again more pronounced at 900°C conditions, where the twin-grain boundary intersection region in the non-serrated case share a similar value of schmid factor, but despite this shows a severe GND density concentration. In contrast, the twin-grain boundary intersection shows more difference in schmid values but was found to have a negligible accumulation of GND densities. The high GND density intersections of this kind in non-serrated microstructures are believed to act as dislocation sources during creep, and possibly cavitation initiation locations. Therefore, further SEM study was conducted near twin-grain boundary intersections in both microstructures. As verified by a number of different locations, triple junctions and twin-grain boundary intersections were confirmed to be prone to cavitation in the non-serrated case. As shown in Figure 5.22, small cracks were frequently found to be associated with those intersections – either twin-grain boundary intersection or triple junctions. However, no such cracks/voids were observed in any

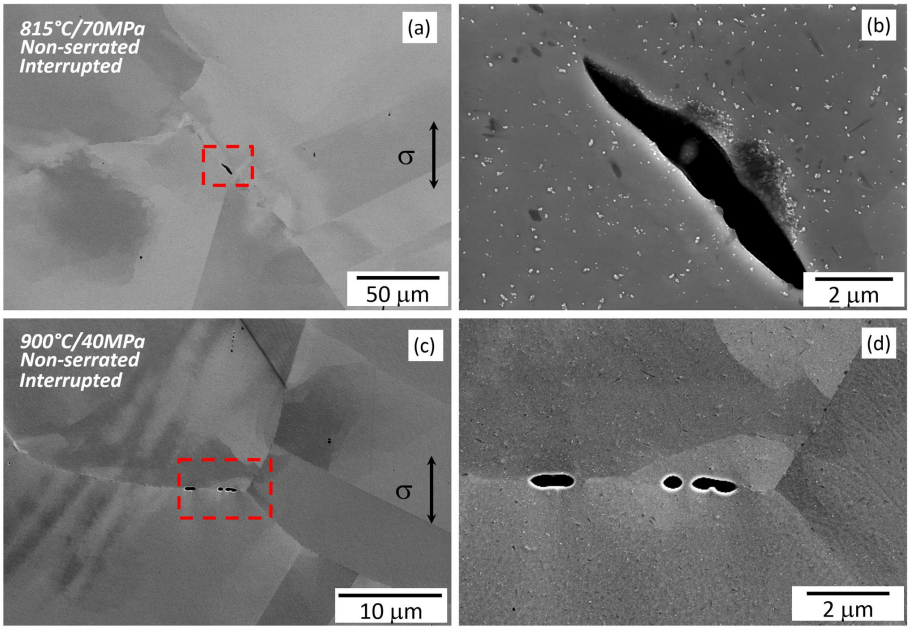


Fig. 5.22 Typical cavities observed in non-serrated material during interrupted creep test at (a) & (b) 815°C/70MPa and (c) & (d) 900°C/40MPa, at different magnifications. It shows that triple junction and twin-grain boundary intersections are the nucleation points of cavities.

interrupted tests on serrated grain boundary architectures, in agreement with the HR-EBSD results. In summary, cavitation initiations are more prone in the non-serrated grain boundary cases, especially in the vicinity of twin-grain boundary intersections.

The tendency of strain concentration build up near twin-grain boundary intersection has been reported by Carter *et al* using a Digital Image Correlation (DIC) approach [157]. The reason why serrated grain boundaries do not suffer from strain accumulation probably relates to coarse carbides near and on grain boundaries. See for example Figure 5.18, where dislocation loops were identified where the carbides are located. This suggests the Orowan-looping and related mechanisms are operative where coarser carbides are more easily bowed around and circumvented.

5.4.3 Assessment of degree of cavitation

In-situ testing at 700°C revealed frequent cavitation events, both in non-serrated and serrated grain boundary samples. The number of cracks that developed during deformation along grain boundaries until 40% strain was counted directly from the SEM images, as illustrated in Figure 5.23. The cavities were labeled by red and green circles on top of initial microsturcture (undeformed), number of grain boundary cavitation sites were shown at 20 & 40% strain. It is clear that non-serrated grain boundary is more susceptible to cavitation than the serrated case, as shown by 22 and 124 cracks as opposed to 1 and 36 cracks at different strain levels. Indeed, grain boundary serration has improved the resistance against grain boundary failure, which is suggested as the reason for enhanced elongation.

Postmortem analysis using SEM has suggests new mechanisms on twin boundary fractures with serration introduced. As demonstrated in Figure 5.24, fractured *in-situ* specimens of both microstructures are displayed with two highlighted regions. The EBSD maps that were taken prior to *in-situ* tests identified twin boundaries as labeled in (b), (c), (e) and (f). It is shown that twin boundaries remained together (though heavily deformed) within the grain in (b) and initiated some cracking (c), However, the twin boundaries cracked severely in the serrated case, see (e) and (f). This is interesting because twin boundaries are usually considered as more stable structures compared to random high angle boundaries. They have been frequently shown resistant to grain boundary sliding, cavitation and fracture [197, 198]. Nevertheless, the frequent fracture of twin boundaries in the serrated case implied toughened grain boundary due

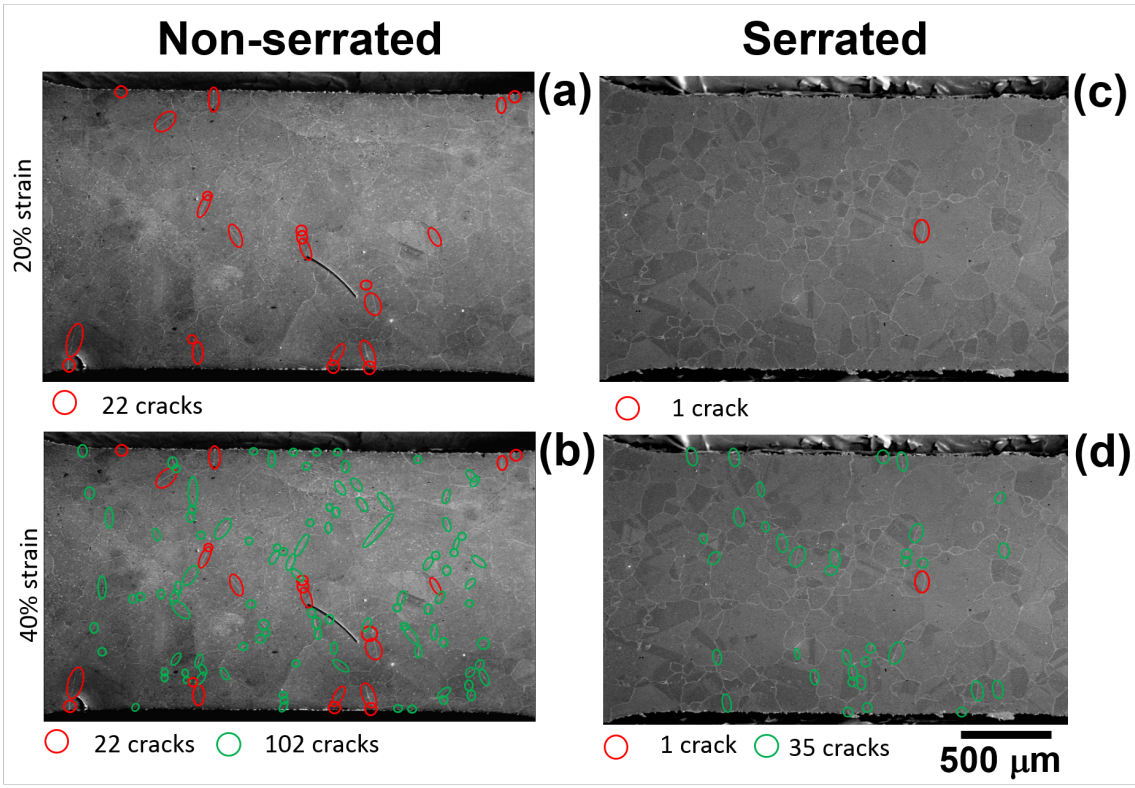


Fig. 5.23 Cavitation counted for non-serrated and serrated case at two strains (20 and 40%) labeled by red and green circles respectively. The circles are drawn on top of initial microstructure for clarity.

to the presence of serration — as the high angle random boundaries are less likely to fracture, some twin boundaries were opened up for accommodating the deformation.

The quantitative cavitation assessment using XCT on crept specimens are discussed now. In terms of total cavitation volume, for non-serrated grain boundary specimens, the extent measured is always remarkably higher – almost twice that in the serrated ones – more damage due to cavitation is expected. Furthermore, an interesting point is that serrated specimens are more frequently shown in 815 - 900°C conditions – 1690 and 6154 counts (serrated) compared to 1053 and 3813 counts (non-serrated) – which is primarily contributed by the small size cavities. This is believed mostly contributed

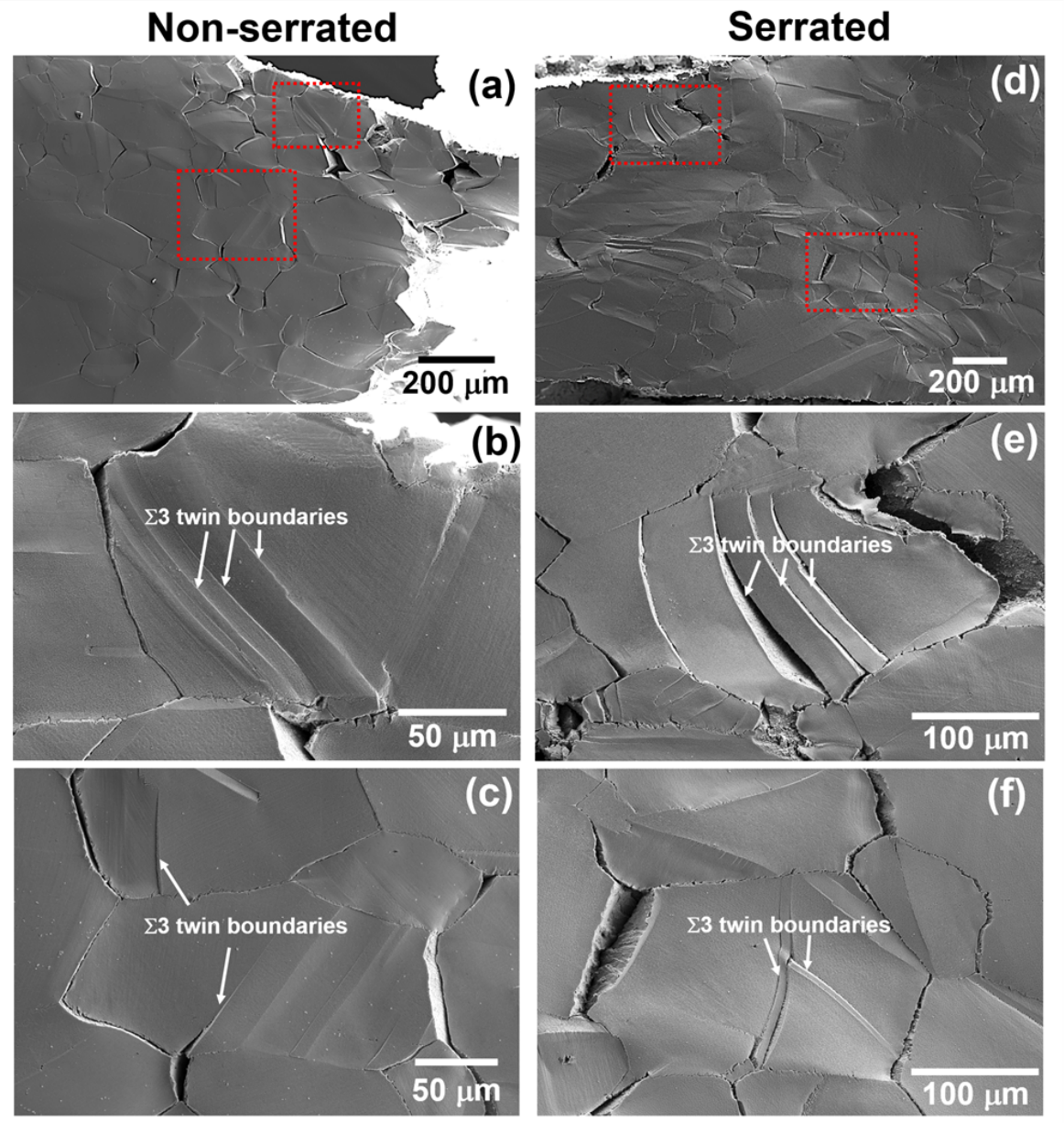


Fig. 5.24 Postmortem analysis on fracture surfaces of *in-situ* specimens and two regions with higher magnifications.

by increased actual grain boundary length due to the nature of serration that provided more cavity nucleation sites. In summary, serrated specimens have more but smaller cavities, whereas non-serrated ones have fewer but larger ones. Moreover, the size and frequency in both microstructures reflects a relation of direct proportionality over significant variations in temperatures and stresses, see Figure 5.25. The cavitation volume is plotted against frequency, so the slope represents average cavity volume is consistent in all conditions, $1.6 \times 10^{-3}\,\mathrm{mm}^3$ and $6.5 \times 10^{-4}\,\mathrm{mm}^3$ for non-serrated and serrated respectively. It is then deduced that the average size of cavitation is independent of the creep conditions, but a function of grain boundary morphologies. A further point to be made here is that the growth behavior is significantly depressed due to serration. Rupture life and ductility improvements are gained by inhibiting cavity link-ups. To author's best knowledge, the present work on quantitative cavitation assessment is the first on understanding the influence of grain boundary serration.

The argument above on cavitation volume and corresponding damage is further supported by the dislocation cell structures that developed at 815 and 900°C. The cell sizes are known to be inversely related to the stress that specimen experiences; therefore, an increase in cell size reflects lower stress applied, which is consistent in both microstructures. Now, we consider the cases in serrated and non-serrated morphologies, while in the same condition, the serrated microstructure always has a larger cell size than the non-serrated cases. The difference in true stress is considered here. The X-ray computed tomography makes it clear that all the samples exhibit considerable porosity. This means the more cavitation damage a material is experiencing, the higher the

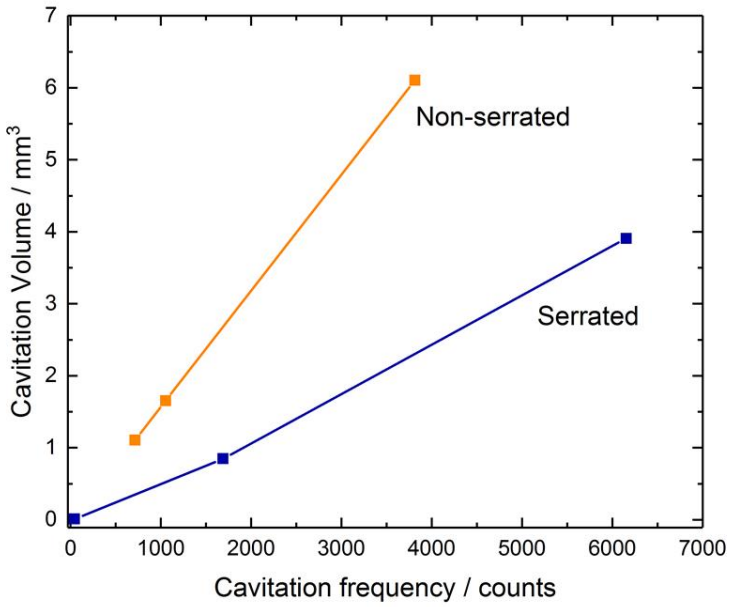


Fig. 5.25 Cavitation volume against frequency for both grain boundary morphology materials. The cavity volume and frequency are directly proportional, and the slope represents the average cavitation volume within each microstructure. The cavity volume is independent of creep conditions but a function of microstructures.

true stress that is experiencing due to a reduction in the load carrying cross-section. Since the bigger cavitation volume that non-serrated microstructure possesses, one can deduce that the true stresses will increase in correspondent to the constant load. As a result, the creep rate accelerates faster than the serrated case.

Frost & Ashby completed a fundamental and comprehensive study on nichrome(Ni-18Cr wt%) [199, 200], a very similar alloy, on the fracture and deformation mechanisms. This is used to rationalise the fracture mode in the present material. The fracture mode determined at 700°C/170MPa is a mixture of transgranular and intergranular consistent with the power law regime. At the 815 - 900°C conditions, the deformation is still power-law controlled but fracture is largely intergranular. This is in agreement

with current observations made by fractography. However, the serrated microstructure always exhibits more transgranular features than the non-serrated case at lower test temperatures, particularly at 815°C. The observation suggests a higher transition temperature is caused by serration due to cavitation resistance. It is well understood in literature, and also verified in the present creep tests, that cavitation limits ductility significantly. Despite some intergranular features are determined to be active during creep, impact of cavitation is limited at 700°C, (the most effective damaging mechanism were contributed by plasticity), understandably due to the significant creep strain. Twelve slip systems could be active regardless of grain boundary morphology, hence no marked change in creep life was observed. Consequently, with decreasing stress and increasing temperature, cavitation damage becomes increasing crucial as fracture mode is switching to intergranular dominant regime. To summarise, in the current study, grain boundary serration has been proven to enhance intergranular cracking resistance, both by stagnation of cavitation nucleation and its subsequent growth. Neither beneficial nor detrimental effects were observed related to serration for transgranular dominate creep or room temperature tensile test. High temperature tensile at 700°C indicated improved elongation but with decreased tensile strength as a sacrifice.

5.5 Summary and Conclusions

The following specific conclusions can be drawn from this work.

1. In alloy Inconel 600, the degree of grain boundary serration is shown to be sensitive to the details of heat treatment and in particular the rate of cooling past the carbide solvus temperature; by varying this, significant differences in the degree of serration arise. Hence, it proved possible to develop microstructures of different degrees of serration but of otherwise identical microstructure: grain size and twin boundary fraction.

2. The creep response of serrated and non-serrated microstructures were assessed. A transition in deformation mode from mainly transgranular at 700°C/170MPa to intergranular cracking at 900°C/40MPa was observed, when the creep ductility was much reduced in comparison. Rupture lives were enhanced by serrated grain boundaries in the high temperature/low stress regime.

3. At 815°C/70MPa and 900°C/40MPa, serrations improved the creep life by about 40%; however, no marked improvement was observed at 700°C/170MPa. Thus serrated grain boundaries conferred no beneficial effects when transgranular-type deformation is dominating, but were more effective for intergranular type fractures.

4. For the 815°C/70MPa and 900°C/40MPa conditions, twin-grain boundary intersections have been shown – consistent with their high GND densities – to be initiation points for dislocation sources and cavitation. Serrated grain boundaries do not suffer as much from this effect and appear to present greater resistance to cavity formation.

5. Cavitation damage becomes more severe with increasing temperature. At the higher temperature conditions employed, serrated samples produce a large number of small cavities but small cavitation volumes overall; non-serrated samples produce larger cavities and bigger cavitation volumes in total. Thus, the growth of cavities is greatly depressed by serration.

6. Cavitation size in Inconel 600 is sensitive to microstructure; its volume and frequency are directly proportional regardless to the creep conditions, for both non-serrated and serrated grain boundary materials. However, average cavitation volume that can be obtained – determined by the slope of this relation – is related to grain boundary morphology.

7. Sub-grain boundary cell dislocation structures were characterised and measured using cross-correlation method based HR-EBSD. The cells were larger for serrated rather than non-serrated samples at the same creep condition. Cavitation had an impact on cell sizes by increasing porosity, which eventually increased the true stress thus accelerating the creep rate.

8. The current study has confirmed life enhancement in time-dependent intergranular deformation on the account of grain boundary serration. The knowledge generated is believed to be transferable to a wide class of engineering alloys that are being used nowadays; with simple alteration in heat treatment, the properties of an alloy can be re-engineered.

Chapter 6

A Rationalisation of Creep Response of a Nickel Based Superalloy for Power Generation Applications

6.1 Introduction and background

Creep — inelastic time-dependent deformation — must be resisted in structures and thus prevented by design. It can cause failure: creep fracture, defect formation, stress relaxation or else excessive deflection [18, 17, 201]. It is an important mechanical response in many high temperature applications such as those involving jet propulsion and power generation [83, 28, 202, 95, 203, 204, 168], for example.

Typically, the risk of creep deformation is assessed by uniaxial isothermal tensile tests of cylindrical geometry, often with the temperature controlled accurately – a temperature change of only 30°C can be sufficient to change the creep rate by a factor of six [205]. For practical reasons, the test piece is often of limited dimensions, at least with regard to the structure and the data are needed for. But it is well known to practitioners of the field that creep results are prone to scatter [206–208]; significantly so, when compared for example with testing in the athermal regime at lower temperatures and/or greater strain rates [209, 210]. There are ramifications of this phenomenon. It can be necessary for example to carry out a larger number of tests than is ideal, often at identical conditions. Furthermore, since there is a stochastic element of the response which complements the deterministic one conferred by the effects of temperature or load [211], there is invariably a need for statistical treatments which are usually empirical. Clearly, one should seek a broader appreciation of the factors influencing the scatter in the creep response, if the situation is to be altered.

In this chapter, the creep response of a polycrystalline nickel-based superalloy is considered. It is tested under representative loading conditions; significant scatter in the creep response is displayed. Here, it is demonstrated that the scatter exhibited is largely due to a grain size which is a significant fraction of the diameter of the specimens employed, so that crystallographic anisotropy results [212–215]; moreover, a change in micromechanism of creep deformation from one involving climb-assisted glide to one requiring particle shearing is also needed to rationalise completely the effects observed.

6.2 Methodology and Experimental Description

6.2.1 Material

An equiaxed polycrystalline nickel-based superalloy MGA1400CC was used for the study, the details on the composition, manufacturing and heat treatment are given in Chapter 3. The material is used for rotating parts of the turbine, and the grain size is found to vary across different locations of the blade — as a result of the inhomogeneous heat flow during the solidification of a large component (over one meter in size). Large grains are located at the blade root and small grains are observed at the airfoil. Three grain size variants were selected to evaluate the creep scattering behaviour, which are fine (1.77 mm), medium (3.52 mm) and coarse (6.82 mm).

6.2.2 Creep testing

The material with three microstructural variants were then machined and tested using creep machines. Two sample designs were utilised for assessing creep properties, that include bar-shaped and plate-shaped specimens, as illustrated in Figure 6.1. For evaluating creep scattering behaviour in relation to creep conditions, a significant variation of temperature and stress levels were chosen to trigger different deformation/failure mechanisms. Three representative creep conditions were utilised that satisfied the aforementioned purpose, *i.e.* 700°C/706MPa, 750°C/608MPa and 870°C/343MPa. Repeat tests were also completed at least six times per grain size and per creep condition. In total, 55 creep tests were completed.

6.2.3 X-ray computed tomography

For gaining understanding in specimen shape change during anisotropic creep testing at various conditions, X-ray computed tomography (XCT) were utilised for 3D reconstruction of fracture tips. Tomography analysis was performed on fracture tips using a North Star Imagix system. The machine was operated at 150 kV and at a current of 27 μA, with a voxel size of 4.9 μm. For each sample, a height of roughly 5 mm was scanned at 30 ms frame rate with 1440 projections. A histogram based method was then used for reconstruction of the 3D volume.

6.2.4 Scanning electron microscopy characterisation

The microstructure before and after the tests were characterised using scanning-based microscopy. Crept specimens were first taken for fractography analysis, and then sectioned by EDM from the middle of fracture tip along the axial direction. A Zeiss Merlin SEM was utilised for revealing phases with a back-scatter electron detector. For resolving secondary and tertiary γ' precipitates, electrolytic etching was then applied using 10% phosphoric acid (H_3PO_4) with 3 volts electricity supply. Chemical analysis on carbides was carried out using energy-dispersive X-ray spectroscopy (EDS). Electron backscatter diffraction (EBSD) maps were acquired using a Zeiss EVO SEM system, where several EBSD images were stitched together to exhibit a large area. The EBSD patterns were stored at 160 $\times$ 120 resolution in a step size of 4.6 μm.

6.2.5 *In-situ* tensile test in SEM

In-situ tensile tests were performed at room temperature under displacement control with a speed of 2 μm s^{-1}, which provides a strain rate, $\dot{\varepsilon}$ of approximately 10^{-3}. A Kammrath-Weiss *In-situ* module was utilised in a Zeiss Evo SEM. Dog bone specimens were machined using EDM that possess a gauge volume of 2 mm length $\times$ 1.5 mm width $\times$ 1 mm thickness. The surfaces were polished using standard metallographic methods. Secondary electron micrographs were taken at 0.5 % increment of engineering strain until failure, capturing deformation evolution. More detailed descriptions on the experimental set up can be found in Chapter 3.

6.2.6 Numerical approach for creep model

A constitutive creep model is constructed to improve understanding of how creep behaviour corresponds to microstructural evolution. The model is modified based on work by Dyson *et al* [216–219], where the instantaneous uniaxial creep rate is expressed as a hyperbolic function of temperature and stress. In addition, the model also considers continuum creep damage mechanics — damage induced by strain and thermal, *i.e.* multiplication of dislocations, coarsening of strengthening particles and grain boundary cavitation, as expressed by damages parameters D_d, D_p and D_c. The instantaneous creep rate can be expressed by

$$\dot{\varepsilon} = \dot{\varepsilon}_0(1 + D_d)\sinh\left[\frac{\sigma(1-H)}{\sigma_0(1-D_p)(1-D_c)}\right]$$

The parameters $\dot{\varepsilon}_0$ and σ_0 are determined by microstructural measurements or physical constants, such as initial dislocation density ρ_i, γ' fraction ϕ_p, mean Taylor factor $\overline{M}$, jog density c_j, Orowan stress σ_{or}, Shear modulus G, Boltzmann constant k, gas constant R, temperature T, Burger's vector b and combined activation energy for diffusion and jog formation $Q_{d/j}$ in the expressions of

$$\dot{\varepsilon}_0 = 2\,\rho_i\,\phi_p^{1/2}\,\overline{M}^{-1}(1-\phi_p)\left(\left[\frac{\pi}{4}\right]^{1/2} - \phi_p^{1/2}\right) c_j\,D_v = \dot{\varepsilon}_0' \exp\left\{\frac{-Q_{d/j}}{RT}\right\}$$

and

$$\sigma_0 = K_{\mathrm{CF}}(\phi_p)\frac{\sigma_{or}kT}{Gb^3}$$

where D_v is the volume diffusivity, which can be expressed as

$$D_v = D_0 \exp\left\{\frac{-Q_{d/j}}{RT}\right\}$$

and the constraint factor K_{CF} is a function of γ' fraction:

$$K_{\mathrm{CF}} = 1 + 2\phi_p^{1/3}/3\sqrt{3\pi}(1-\phi_p^{1/3})$$

The evolution of back stress is given as a differential equation in the form of

$$\dot{H} = \frac{h'}{\sigma}\left(1 - \frac{H}{H^*}\right)\dot{\varepsilon}$$

Parameter h' equals $E\phi_p$, where E is Young's Modulus, σ is the applied stress, and H^* is given as $\frac{2\phi_p}{(1+2\phi_p)}$. Other parameters such as D_d, D_p and D_c are damage parameters that evolute with time, they are for increased dislocation density, particle coarsening and grain boundary cavitation respectively. Thus

$$\dot{D}_d = C\dot{\varepsilon}$$

$$\dot{D}_p = \frac{K_p}{3}(1-D_p)^4$$

$$\dot{D}_c = \frac{k_c}{\varepsilon_f}\dot{\varepsilon}$$

where C, K_p and K_c are kinetics and geometrical constants.

Effect of γ' size on the creep rate is also considered in the study. Bhowal *et al* [127] found the minimum creep rate is strongly correlated to the square of the inter-particle spacing $\overline{\lambda}$ of γ' precipitates, which is related to average particle size $\overline{r}$ in the function of $\overline{\lambda} = \left((\pi/\phi_p)^{1/2} - 2\right)(2/3)^{1/2}\overline{r}$. The relation is later modelled by Kim *et al* in the form of $\dot{\varepsilon} \propto \overline{\lambda}^2$ [220]. The modified parameter $\dot{\varepsilon}_0$ obtains a new constant C_g and now becomes

$$\dot{\varepsilon}_0 = 2\,\rho_i\,\phi_p^{1/2}\,\overline{M}^{-1}(1-\phi_p)\left(\left[\frac{\pi}{4}\right]^{1/2} - \phi_p^{1/2}\right)c_j\,D_v C_g\left(\frac{\overline{\lambda}}{b}\right)^2$$

6.3 Results

6.3.1 Creep rupture life: influence of grain size and creep conditions

Stress rupture test results are displayed in the Larson-Miller Parameter (LMP) plot as shown in Figure 6.1. It is clear that the trend of creep life scatter is most pronounced at the highest stress level, and becomes less prominent with lower applied stress. The difference of LMP has decreased from 1.24 at 706 MPa to 0.34 at 343 MPa. Detailed rupture life chart in relation to grain size and creep conditions are exhibited in Figure 6.2 (a), where average creep life is quoted for each condition and spanned in two standard deviations. Interestingly, grain size has been demonstrated to vary creep life to a large extent, particularly at 700°C/706MPa, where average creep life for small grain size samples possess a mean life of 338.8 hours as opposed to 86.6 hours for large grain size samples. The same trend has continued with other creep conditions, though the differences are less significant.

The scattering behaviour is further elucidated using percent deviation, which is calculated by one standard deviation divided by the mean value, as illustrated in Figure 6.2 (b). The normalised metric represents how much scattering is obtained for each grain size and condition. For example, despite the fact that that large grain size samples possess shorter creep lives, the level of scattering remained similar at each condition: ∼50 % difference at 700°C/706MPa and ∼14 % difference at 870°C/343MPa. Indeed, creep scattering behaviour has shown a strong dependency

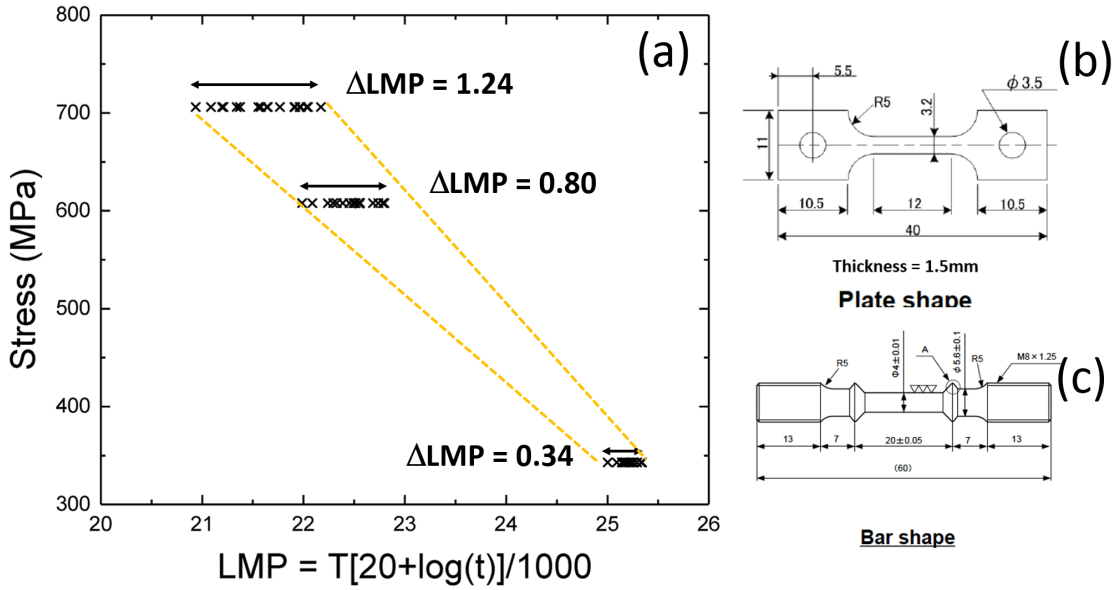


Fig. 6.1 (a): Larson-Miller Parameter of MGA1400CC as a function of stress level. Creep scattering demonstrates a positive correlation with stress level. (b) & (c): two sample geometries used for the test.

according to conditions, as well as the average creep life also being a function of grain size. The dependency is stronger at higher stress level and lower temperature conditions.

6.3.2 Microstructure characterisation: virgin and crept materials

Virgin material: fine & coarse grain size

The microstructures of MC carbide and γ' particles for as heat treated (virgin) material with coarse and fine grain sizes are displayed in Figure 6.3 and Figure 6.4. A distinctive distribution of MC carbide and γ' is observed — MC carbides are larger and more sparsely distributed in the large grain material compared with small grained, as a

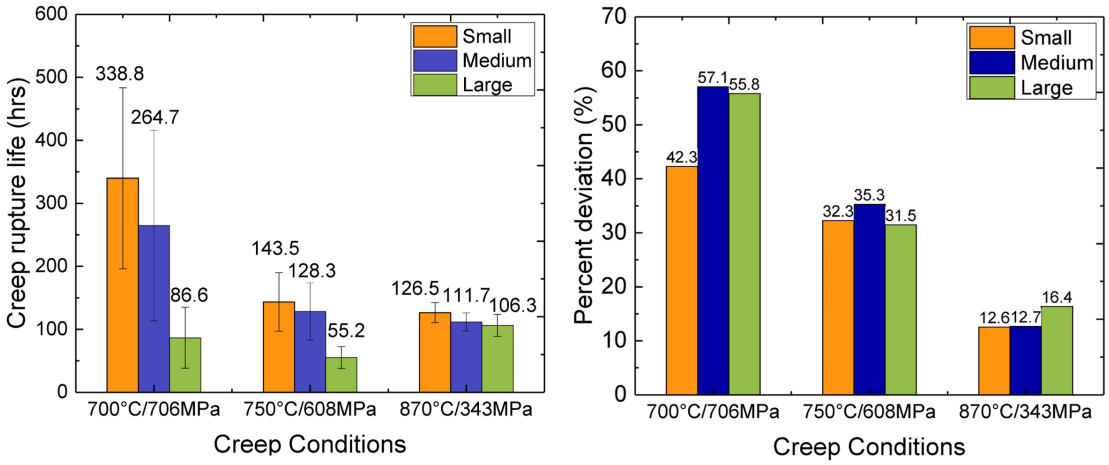


Fig. 6.2 Creep life scattering in relation to grain size and creep conditions. (a) displayed average creep rupture life for three conditions and grain sizes, the error bar represents two standard deviation. (b) percent deviation for three conditions and grain sizes. Percent deviation equals standard deviation divided by average rupture life.

result of dendrite arm spacing difference. The average size measured for coarse and fine MC carbides are 73.1 and 22.7 μm^2 and their area fractions are 1.03 and 1.23 % respectively.

Secondary γ' precipitate size also exhibit larger in the coarse grain, and smaller in the fine grain material. Their size are displayed in Figure 6.4. The average γ' size in the dendrite cores for large and small grains are 860 and 528 nm respectively. Thermodynamic calculations indicated the alloy contains ~55 % of γ' fraction at 700°C by the ThermoCalc software (TTNI8 database).

Chemical anaylsis using EDS were conducted on grain boundaries of materials with the two grain sizes, as shown in Figure 6.5. Both script-like and blocky MC type carbides were revealed maintaining similar elemental distribution, which were enriched in Ta, Ti and W. In addition, some smaller (~1 μm in size) carbides phases were also

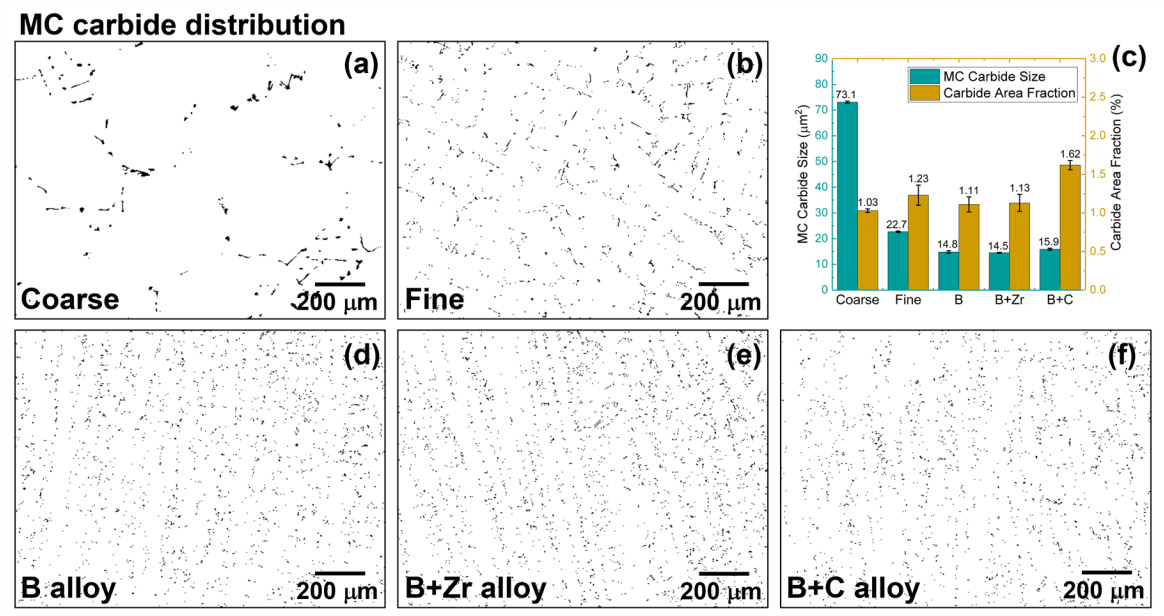


Fig. 6.3 Outline of MC carbide distribution using image processing in coarse grain (a), fine grain (b), B alloy (d), B+Zr alloy (e) and B+C alloy (f). The quantified size and area fraction are displayed in (c).

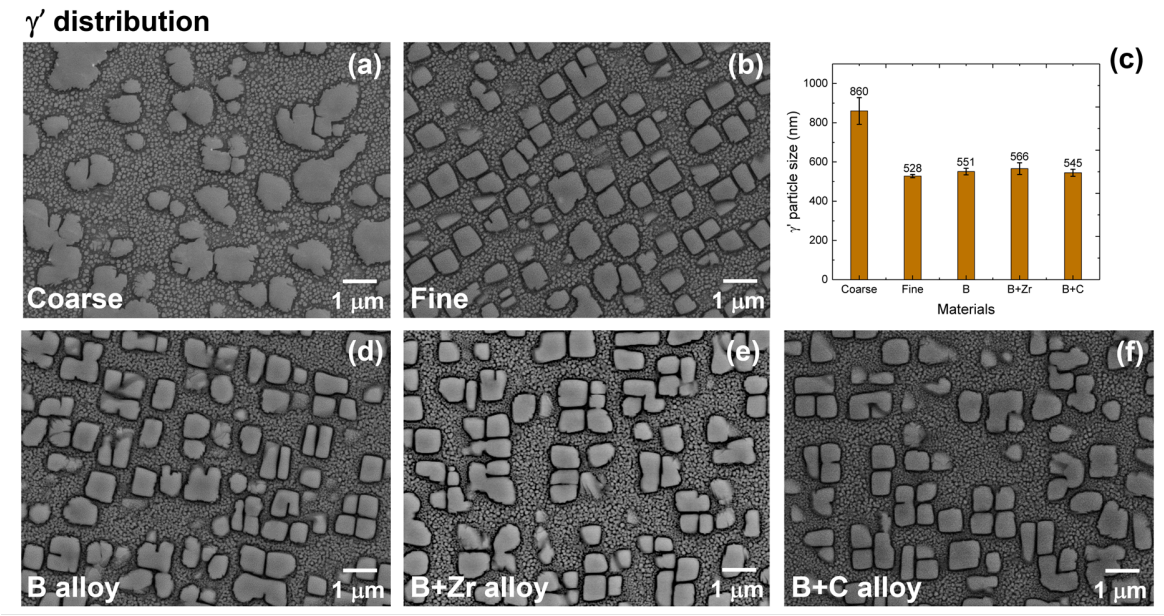


Fig. 6.4 γ' distribution using image processing in coarse grain (a), fine grain (b), B alloy (d), B+Zr alloy (e) and B+C alloy (f). The quantified size are displayed in (c).

captured, which were enriched in W, Mo and Cr. The composition suggests these carbide species are a mixture of M_6C and $M_{23}C_6$ types [221, 36, 94].

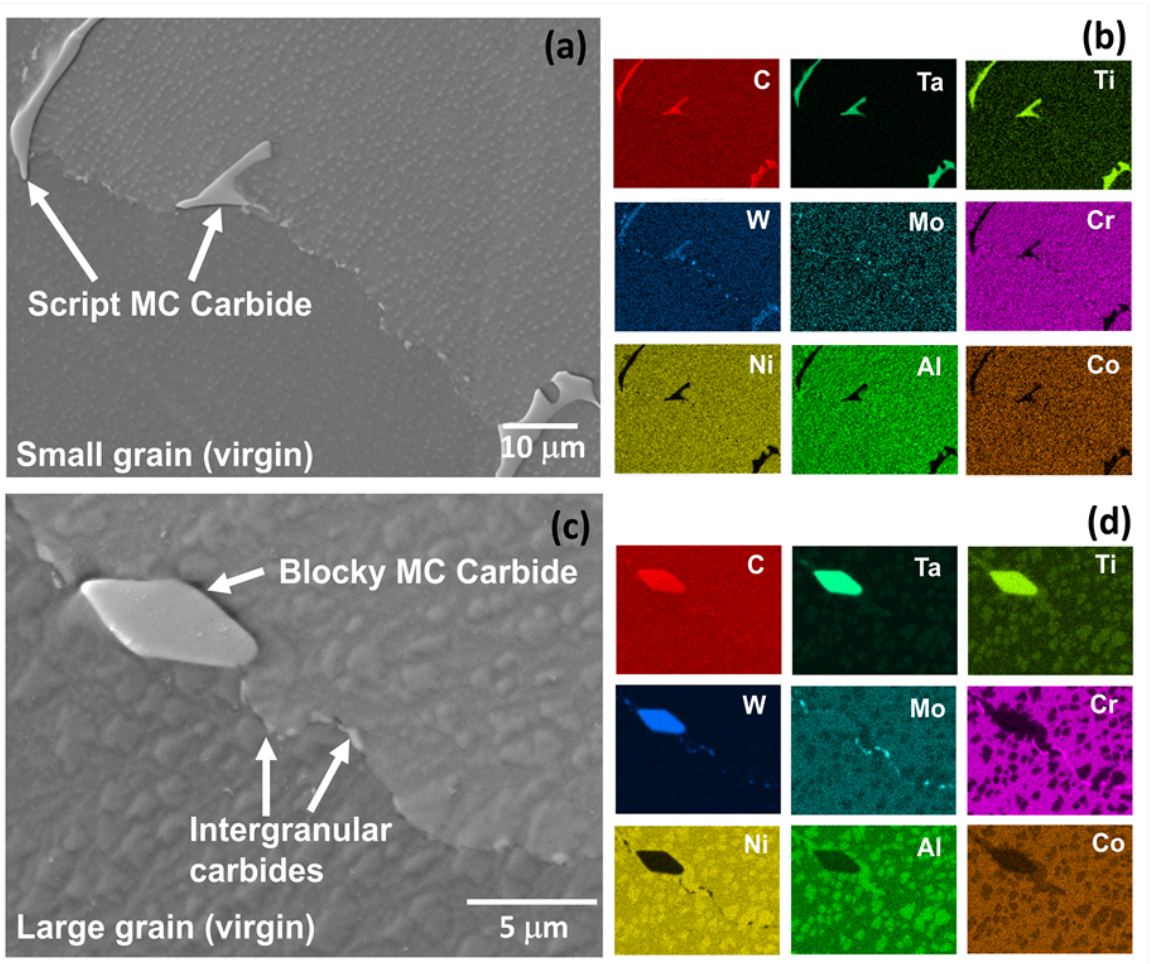


Fig. 6.5 Energy dispersive X-ray spectroscopy scan of a grain boundary that revealed Ta/Ti/W/Mo/Cr rich carbides.

Crept material: fractography

Fracture surfaces of various specimens were examined. It was found that the fracture tips crept at the same conditions obtains very similar morphological features. Figure 6.6 illustrated two typical fracture surfaces ruptured at 700°C/706MPa and 870°C/343MPa. Both intergranular and transgranular type fracture surfaces were observed in both conditions, denoted as area A and B. At 700°C/706 MPa condition, the fracture is dominated by intergranular type fracture, whereas transgranular failure dominated the

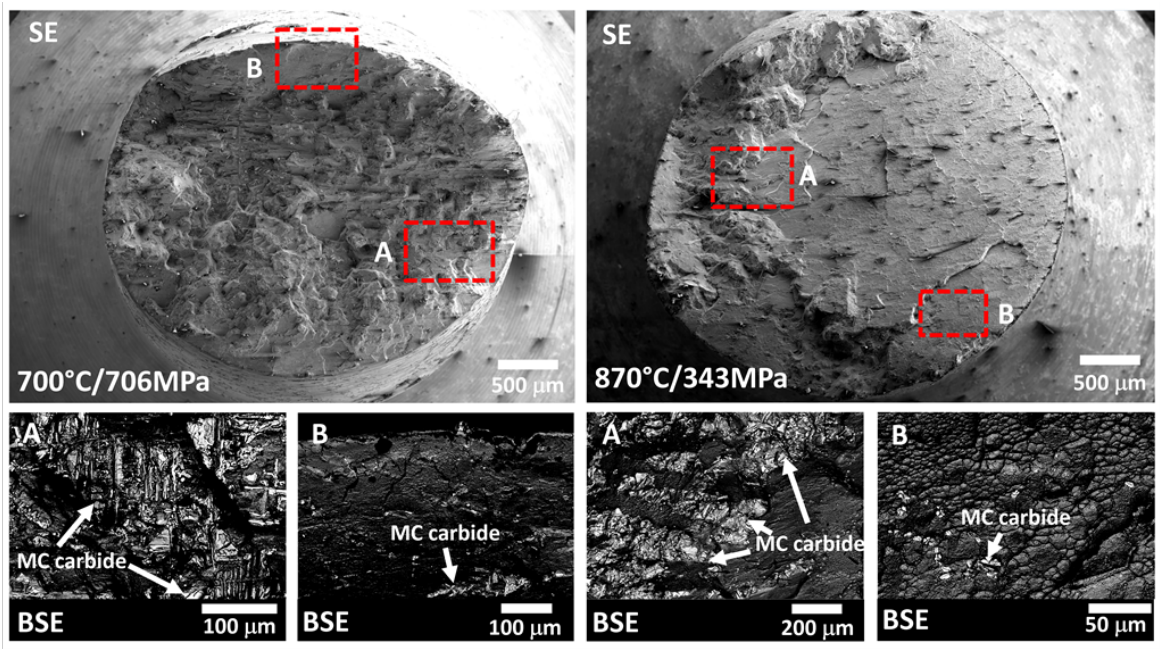


Fig. 6.6 Fracture surfaces of samples crept at 700°C/706MPa and 870°C/343MPa. Two areas each were captured with higher magnifications using back scattered electron detector that revealed MC carbide distribution.

870°C/343MPa condtion. The dominant type failure is indicated by area fraction of the surface with intergranular/transgranular features. Furthermore, with back scatter electron detector, large amount of delaminated/cracked MC carbides were frequently seen to associate with intergranular surfaces. By contrast, little MC carbide appeared at transgranular dominant surfaces (area B).

EBSD was performed to gain further understanding on deformation mechanisms. Figure 6.7 (a) is a stitched inverse pole figure (IPF) along Y axis of a sample crept at 700°C/706MPa, which it shows the fractured tip sectioned along its loading direction. Since the grain size is comparable to gauge section, and in this case, a near single crystal creep condition is achieved. The grain near [101] direction (green in pole figure) has shown severe deformation ∼45° to loading axis. The shifting of poles indicated

in IPF from [101] to [111] implied large amount of lattice rotation that had occurred. The movement of the pole was traced from yellow (initial) to red circles (final) on the stitched EBSD. As suggested by MacKay and Maier [222] with single crystal Mar-M247, the trace implies the active slip system is $\{1\ 1\ 1\}\ \langle 1\ 1\ 2\rangle$. Similarly, the same analytical approaches were carried out with a sample crept at 870°C/343MPa, see Figure 6.8. By tracing the stereographic projection across the specimen as illustrated in Figure 6.8 (a), the shifting poles demonstrate a better match with $\{1\ 1\ 1\}\ \langle 1\ 1\ 0\rangle$ slip. Although not fitting perfectly, it suggests a transition from $\langle 1\ 1\ 2\rangle$ to $\langle 1\ 1\ 0\rangle$ mechanism. Similar to the representative fracture tips shown in Figure 6.7 and Figure 6.8, more EBSD maps also suggest the fracture is frequently associated with the grain near $\langle 1\ 0\ 1\rangle$ direction, which implies the $\langle 1\ 0\ 1\rangle$ is the weak orientation.

6.3.3 Specimen shape change due to creep anisotropy

Crept specimen fracture tips exhibited notable degree of ellipticity at all conditions, which can be observed even with naked eyes. The shape change is believed to relate strongly with creep mechanisms, *i.e.* as a reflection of creep anisotropy. The measurement of shape change was conducted using 3D reconstruction of XCT data on two specimens crept at 700°C/706MPa and 870°C/343MPa respectively. The cross-sections usually appeared approximately elliptical, and hence, the aspect ratio profile between minor and major axes (namely b & a) was plotted against distance in Figure 6.9. The 700°C/706MPa condition demonstrated marked anisotropy, where a dip in aspect ratio is also observed. This phenomenon implies the quasi-brittle failure, as the fracture

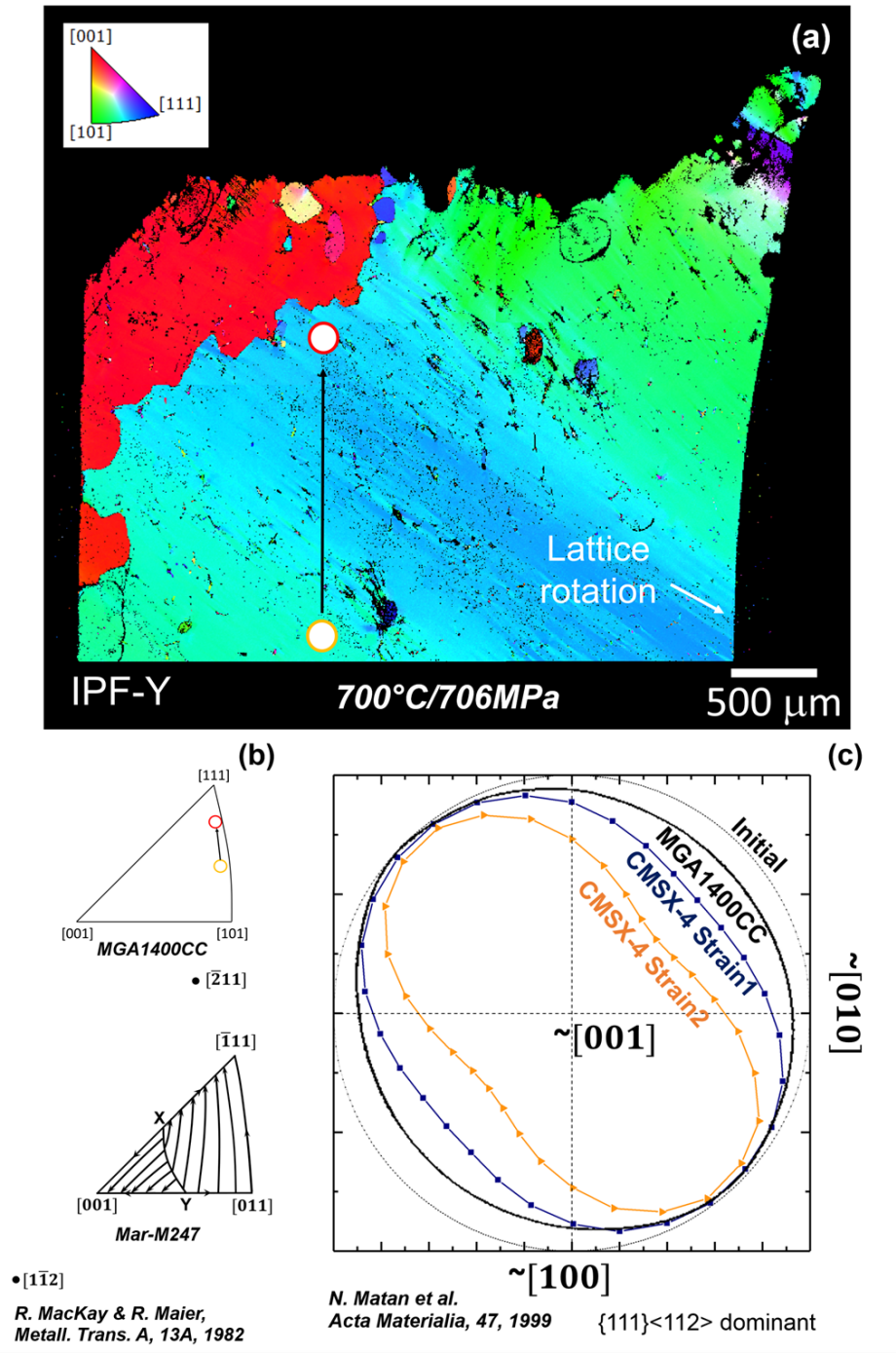


Fig. 6.7 EBSD coupled XCT technique for identification of dominant slip system. (a) Stitched EBSD images from Y axis of specimen crept at 700°C/706MPa. (b) Stereographic projection movement as indicated in (a), which is compared to single crystal Mar-M247 in literature [222]. (c) Circumference measurements using XCT and plotted against single crystal CMSX-4 in literature [223]

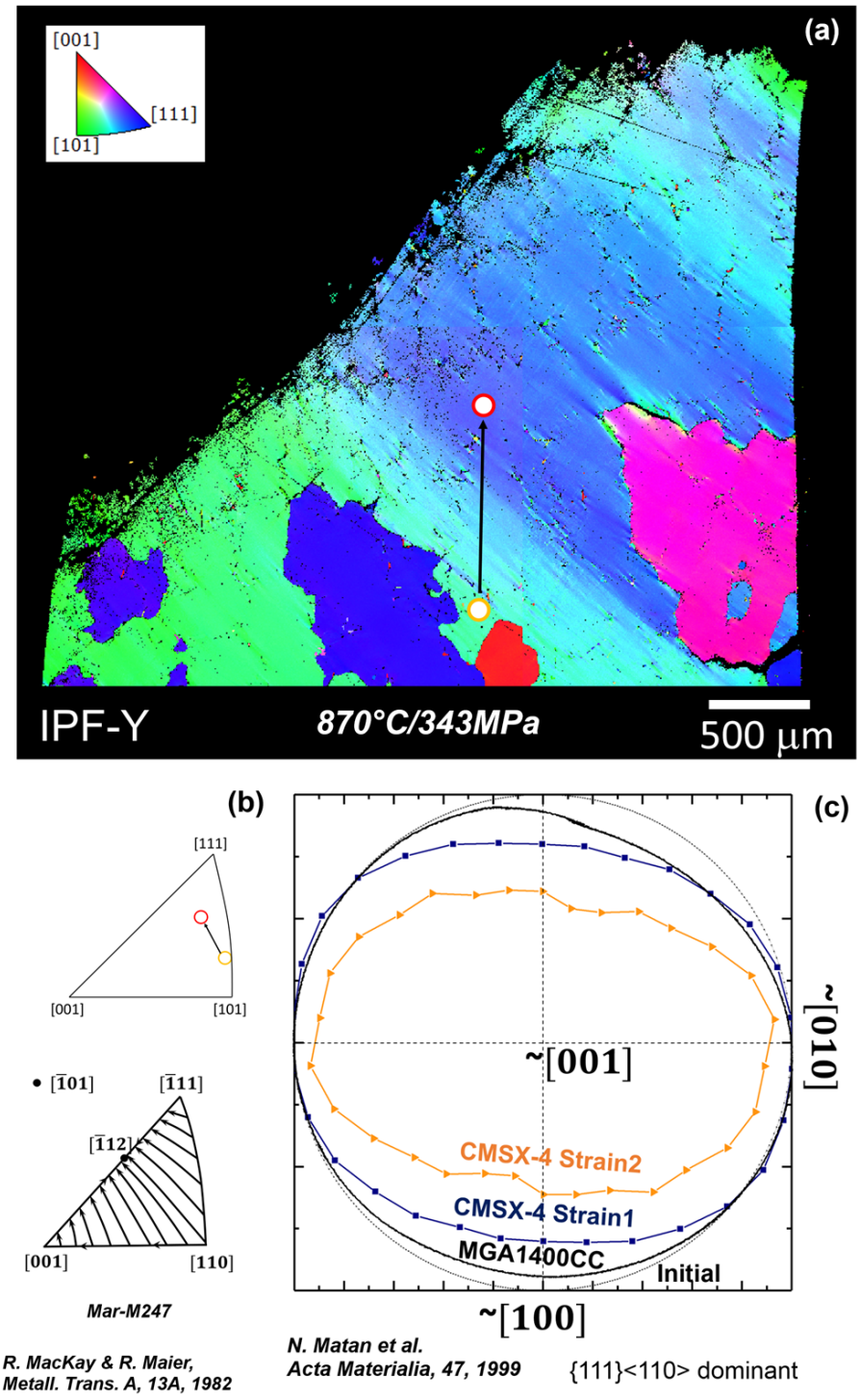


Fig. 6.8 EBSD coupled XCT technique for identification of dominant slip system. (a) Stitched EBSD images from Y axis of specimen crept at 870°C/343MPa. (b) Stereographic projection movement as indicated in (a), which is compared to single crystal Mar-M247 in literature [222]. (c) Circumference measurements using XCT and plotted against single crystal CMSX-4 in literature [223]

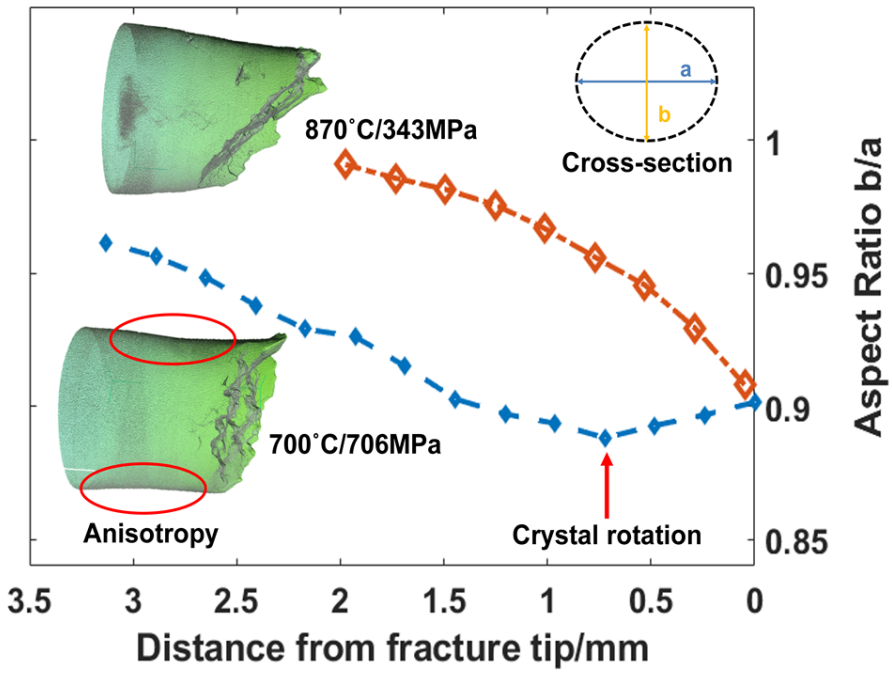


Fig. 6.9 XCT reconstruction showing the cross-sectional aspect ratio plot against distance of specimens crept at different conditions. 700°C/706MPa specimen demonstrated aspect ratio dip, which indicates severe creep anisotropy. 870°C/343MPa specimen demonstrated less anisotropy.

did not occur at the thinnest region (circled in red). On the contrary, the specimen suffered less from creep anisotropy at 870°C/343MPa, as the cross-section aspect ratio increased rapidly with distance. The circumference of each specimen was also plotted with corresponding crystallographic orientations, using Euler angles that obtained from EBSD maps. The circumferences are plotted in Figure 6.7 (c) and Figure 6.8 (c), overlayed with CMSX-4 cross-sectional shape at two different strains acquired by Matan *et al* [223]. The cross-sectional shape measurements further suggested the dominant slip system in action is {1 1 1} ⟨1 1 2⟩ for 700°C/706MPa and {1 1 1} ⟨1 1 0⟩ for 870°C/343MPa condition.

Creep model calibration

The creep model is constructed to improve the understanding on microsturcture in relation to creep life, with a particular focus at 700°C/706MPa. Because the creep rupture life is most sensitive to grain size as well as the scattering event is most significant at this condition. The parameters used for the creep model was calibrated using the average creep life for samples, *i.e.* 338.8 hours for small grains and 86.6 hours for large grains, and the creep rupture strain is defined as 6%. The optimised parameters are displayed in Table 6.1.

Table 6.1 Optimised creep model parameters for MGA1400CC

$\dot{\varepsilon}'_0$	$Q_{d/j}$	C	H^*	K'_p	K'_c	Q_p	σ_0	C_g	h'
(s^{-1})	(kJ/mol)			(s^{-1})	(μm^{-2})	(kJ/mol)	MPa		MPa
1.5×10^4	315	38000	0.524	10^6	2×10^{-5}	305	29	6×10^{-9}	1×10^5

6.4 Discussion

6.4.1 Creep scattering: influence of dominant slip system and carbide

The Effect of Creep Anisotropy

The scattering of creep life demonstrates strong sensitivity to creep conditions, the most drastic scattering occurred at 700°C/706MPa. Since the grain size is too large and the situation is near single crystal loading, the creep anisotropy played a pivotal role. As elucidated by coupled EBSD and XCT results, the dominant slip system in

operation at this condition is suggested as {1 1 1} ⟨1 1 2⟩. The dislocations at this slip system shears the γ' precipitates, which mechanism is captured in Figure 6.10 (b). During creep deformation, the crystal rotated toward to the slip directions. For {1 1 1} ⟨1 1 2⟩ shear to be active, large amount of lattice rotation is required, as witnessed by the specimen shape change, see Figure 6.7 (a) and Figure 6.9. Consequently, the cross-sectional area reduction is drastic, which increases the true stress to the specimen that provides an acceleration effect. In addition, the large amount of rotation inevitably breaks the large MC carbide, particularly the script-like morphology ones, due to their intrinsic stiff and brittle nature. The cracked carbides are no longer able to carry load and served as cavities that facilitates rapid crack propagation. As a result, the fracture is mainly intergranular that associated with fractured carbides and behaved quasi-brittle — the life is governed by the onset of tertiary creep, which is dependent upon cavitation link-up assisted by carbides. Figure 6.11 demonstrates a schematic drawing of damage mechanisms that operate during creep testing while {1 1 1} ⟨1 1 2⟩ is active. The evidence of each of these mechanisms are acquired using SEM and displayed in Figure 6.10. On the contrary, the creep scattering is alleviated with increased temperature and decreased stress level. As interpreted using a combination of EBSD and XCT techniques, the dominant deformation mechanism is controlled by more homogeneous {1 1 1} ⟨1 1 0⟩ slip system, *i.e.* so-called octahedral slip. In the ideal case of this mode, dislocation movements is controlled by a combination of glide and climb, where the crystal rotation required for the dislocations to operate is less. In the cases of encountering obstacles, dislocations are able to climb and bypass it.

Though in the real case, the ⟨1 1 0⟩ mechanism may not be the only one that is in action, since the creep condition may not completely satisfy the octahedral slip. The effect of MC carbide cracking on facilitating crack propagation is clearly mitigated. As a result, the specimens failed in a transgranular dominant fashion which usually contains little fraction of MC carbide on the fracture surface.

The effect of MC Carbide on Failure at Lower Temperatures

For further supporting the evidence of MC carbide in facilitating intergranular crack initiation and propagation, an *in-situ* tensile test was performed at room temperature for validation. From the aforementioned mechanistic analysis, it is deduced that the MC carbide governs the failure at lower temperatures as no climb assisted mechanisms are operative. Figure 6.12 demonstrates the *in-situ* crack evolution until failure at a strain rate $\sim 10^{-3}$ s^{-1}. The crack initiation sites are marked by red arrows, which are opening in the direction transverse to the loading axis. Moreover, with more detailed postmortem microscopy examination, the crack initiation sites are always associated with MC carbide cracking or delamination, see Figure 6.13. The fracture surface scanned using back scattered electron detector revealed a large fraction of carbides that present at fracture than at normal surfaces, see Figure 6.13 (b) and (d). Despite dislocation dynamics are different at room temperature and at 700°C, the fracture mode and crack propagation assisted by MC carbides still can be extrapolated.

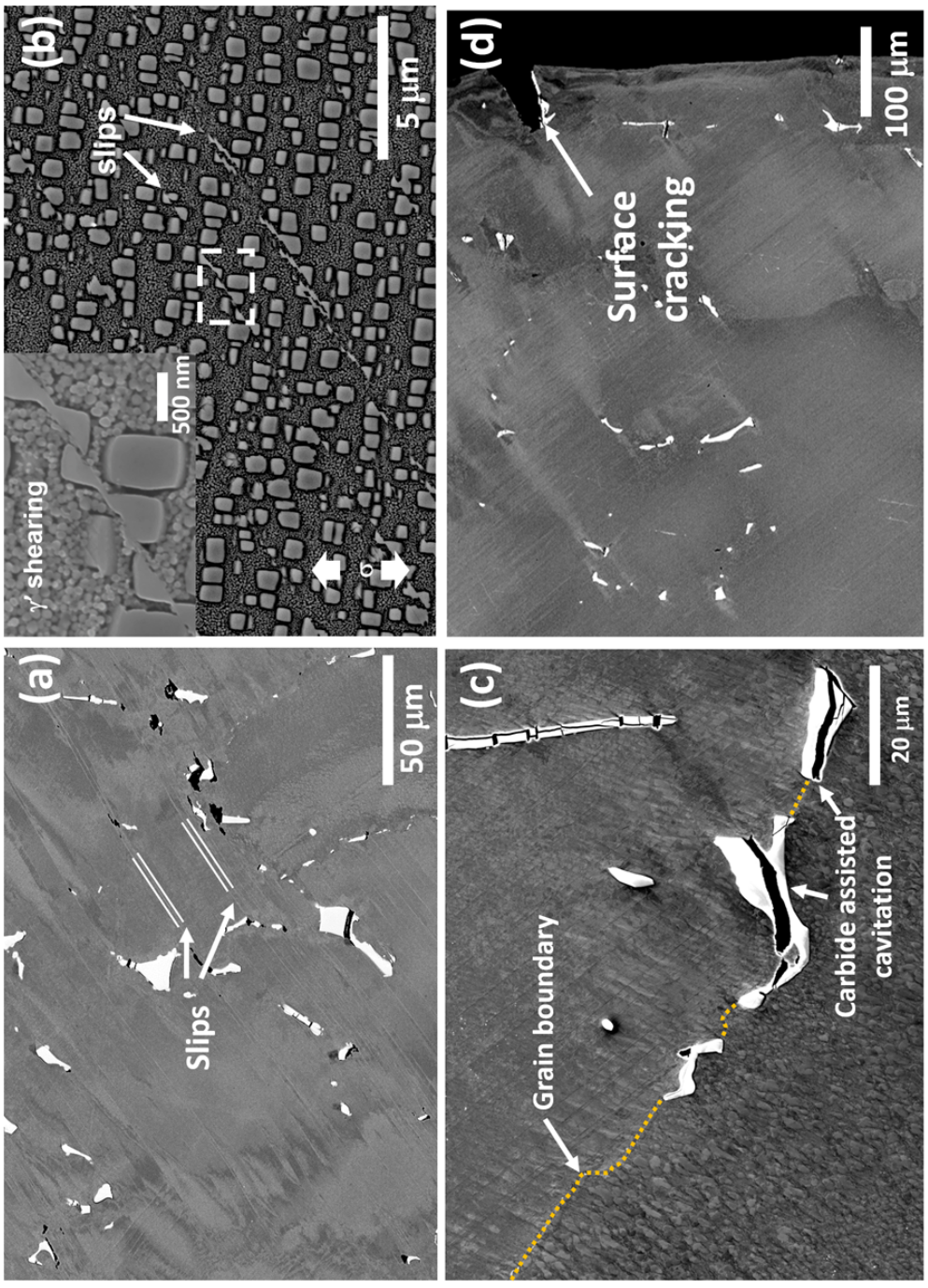


Fig. 6.10 Electron microscopy with evidence on deformation evolution for a specimen crept under $\{1\ 1\ 1\}\ \langle 1\ 1\ 2\rangle$ shear mechanism.

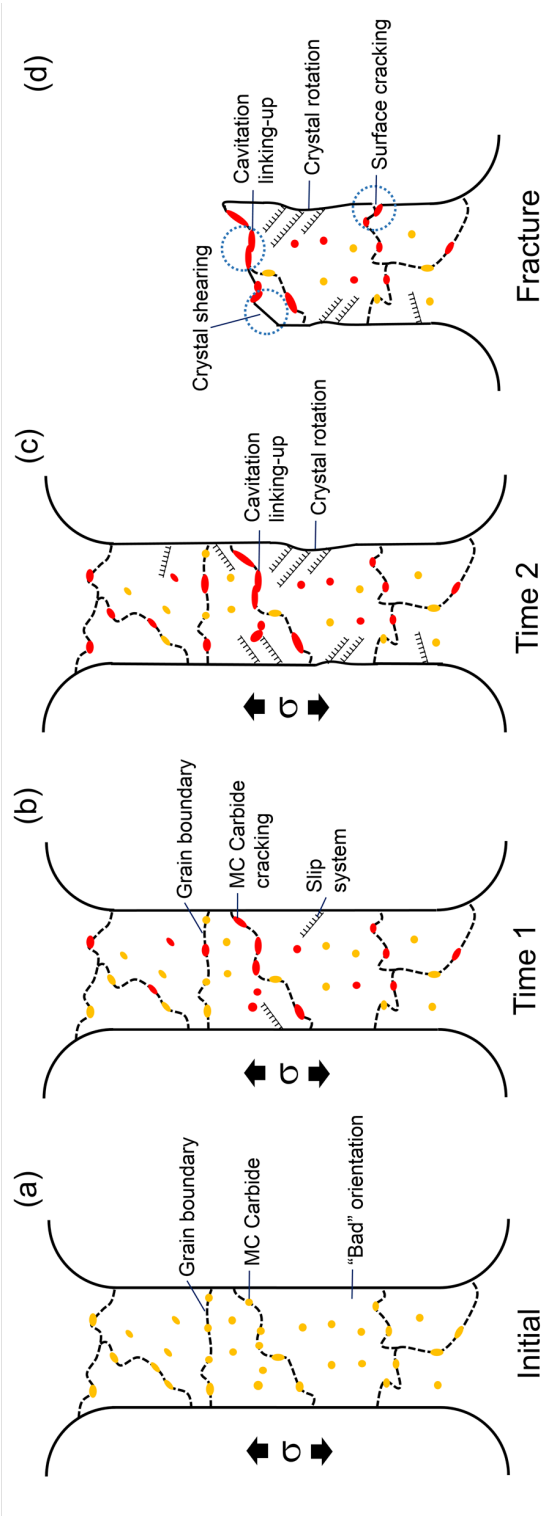


Fig. 6.11 Schematic drawing of the deformation and fracture evolution for a specimen crept under $\{1\ 1\ 1\}\ \langle 1\ 1\ 2\rangle$ shearing mechanism.

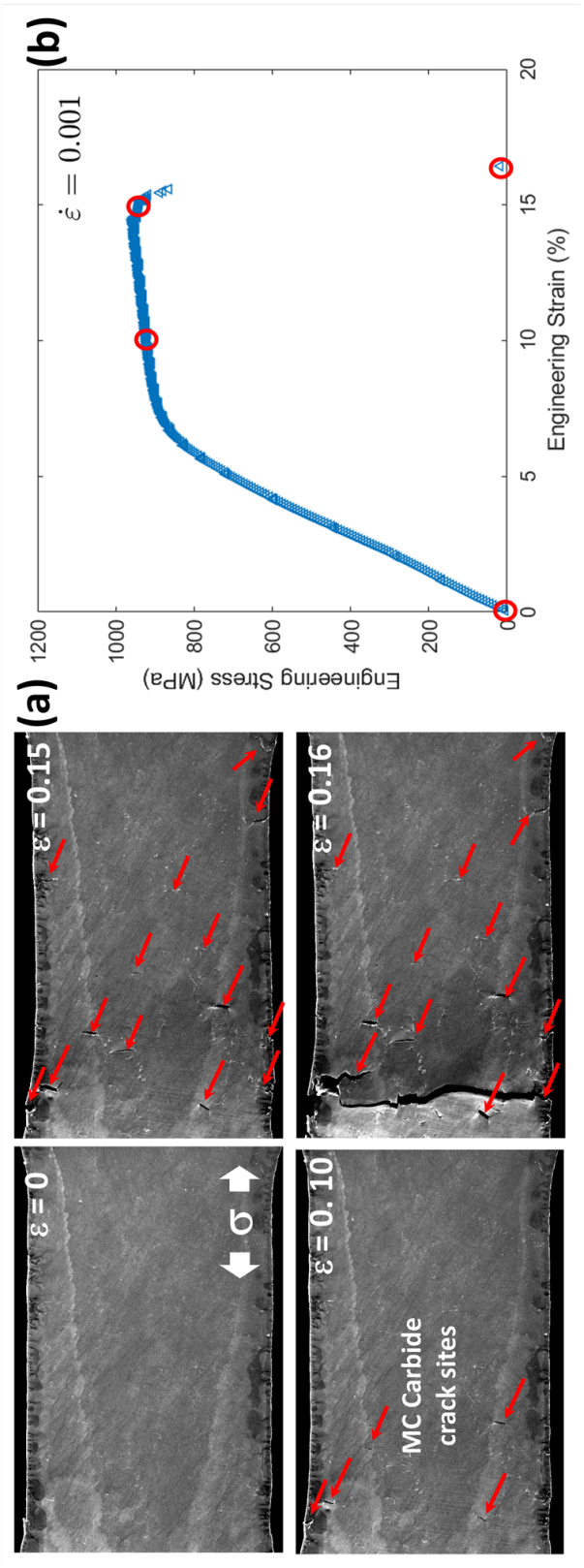


Fig. 6.12 *In-situ* tensile test carried out in SEM at different strains. MC carbide were shown to facilitate crack initiation and propagation.

Crystal plasticity modelling on intergranular phases

A crystal plasticity model was used to prove the concept of creep behaviour in relation to intergranular phases. This part of work is supplied by a private communication from Adziman *et al* [224]. As illustrated in Figure 6.14, a bicrystal testing situation is simulated at 700°C/706MPa, where a random high angle grain boundary separates the two grains. Three grain boundary cases were models for creep tests, *i.e.* with carbides (modelled as hard inclusions), no carbides and with voids. The simulated creep tests has demonstrate prolonged creep life in presence of carbide and decreased creep life due to voids. The simulation results are in line with our experimental observations — although MC carbide provided hardening of the material as a strong second phase, the carbide cracking facilitate rapid crack propagation due to its intrinsic brittleness. During a creep test, strong carbides degraded to voids as soon as the cracking happened as a result of large crystal rotation, therefore, the strengthening effect rapidly switched over to a weakening effect.

6.4.2 Influence of microstructure in relation to chemical modification

Creep life has shown strong dependency on grain size, particularly at low temperature/high stress conditions. Large grain size specimen possessed much shorter creep life compared to small grained samples. Two reasons are believed to be responsible for this. The primary reason is suggested as the change of microstructure, *i.e.* the

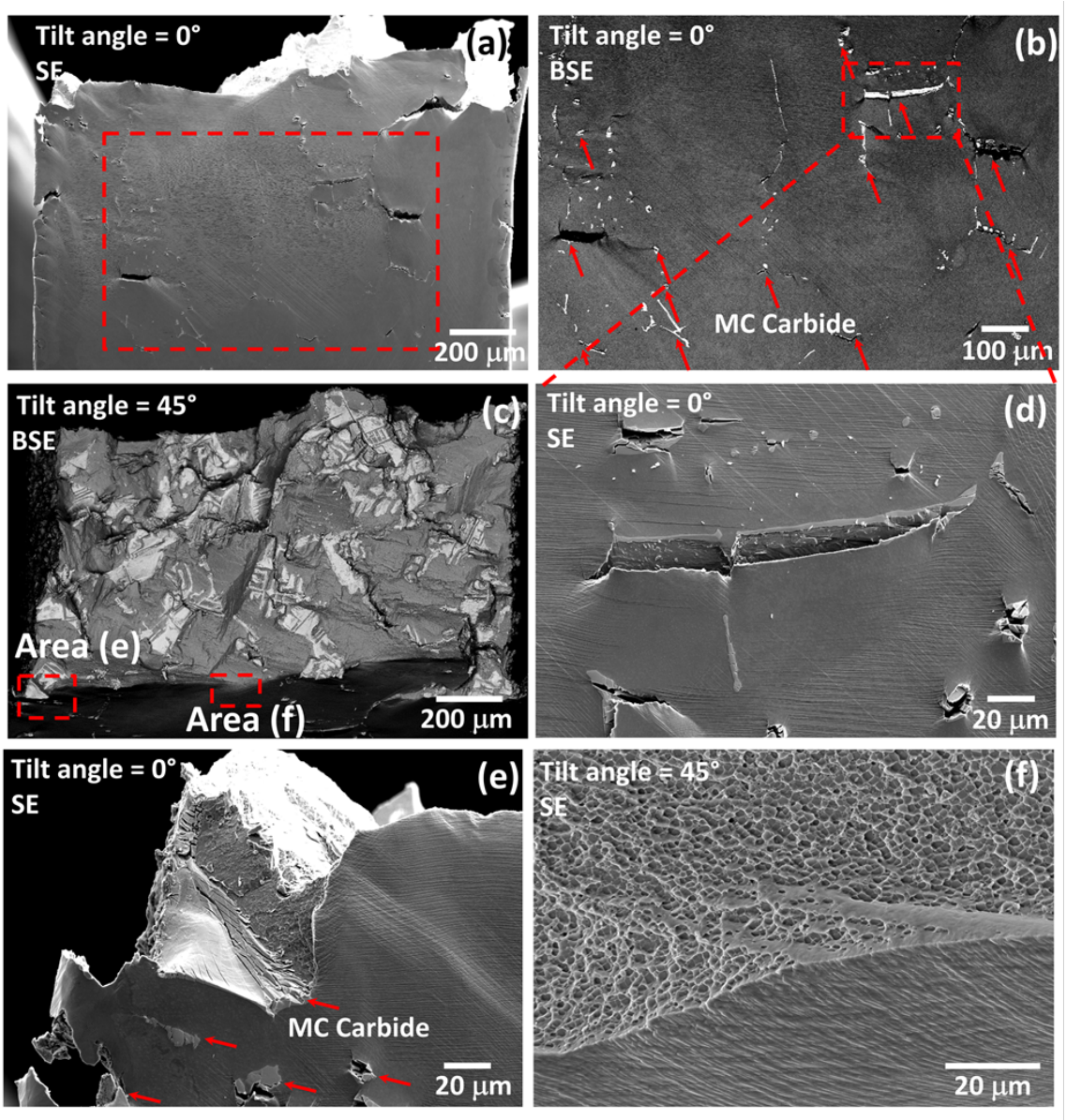


Fig. 6.13 Fracture analysis of the *in-situ* specimen. MC carbide cracking and delamination at fracture tip implies the source of failure. Ductile failure is shown in (f).

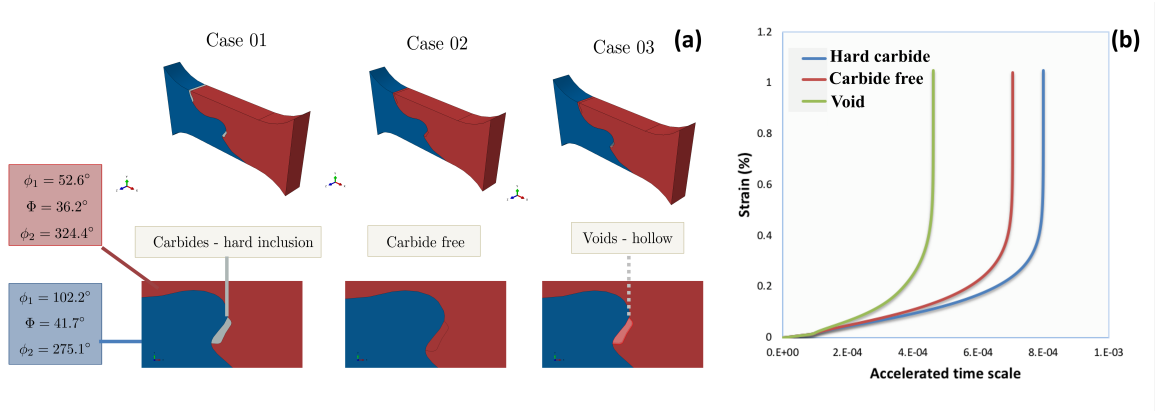


Fig. 6.14 Crystal plasticity creep model showing three grain boundary cases, *i.e.* with carbides (hard inclusions), carbide free and voids. The accelerated creep curves are shown in (b). Adapted from [224].

distribution of MC Carbide and γ' are hugely different for various grain sizes. The secondary reason is due to creep anisotropy, as near single crystal testing situation is more likely to be achieve with increasing grain size, which it accelerates the creep rate due to the reduction of area. The Dyson creep model takes measurements of γ' precipitates, however, the cavitation parameter is only optimised empirically at this point. Since the cavitation behaviour is shown to be assisted by carbide, where the propagation is dependent upon how the carbide network linking-up together, the fraction and size of carbide are considered proportional to the likelihood of cavitation damage. Thus it suggests the relation of geometrical parameter for cavitation damage $K_c = K_c' \, \phi_{MC} A_{MC}$, where are ϕ_{MC} and A_{MC} are area fraction and size of MC carbide respectively. An additional parameter K_c' has been introduced for maintaining the equation.

For understanding the effect of minor elements on microsturcture alteration and creep performance, three other model alloys were experimentally cast in bar form (40

mm diameter & 200 mm height) to reproduce the large grain sizes material. The new minor compositions are: 0.03 wt% Boron (B alloy), 0.03 wt% Boron with 0.06 wt% Zirconium (B+Zr alloy) and 0.03 wt% Boron with 0.11 wt% Carbon (B+C alloy). The full composition table can be found in Chapter 3. As suggested by literature [225, 226], the B and Zr are added intentionally to improve grain boundary cohesion and carbon is added to improve understanding of the carbide effect. The Dyson creep model is then used to simulate creep rupture times, which were 362, 353 & 356 hours for B, B+Zr and B+C alloys respectively. Initial creep tests showed the lives were 721, 245 & 218 hours, indeed more tests are needed for full validation of the composition modifications. However, given the scattering of creep life at 706MPa condition, the Dyson model still demonstrated prediction of creep lives within the range of 2σ. In comparison to the average life of large grain size material of 86.6 hours, minor addition has drastically improved the rupture time. The microstructural analysis on carbide and γ' distributions are exhibited in Figure 6.3 and 6.4. The connectivity of the carbide network has been suppressed, as witnessed by the significant decrease of carbide mean size due to the presence of boron. Since boron is smaller and hence more mobile, the boron atoms segregate to grain boundaries faster than carbon. As a result, borides formed at the expense of $M_{23}C_6$ carbides during solidification and are relatively uniform along grain boundaries. The detailed mechanism is thoroughly discussed by Kontis *et al* [41]. Subsequently, the boride distribution along the grain boundary or between dendrite arms blocked the channel for coarse MC carbide formation. Consequently, the connectivity of MC carbide network is declined deduced by its average size. It is necessary to

point out that boride formation has negligible influence on the thermodynamics of MC carbide formation, as the common boride species M_3C_2 and $M_5C_3$are enriched in Cr, which is partitioned by MC carbide. The invariable MC carbide fraction is witnessed by alloys with or without boron addition, see Figure 6.3. However, the MC connectivity is indeed modified due to geometric reasons. Moreover, the γ' precipitate sizes are observed smaller, which imposes a positive effect on the creep resistance. Despite the fact that the carbon addition in B+C alloy has increased the carbide volume fraction, it is still sufficiently lower in comparison to virgin large grains, hence the carbide-assisted damage is significantly alleviated.

6.4.3 Materials development framework

Admittedly, superalloy development and optimisation is an expensive process in the aspects of time and resources, particularly with long term testing such as creep and fatigue. Thus modelling is essential for accelerating the progress for property predictions. Here, a framework is proposed for the rapid assessment of alloys developed through new technologies, such as processing routes and/or composition modifications. As illustrated in Figure 6.15, the starting property targets may include creep life and creep ductility. Next, new microsturcture obtained from new technologies were characterised, critical defects such as casting porosity or detrimental phases were inspected. Then, distribution of MC carbide and γ' particle sizes are then quantified digitally with aid of software, the values are further carried out for the creep model. Finally, creep tests were performed to validate the new technology acquirement. The materials down-selection

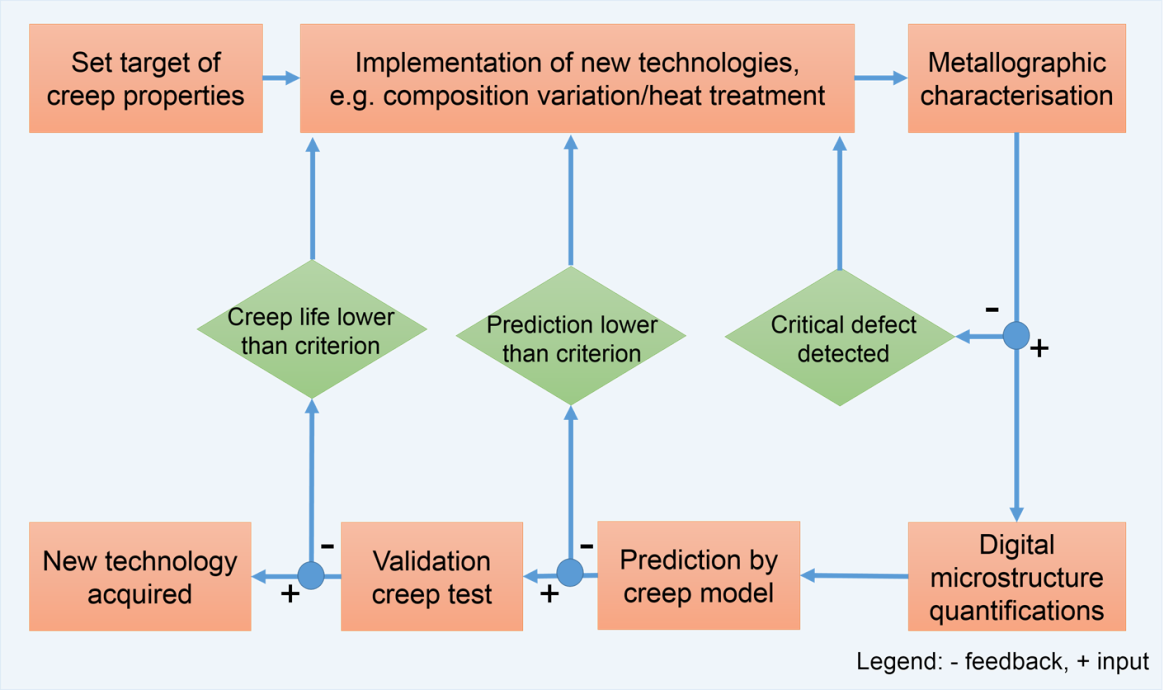


Fig. 6.15 The framework used for the current alloy development program acquiring new technologies.

procedures based on quantified microstructural phases have demonstrated useful for the present study, as the three modified materials were down selected from 21 candidates for validation, and they all exhibited improved rupture time. The application of the framework avoided numerous redundant creep testing with problematic phases, which were the time limiting step, as they were screened out in the early stage by predicted alloy life using the computational model that is based on the microstructure.

6.5 Summary and Conclusions

The following specific conclusions can be drawn from this work.

1. The nature of creep scattering in a polycrystalline superalloy has been identified. Effects originating from anisotropic creep deformation, active slip systems, grain boundary phases and microstructure inhomogeneity have been analysed.

2. A transition in dominant deformation mode of the material was determined using a combination of X-ray tomography & EBSD techniques at two creep conditions. The active slip systems altered from $\{1\ 1\ 1\}\ \langle 1\ 1\ 2\rangle$ at 700°C/706MPa to $\{1\ 1\ 1\}\ \langle 1\ 1\ 0\rangle$ at 870°C/343MPa.

3. Large amount of lattice rotation is required for $\{1\ 1\ 1\}\ \langle 1\ 1\ 2\rangle$ shear mechanism to operate, which led to a strong anisotropic effect at 700°C/706MPa. The anisotropic deformation further causes a higher effective stress that accelerates creep strain rate. Therefore, crystals with less favoured orientations possessed short stress rupture lives and *vice versa*. As a result, most pronounced creep scattering is observed at this condition.

4. Stress rupture life at 700°C has demonstrated strong dependency upon the onset of tertiary creep. In which regime, the grain boundary MC carbide cracking and decohesion is determined to be the root cause of quasi brittle failure. Thus, the creep displacement in this unconstrained cavity growth regime is controlled by the likelihood of carbide cracking.

5. A constitutive creep model was established and parameters are optimised for 700°C condition based on experimental input. It has characterised the influence of microstructural inhomogeneity between different grain sizes. Effect of γ' phase

and Ta/Ti rich MC-type carbide were evaluated critically, which related are closely to secondary and tertiary creep regime respectively.

6. Addition of boron level encouraged the formation of fine borides with refractory elements rather than carbides. Consequently, carbide size is suppressed as well as its connectivity. Therefore, stress rupture life is greatly enhanced at 700°C where $\langle 1\ 1\ 2 \rangle$ is operative, but no significant change at 870°C where $\langle 1\ 1\ 0 \rangle$ shear is dominant.

7. A computational framework for fast alloy development has been constructed, which integrated microstructure quantification, creep prediction and benchmark testing. It enables fast screening of microstructural optimisation through new technologies based on predicted creep life. It is verified reliable and advantageous for the alloy system investigated.

Chapter 7

Conclusions and Future Work

7.1 Conclusion remarks

The aim of the current research is to characterise the role of intergranular phases on modifying grain boundaries and to elucidate the effect on property change correspondent to the microstructure alteration in nickel-based alloys. Three main aspects related to grain boundary engineering — processing, mechanism and effect — were thoroughly discussed and linked together via a combination of multiscale mechanical testing and charaterisation techniques.

In Chapter 4, a mechanistic study on grain boundary serration was presented. A matrix of heat treatment was applied to Inconel 600 for generating different grain boundary morphologies. For hundreds of grain boundaries characterised and quantified, six types of grain boundaries were categorised. A new quantification method based on a combination of digital processing and fast Fourier transformation (FFT) was constructed

and verified robust on analysing the degree of grain boundary serration accurately and objectively. Serration index, a new metric for describing serration influence, was derived from the quantification method. This enabled relationship between processing parameters to be linked to final microsturcture, which is determined by the processing map constructed. Additionally, a combination of high resolution transmission based electron microscopy techniques jointly demonstrated the necessity of M_7C_3 carbide on promoting the formation of serration via two underlying mechanisms.

The work is then furthered in Chapter 5 on characterising the effect of grain boundary serration in the alloy under various conditions. It is shown that serrated grain boundaries effectively prolonged creep life in the high temperature/low stress regime, where intergranular cracking mechanism was dominating the failure. Strain analysis using HR-EBSD identified strain concentrators that were active in the non-serrated case, however, no strain concentrators were found in similar locations for the serrated case. Postmortem analysis proved the strain concentrators are responsible for cavity nucleation. *In-situ* tensile testing further consolidated the above argument. XCT facilitated the 3D assessment of fractured specimens, which provided a detailed overview of cavitation behaviour. It is found serration also have prohibited the development of grain boundary cavitation, which is strongly backed up by quantified measurements. On the other hand, in the case where transgranular failure is the dominant cause, then grain boundary serration does not provide further strengthening. Moreover, by investing in intergranular strength by generating serrated grain boundaries, some

weakening effect are expected through grain interior. This should be considered for the design and use of the alloys.

In chapter 6, the concept of grain boundary engineering was applied to an industrial gas turbine material with the aim of improving creep life. The alloy used was very complicated and a number of factors are contributing simultaneously. The level of creep life scattering is prominent, which was rationalised by deformation mechanisms which caused it. It is characterised by EBSD coupled XCT that the $\{1\ 1\ 1\}\ \langle 1\ 1\ 2\rangle$ shear mechanism was dominant at the low temperature/high stress regime, which required large lattice rotation. As a result, intergranular MC carbide fractured and facilitated rapid growth of grain boundary cavitation. A creep model based on the phenomenon was developed for rationalisation of micromechanics. New technologies concerning the role of grain boundary carbide were conducted. Boron addition to the alloy resulted a decrease in MC carbide size, which undermined the connectivity of the MC carbide network and thus achieved significant creep life improvement.

In summary, the study on grain boundary engineering have demonstrated significant influence on the material properties that can be altered by intergranular second phase particles controlled by processing parameters. A balanced strength between grain boundaries and matrix is required to be designed carefully for optimum properties.

7.2 Future Work

Based on current studies, three research topics are suggested for future attentions as continuous effort.

7.2.1 Extension on other alloys

Current study has clearly demonstrated the beneficial effect on creep by grain boundary serration in Inconel 600. The ultimate goal is far beyond than improving the creep property of a single alloy, but to gain insight into the mechanism that can be extended to a range of engineering alloys. The same philosophy should be applied to other alloys with carefully controlled experimentation for generalisation of the serration effect, in the hope of pushing operation temperature of components even higher. Such rationalisation can be challenging because more deformation mechanisms needed to be considered as the alloy systems become more complicated. For example, the interaction between dislocation and intragranular strengthening particles, deleterious effect by deformation twinning, etc.

An example of the systematic approach is outlined here. Extension on engineering alloys can be achieved with a few model alloys on understanding the potency of γ' on the generation of serrated grain boundaries. This can be validated by constructing corresponding processing maps with model alloys containing different Al/Ti contents. Creep properties can be evaluated accordingly at different conditions. The results from

the above procedures can then be characterised on the sensitivity of serration effect in relation to γ' fraction or particle size, for example.

Since the formation of grain boundary serration is a result of interaction between coherent particles and grain boundaries. It is possible that the knowledge gained from current studies on nickel-alloys may also be useful in other crystal systems, for example FCC (Al, Cu, Co), HCP (Ti, Zr) or BCC (Fe, high entropy alloys). Some of these metals suffer from high temperature deformation and/or intergranular failure during service, grain boundary serration indeed can be an intriguing topic for exploration in search of novel toughening technologies.

7.2.2 Extension on other properties

Grain boundary engineering was only invesitgated regarding to creep properties in the current study. Many other properties are still unknown as a fact that they have not been thoroughly tested. Positive effects are expected in low cycle fatigue, crack growth rate and toughness properties, as they are all susceptible to intergranular damage. This is based on the knowledge of increased interface cohesion using serrated morphology or decreased MC carbide size. Nonetheless, the designing of a component should always consider these properties at least with benchmark testing, after all, creep is not the only limiting property in all applications.

Other properties that may or may not be benefited from serrated grain boundaries include hydrogen embrittlement, stress corrosion cracking and other environmental assisted cracking. The difference between them and creep or fatigue is extra chemical

attack. New mechanisms inevitably arise due to the change of environment, and effect of serrated grain boundaries may be detrimental or neutral. Grain boundary serration has very rarely been considered as a form of engineering to those properties. Particularly, the effect on the properties must be carefully considered if the component is designed to operate in conditions with severe environmental attack. Therefore, the results are not only highly valuable in science, but also of great importance to industrial design.

7.2.3 Generalisation of grain boundary engineering with modelling

Formation mechanism and quantification of grain boundary serration have been well characterised by a spectrum of techniques in Inconel 600. The material was chosen for its simplicity of composition, as effects come from factors that can be easily eliminated or controlled. The knowledge acquired from the current study is expected to be generalised. This cannot be achieved without modelling effort, as the empirical approaches are usually too specific that finds narrow window for applications.

Although constructing serration models were not feasible within the time frame of the present study, some specific ideas and suggestions are provided here. Since the relationships between the degree of grain boundary serration and processing parameters, such as cooling rate or solution temperatures are characterised experimentally. These can then be translated for predicting the final grain boundary structure in other alloys, with aid of materials dependent parameters. For instance, the processing

informed microstructure may be generalised based on chemical compositions or physical properties, such as carbon content or γ' solution temperatures. On the property modelling, approaches based on continuum damage and microctructure may be coupled together. By characterising microstructure evolution within grain interior and also grain boundaries as a function of processing parameters, it is possible to model damage parameters that are sensitive to key microstructural features, *e.g.* particle distribution, likewise to the modified creep model developed in Chapter 6 on simulating MC carbide fraction and size on cavitation damage.

References

[1] N. L. S. Carnot, Reflections on the Motive Power of Heat, John Wiley & Sons, Inc., 1897.

[2] D. Kondepudi, I. Prigonine, Modern Thermodynamics - From Heat Engines to Dissipative Structures, John Wiley & Sons, Inc., 1998.

[3] N. Cumpsty, Jet Propulsion: A Simple Guide to the Aerodynamic and Thermodynamic Design and Performance of Jet Engines, Cambridge University Press, 2003.

[4] O. Miyagawa, M. Yamanoto, M. Kobayashi, Zig-Zag Grain Boundaries and Strength of Heat Resisting Alloys, in: Superalloys 1976, Superalloys 1976, 1976, pp. 245 – 254.

[5] J. M. Larson, Carbide Morphology in P/M IN-792, Metallurgical and Materials Transactions A 7 (10) (1976) 1497–1502.

[6] P. Caron, T. Khan, Evolution of Ni-based Superalloys for Single Crystal Gas Turbine Blade Applications, Aerospace Science and Technology 3 (8) (1999) 513 – 523. doi:https://doi.org/10.1016/S1270-9638(99)00108-X.
URL http://www.sciencedirect.com/science/article/pii/S127096389900108X

[7] D. Furrer, H. Fecht, Ni-Based Superalloys for Turbine Discs, JOM 51 (1) (1999) 14–17. doi:10.1007/s11837-999-0005-y.
URL https://doi.org/10.1007/s11837-999-0005-y

[8] C. S. Giggins, F. S. Pettit, Oxidation of Ni-Cr-Al Alloys Between 800° and 1200°C, Transactions of the Metallurgical Society of AIME 245 (1969) 2495.

[9] C. Giggins, F. Pettit, Oxidation of Ni-Cr-Al Alloys Between 1000° and 1200°C, Journal of the Electrochemical Society 118 (11) (1971) 1782–1790.

[10] R. N. Jarrett, J. K. Tien, Effects of Cobalt on Structure, Microchemistry and Properties of a Wrought Nickel-Base Superalloy, Metallurgical Transactions A 13 (6) (1982) 1021–1032. doi:10.1007/BF02643399.
URL https://doi.org/10.1007/BF02643399

[11] J. Gayda, P. Kantzos, J. Miller, Quench Crack Behavior of Nickel-base Disk Superalloys, Practical Failure Analysis 3 (1) (2003) 55–59. doi:10.1007/BF02717409.
URL https://doi.org/10.1007/BF02717409

[12] C. K. L. Davies, P. W. Davies, B. Wilshire, The Effect of Variations in Stacking-Fault Energy on the Creep of Nickel-Cobalt Alloys, The Philosophical Magazine: A Journal of Theoretical Experimental and Applied Physics 12 (118) (1965) 827–839. arXiv:https://doi.org/10.1080/14786436508218920, doi:10.1080/14786436508218920.
URL https://doi.org/10.1080/14786436508218920

[13] F. A. Mohamed, T. G. Langdon, The Transition From Dislocation Climb to Viscous Glide in Creep of Solid Solution Alloys, Acta Metallurgica 22 (6) (1974) 779 – 788. doi:https://doi.org/10.1016/0001-6160(74)90088-1.
URL http://www.sciencedirect.com/science/article/pii/0001616074900881

[14] H. A. Roth, C. L. Davis, R. C. Thomson, Modeling Solid Solution Strengthening in Nickel Alloys, Metallurgical and Materials Transactions A 28 (6) (1997) 1329–1335. doi:10.1007/s11661-997-0268-2.
URL https://doi.org/10.1007/s11661-997-0268-2

[15] C. Rae, R. Reed, The Precipitation of Topologically Close-Packed Phases in Rhenium-Containing Superalloys, Acta Materialia 49 (19) (2001) 4113 – 4125. doi:https://doi.org/10.1016/S1359-6454(01)00265-8.
URL http://www.sciencedirect.com/science/article/pii/S1359645401002658

[16] X. Liu, B. Kang, K.-M. Chang, The Effect of Hold-Time on Fatigue Crack Growth Behaviors of WASPALOY Alloy at Elevated Temperature, Materials Science and Engineering: A 340 (1) (2003) 8 – 14. doi:https://doi.org/10.1016/S0921-5093(02)00074-6.
URL http://www.sciencedirect.com/science/article/pii/S0921509302000746

[17] T. Pollock, S. Tin, Nickel-Base Superalloy for Advanced Turbine Engine: Chemistry, Microstructure and Properties, Journal of Propulsion and Power 22 (2) (2006) 361–374.

[18] R. C. Reed, The Superalloys: Fundamentals and Applications, Cambridge University Press, 2006.

[19] X. Lu, J. Du, Q. Deng, J. Zhuang, Stress Rupture Properties of GH4169 Superalloy, Journal of Materials Research and Technology 3 (2) (2014) 107 – 113. doi:https://doi.org/10.1016/j.jmrt.2014.03.003.
URL http://www.sciencedirect.com/science/article/pii/S2238785414000210

[20] Y. Koizumi, T. Kobayashi, T. Yokokawa, J. Zhang, M. Osawa, H. Harada, Y. Aoki, M. Arai, Development of Next Generation Ni-Base Single Crystal Superalloys, in: Superalloys 2004, 2004.

[21] T. T. Gabb, J. Telesman, A. Banik, E. McDevitt, Use of Slow Strain Rate Tensile Testing to Assess the Ability of Several Superalloys to Resist Environmentally-Assisted Intergranular Cracking, in: 8th International Symposium on Superalloy 718 and Derivatives, 2014.

[22] M. Ramsperger, R. F. Singer, C. Körner, Microstructure of the Nickel-Base Superalloy CMSX-4 Fabricated by Selective Electron Beam Melting, Metallurgical and Materials Transactions A 47 (3) (2016) 1469–1480. doi:10.1007/s11661-015-3300-y.
URL https://doi.org/10.1007/s11661-015-3300-y

[23] C. F. Miller, G. Simmons, R. P. Wei, Mechanism for Oxygen Enhanced Crack Growth in Inconel 718, Scripta Materialia 44 (2001) 2405–2410.

[24] S. Everitt, M. Starink, P. Reed, Temperature and Dwell Dependence of Fatigue Crack Propagation in Various Heat Treated Turbine Disc Alloys, in: Superalloys 2008, 2008.

[25] S. Ochial, Y. Oya, T. Suzuki, Alloying Behaviour of Ni3Al, Ni3Ga, Ni3Si and Ni3Ge, Acta Metallurgica 32 (2) (1984) 289 – 298. doi:https://doi.org/10.1016/0001-6160(84)90057-9.
URL http://www.sciencedirect.com/science/article/pii/0001616084900579

[26] L. Vegard, Die Röntgenstrahlen im Dienste der Erforschung der Materie, Crystalline Materials 67 (1928) 239–259.

[27] R. Ricks, A. Porter, R. Ecob, The Growth of γ' Precipitates in Nickel-Base Superalloy, Acta Mechanica 31 (1983) 43–53.

[28] C. T. Sims, A Contemporary View of Nickel-Base Superalloys, JOM 18 (10) (1966) 1119–1130. doi:10.1007/BF03378505.
URL https://doi.org/10.1007/BF03378505

[29] J. Belan, GCP and TCP Phases Presented in Nickel-Base Superalloys, Materials Today: Proceedings 3 (4) (2016) 936 – 941, 32nd DANUBIA ADRIA SYMPOSIUM on Advanced in Experimental Mechanics. doi:https://doi.org/10.1016/j.matpr.2016.03.024.
URL http://www.sciencedirect.com/science/article/pii/S2214785316002297

[30] O. Ojo, H. Zhang, Analytical Electron Microscopy Study of Boron-Rich Grain Boundary Microconstituent in Directionally Solidified RENE 80 Superalloy, Metallurgical and Materials Transactions A 39 (12) (2008) 2799–2803. doi:10.1007/s11661-008-9646-7.
URL https://doi.org/10.1007/s11661-008-9646-7

[31] G. P. Sabol, R. Stickler, Microstructure of Nickel-Based Superalloys, physica status solidi (b) 35 (1) (1969) 11–52. arXiv:https://onlinelibrary.wiley.

com/doi/pdf/10.1002/pssb.19690350102, doi:10.1002/pssb.19690350102.
URL https://onlinelibrary.wiley.com/doi/abs/10.1002/pssb.19690350102

[32] J. Chen, J. Lee, C. Jo, S. Choe, Y. Lee, MC Carbide Formation in Directionally Solidified MAR-M247 LC Superalloy, Materials Science and Engineering: A 247 (1) (1998) 113 – 125. doi:https://doi.org/10.1016/S0921-5093(97)00761-2.
URL http://www.sciencedirect.com/science/article/pii/S0921509397007612

[33] P. S. Kotval, J. D. Venables, R. W. Calder, The Role of Hafnium in Modifying the Microstructure of Cast Nickel-Base Superalloys, Metallurgical and Materials Transactions B 3 (2) (1972) 457–462. doi:10.1007/BF02642049.
URL https://doi.org/10.1007/BF02642049

[34] J. Yang, Q. Zheng, M. Ji, X. Sun, Z. Hu, Effects of Different C Contents on the Microstructure, Tensile Properties and Stress-Rupture Properties of IN792 Alloy, Materials Science and Engineering: A 528 (3) (2011) 1534 – 1539. doi:https://doi.org/10.1016/j.msea.2010.11.003.
URL http://www.sciencedirect.com/science/article/pii/S0921509310012906

[35] L. He, Q. Zheng, X. Sun, H. Guan, Z. Hu, A. Tieu, C. Lu, H. Zhu, Effect of Carbides on the Creep Properties of a Ni-Base Superalloy M963, Materials Science and Engineering: A 397 (1) (2005) 297 – 304. doi:https://doi.org/10.1016/j.msea.2005.02.038.
URL http://www.sciencedirect.com/science/article/pii/S0921509305001759

[36] J. Yang, Q. Zheng, X. Sun, H. Guan, Z. Hu, Relative Stability of Carbides and Their Effects on the Properties of K465 Superalloy, Materials Science and Engineering: A 429 (1) (2006) 341 – 347. doi:https://doi.org/10.1016/j.msea.2006.05.091.
URL http://www.sciencedirect.com/science/article/pii/S0921509306009087

[37] H. Hong, I. Kim, B. Choi, M. Kim, C. Jo, The Effect of Grain Boundary Serration on Creep Resistance in a Wrought Nickel-Based superalloy, Materials Science and Engineering: A 517 (2009) 125 – 131.

[38] Y. S. Lim, D. J. Kim, S. S. Hwang, H. P. Kim, S. W. Kim, $M_{23}C_6$ precipitation behavior and grain boundary serration in Ni-based alloy 690, Mater. Charact. 96 (2014) 28 – 39.

[39] X. W. Jiang, D. Wang, G. Xie, H. Li, L. H. Lou, J. Zhang, The Effect of Long-Term Thermal Exposure on the Microstructure and Stress Rupture Property of a Directionally Solidified Ni-Based Superalloy, Metallurgical and Materials Transactions A 45 (13) (2014) 6016–6026. doi:10.1007/s11661-014-2559-8.
URL https://doi.org/10.1007/s11661-014-2559-8

[40] J. C. Stinville, K. Gallup, T. M. Pollock, Transverse Creep of Nickel-Base Superalloy Bicrystals, Metallurgical and Materials Transactions A 46 (6) (2015) 2516–2529. doi:10.1007/s11661-015-2869-5.
URL https://doi.org/10.1007/s11661-015-2869-5

[41] P. Kontis, H. M. Yusof, S. Pedrazzini, M. Danaie, K. Moore, P. Bagot, M. Moody, C. Grovenor, R. Reed, On the Effect of Boron on Grain Boundary Character in a New Polycrystalline Superalloy, Acta Materialia 103 (2016) 688 – 699.

[42] R. C. Reed, M. P. Jackson, Y. S. Na, Characterization and Modeling of the Precipitation of the σ Phase in UDIMET 720 and UDIMET 720Li, Metallurgical and Materials Transactions A 30 (3) (1999) 521–533. doi:10.1007/s11661-999-0044-6.
URL https://doi.org/10.1007/s11661-999-0044-6

[43] R. J. Mitchell, C. M. F. Rae, S. Tin, Grain Boundary Transformations During Isothermal Exposure of Powder Metallurgy Nickel Base Superalloys for Turbine Disc Applications, Materials Science and Technology 21 (1) (2005) 125–132. arXiv:https://doi.org/10.1179/174328405X16261, doi:10.1179/174328405X16261.
URL https://doi.org/10.1179/174328405X16261

[44] P. Lejcek, Grain Boundary Segregation in Metals, Springer-Verlag Berlin Heidelberg, 2010.

[45] D. Raabe, M. Herbig, S. S. des, Y. Li, D. Tytko, M. Kuzmina, D. Ponge, P.-P. Choi, Grain Boundary Segregation Engineering in Metallic Alloys: A Pathway to the Design of Interfaces, Current Opinion in Solid State and Materials Science 18 (4) (2014) 253 – 261, slip Localization and Transfer in Deformation and Fatigue of Polycrystals. doi:https://doi.org/10.1016/j.cossms.2014.06.002.
URL http://www.sciencedirect.com/science/article/pii/S1359028614000394

[46] A. P. Sutton, R. W. Balluffi, Interface in Crystalline Materials, Oxford: Clarendon Press, 1995.

[47] L. Priester, Grain Boundaries and Crystalline Plasticity, Wiley-ISTE, 2011.

[48] D. McLean, Grain boundaries in Metals, Oxford: Clarendon Press, 1957.

[49] P. Keblinski, S. Phillpot, D. Wolf, H. Gleiter, Amorphous Structure of Grain Boundaries and Grain Junctions in Nanocrystalline Silicon by Molecular-Dynamics Simulation, Acta Materialia 45 (3) (1997) 987 – 998. doi:https://doi.org/10.1016/S1359-6454(96)00236-4.
URL http://www.sciencedirect.com/science/article/pii/S1359645496002364

[50] D. Wolf, Structure-Energy Correlation for Grain Boundaries in F.C.C. metals III. Symmetrical Tilt Boundaries, Acta Metallurgica et Materialia 38 (5) (1990) 781 – 790. doi:https://doi.org/10.1016/0956-7151(90)90030-K.
URL http://www.sciencedirect.com/science/article/pii/095671519090030K

[51] D. Wolf, Structure-Energy Correlation for Grain Boundaries in F.C.C. Metals IV. Asymmetrical Twist (General) Boundaries, Acta Metallurgica et Materialia 38 (5) (1990) 791 – 798. doi:https://doi.org/10.1016/0956-7151(90)90031-B.
URL http://www.sciencedirect.com/science/article/pii/095671519090031B

[52] K. L. Merkle, Atomic Structure of Grain Boundaries, Journal of Physics and Chemistry of Solids 55 (10) (1994) 991 – 1005. doi:https://doi.org/10.1016/0022-3697(94)90119-8.
URL http://www.sciencedirect.com/science/article/pii/0022369794901198

[53] W. T. Read, W. Shockley, Dislocation Models of Crystal Grain Boundaries, Physical Review.

[54] G. Bishop, B. Chalmers, A Coincidence - Ledge - Dislocation Description of Grain Boundaries, Scripta Metallurgica 2 (2) (1968) 133 – 139. doi:https://doi.org/10.1016/0036-9748(68)90085-9.
URL http://www.sciencedirect.com/science/article/pii/0036974868900859

[55] B. Baroux, M. Biscondi, C. Goux, A Structural Model for Grain Boundaries in Pure Metals, physica Status solidi (b) 38 (1) (1970) 415–424. arXiv:https://onlinelibrary.wiley.com/doi/pdf/10.1002/pssb.19700380143, doi:10.1002/pssb.19700380143.
URL https://onlinelibrary.wiley.com/doi/abs/10.1002/pssb.19700380143

[56] A. P. Sutton, On the Structure of (001) Twist Boundaries in F.C.C. Metals, Philosophical Magazine A 46 (1) (1982) 171–176. arXiv:https://doi.org/10.1080/01418618208236216, doi:10.1080/01418618208236216.
URL https://doi.org/10.1080/01418618208236216

[57] A. P. Sutton, On the Structural Unit Model of Grain Boundary Structure, Philosophical Magazine Letters 59 (2) (1989) 53–59. arXiv:https://doi.org/10.1080/09500838908214777, doi:10.1080/09500838908214777.
URL https://doi.org/10.1080/09500838908214777

[58] J. Han, V. Vitek, D. J. Srolovitz, The Grain-Boundary Structural Unit Model Redux, Acta Materialia 133 (2017) 186 – 199. doi:https://doi.org/10.1016/j.actamat.2017.05.002.
URL http://www.sciencedirect.com/science/article/pii/S1359645417303798

[59] M. Ashby, F. Spaepen, S. Williams, The Structure of Grain Boundaries Described as a Packing of Polyhedra, Acta Metallurgica 26 (11) (1978) 1647 – 1663. doi:https://doi.org/10.1016/0001-6160(78)90075-5.
URL http://www.sciencedirect.com/science/article/pii/0001616078900755

[60] R. W. Balluffi, R. F. Mehl, Grain Boundary Diffusion Mechanisms in Metals, Metallurgical Transactions A 13 (12) (1982) 2069–2095. doi:10.1007/BF02648378.
URL https://doi.org/10.1007/BF02648378

[61] R. Balluffi, A. Brokman, Simple Structural Unit Model for Core-Dependent Properties of Symmetrical Tilt Boundaries, Scripta Metallurgica 17 (8) (1983) 1027 – 1030. doi:https://doi.org/10.1016/0036-9748(83)90444-1.
URL http://www.sciencedirect.com/science/article/pii/0036974883904441

[62] G. Wang, V. Vitek, Relationships Between Grain Boundary Structure and Energy, Acta Metallurgica 34 (5) (1986) 951 – 960. doi:https://doi.org/10.1016/0001-6160(86)90068-4.
URL http://www.sciencedirect.com/science/article/pii/0001616086900684

[63] G. Hasson, J.-Y. Boos, I. Herbeuval, M. Biscondi, C. Goux, Theoretical and Experimental Determinations of Grain Boundary Structures and Energies: Correlation with Various Experimental Results, Surface Science 31 (1972) 115 – 137. doi:https://doi.org/10.1016/0039-6028(72)90256-7.
URL http://www.sciencedirect.com/science/article/pii/0039602872902567

[64] M. L. Kronberg, F. H. Wilson, Secondary Recrystallization in Copper, Metal Transaction.

[65] N. H. Fletcher, Advances in Materials Research, Wiley, 1971, Ch. Crystal Interface Models – A Critical Survey.

[66] S. Kobayashi, S. Tsurekawa, T. Watanabe, A New Approach to Grain Boundary Engineering for Nanocrystalline Materials, Beilstein Journal of Nanotechnology 7 (2016) 1829–1849. doi:10.3762/bjnano.7.176.

[67] W. Bollmann, Crystal Defects and Crystal Interfaces, Springer Berlin Heidelberg, 1970.

[68] R. Balluffi, Interfacial Segregation, ASM, 1979, Ch. Grain Boundary Structure and Segregation.

[69] M. W. Finnis, M. Rühle, Materials Science and Technology, WILEY-VCH Verlag GmbH & Co KGaA, 2006, Ch. Structures of Interfaces in Crystalline Solids. arXiv:https://onlinelibrary.wiley.com/doi/pdf/10.1002/9783527603978.mst0009, doi:10.1002/9783527603978.mst0009.
URL https://onlinelibrary.wiley.com/doi/abs/10.1002/9783527603978.mst0009

[70] E. R. Parker, Brittle Behavior of Engineering Structures, John Wiley and Sons, 1957.

[71] D. Raabe, S. Sandlö, J. Millán, D. Ponge, H. Assadi, M. Herbig, P.-P. Choi, Segregation Engineering Enables Nanoscale Martensite to Austenite Phase Transformation at Grain Boundaries: A Pathway to Ductile Martensite, Acta Materialia 61 (16) (2013) 6132 – 6152. doi:https://doi.org/10.1016/j.actamat.2013.06.055.
URL http://www.sciencedirect.com/science/article/pii/S1359645413005004

[72] R. Faulkner, Creep-resistant steels, Woodhead Publishing, 2008, Ch. Grain boundaries in creep-resistant steels.

[73] M. P. Seah, E. D. Hondros, Grain Boundary Segregation, in: Proceedings of the Royal Society of London, Vol. 335 of A, Royal Society, 1973, pp. 191–212.

[74] E. D. Hondros, D. McLean, Cohesion Margin of Copper, Philosophical Magazine 29 (4) (1974) 771–795.

[75] M. Guttmann, Equilibrium Segregation in a Ternary Solution: A Model for Temper Embrittlement, Surface Science 53 (1) (1975) 213 – 227. doi:https://doi.org/10.1016/0039-6028(75)90125-9.
URL http://www.sciencedirect.com/science/article/pii/0039602875901259

[76] M. Guttmann, D. McLean, Interfacial Segregation, ASM, 1979, Ch. Grain boundary segregation in multicomponent systems.

[77] G. Ciccotti, M. Guillopé, V. Pontikis, High-Angle Grain-Boundary Premelting Transition: A Molecular-Dynamics Study, Physical Review B.

[78] R. Faulkner, Combined Grain Boundary Equilibrium and Non-Equilibrium Segregation in Ferritic/Martensitic Steels, Acta Metallurgica 35 (12) (1987) 2905 – 2914. doi:https://doi.org/10.1016/0001-6160(87)90289-6.
URL http://www.sciencedirect.com/science/article/pii/0001616087902896

[79] H. K. Bhadeshia, Prevention of Hydrogen Embrittlement in Steels, ISIJ International.

[80] W. H. Johnson, On Some Remarkable Changes Produced in Iron and Steel by the Action of Hydrogen and Acids, in: Proceedings of Royal Society of London, 1875.

[81] F. Otto, G. Viswanathan, E. Payton, J. Frenzel, G. Eggeler, On the Effect of Grain Boundary Segregation on Creep and Creep Rupture, Acta Materialia 60 (6) (2012) 2982 – 2998. doi:https://doi.org/10.1016/j.actamat.2012.02.004.
URL http://www.sciencedirect.com/science/article/pii/S1359645412001000

[82] D. Tytko, P.-P. Choi, J. K. wer, A. Kostka, G. Inden, D. Raabe, Microstructural Evolution of a Ni-Baseased Superalloy (617B) at 700°C Studied by Electron Microscopy and Atom Probe Tomography, Acta Materialia 60 (4) (2012) 1731 – 1740. doi:https://doi.org/10.1016/j.actamat.2011.11.020.
URL http://www.sciencedirect.com/science/article/pii/S135964541100810X

[83] W. Betteridge, The Nimonic Alloys and Other Nickel-Base High-Temperature Alloys, Edward Arnold & Co, 1959.

[84] C. T. Sims, W. C. Hagel, The Superalloys, Wiley-interscience, 1972.

[85] E. Ezugwu, Z. Wang, A. Machado, The Machinability of Nickel-Based Alloys: A Review, Journal of Materials Processing Technology 86 (1) (1999) 1 – 16. doi:https://doi.org/10.1016/S0924-0136(98)00314-8.
URL http://www.sciencedirect.com/science/article/pii/S0924013698003148

[86] M. Rombouts, G. Maes, M. Mertens, W. Hendrix, Laser Metal Deposition of Inconel 625: Microstructure and Mechanical Properties, Jounral of Laser Applications 24 (5) (2012) 1–6.

[87] W. E. Frazier, Metal Additive Manufacturing: A Review, Journal of Materials Engineering and Performance 23 (6) (2014) 1917–1928. doi:10.1007/s11665-014-0958-z.
URL https://doi.org/10.1007/s11665-014-0958-z

[88] N. Srinivasan, Y. V. R. K. Prasad, Microstructural Control in Hot Working of IN-718 Superalloy Using Processing Map, Metallurgical and Materials Transactions A 25 (10) (1994) 2275–2284. doi:10.1007/BF02652327.
URL https://doi.org/10.1007/BF02652327

[89] F.-L. Sui, L.-X. Xu, L.-Q. Chen, X.-H. Liu, Processing Map for Hot Working of Inconel 718 Alloy, Journal of Materials Processing Technology 211 (3) (2011) 433 – 440. doi:https://doi.org/10.1016/j.jmatprotec.2010.10.015.
URL http://www.sciencedirect.com/science/article/pii/S0924013610003249

[90] M. Benz, Impurities in Engine Materials: Impact, Reliability and Control, Marcel Dekker Inc, 1999, Ch. Preparation of Clean Superalloys.

[91] R. F. Smart, High Strength and Intergrity Investment Casting, Materials and Design 10 (6) (1989) 301–305.

[92] T. Pettersson, Characterization of Metal Powder Produced by Two Gas Atomising Methods for Thermal Spraying Applications, Master's thesis, KTH Royal Institute of Technology in Stockhom (2015).

[93] B. C. Wilson, J. A. Hickman, G. E. Fuchs, The Effect of Solution Heat Treatment on a Single-Crystal Ni-Based Superalloy, JOM 55 (3) (2003) 35–40. doi:10.1007/s11837-003-0158-z.
URL https://doi.org/10.1007/s11837-003-0158-z

[94] J. Safari, S. Nategh, On The Heat Treatment of Rene-80 Nickel-Base Superalloy, Journal of Materials Processing Technology 176 (1) (2006) 240 – 250. doi:https://doi.org/10.1016/j.jmatprotec.2006.03.165.
URL http://www.sciencedirect.com/science/article/pii/S0924013606003104

[95] C. T. Sims, N. S. Stoloff, W. C. Hagel, Superalloys II.: High-Temperature Materials For Aerospace and Industrial Power, John Wiley & Sons, Inc., 1987.

[96] M. Durand-Chare, The Microstructure of Superalloys, Overseas Publishers Association, 1997.

[97] E. Francis, B. Grant, J. Q. da Fonseca, P. Phillips, M. Mills, M. Daymond, M. Preuss, High-Temperature Deformation Mechanisms in a Polycrystalline Nickel-Base Superalloy Studied by Neutron Diffraction and Electron Microscopy, Acta Materialia 74 (2014) 18 – 29. doi:https://doi.org/10.1016/j.actamat.2014.04.028.
URL http://www.sciencedirect.com/science/article/pii/S1359645414002791

[98] H. Li, J. Sun, M. Hardy, H. Evans, S. Williams, T. Doel, P. Bowen, Effects of Microstructure on High Temperature Dwell Fatigue Crack Growth in a Coarse Grain P/M Nickel Based Superalloy, Acta Materialia 90 (2015) 355 – 369.

[99] J. Gayda, The effect of Stabilization Heat Treatment on the Tensile and Creep Behavior of an Advanced Nickel-Based Disk Alloy, Tech. rep., NASA (2003).

[100] A. Singh, S. Nag, J. Hwang, G. Viswanathan, J. Tiley, R. Srinivasan, H. Fraser, R. Banerjee, Influence of Cooling Rate on the Development of Multiple Generations of γ' Precipitates in a Commercial Nickel Base Superalloy, Materials Characterization 62 (9) (2011) 878 – 886.

[101] R. J. Mitchell, M. Hardy, M. Preuss, S. Tin, Development of γ' morphology in a P/M Rotor Disc Alloys During Heat Treatment, in: Superalloys 2004, Superalloys 2004, 2004, pp. 361 – 370.

[102] P. G. Bailey, HIP Densification of Castings, in: Superalloys 1976, 1976.

[103] Y. Ning, Z. Yao, M. Fu, H. Guo, Recrystallization of the Hot Isostatic Pressed Nickel-Base Superalloy FGH4096: I. Microstructure and Mechanism, Materials Science and Engineering: A 528 (28) (2011) 8065 – 8070. doi:https://doi.org/10.1016/j.msea.2011.07.053.
URL http://www.sciencedirect.com/science/article/pii/S092150931100832X

[104] C. Qiu, M. Attallah, X. Wu, P. Andrews, Influence of Hot Isostatic Pressing Temperature on Microstructure and Tensile Properties of a Nickel-Based Superalloy Powder, Materials Science and Engineering: A 564 (2013) 176 – 185. doi:https://doi.org/10.1016/j.msea.2012.11.084.
URL http://www.sciencedirect.com/science/article/pii/S092150931201636X

[105] J. Li, C. Yuan, J. Guo, J. Hou, L. Zhou, Effect of Hot Isostatic Pressing on Microstructure of Cast Gas-Turbine Vanes of K452 Alloy, Progress in Natural Science: Materials International 24 (6) (2014) 631 – 636. doi:https://doi.org/10.1016/j.pnsc.2014.10.008.
URL http://www.sciencedirect.com/science/article/pii/S1002007114001324

[106] D. M. Lambert, IN718 Additive Manufacturing Properties and Influences, in: JANNAF Conference, 2015.

[107] A. Mostafa, I. P. Rubio, V. Brailovski, M. Jahazi, M. Medraj, Structure, Texture and Phases in 3D Printed IN718 Alloy Subjected to Homogenization and HIP Treatments, Metals 196 (7) (2017) 1–23.

[108] A. Baldan, Rejuvenation procedures to recover creep properties of nickel-base superalloys by heat treatment and hot isostatic pressing techniques, Journal of Materials Science 26 (13) (1991) 3409–3421. doi:10.1007/BF00557126.
URL https://doi.org/10.1007/BF00557126

[109] B. Ruttert, D. Burger, L. M. Roncery, A. B. Parsa, P. Wollgramm, G. Eggeler, W. Theisen, Rejuvenation of Creep Resistance of a Ni-Base Single-Crystal Superalloy by Hot Isostatic Pressing, Materials & Design 134 (2017) 418 – 425. doi:https://doi.org/10.1016/j.matdes.2017.08.059.
URL http://www.sciencedirect.com/science/article/pii/S0264127517308171

[110] N. Loh, K. Sia, An Overview of Hot Isostatic Pressing, Journal of Materials Processing Technology 30 (1) (1992) 45 – 65. doi:https://doi.org/10.1016/0924-0136(92)90038-T.
URL http://www.sciencedirect.com/science/article/pii/092401369290038T

[111] B. Zhou, T. R. Bieler, T.-K. Lee, W. Liu, Characterization of Recrystallization and Microstructure Evolution in Lead-Free Solder Joints Using EBSD and 3D-XRD, Journal of Electronic Materials 42 (2) (2013) 319–331. doi:10.1007/s11664-012-2307-z.
URL https://doi.org/10.1007/s11664-012-2307-z

[112] Y. G. Krasnoperova, M. V. Degtyarev, L. M. Voronova, T. I. Chashchukhina, Effect of Annealing Temperature on the Recrystallization of Nickel with Different Ultradisperse Structures, The Physics of Metals and Metallography 117 (3) (2016) 267–274. doi:10.1134/S0031918X16030078.
URL https://doi.org/10.1134/S0031918X16030078

[113] T. Krämer, L. Eisenhut, L. Germain, D. Rupp, E. Detemple, C. Motz, Assessment of EBSD Analysis and Reconstruction Methods as a Tool for the Determination of Recrystallized Fractions in Hot-Deformed Austenitic Microstructures, Metallurgical and Materials Transactions A 49 (7) (2018) 2795–2802. doi:10.1007/s11661-018-4593-4.
URL https://doi.org/10.1007/s11661-018-4593-4

[114] W. A. Johnson, R. F. Mehl, Reaction Kinetics in Processes of Nucleation and Growth, Transactions of the American Institute of Mining and Metallurgical Engineers 41A (11) (1939) 2713–2775.

[115] M. Todinov, On Some Limitations of the Johnson-Mehl-Avrami-Kolmogorov Equation, Acta Materialia 48 (17) (2000) 4217 – 4224. doi:https://doi.org/10.1016/S1359-6454(00)00280-9.
URL http://www.sciencedirect.com/science/article/pii/S1359645400002809

[116] H. Hallberg, Approaches to Modelling of Recrystallization, Metals 1 (2011) 16–48.

[117] M. Yamazaki, The Effect of Two-Step Solution Treatment on the Creep Rupture Properties of a High Carbon 18Cr-12Ni Stainless Steel, Journal of the Japan Institute of Metals 30 (11) (1966) 1032–1036. doi:10.2320/jinstmet1952.30.11_1032.

[118] M. Kobayashi, M. Yamanoto, O. Miyagawa, T. Saga, F. D, Journal of Iron and Steel Institute 58 (1972) 859–871.

[119] A. Koul, G. Gessinger, On the Mechanism of Serrated Grain Boundary Formation in Ni-Based Superalloys, Acta Metallurgica 31 (7) (1983) 1061 – 1069.

[120] J. L. Carter, J. M. Sosa, P. A. Shade, H. L. Fraser, M. D. Uchic, M. J. Mills, The Potential Link Between High Angle Grain Boundary Morphology and Grain Boundary Deformation in a Nickel-Based Superalloy, Materials Science and Engineering: A 640 (2015) 280 – 286. doi:http://dx.doi.org/10.1016/j.msea.2015.05.031.
URL http://www.sciencedirect.com/science/article/pii/S0921509315005535

[121] D. Dorner, Y. Adachi, K. Tsuzaki, Periodic Crystal Lattice Rotation in Microband Groups in a BCC Metal, Scripta Materialia 57 (8) (2007) 775 – 778. doi:https://doi.org/10.1016/j.scriptamat.2007.06.048.
URL http://www.sciencedirect.com/science/article/pii/S1359646207004253

[122] J. L. Urai, W. D. Means, G. S. Lister, Dynamic Recrystallization of Minerals, Mineral and Rock Deformation: Laboratory Studies – The Paterson Volume.

[123] M. J. Weins, J. J. Weins, Grain Boundary Kinking in f.c.c. Bi-Crystals, The Philosophical Magazine: A Journal of Theoretical Experimental and Applied Physics.

[124] A. Wisniewski, J. Beddoes, Influence of Grain-Boundary Morphology on Creep of a Wrought Ni-Base Superalloy, Materials Science and Engineering: A 510 - 511 (2009) 266 – 272.

[125] G. V. Drunen, J. L. L. Wallace, T. Terada, Hot Isostatic Processing of IN-738 Turbine Blades, in: AGARD Conference Proceedings on Advanced Fabrication Processes, Florence, 1978.

[126] J. Beddoes, W. Wallace, Heat Treatment of Hot Isostatically Processed IN738 Investment Castings, Metallography 13 (1980) 185 – 194.

[127] P. R. Bhowal, E. F. Wright, E. L. Raymond, Effects of Cooling Rate and γ' Morphology on Creep and Stress-Rupture Properties of a Powder Metallurgy Superalloy, Materials & Metallurgical Transactions A 21 (6) (1990) 1709–1717.

[128] H. Danflou, M. Marty, A. Walder, Formation of Serrated Grain Boundaries and Their Effect on the Mechanical Properties in a P/M Nickel Base Superalloy, in: Superalloys 1992, Superalloys 1992, 1992, pp. 63 – 72.

[129] M. F. Henry, Y. S. Yoo, D. Y. Yoon, J. Choi, The Dendritic Growth of γ' Precipitates and Grain Boundary Serration in a Model Nickel-Base Superalloy, Metallurgical Transactions A 24 (8) (1993) 1733–1743.

[130] H. L. Danflou, M. Macia, T. H. Sanders, T. Khan, Mechanisms of Formation of Serrated Grain Boundaries in Nickel Base Superalloys, in: Superalloys 1996, Superalloys 1996, 1996, pp. 119 – 127.

[131] D. Rice, P. Kantzos, B. Hann, J. Neumann, R. Helmink, P/M AAlloy 10 - A 700°C Capable Nickel-Based Superalloy For Turbine Disk Applications, in: Superalloys 2008, Superalloys 2008, 2008, pp. 139 – 147.

[132] L. Jiang, R. Hu, H. Kou, J. Li, G. Bai, H. Fu, The Effect of $M_{23}C_6$ Carbides on the Formation of Grain Boundary Serrations in a Wrought Ni-Based Superalloy, Materials Science and Engineering: A 536 (2012) 37 – 44.

[133] M. Terner, H. U. Hong, J. H. Lee, B. G. Choi, On the Role of Alloying Elements in the Formation of Serrated Grain Boundaries in Ni-Based Alloys, International Journal of Materials Research 107 (2016) 229 – 238.

[134] Y. Shimanuki, Y. Nishino, M. Masui, H. Doi, Microstructure and Mechanical Properties of HIP-Consolidated René 95 Powders, Journal of the Japan Society of Powder and Powder Metallurgy 25 (8) (1978) 262–267. doi:10.2497/jjspm.25.262.

[135] A. K. Koul, R. Thamburaj, Serrated Grain Boundary Formation Potential of Ni-Based Superalloys and Its Implications, Metallurgical and Materials Transactions A 16 (1) (1985) 17–26.

[136] A. K. Koul, R. Castillo, Assessment of Service Induced Microstructural Damage and Its Rejuvenation in Turbine Blades, Metallurgical Transactions A 19 (8) (1988) 2049–2066. doi:10.1007/BF02645208.
URL https://doi.org/10.1007/BF02645208

[137] R. Mitchell, H. Li, Z. Huang, On the Formation of Serrated Grain Boundaries and Fan Type Structures in an Advanced Polycrystalline Nickel-Base Superalloy, Journal of Materials Processing Technology 209 (2) (2009) 1011 – 1017.

[138] X. Lu, Q. Deng, J. Du, J. Qu, J. Zhuang, Z. Zhong, Effect of Slow Cooling Treatment on Microstructure of Difficult Deformation GH4742 Superalloy, Journal of Alloys and Compounds 477 (1) (2009) 100 – 103.

[139] X. Yao, Y. Fang, H. Kim, J. Choi, The Microstructural Characteristics in a Newly Developed Nickel-Base Cast Superalloy, Materials Characterization 38 (2) (1997) 97 – 102.

[140] L. Viskari, Y. Cao, M. Norell, G. Sjoberg, K. Stiller, Grain Boundary Microstructure and Fatigue Crack Growth in Allvac 718Plus Superalloy, Materials Science and Engineering: A 528 (6) (2011) 2570 – 2580. doi:https://doi.org/10.1016/j.msea.2010.11.080.
URL http://www.sciencedirect.com/science/article/pii/S0921509310013675

[141] A. C. Yeh, K. W. Lu, C. M. Kuo, H. Bor, C. N. Wei, Effect of Serrated Grain Boundaries on the Creep Property of Inconel 718 Superalloy, Mater. Sci. Eng., A 530 (2011) 525 – 529.

[142] E. Pickering, H. Mathur, A. Bhowmik, O. Messe, J. Barnard, M. Hardy, R. Krakow, K. Loehnert, H. Stone, C. Rae, Grain-boundary precipitation in Allvac 718Plus, Acta Materialia 60 (6) (2012) 2757 – 2769. doi:https://doi.org/10.1016/j.actamat.2012.01.042.
URL http://www.sciencedirect.com/science/article/pii/S1359645412000808

[143] S. Azadian, L.-Y. Wei, R. Warren, Delta Phase Precipitation in Inconel 718, Materials Characterization 53 (1) (2004) 7 – 16. doi:https://doi.org/10.1016/j.matchar.2004.07.004.
URL http://www.sciencedirect.com/science/article/pii/S1044580304001603

[144] B. Tang, L. Jiang, R. Hu, Q. Li, Correlation Between Grain Boundary Misorientation and $M_{23}C_6$ Precipitation Behaviors in a Wrought Ni-based Superalloy, Materials Characterization 78 (2013) 144 – 150. doi:http://dx.doi.org/10.1016/j.matchar.2013.02.006.
URL http://www.sciencedirect.com/science/article/pii/S1044580313000351

[145] F. Latief, H. Hong, T. Blanc, I. Kim, B. Choi, C. Jo, J. Lee, Influence of Chromium Content on Microstructure and Grain Boundary Serration Formation in a Ternary Ni-xCr-0.1C Model Alloy, Materials Chemistry and Physics 148 (3) (2014) 1194 – 1201. doi:http://dx.doi.org/10.1016/j.matchemphys.2014.09.047.
URL http://www.sciencedirect.com/science/article/pii/S0254058414006294

[146] J. Lee, D. Kim, H. Hong, A New Approach to Strengthen Grain Boundaries for Creep Improvement of a NiCrCoMo Superalloy at 950°C, Materials Science and Engineering: A 625 (2015) 164 – 168.

[147] J. Yoon, H. Jeong, Y. Yoo, H. Hong, Influence of Initial Microstructure on Creep Deformation Behaviors and Fracture Characteristics of Haynes 230 Superalloy at 900°C, Materials Characterization 101 (2015) 49 – 57.

[148] J. Choi, J. Lee, J. Lee, H. Hong, D. Kim, Formation of Serrated Grain Boundaries and Its Effect on Tensile Properties at 950°C in Alloy 617 for Very High Temperature Reactor, Korean Journal of Metals and Materials 53 (2015) 1 – 12.

[149] M. Qian, J. Lippold, The Effect of Annealing Twin-Generated Special Grain Boundaries on HAZ Liquation Cracking of Nickel-Base Superalloys, Acta Materialia 51 (12) (2003) 3351 – 3361. doi:https://doi.org/10.1016/S1359-6454(03)00090-9.
URL http://www.sciencedirect.com/science/article/pii/S1359645403000909

[150] H. Hong, I. Kim, B. Choi, Y. Yoo, C. Jo, On the Mechanism of Serrated Grain Boundary Formation in Ni-Based Superalloys with Low γ' Volume Fraction, in: Superalloys 2012, 2012, pp. 53–61, cited By 7. doi:10.1002/9781118516430.ch6.
URL https://www.scopus.com/inward/record.uri?eid=2-s2.0-84886645318&doi=10.1002%2f9781118516430.ch6&partnerID=40&md5=0c309749eb4963283d01a56b97d25414

[151] R. Hu, G. Bai, J. Li, J. Zhang, T. Zhang, H. Fu, Precipitation Behavior of Grain Boundary $M_{23}C_6$ and Its Effect on Ttensile Properties of Ni-Cr-W Based Superalloy, Materials Science and Engineering: A 548 (2012) 83 – 88. doi:https://doi.org/10.1016/j.msea.2012.03.092.
URL http://www.sciencedirect.com/science/article/pii/S0921509312004649

[152] N. Medvedeva, D. V. Aken, J. Medvedeva, Stability of binary and ternary m23c6 carbides from first principles, Computational Materials Science 96 (2015) 159 – 164. doi:https://doi.org/10.1016/j.commatsci.2014.09.016.
URL http://www.sciencedirect.com/science/article/pii/S0927025614006272

[153] P. Kontis, E. Alabort, D. Barba, D. M. Collins, A. J. Wilkinson, R. C. Reed, On the Role of Boron on Improving Ductility in a New Polycrystalline Superalloy, Acta Materialia 124 (2017) 489 – 500.

[154] J. Larson, S. Floreen, Metallurgical Factors Affecting the Crack Growth Resistance of a Superalloy, Metallurgical Transactions A 8 (1) (1977) 51–55. doi:10.1007/BF02677263.
URL http://dx.doi.org/10.1007/BF02677263

[155] G. Van Drunen, J. Liburidi, W. Wallace, T. Terada, Hot Isostatic Processing of IN-738 Turbine Blades, in: Proceedings of the Conference on Advanced Fabrication Processes (3rd ed.), 1978.

[156] J. Carter, N. Zhou, J. Sosa, P. Shade, A. Pilchak, M. Kuper, Y. Wang, H. Fraser, M. Uchic, M. Mills, Characterization of Strain Accumulation at Grain Boundaries of Nickel-Based Superalloys, in: Superalloys 2012, 2012, pp. 43–52. doi:10.1002/9781118516430.ch5.
URL http://dx.doi.org/10.1002/9781118516430.ch5

[157] J. L. Carter, M. W. Kuper, M. D. Uchic, M. J. Mills, Characterization of Localized Deformation Near Grain Boundaries of Superalloy René-104 at Elevated Temperature, Materials Science and Engineering: A 605 (2014) 127 – 136.

[158] Y. Zhang, F. Marquis, Effect of Grain Boundary Morphology and Dislocation Substructure on the Creep Behaviour of Unimet 710, in: Superalloys 1996, 1996.

[159] E. Alabort, D. Barba, S. Sulzer, M. Liβner, N. Petrinic, R. Reed, Grain Boundary Properties of a Nickel-Based Superalloy: Characterisation and Modelling, Acta Materialia 151 (2018) 377–394.

[160] M. J. Blackburn, R. A. Sprague, Production of Components by Hot Isostatic Pressing of Nickel-Base Superalloy Powders, Metals Technology 4 (1) (1977) 388–395. arXiv:https://doi.org/10.1179/030716977803292231, doi:10.1179/030716977803292231.
URL https://doi.org/10.1179/030716977803292231

[161] C. Ducrocq, A. Lasalmonie, Y. Honnorat, N18, a New Damage Tolerant PM Superalloy for High Temperature, in: Superalloy 1988, 1988.

[162] K. Chen, J. Wu, H. Shi, X. Chen, Z. Shen, M. Zhang, L. Zhang, A. Shan, Transition of Deformation Behavior and its Related Microstructure Evolution in Nimonic 80A under Hot-To-Warm Working, Materials Characterization 106 (2015) 175 – 184. doi:http://dx.doi.org/10.1016/j.matchar.2015.05.034.
URL http://www.sciencedirect.com/science/article/pii/S1044580315001928

[163] J. Li, R. Wahi, Investigation of γ/γ' Lattice Mismatch in the Polycrystalline Nickel-Base Superalloy IN738LC: Influence of Heat Treatment and Creep Deformation, Acta Metallurgica et Materialia 43 (2) (1995) 507 – 517. doi:https://doi.org/10.1016/0956-7151(94)00252-D.
URL http://www.sciencedirect.com/science/article/pii/095671519400252D

[164] H.-A. Kuhn, H. Biermann, T. U. r, H. Mughrabi, An X-ray Study of Creep-Deformation Induced Changes of the Lattice Mismatch in the γ'-Hardened Monocrystalline Nickel-Base Superalloy SRR 99, Acta Metallurgica et Materialia 39 (11) (1991) 2783 – 2794. doi:https://doi.org/10.1016/0956-7151(91)90095-I.
URL http://www.sciencedirect.com/science/article/pii/095671519190095I

[165] J. Zhang, J. Wang, H. Harada, Y. Koizumi, The Effect of Lattice Misfit on the Dislocation Motion in Superalloys During High-Temperature Low-Stress Creep,

Acta Materialia 53 (17) (2005) 4623 – 4633. doi:https://doi.org/10.1016/j.actamat.2005.06.013.
URL http://www.sciencedirect.com/science/article/pii/S135964540500368X

[166] L. Dirand, J. Cormier, A. Jacques, J.-P. Chateau-Cornu, T. Schenk, O. Ferry, P. Bastie, Measurement of the Effective γ/γ' Lattice Mismatch During High Temperature Creep of Ni-Based Single Crystal Superalloy, Materials Characterization 77 (2013) 32 – 46. doi:https://doi.org/10.1016/j.matchar.2012.12.003.
URL http://www.sciencedirect.com/science/article/pii/S1044580312003142

[167] L. Mitsubishi Hitachi Power Systems, MHPS Gas Turbine M501J/M701J, Mitsubishi Hitachi Power Systems, Japan.

[168] M. Yuri, J. Masada, K. Tsukagoshi, E. Ito, S. Hada, Development of 1600°C-Class High Efficiency Gas Turbine for Power Generation Applying J Type Technology, Mitsubushi Heavy Industries Technical Review 50 (3).

[169] A. J. Wilkinson, G. Meaden, D. J. Dingley, High-Resolution Elastic Strain Measurement From Electron Backscatter Diffraction Patterns: New Levels of Sensitivity, Ultramicroscopy 106 (4) (2006) 307 – 313.

[170] A. J. Wilkinson, D. Randman, Determination of Elastic Strain Fields and Geometrically Necessary Dislocation Distributions Near Nanoindents Using Electron Back Scatter Diffraction, Philosophical Magazine 90 (9) (2010) 1159–1177.

[171] T. Britton, A. J. Wilkinson, High Resolution Electron Backscatter Diffraction Measurements of Elastic Strain Variations in the Presence of Larger Lattice Rotations, Ultramicroscopy 114 (2012) 82 – 95.

[172] V. Randle, Special Boundaries and Grain Boundary Plane Engineering, Scripta Materialia 54 (6) (2006) 1011 – 1015, viewpoint Set No. 40: Grain Boundary Engineering. doi:http://dx.doi.org/10.1016/j.scriptamat.2005.11.050.
URL http://www.sciencedirect.com/science/article/pii/S1359646205007979

[173] T. Liu, S. Xia, H. Li, B. Zhou, Q. Bai, The Highly Twinned Grain Boundary Network Formation During Grain Boundary Engineering, Materials Letters 133 (2014) 97 – 100. doi:https://doi.org/10.1016/j.matlet.2014.06.166.
URL http://www.sciencedirect.com/science/article/pii/S0167577X14012300

[174] M. Detrois, J. Rotella, R. L. Goetz, R. C. Helmink, S. Tin, Grain Boundary Engineering of Powder Processed Ni-Base Superalloy RR1000: Influence of the Deformation Parameters, Materials Science and Engineering: A 627 (2015) 95 – 105. doi:http://dx.doi.org/10.1016/j.msea.2014.12.112.
URL http://www.sciencedirect.com/science/article/pii/S0921509314016232

[175] C. M. Barr, A. C. Leff, R. W. Demott, R. D. Doherty, M. L. Taheri, Unraveling the Origin of Twin Related Domains and Grain Boundary Evolution During

Grain Boundary Engineering, Acta Materialia 144 (2018) 281 – 291. doi:https://doi.org/10.1016/j.actamat.2017.10.007.
URL http://www.sciencedirect.com/science/article/pii/S1359645417308558

[176] A. Devaraj, L. Kovarik, E. Kautz, B. Arey, S. Jana, C. Lavender, V. Joshi, Grain Boundary Engineering to Control the Discontinuous Precipitation in Multicomponent U10Mo Alloy, Acta Materialia 151 (2018) 181 – 190. doi:https://doi.org/10.1016/j.actamat.2018.03.039.
URL http://www.sciencedirect.com/science/article/pii/S1359645418302374

[177] Y. J. Kwon, S.-P. Jung, B.-J. Lee, C. S. Lee, Grain Boundary Engineering Approach to Improve Hydrogen Embrittlement Resistance in FeMnC TWIP Steel, International Journal of Hydrogen Energy 43 (21) (2018) 10129 – 10140. doi:https://doi.org/10.1016/j.ijhydene.2018.04.048.
URL http://www.sciencedirect.com/science/article/pii/S036031991831173X

[178] T. Liu, S. Xia, Q. Bai, B. Zhou, L. Zhang, Y. Lu, T. Shoji, Three-Dimensional Study of Grain Boundary Engineering Effects on Intergranular Stress Corrosion Cracking of 316 Stainless Steel in High Temperature Water, Journal of Nuclear Materials 498 (2018) 290 – 299. doi:https://doi.org/10.1016/j.jnucmat.2017.10.004.
URL http://www.sciencedirect.com/science/article/pii/S0022311517306190

[179] Y. T. Tang, A. J. Wilkinson, R. C. Reed, Grain Boundary Serration in Nickel-Based Superalloy Inconel 600: Generation and Effects on Mechanical Behavior, Metallurgical and Materials Transactions A 49 (9) (2018) 4324–4342. doi:10.1007/s11661-018-4671-7.
URL https://doi.org/10.1007/s11661-018-4671-7

[180] J. Jiang, T. B. Britton, A. J. Wilkinson, The Orientation and Strain Dependence of Dislocation Structure Evolution in Monotonically Deformed Polycrystalline Copper, International Journal of Plasticity 69 (2015) 102 – 117.

[181] A. Ametani, The Application of the Fast Fourier Transform to Electrical Transient Phenomena, International Journal of Electrical Engineering Education 10 (4) (1973) 277–287.

[182] S. V. Tsinopoulos, An Advanced Boundary Element/Fast Fourier Transform Axisymmetric Formulation for Acoustic Radiation and Wave Scascatter Problems, The Journal of the Acoustical Society of America 105 (3) (1999) 1517–1526.

[183] L. D. Mitchell, Improved Methods for the Fast Fourier TransTransform (FFT) Calculation of the Frequency Response Function, Journal of Mechanical Design.

[184] B. Kaplan, A. Blomqvist, C. Arhammar, M. Selleby, S. Norgren, Structural Determination of Cr, Co_7C_3, in: 18th Plansee Seminar, 2013.

[185] H. McQueen, N. Ryan, E. Konopleva, X. Xia, Formation and Application of Grain Boundary Serrations, Canadian Metallurgical Quarterly 34 (3) (1995) 219 – 229. doi:http://dx.doi.org/10.1016/0008-4433(95)00001-E.
URL http://www.sciencedirect.com/science/article/pii/000844339500001E

[186] S. Gu, C. Zhang, L. Zhang, W. Shen, Characteristics of Metadynamic Recrystallization of Nimonic 80A Superalloy, Journal of Materials Research 30 (2015) 538–546. doi:10.1557/jmr.2015.7.
URL http://journals.cambridge.org/article_S0884291415000072

[187] M. Zouari, N. Bozzolo, R. E. Loge, Mean Field Modelling of Dynamic and Post-Dynamic Recrystallization During Hot Deformation of Inconel 718 in the Absence of δ' Phase Particles, Materials Science and Engineering: A 655 (8) (2016) 408 – 424. doi:http://dx.doi.org/10.1016/j.msea.2015.12.102.
URL http://www.sciencedirect.com/science/article/pii/S0921509315307930

[188] J. Tuleja, Z. Zatorski, Numerical Modelling of Micro-Stresses in Carbonised Austenitic Cast Steel under Rapid Cooling Condition, Archives of Metallurgy and Materials 62 (2) (2017) 635–641.

[189] F. Ernst, D. Li, H. Kahn, G. M. Michal, A. H. Heuer, The Carbide M7C3 in Low-Temperature-Carburized Austenitic Stainless Steel, Acta Materialia 59 (6) (2011) 2268 – 2276. doi:https://doi.org/10.1016/j.actamat.2010.11.058.
URL http://www.sciencedirect.com/science/article/pii/S135964541000813X

[190] M. A. Rouault, P. Herpin, M. R. Fruchart, Etude cristallographique des carbures Cr_7C_3et Mn_7C_3, Annales de Chimie 5 (1970) 461.
URL http://nanocrystallography.org/information_card.php?cif=1009019

[191] S. Raju, K. Sivasubramanian, D. Ramachandran, G. Panneerselvam, A. Banerjee, E. Mohandas, M. P. Antony, Thermal Expansion Studies On Inconel-600 By High Temperature X-Ray Diffraction, Journal of Nuclear Materials.

[192] K. K. Mehta, R. Mitra, S. Chawla, Effect of Post-Solutionizing Cooling Rate on Microstructure and Low Cycle Fatigue Behavior of a Cast Nickel Based Superalloy, Materials Science and Engineering: A 611 (2014) 280 – 289.

[193] J. R. Davis, ASM Specialty Handbook: Heat-Resistant Material, ASM International, 1997.

[194] T. J. A. Slater, R. S. Bradley, G. Bertali, R. Geurts, S. M. Northover, M. G. Burke, S. J. Haigh, T. L. Burnett, P. J. Withers, Multiscale Correlative Tomography: An Investigation of Creep Cavitation in 316 Stainless Steel, Scientific Reports.

[195] P. S. Karamched, A. J. Wilkinson, High Resolution Electron Back-Scatter Diffraction Analysis of Thermally and Mechanically Induced Strains Near Carbide Inclusions in a Superalloy, Acta Materialia 59 (1) (2011) 263 – 272.

[196] Z. Zhu, H. Basoalto, N. Warnken, R. C. Reed, A Model for the Creep Deformation Behaviour of Nickel-Based Single Crystal Superalloys, Acta Materialia 60 (12) (2012) 4888 – 4900.

[197] G. Palumbo, P. King, P. Lichtenberger, K. Aust, U. Erb, Grain Boundary Structure Control for Intergranular Stress-Corrosion Resistance, in: MRS Proceedings, 1991.

[198] E. Lehockey, G. Palumbo, On the Creep Behaviour of Grain Boundary Engineered Nickel, Materials Science and Engineering: A 237 (2) (1997) 168 – 172. doi:https://doi.org/10.1016/S0921-5093(97)00126-3.
URL http://www.sciencedirect.com/science/article/pii/S0921509397001263

[199] M. F. Ashby, C. Gandhi, D. Taplin, Overview No. 3 Fracture-Mechanism Maps and Their Construction for F.C.C. Metals and Alloys, Acta Metallurgica 27 (5) (1979) 699 – 729.

[200] H. J. Frost, M. F. Ashby, Deformation-Mechanism Maps, The Plasticity and Creep of Metals and Ceramics, Pregamon Press, 1982, 1982.

[201] B. Foss, S. Gray, M. Hardy, S. Stekovic, D. McPhail, B. Shollock, Analysis of Shot-Peening and Residual Stress Relaxation in the Nickel-Based Superalloy RR1000, Acta Materialia 61 (7) (2013) 2548 – 2559. doi:https://doi.org/10.1016/j.actamat.2013.01.031.
URL http://www.sciencedirect.com/science/article/pii/S135964541300058X

[202] G. H. Gessinger, M. J. Bomford, Powder Metallurgy of Superalloys, International Metallurgical Reviews 19 (1) (1974) 51–76. arXiv:https://doi.org/10.1179/imtlr.1974.19.1.51, doi:10.1179/imtlr.1974.19.1.51.
URL https://doi.org/10.1179/imtlr.1974.19.1.51

[203] C. Yuan, J. Guo, H. Yang, S. Wang, Deformation Mechanism For High Temperature Creep of A Directionally Solidified Nickel-Base Superalloy, Scripta Materialia 39 (7) (1998) 991 – 997. doi:https://doi.org/10.1016/S1359-6462(98)00255-3.
URL http://www.sciencedirect.com/science/article/pii/S1359646298002553

[204] M. Naeem, Implications of Day Temperature Variation For An Aero-Engine's HP Turbine-Blade's Creep Life-Consumption, Aerospace Science and Technology 13 (1) (2009) 27 – 35. doi:https://doi.org/10.1016/j.ast.2008.02.004.
URL http://www.sciencedirect.com/science/article/pii/S1270963808000321

[205] P. Wollgramm, D. Bürger, A. B. Parsa, K. Neuking, G. Eggeler, The Effect of Stress, Temperature and Loading Direction on The Creep Behaviour of Ni-Base Single Crystal Superalloy Miniature Tensile Specimens, Materials at High Temperatures 33 (4-5) (2016) 346–360. arXiv:https://doi.org/10.1080/09603409.

2016.1186414, doi:10.1080/09603409.2016.1186414.
URL https://doi.org/10.1080/09603409.2016.1186414

[206] J. Weertman, P. Shahinian, Creep of Polycrystalline Nickel, Journal of Metals 8 (10) (1956) 1223–1226. doi:10.1007/BF03377854.
URL https://doi.org/10.1007/BF03377854

[207] A. Koul, R. Castillo, K. Willett, Creep Life Predictions in Nickel-Based Superalloys, Materials Science and Engineering 66 (2) (1984) 213 – 226. doi:https://doi.org/10.1016/0025-5416(84)90182-4.
URL http://www.sciencedirect.com/science/article/pii/0025541684901824

[208] T. Ohtani, H. Ogi, M. Hirao, Acoustic Damping Characterization and Microstructure Evolution in Nickel-Based Superalloy During Creep, International Journal of Solids and Structures 42 (9) (2005) 2911 – 2928. doi:https://doi.org/10.1016/j.ijsolstr.2004.09.037.
URL http://www.sciencedirect.com/science/article/pii/S0020768304005396

[209] A. Bertram, J. Olschewski, Anisotropic Creep Modelling of The Single Crystal Superalloy SRR99, Computational Materials Science 5 (1) (1996) 12 – 16, computational Modelling of the Mechanical Behaviour of Materials. doi:https://doi.org/10.1016/0927-0256(95)00053-4.
URL http://www.sciencedirect.com/science/article/pii/0927025695000534

[210] S. Linn, A. Scholz, M. Oechsner, C. Berger, O. Luesebrink, Evaluation of Property Scatter of Ni-Base Alloy in 738 LC, Materials Science and Engineering: A 528 (13) (2011) 4676 – 4682. doi:https://doi.org/10.1016/j.msea.2011.02.052.
URL http://www.sciencedirect.com/science/article/pii/S0921509311002164

[211] N. Roy, S. Bose, R. Ghosh, Stochastic Aspects of Evolution of Creep Damage in Austenitic Stainless Steel, Materials Science and Engineering: A 527 (18) (2010) 4810 – 4817. doi:https://doi.org/10.1016/j.msea.2010.04.013.
URL http://www.sciencedirect.com/science/article/pii/S0921509310004107

[212] T. Pollock, A. Argon, Creep Resistance of CMSX-3 Nickel Base Superalloy Single Crystals, Acta Metallurgica et Materialia 40 (1) (1992) 1 – 30. doi:https://doi.org/10.1016/0956-7151(92)90195-K.
URL http://www.sciencedirect.com/science/article/pii/095671519290195K

[213] L. Agudo Jácome, P. Nörtershäser, C. Somsen, A. Dlouhý, G. Eggeler, On The Nature of γ' Phase Cutting and Its Effect on High Temperature and Low Stress Creep Anisotropy of Ni-Base Single Crystal Superalloys, Acta Materialia 69 (2014) 246 – 264. doi:https://doi.org/10.1016/j.actamat.2014.01.021.
URL http://www.sciencedirect.com/science/article/pii/S1359645414000305

[214] G. Wang, J. Liu, J. Liu, T. Jin, X. Sun, X. Sun, Z. Hu, High Temperature Stress Rupture Anisotropy of a Ni-Based Single Crystal Superalloy, Journal of Materials

& Technology 32 (10) (2016) 1003 – 1007. doi:https://doi.org/10.1016/j.jmst.2016.08.018.
URL http://www.sciencedirect.com/science/article/pii/S1005030216301402

[215] Y. Lu, G. Xie, D. Wang, S. Zhang, W. Zheng, J. Shen, L. Lou, J. Zhang, Anisotropy of High Temperature Creep Properties of a Co-Base Single Crystal Superalloy, Materials Science and Engineering: A 720 (2018) 69 – 74. doi:https://doi.org/10.1016/j.msea.2018.02.063.
URL http://www.sciencedirect.com/science/article/pii/S0921509318302715

[216] M. McLean, B. F. Dyson, Modeling the Effects of Damage and Microstructural Evolution on the Creep Behavior of Engineering Alloys, Journal of Engineering Materials and Technology 122 (2000) 273–278.

[217] B. F. Dyson, M. McLean, Micromechanism-Quantification for Creep Constitutive Equations, in: S. Murakami, N. Ohno (Eds.), IUTAM Symposium on Creep in Structures, Springer Netherlands, Dordrecht, 2001, pp. 3–16.

[218] H. Basoalto, S. K. Sondhi, B. F. Dyson, M. McLean, A Generic Microstructure-Explicit Model of Creep in Nickel-base Superalloys, in: Superalloys 2004, 2004.

[219] B. F. Dyson, Microstructure Based Creep Constitutive Model For Precipitation Strengthened Alloys: Theory And Application, Materials Science and Technology 25 (2) (2009) 213–220. arXiv:https://doi.org/10.1179/174328408X369348, doi:10.1179/174328408X369348.
URL https://doi.org/10.1179/174328408X369348

[220] Y.-K. Kim, D. Kim, H.-K. Kim, C.-S. Oh, B.-J. Lee, An Intermediate Temperature Creep Model for Ni-Based Superalloys, International Journal of Plasticity 79 (2016) 153 – 175. doi:https://doi.org/10.1016/j.ijplas.2015.12.008.
URL http://www.sciencedirect.com/science/article/pii/S0749641915002077

[221] A. Inoue, T. Masumoto, Carbide Reactions ($M_3C \rightarrow M_7C_3 \rightarrow M_{23}C_6 \rightarrow M_6C$) During Tempering of Rapidly Solidified High Carbon Cr-W and Cr-Mo Steels, Metallurgical Transactions A 11 (5) (1980) 739–747. doi:10.1007/BF02661203.
URL https://doi.org/10.1007/BF02661203

[222] R. A. MacKay, R. D. Maier, The Influence of Orientation on the Stress Rupture Properties of Nickel-Base Superalloy Single Crystals, Metallurgical Transactions A 13 (10) (1982) 1747–1754. doi:10.1007/BF02647830.
URL https://doi.org/10.1007/BF02647830

[223] N. Matan, D. Cox, P. Carter, M. Rist, C. Rae, R. Reed, Creep of CMSX-4 Superalloy Single Crystals: Effects of Misorientation and Temperature, Acta Materialia 47 (5) (1999) 1549 – 1563. doi:https://doi.org/10.1016/S1359-6454(99)00029-4.
URL http://www.sciencedirect.com/science/article/pii/S1359645499000294

[224] F. Adziman, Y. T. Tang, R. C. Reed, Private Communication on Crystal Plasticity Modelling (2017).

[225] S. Floreen, J. M. Davidson, The Effects of B and Zr on The Creep And Fatigue Crack Growth Behavior of a Ni-Base Superalloy, Metallurgical Transactions A 14 (4) (1983) 895–901. doi:10.1007/BF02644294.
URL https://doi.org/10.1007/BF02644294

[226] H. E. Huang, C. H. Koo, Effect of Zirconium on Microstructure and Mechanical Properties of Cast Fine-Grain CM247LC Superalloy, Materials Transactions 45 (2) (2004) 554–561. doi:10.2320/matertrans.45.554.